

Optical response in planar heterostructures:
From artificial magnetism to Angstrom-scale
metamaterials

Thesis by
Georgia Theano Papadakis

In Partial Fulfillment of the Requirements for the
degree of
Doctor of Philosophy

CALIFORNIA INSTITUTE OF TECHNOLOGY
Pasadena, California

2018
Defended February 23, 2018

© 2018

Georgia Theano Papadakis
ORCID: 0000-0001- 8107-9221

All rights reserved

For Souzanna Papadopoulou &
for John and Katerina Papadakis,
with gratitude to Eleftherios Economou and to Pochi Yeh.

*“Εμείς δεν τραγουδάμε για να ξεχωρίσουμε αδερφέ μου απ’τον κόσμο,
εμείς τραγουδάμε για να σμίξουμε το κόσμο.”*

*“We do not sing to distinguish ourselves from the world,
my brother, we sing to connect the world.”*

The Fourth Dimension, Yannis Ritsos

ACKNOWLEDGEMENTS

Being admitted to Caltech in the graduate program of Applied Physics has transformed my life path and my perspective. The completion of my PhD is the result of the support that I received from numerous people to whom I will always be grateful.

I thank Prof. Kiriaki Kiriakie, at the National Technical University of Athens (NTUA) in Greece, for motivating me to pursue a PhD and for believing in me. I also thank Prof. Ioannis Roumeliotis at NTUA for teaching me most of what I know about electromagnetism, and for his support through these years.

By pursuing science, I have had the privilege to travel much and meet extraordinary people around the world. I have been lucky to conduct research in Greece (NTUA), in Switzerland (CERN), in the Netherlands (AMOLF), and at Caltech. The support I received from young, exceptionally bright friends and colleagues has been instrumental. I thank Dr. Dimitris Calavrouziotis, Dr. Loukas Gouskos, Maria Anastasiou, Prof. Kosmas L. Tsakmakidis, Dr. Ruben Maas, Dr. Pankaj K. Jha, and Dr. Giulia Tagliabue for what they taught me and for their support and friendship.

Large portions of the work I conducted at Caltech was supported by Northrop Grumman Corporation, and particularly NG NEXT. I thank Dr. Luke Sweatlock, Dr. John Spargo, Dr. Philip Hon, and the staff at NG NEXT for supporting my research and investing in me. I also thank Prof. Prihena Narang at Harvard for her support and for always believing in my research.

When I arrived at Caltech I knew very little about physics. I will always remember the first years at Caltech as extremely eye-opening and creative ones. I thank the Applied Physics Class of 2012 for many hours of studying together, and particularly Magnus Haw, Teddy Albertson, Yu-Hung Lai, and Matthew Fishman. I also thank Prof. Sandra Troian, the option representative for the Applied Physics Class of 2012, for her advice and encouragement, and for enjoyable conversations and exchange of ideas.

At Caltech I have made great friends. I thank Magnus Haw, Dr. Costas Sideris, and Dr. Evan Miyazono for their compassion and friendship. I thank Dr. Gina Panopoulou, Jane Herriman, Dr. Victoria Chernow, Dr. Samatha Johnson, and Prof. Rebecca Saive for being exceptional friends and also role models

for women in tech, science, and engineering. I also thank my good friend Dr. Christos Santis for his support and guidance. I am grateful to Dr. Panagiotis Vergados and Dr. Christos Thrapoulidis for their unwavering support, and for many empowering conversations and fun times. I have received invaluable advice from Dr. Vasilios Christopoulos and I have enjoyed many fun times with Marilena Dimotsantou, to whom I wish the best.

My officemates have made my time at work particularly enjoyable. I thank Dr. Ragip Pala for his unwavering support, and I wish him the best. I thank Dr. Ognjen Ilic for many long conversations and exchange of ideas and for his advice and encouragement. I thank Prof. Howard Lee, who inspired me with his determination and hard work as an exceptional experimentalist, and I am grateful for what he taught me. I thank my friend and collaborator Jeremy Brouillet for his hard work in our joint projects and for his support and friendship. I also thank Ghazaleh Kafaie for great times in the office and for her candid friendship.

My most enjoyable work at Caltech was conducted together with Dr. Artur Davoyan and Dagny Fleischman. I thank Artur for his guidance, for teaching me new things, and for being a good friend. His clarity of mind is limitless and I envy his drive and talent in physics. I thank Dagny, who is an impressive material scientist, for being exceptionally professional while also being a supportive friend and a wonderful source of optimism, and for believing in my research.

As a graduate student I was very fortunate to collaborate with leaders in the field of photonics. I thank Prof. Albert Polman at AMOLF for hosting me in his group in 2014. I also thank Prof. Shankar Sundararaman at RPI and Prof. Marin Soljacic at MIT for their support and collaboration through NG NEXT in the years 2016-2017. I thank Prof. Nader Engheta at UPENN for our collaboration, for his trust and support, and for being an academic role model. I also thank Prof. Costas Soukoulis at Iowa State University and IESL FORTH (Greece) for his support through the years.

I greatly appreciate the insightful feedback, honesty, and kindness of Prof. Keith Schwab. I thank Prof. Kerry Vahala, Prof. Hyuck Choo, Prof. Andrei Faraon, and Prof. Chiara Daraio, who took the time to be in my candidacy and thesis committees. I also thank Prof. Amnon Yariv for our enjoyable conversations and, most importantly, for introducing me to his former student,

Prof. Pochi Yeh.

I reached out to Prof. Pochi Yeh during my second year at Caltech. He invited me to his house to discuss my research, without knowing who I was or what I was looking for. I am still in awe for his humbleness, I admire his pure academic curiosity and his generosity in providing all he knows. Prof. Yeh has been instrumental in my academic path; he has been my teacher and supporter, and I will never be able to thank him enough.

I have been fortunate to be given a family of great kindness and generosity. None of what I have done so far would have been possible without guidance from my father, John. He has been my mental anchor and my source of courage and perseverance. I thank my mother for providing me a role model for women in science and for being my source of optimism. I thank my god-mother Souzanna Papadopoulou for teaching me mathematics and motivating my curiosity. But most importantly, I thank her for her generosity, for her unwavering trust in me, and for being courageous in difficult times. I am sincerely indebted to Prof. Eleftherios Economou for noticing potential in me and encouraging me to never stop learning. I also thank my siblings Paul, Denise, Alison, and Sterg for their support and love.

I am grateful for the generous financial support for the work in this thesis, mainly provided by the National Science Foundation, the American Association for University Women and NG NEXT at Northrop Grumman Corporation. I thank Christy Jenstad, Tiffany Kimoto, Jennifer Blankeship, Jonathan Gross, and Lyann Lau for their support, advice, and enthusiasm through these years.

Finally, with much gratitude, I thank my advisor, Prof. Harry A. Atwater, for investing in me and giving me the opportunity to come to Caltech. I am honored for the freedom he has given me and I appreciate his trust in me, his support, and his encouragement. I am in debt to him for setting the bar high, and I admire his ethics and his tireless enthusiasm for science.

Georgia Theano Papadakis
February 2018
Pasadena, CA

ABSTRACT

The idea of expanding the range of properties of natural substances with artificial matter was introduced by V. G. Veselago in 1967. Since then, the field of metamaterials has dramatically advanced. Man-made structures can now exhibit a plethora of extraordinary electromagnetic properties, such as negative refraction, optical magnetism, and super-resolution imaging. Typical metamaterial motifs include split ring resonators, dielectric and plasmonic particles, fishnet and wire arrays. The principle of operation of these elements is now well-understood, and they are being exploited for practical applications on a global scale, ranging from telecommunications to sensing and biomedicine, in the radio frequency and terahertz domains. Accessing and controlling optical and near-infrared phenomena requires scaling down the dimensions of metamaterials to the nanometer regime, pushing the limits of state-of-the-art nanolithography and requiring structurally less complex geometries. Hence, within the last decade, research in metamaterials has revisited a simpler, lithography-free structure, particularly planar arrangements of alternating metal and dielectric layers, termed hyperbolic metamaterials. Such media are readily realizable with well-established thin-film deposition techniques. They support a rich canvas of properties ranging from surface plasmonic propagation to negative refraction, and they can enhance the photoluminescence properties of quantum emitters at any frequency range.

Here, we introduce a computational approach that allows tailoring the dielectric and magnetic effective properties of planar metamaterials. Previously, planar hyperbolic metamaterials have been considered non-magnetic. In contrast, we show theoretically and experimentally that planar arrangements composed of non-magnetic constituents can be engineered to exhibit a non-trivial magnetic response. This realization simplifies the structural requirements for tailoring optical magnetism up to very high frequencies. It also provides access to previously unexplored phenomena, for example artificially magnetic plasmons, for which we perform an analysis on the basis of available materials for achieving polarization-insensitive surface wave propagation. By combining the concept of metamaterials' homogenization with previous transfer matrix approaches, we develop a general computational method for surface waves calculations that is free of previous assumptions, for example infinite or purely periodic media. Furthermore, we theoretically demonstrate that hyper-

bolic metamaterials can be dynamically tunable via carrier injection through external bias, using transparent conductive oxides and graphene, at visible and infrared frequencies, respectively. Lastly, we demonstrate that planar graphene-based van der Waals heterostructures behave effectively as supermetals, exhibiting reflective properties that surpass the reflectivity of gold and silver that are currently considered the state-of-the-art materials for mirroring applications in space applications. The (meta)materials we introduce exhibit an order-of-magnitude lower mass density, making them suitable candidates for future light-sail technologies intended for space exploration.

LIST OF PUBLICATIONS

G. T. Papadakis, A. Davoyan, P. Yeh, H. A. Atwater, “Phonons and excitons for omnipolarization surface waves”, (in preparation) (2018)

G.T.P. developed the theoretical model together with A.D., carried out the numerical simulations and calculations, and lead the writing of the manuscript.

G. T. Papadakis, D. Fleischman, A. Davoyan, P. Yeh, H. A. Atwater, “Optical Magnetism in Planar Metamaterial Heterostructures”, *Nature Communications* 9 (2018), p. 296. DOI: 10.1038/s41467-017-02589-8.

G.T.P. developed the theoretical model together with A.D., carried out the numerical simulations and calculations, the experimental measurements and ellipsometric fittings, and lead the writing of the manuscript.

G. T. Papadakis, P. Narang, R. Sundararaman, N. Rivera, H. Buljan, N. Engheta, M. Soljagic, “Ultra-light Å-scale Optimal Optical Reflectors”, *ACS Photonics* 5 (2018), p. 384. DOI: 10.1021/acsp Photonics.7b00609.

G.T.P. participated in developing the theoretical model, carried out the numerical calculations of the photonic properties discussed in the manuscript, and participated in the writing of the manuscript.

G. T. Papadakis H. A. Atwater, “Field effect-induced tunability in hyperbolic metamaterials”, *Phys. Rev. B* 92 (2015), p. 184101. DOI: 10.1103/PhysRevB.92.184101.

G.T.P. developed the theoretical model, carried out the numerical calculations and the writing of the manuscript.

G. T. Papadakis, P. Yeh H. A. Atwater, “Retrieval of material parameters for uniaxial metamaterials”, *Phys. Rev. B* 91 (2015), p. 155406. DOI: 10.1103/PhysRevB.91.155406.

G.T.P. developed the theoretical model, carried out the numerical calculations and the writing of the manuscript.

H. W. Lee, G. T. Papadakis, S. P. Burgos, K. Chander, A. Kriesch, R. Pala, U. Peschel, H. A. Atwater, “Nanoscale Conducting Oxide PlasMOSTor”, *Nano Lett.* 14 (2014), p. 6463-6468. DOI: 10.1021/nl502998z.

G.T.P. participated in carrying out the numerical calculations, performed experimental characterization of conducting oxides, and participated in the writing of the manuscript.

TABLE OF CONTENTS

Acknowledgements	iv
Abstract	vii
Table of Contents	x
List of Illustrations	xii
List of Tables	xiv
Chapter I: Introduction: Metamaterials today	1
1.1 From atoms to materials, from resonators to metamaterials	1
1.2 Negative refraction: The wire array and the split ring resonator	5
1.3 Planar heterostructures: from photonic crystals to metamaterials	7
1.4 Hyperbolic metamaterials	10
1.5 Scope and structure of the thesis	13
Chapter II: Metamaterials' homogenization	15
2.1 The concept of homogenization and S-parameter retrieval	15
2.2 Effective medium approximations and the Maxwell Garnett result for 1D metamaterials	19
2.3 The Bloch wavenumber	21
2.4 S-parameter retrieval for 1D metamaterials	23
2.5 A sanity check	27
2.6 Comparison between S-parameter retrieval and EMAs: $\mu \neq 1!$	29
2.7 Conclusion	32
Chapter III: Artificial magnetism in planar metamaterials	33
3.1 Previous approaches: Artificial magnetism in 3D and 2D	33
3.2 Parameter space for μ and ϵ	34
3.3 Artificial magnetism in 1D	36
3.4 Another sanity check: Impedance matching	39
3.5 Experimental method: Spectroscopic ellipsometry for metamaterials	41
3.6 Experimental verification of artificial magnetism in 1D	42
3.7 Implications of $\mu \neq 1$ for bulk propagating modes	45
3.8 Implications of $\mu \neq 1$ for surface waves	48
3.9 Conclusion	50
Chapter IV: Beyond plasmons: Omnipolarization surface waves	51
4.1 " <i>Large permittivity begets high-frequency magnetism</i> "	51
4.2 Material requirements for surface-confined propagation beyond plas- monics	55
4.3 Generalized retrieval approach for surface wave computations	58
4.4 Figures of merit for surface-confined propagation	64
4.5 Theory of plasmons and results for silver	64
4.6 Phonons and excitons	68
4.7 Surface-confined waves on SiC on Si	72
4.8 Surface-confined waves on WS ₂ on Si	74
4.9 The case of a plasmon and a phonon	75

4.10	The case of a plasmon and an exciton	79
4.11	Conclusion	81
Chapter V: Active tunability in planar metamaterials		83
5.1	Tuning the optical response	83
5.2	Transparent conductive oxides as active components	84
5.3	Tunable hyperbolic response at optical frequencies	87
5.4	Sensitivity analysis	93
5.5	Graphene as an active component	96
5.6	Tunable hyperbolic response at infrared frequencies	98
5.7	Conclusion	102
Chapter VI: Ultra-light van der Waals heterostructures as supermetals		104
6.1	What makes a perfect reflector? Beyond noble metals	104
6.2	Graphene-based van der Waals heterostructures	105
6.3	Computational approach and effective mass	106
6.4	Shinier than gold and silver!	110
6.5	Loss tangent and quality factors	111
6.6	Plasmonic propagation in vdW heterostructures	112
6.7	Conclusion	114
Chapter VII: Summary & Outlook		115
7.1	Summary	115
7.2	Outlook	117
Bibliography		123
Appendix A: Appendix		138
A.1	Transfer Matrix Equations for an infinite bilayer heterostructure	138
A.2	Counting optical states with the reflection pole method	139
A.3	Details on the electronic structure calculations in vdW heterostructures	140

LIST OF ILLUSTRATIONS

<i>Number</i>	<i>Page</i>
1.1 From atoms to materials, from resonators to metamaterials	3
1.2 The next photonic revolution by N. Zheludev	4
1.3 First demonstration of negative refraction	6
1.4 1D photonic crystals, 1977 by Pochi A. Yeh <i>et al.</i>	8
1.5 The photonic crystal and metamaterial regimes	9
1.6 Dispersion diagrams and equifrequency contours	11
1.7 Hyperbolic metamaterials	12
2.1 The concept of homogenization	16
2.2 Maxwell Garnett and Bloch approaches	20
2.3 Parameter retrieval for uniaxial structures	25
2.4 Parameter retrieval flow chart	26
2.5 Wave parameters for a known system	28
2.6 Restored material parameters for a known system	29
2.7 Effective dielectric permittivity in metallodielectric HMMs	30
2.8 Effective magnetic permeability in metallodielectric HMMs	31
3.1 SRR, fishnet and wire-based 3D and 2D magnetic metamaterials	33
3.2 Main motifs for 3D and 2D magnetic metamaterials	34
3.3 Parameter space for μ and ϵ	36
3.4 Artificial magnetism in 1D: the concept	37
3.5 Multilayer configurations for artificial magnetism	38
3.6 Impedance matching sanity checks	40
3.7 TEM images of fabricated multilayer magnetic metamaterials	41
3.8 Experimental approach and flow chart	42
3.9 Experimentally measured ϵ_{eff} and μ_{eff}	43
3.10 Comparison between model and raw experimental data	44
3.11 Bulk propagating modes in planar magnetic HMMs	46
3.12 Surface waves in planar magnetic HMMs	49
4.1 Permittivity resonances in polar dielectrics and excitonic materials	53
4.2 Naturally occurring excitonic and polar dielectric materials	54
4.3 Guided modes in $\epsilon < 0$ and $\epsilon > 0$ material systems	55
4.4 SPP dispersion and high- ϵ materials dispersion	57
4.5 Definition of a photonic and a surface-confined mode	60
4.6 Generalized retrieval approach for surface wave computations	62

4.7	Surface plasmon polaritons in Drude metals	65
4.8	Surface plasmon polaritons in silver	67
4.9	Surface phonon polaritons and TE counterparts in polar dielectrics	69
4.10	Surface-confined waves in excitonic materials	71
4.11	Omnipolarization surface-confined waves on SiC on Si	73
4.12	Omnipolarization surface-confined waves on WS ₂ on Si	76
4.13	Omnipolarization surface waves from plasmons and phonons	78
4.14	Omnipolarization surface waves from plasmons and excitons	80
5.1	Schematic of TCO-based tunable HMM	85
5.2	Complex dielectric permittivity of indium tin oxide	88
5.3	Extraordinary permittivity of a TCO-based tunable HMM	89
5.4	Ordinary permittivity of a TCO-based tunable HMM	90
5.5	Tunable birefringence and dichroism	92
5.6	Tunable figure of merit of a TCO-based tunable HMM	93
5.7	Complex isofrequency contours at different gate biases	94
5.8	Three-dimensional tunable dispersion surface	95
5.9	Sensitivity analysis of ENP condition	96
5.10	Schematic of graphene-based tunable HMM	97
5.11	Complex effective dielectric permittivity of graphene/SiO ₂ HMM	99
5.12	Hyperbolic and elliptical regimes of graphene/SiO ₂ HMM	100
5.13	Topological transitions at IR frequencies	101
6.1	Schematic of vdW heterostructures vs noble metals, m_{eff} and ϵ	107
6.2	Reflectance: vdW heterostructures vs noble metals	111
6.3	Quality factors and loss tangent	112
6.4	Plasmonic dispersion in vdW heterostructures	113
7.1	Outlook: concepts and applications	118
A.1	Low density of optical states in magnetic HMMs	142
A.2	High density of optical states in magnetic HMMs	143

LIST OF TABLES

<i>Number</i>		<i>Page</i>
4.1	Comparison of propagation characteristics between surface plasmon polaritons in Ag and omnipolarization surface-confined waves in SiC and in WS ₂	82
5.1	Breakdown voltage and carrier density in transparent conductive oxide gating schemes	87
5.2	Birefringent dielectric media	91
6.1	List of the twenty most conductive elemental metals	105

GLOSSARY OF ACRONYMS

IR	Infrared
UV	Ultraviolet
SRR	Split ring resonator
HMM	Hyperbolic metamaterial
EMA	Effective medium approximation
TE	Transverse electric polarization
TM	Transverse magnetic polarization
ENZ	Epsilon-near-zero
EMNZ	Epsilon-and-mu-near-zero
ENP	Epsilon-near-pole
RF	Radio frequencies
SPP	Surface plasmon polariton
RPM	Reflection pole method
DOS	Density of optical states
TMDC	Transition-metal dichalcogenides
SPhP	Surface phonon polariton
HWHM	Half-width-half-maximum
TCO	Transparent conductive oxide
ITO	Indium tin oxide
MOS	Metal/oxide/semiconductor
FOM	Figure of merit
CNP	Charge neutrality point
vdW	van der Waals
PEC	Perfect electrical conductor
DFT	Density functional theory

Chapter 1

INTRODUCTION: METAMATERIALS TODAY

“All things are made of atoms; little particles that move around in perpetual motion, attracting each other when they are a little distance apart, but repelling upon being squeezed into one another. In that one sentence [...] there is an enormous amount of information about the world.”

Richard P. Feynman, Six Easy Pieces, 1995

“I can’t see exactly what would happen, but I can hardly doubt that when we have some control of the arrangement of things on a small scale we will get an enormously greater range of possible properties that substances can have, and of different things that we can do.”

Richard P. Feynman, Plenty of Room at the Bottom, 1959

1.1 From atoms to materials, from resonators to metamaterials

The electromagnetic response and optical properties of natural materials arise from their electronic structure: the way that electrons interact with each other and with the nuclei (Fig. 1.1a). For example, a material with nearly free electrons behaves like a metal by screening any incident electric field, whereas when electrons are bound to the nuclei materials act as transparent media (dielectrics) and fields are allowed to propagate within them. The electromagnetic response of materials is typically described through their dielectric and magnetic properties, namely the dielectric permittivity ϵ and magnetic permeability μ that enter Maxwell’s macroscopic equations through the constitutive or material relations [1, 2]. Both ϵ and μ , together with more complex electromagnetic parameters, for example chirality, bianisotropy, and nonlinearities of materials, are all derived from their crystallographic arrangement and electronic band structure.

Despite a plethora of naturally available materials, their range of electromagnetic properties is limited. Listing the most desirable material responses that are unfound in nature is a matter of personal preference and application of interest. For example, near-unity material absorption at visible and near-infrared (IR) frequencies is desirable for solar harvesting, photovoltaic applications, sensing, and detection. Hence this functionality is highly pursued with artificial matter [3–5]. With respect to

imaging technology, the diffraction limit restricts the resolution of an optical system to λ/n , where λ is the free space wavelength and n is the index of refraction of the transparent medium. Hence, an infinitely large index of refraction could allow for perfect imaging resolution, however, the refractive indices of natural materials range approximately from 0 to 4. Alternatively, the diffraction limit restrictions can be alleviated with a negative index of refraction, also not observable in nature. Specifically, a negative index allows for super-resolution imaging and has been one of the most targeted functionalities in metamaterials research [6–10]. Another natural limitation pertains to an asymmetry in the dielectric and magnetic response of natural materials; although their dielectric permittivity ϵ obtains positive, negative, and near-zero values for frequencies up to the ultraviolet (UV) regime, the magnetic permeability μ of natural materials is unity for frequencies beyond the terahertz (THz) range [2, 11, 12]. Hence natural materials do not interact strongly with magnetic fields at high frequencies, limiting the degree of control of light-matter interactions in the visible and IR regime.

The idea of expanding the properties of natural substances was introduced by V. G. Veselago in 1967 [6]. In his original work, he discussed the implications of a hypothetical medium with simultaneously negative ϵ and μ . Veselago made speculations about conducting ferromagnets with $\epsilon < 0$ and $\mu < 0$, however such properties have not been observed in any naturally occurring material system, to date. Thirty-three years later, a simultaneously negative ϵ and μ system composed of a periodic array of conducting split ring resonators and wires was experimentally realized by D. R. Smith *et al.* [13]. At that time, the name “metamaterial” was established as the general term for artificially constructed matter, made of periodically positioned resonant subwavelength elements, often referred to as “meta-atoms”.

Rather than acquiring their macroscopic electromagnetic response from their chemical composition and electronic structure, as in natural materials (Fig. 1.1a), metamaterials obtain their properties from the collective response of the meta-atoms, which are typically resonators that act as mesoscopic artificial electric and magnetic dipoles. For incident wavelengths much larger than the metamaterial periodicity, the metamaterial microstructure is not resolved by the incident electromagnetic fields. Instead, electromagnetic radiation senses the net response of the composite (Fig. 1.1b). Hence the notion of an “effective medium” is typically introduced to describe the response of such a system. As discussed in the pioneering work by J. B. Pendry in *et al.* in [14], “*Long wavelength radiation is too myopic to detect internal structure and, in this limit, an effective permittivity and permeability is a valid concept*”. By employing different meta-atoms, a plethora of new material functionalities have been demonstrated within the last twenty years. Positive, zero, and negative values

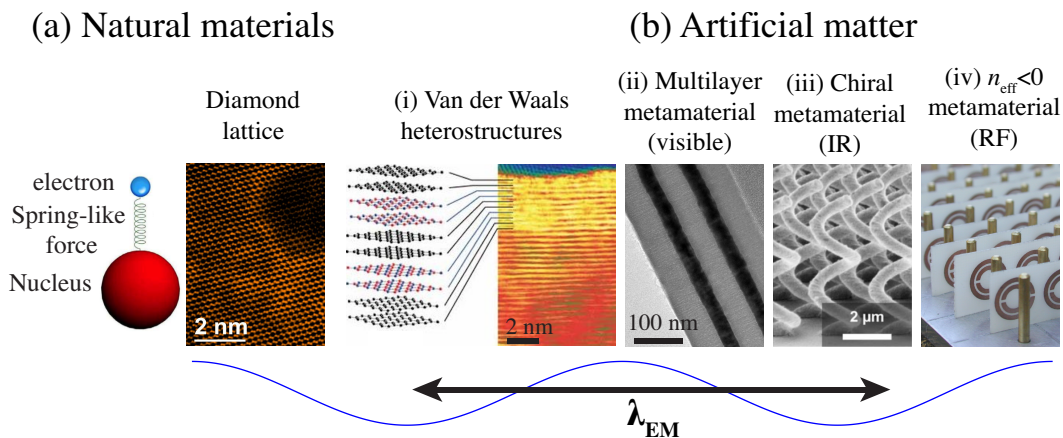


Figure 1.1: (a) SuperSTEM image of a faceted nano-void in diamond, from the SuperSTEM facility at the STFC Daresbury laboratory (UK). (b) (i) STEM image of a stack of graphene and hBN bilayers with the layer sequence schematically shown to the left, from [15], (ii) TEM image of a Ge/Ag multilayer metamaterial operating at optical frequencies [12] (iii) SEM image of helical metamaterial operating at infrared frequencies, adapted from [16] (iv) picture of a negative index metamaterial with unit cell size in the mm-scale, operating at microwave frequencies, adapted from [17].

of effective permittivity and permeability at any frequency range are now a reality, using accurate metamaterial design.

Initial experimental results in metamaterial research in the 2000's pertained to the microwave frequency range, with metamaterial elements in the millimeter (mm)-scale; the photograph in Fig. 1.1b (iv) demonstrates a negative refractive index composite system, adapted from from [13], which we will discuss in more detail in what follows. Drastic technological progress in nanofabrication has allowed scaling the dimensions of metamaterial elements down to the micrometer (μm) and nanometer (nm)-regime. In Fig. 1.1b (iii) we show a scanning electron microscopy (SEM) image of a triple-helix metamaterial operating as a circular polarizer at IR frequencies, realized using three-dimensional laser lithography [16]. Fig. 1.1b (ii) shows a multilayer germanium/silver metamaterial operating at visible wavelengths, adapted from [12], which will be discussed in detail in Chapter 3, realized with electron-beam thin-film deposition. Impressively, as of 2012 and despite the dozens of steps involved, it is now possible to stack two-dimensional materials with interlayer separation in the \AA -regime. Fig. 1.1b (i) (right) shows a cross-section scanning transmission electron microscopy (STEM) image of a van der Waals heterostructure composed of six alternating bilayers of graphene and hexagonal boron nitride, as illustrated on the left, adapted from [15]. The van der Waals interlayer separation

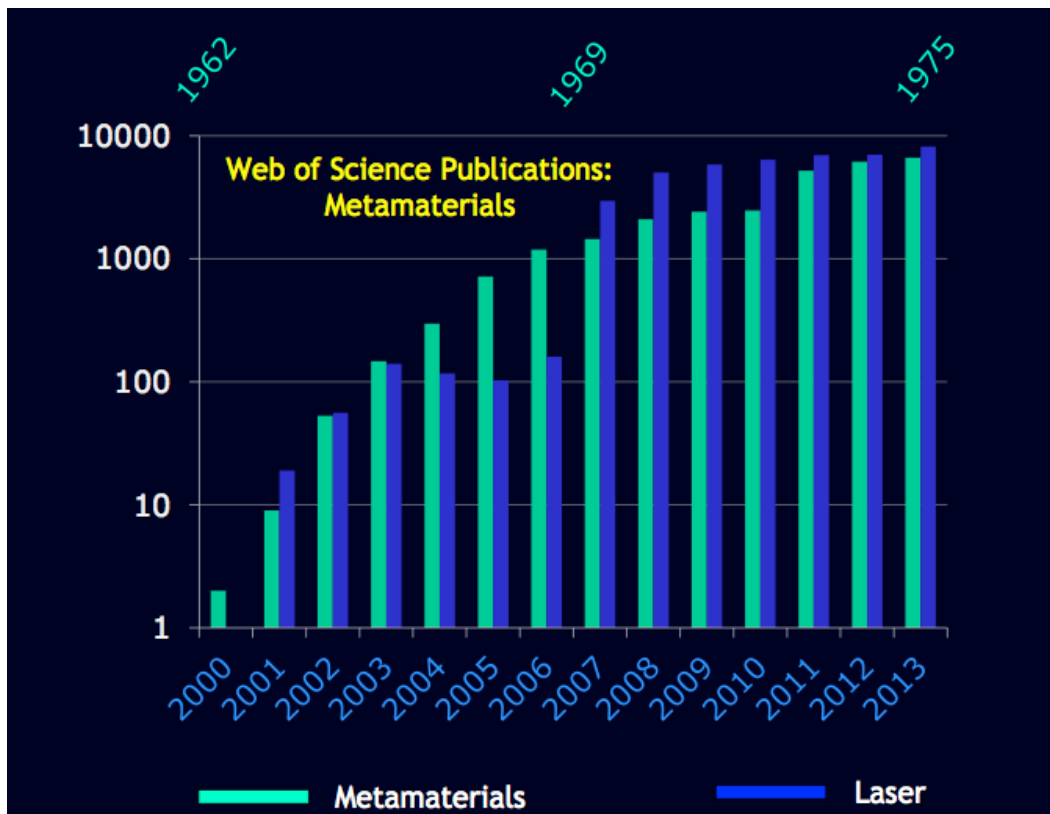


Figure 1.2: “The next photonic revolution: Metamaterials”, adapted from N. Zheludev, Plenary talk, CIMTEC 2014, Optical functionalities on demand: from metamaterials to metadevices

regime coincides with the interatomic separation distance in natural materials, as shown in Fig. 1.1a. Hence, today we are able to access and control the arrangement of material systems in the sub-nm regime. In this regime, electronic and electromagnetic degrees of freedom compete, paving the way for new classes of artificial materials composed of layered combinations of two-dimensional (2D) materials in van der Waals heterostructures. Namely, by controlling simultaneously the geometrical structure, for example by selecting appropriate layer sequencing, together with controlling the electronic interactions between adjacent van der Waals layers, by selecting appropriate 2D materials, we are in the position to design new Å-scale (meta)materials with a bottom-up approach. We discuss this regime in Chapter 6 [18].

Since the 2000’s the field of metamaterials has dramatically advanced and transitioned from the mature research area of electrical engineering at microwave frequencies to the emerging field of nanophotonics, plasmonics, and the physics of light coupled to nanostructures. Fig 1.2 is a histogram of the number of scientific pub-

lications in the field of lasers in the 1960's and 1970's in comparison to the field of metamaterials up to 2012. The similar trends in the publication rates, together with the dramatic technological impact of the lasers in the past, present, and future, show the potential of metamaterials as an emerging field of both fundamental scientific merit and technological promise.

1.2 Negative refraction: The wire array and the split ring resonator

It took thirty-three years for Veselago's original proposal of a medium with negative refractive index to be experimentally demonstrated by D. R. Smith *et al.* [6, 13]. This delay is justified as building intuition about the metamaterial structural requirements for yielding on demand values of ϵ and μ was, and often remains, a challenging task. Successful demonstration of negative refraction was achieved with the structure depicted in Fig. 1.3c, consisting of a periodic array of interspaced conducting nonmagnetic split ring resonators and continuous wires. The wire medium and the split ring resonator are now widespread in metamaterial design and their principle of operation deserves special attention.

The wire array was introduced by J. B. Pendry *et al.* in [19] in 1996, as a structure that behaves effectively like a metal with plasma frequency controllable through the metallic filling fraction of the wires. Hence the plasmonic response of this composite system could be tuned at will, leading to surface plasmonic propagation at frequencies much lower than the plasma resonance of most noble metals that are physically bound to the ultraviolet (UV) and visible regime. The principle of operation of the wire array is based on the fact that conducting channels composed of wires yield a metallic response with $\epsilon_{\text{eff}} < 0$, and by placing metallic wires along all three coordinate directions (Fig.1.3a) the response becomes isotropic.

The split ring resonator (SRR) was originally discussed by J. B. Pendry *et al.* in [14] in 1999, as a way to achieve isotropic negative μ_{eff} . The search for negative permeability is motivated by the lack of natural magnetism at high frequencies. As stated by Pendry *et al.* in [14], "*atoms and molecules prove to be a rather restrictive set of elements from which to build a magnetic material. This is particularly true at frequencies in the gigahertz range where the magnetic response of most materials is beginning to tail off.*". The SRR, shown on the left of 1.3b, is composed of non-magnetic metal and operates similar to a magnetic dipole; for an incident magnetic field parallel to the axis of the rings, induced current can produce a magnetic field that may either oppose ($\mu_{\text{eff}} < 1$) or enhance ($\mu_{\text{eff}} > 1$) the incident field. The gaps between the rings in Fig.1.3b serve as control knobs for tuning the magnetic resonance at wavelengths much larger than the diameter of the rings. The smaller ring has a gap oriented in the opposite side to the large ring in order to generate a large

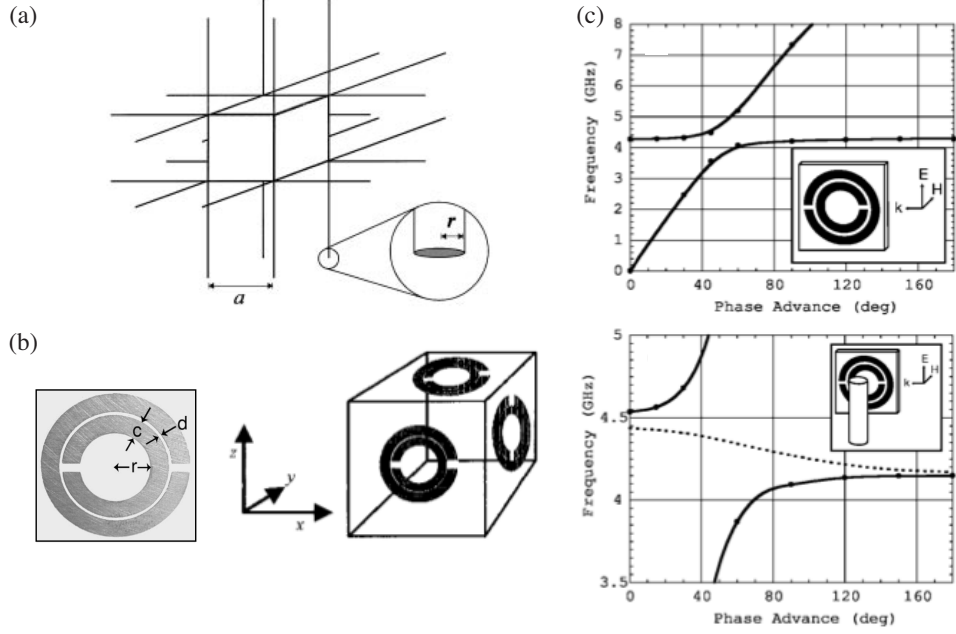


Figure 1.3: (a) Schematic of an isotropic $\epsilon_{\text{eff}} < 0$ medium composed of a three-dimensional periodic lattice of ultra-thin metallic wires, adapted from [19]. (b) Left-planar view of a SRR, adapted from [13], right-schematic of an isotropic $\mu_{\text{eff}} < 0$ medium composed of SRRs, adapted from [14]. (c) Top-dispersion curve for a periodic array of SRRs for magnetic field polarized along the SRR axis. Bottom-dispersion curve for a directional negative refractive index n_{eff} metamaterial composed of wires and SRRs and wires, adapted from [13].

capacitance in the small gap region and further lower the magnetic resonance. By constructing a lattice of closely packed SRRs the axes of which are oriented along all three coordinate directions, as shown on the right of 1.3b, one can achieve an isotropic $\mu_{\text{eff}} < 0$.

By combining a two-dimensional array of periodically placed conducting wires with layers of square arrays of SRR (as shown in Fig. 1.1b (iv)), D. R. Smith *et al.* realized the first negative index metamaterial in 2000 [13]. A 2D wire array can be modeled with an effective dielectric permittivity given by

$$\epsilon_{\text{eff}} = 1 - \frac{\omega_p^2}{\omega^2} \quad (1.1)$$

where ω is the frequency of incident radiation, and with $\omega_p = (\alpha_W^2 L(r) \epsilon_0)^{-1/2}$, where α_W is the wire spacing (Fig.1.3a), $L(r)$ is the self-inductance of a single wire and ϵ_0 is the dielectric permittivity of free space. Similarly, the SRR periodic arrangement is modeled via

$$\mu_{\text{eff}} = 1 - \frac{\pi(r/\alpha_{\text{SRR}})^2}{1 - 3l/\mu_0 C r^3 (\pi\omega)^2 + i(2l\rho/\omega r \mu_0)} \quad (1.2)$$

where r is smaller ring's radius (Fig.1.3b (left)), α_{SRR} is the SRR lattice parameter, l is the distance between SRR layers, ρ is the resistance per unit length of the rings measured around the circumference, C is the capacitance associated with the gaps between the rings, and μ_o is the magnetic permeability of free space. By appropriately positioning the wire array and SRR lattice so that the resonant frequencies of the two align, a negative index regime occurs ($n_{\text{eff}} = \sqrt{\epsilon_{\text{eff}}\mu_{\text{eff}}}$).

For the SRR lattice alone, the frequency dispersion of the supported modes is shown in Fig.1.3c (top). The band gap corresponds to the frequency regime for which $\mu_{\text{eff}} < 0$. By appropriately intersecting the wire array (inset in Fig.1.3c (bottom)), the band gap is eliminated and the emerging passband, shown with the dashed line, exhibits negative group velocity due to a simultaneously negative ϵ_{eff} , which arises from the plasmonic response of the wires. We note that the negative refraction of the system introduced by Smith *et al.* is limited to the polarization depicted at the inset of Fig.1.3c (bottom); for magnetic fields not aligned with the SRR axes, or for electric fields not aligned with the wires axes, the passband exhibits a positive slope, and hence the group velocity is positive. The seminal works by D. R. Smith, J. B. Pendry and co-authors shaped the roadmap for research in artificial matter and established fundamental metamaterial elements that are now widespread in metamaterial design.

1.3 Planar heterostructures: from photonic crystals to metamaterials

Following the realization of SRR metamaterials and wire arrays, a plethora of sub-wavelength structures have been reported to exhibit interesting and unprecedented electromagnetic properties, c.f. Fig. 1.1b. Dielectric nanoparticles [20, 21], fishnet structures [22–24], helical metamaterials [16], and nanowires [25] have been developed, operating at IR and even near-IR and visible frequencies. The experimental realization of such three-dimensional (3D) and two-dimensional (2D) motifs calls for high resolution nanofabrication methods including electron beam lithography, nanoimprint, focused ion beam milling, and three-photon lithography. Extending the properties of such 3D and 2D metamaterials to the visible and UV regime requires reducing their dimensions so that the unit cell does not exceed a threshold of roughly tens to few hundreds of nanometers.

By contrast to the fabrication requirements of 3D and 2D unit cells of metamaterials, the experimental realization of unpatterned, one-dimensional (1D) planar layered media has been well established since the 1980s with thin-film deposition techniques. Today, thin-film deposition systems include thermal and electron beam evaporation, sputtering, molecular beam epitaxy (MBE) and atomic layer deposition (ALD), with accuracy in layer thickness that can reach sub-nm scales in state-of-the-art systems.

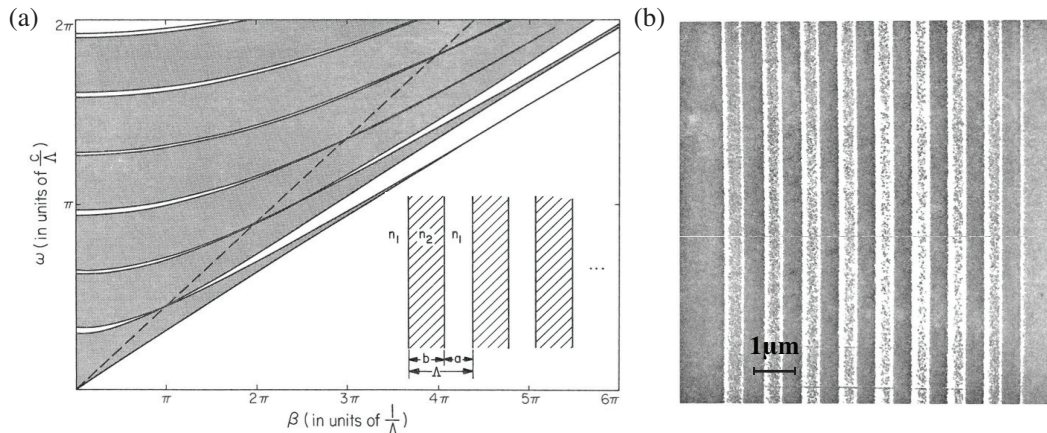


Figure 1.4: (a) Band structure of a 1D photonic crystal: dark zones represent the allowed bands. (b) SEM image of a 1D photonic crystal composed of alternating layers of GaAs and $\text{Al}_{0.20}\text{Ga}_{0.80}\text{As}$, adapted from the seminal work by P. A Yeh *et al.* in 1977 [1, 26].

The precursor of 1D planar multilayer metamaterials is the field of all-dielectric 1D photonic crystals; structures that flourished within the 1970's and 1980's due to their property to selectively reflect and transmit electromagnetic radiation [1, 26–29].

Similarly to Bragg diffraction in crystals, where X rays are diffracted by the periodic energy potential of crystalline solids, 1D photonic crystals operate based on diffraction of light. They are usually composed of a periodic alteration of two dielectric materials, typically exhibiting a low- and a high-refractive index. One of the pioneering contributions to the field of 1D photonic crystals was by P. A. Yeh, during his graduate school years at Caltech, when he developed a transfer matrix formulation for layered media [1, 26], heavily used in this thesis and in the literature. The mathematical formulation of electromagnetic fields propagating in the form of plane waves inside 1D photonic crystals is identical to the problem of an electron propagating in a periodic potential, which is treated with Bloch's theorem [30]. Therefore, similar to the electronic bands and bandgaps in semiconductors, periodic layered media exhibit photonic bands and bandgaps. Figure 1.4 (a), adapted from Yeh's original thesis authored in 1978, shows the typical 1D photonic crystal structure (inset) and its characteristic band structure, where the dark zones represent the allowed bands, ω is the frequency of the incident light, and β is the in-plane propagation constant. In Fig. 1.4 (b) we show an SEM image of a Bragg reflector composed of alternating layers of GaAs and $\text{Al}_{0.20}\text{Ga}_{0.80}\text{As}$, discussed in Yeh's thesis. Realizing that a simple periodic dielectric layered medium can support omnidirectional reflection [29], where Maxwell's equations have no propagating

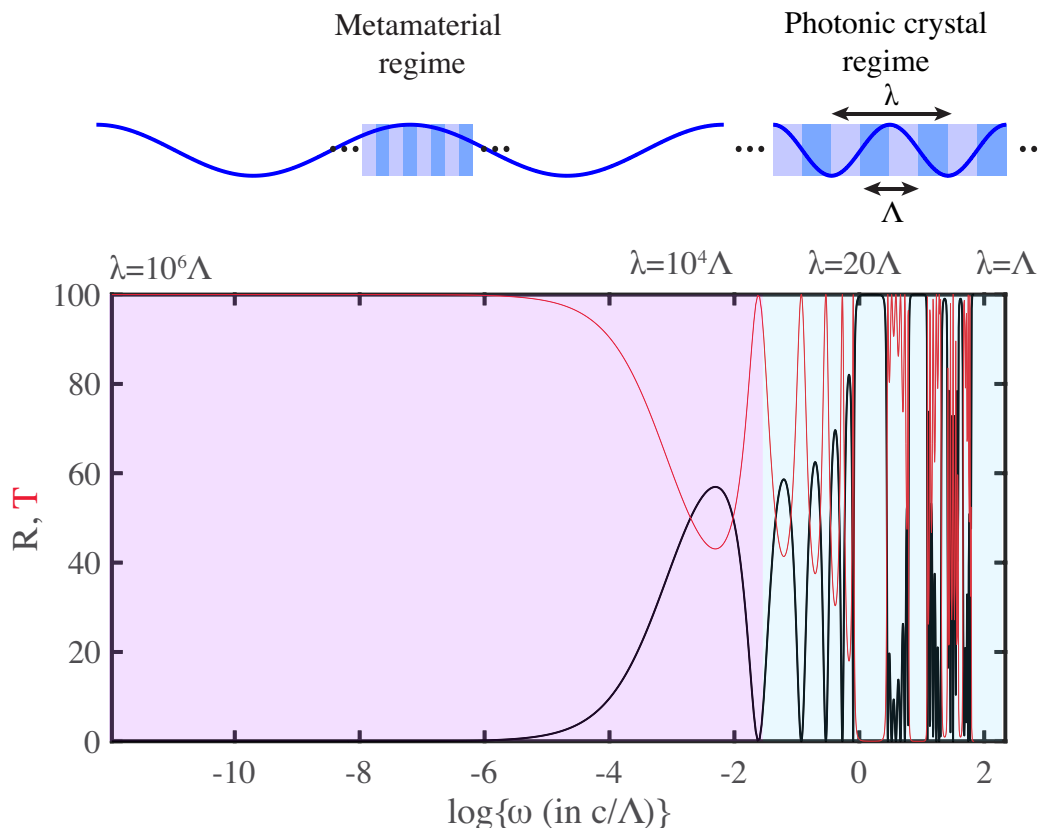


Figure 1.5: Reflectance and transmittance spectra of an all-dielectric 1D layered medium composed of eleven alternating layers of refractive index $n_1 = 1.4$, $n_2 = 3.5$.

solutions, led to a broad range of applications and photonic devices, with the most well-known being the anti-reflection coating.

Contrary to the metamaterial limit, where the wavelength of light oughts to be much larger than the unit cell periodicity ($\lambda \gg \Lambda$), photonic crystals operate at wavelengths comparable to the periodicity. This comparison is shown in the schematics of Fig. 1.5. In this figure, regions of unity transmittance and reflectance correspond to photonic bands and band gaps, respectively, for a 1D periodic layered medium (frequency scale to be compared to Fig. 1.4 (a)). The band gaps disappear in the metamaterial subwavelength regime, $\lambda \gg \Lambda$. In this regime, the field is too myopic to the internal structure of the composite and, instead, experiences an average, homogeneous dielectric environment. In the particular example of Fig. 1.5, the selected materials are purely dielectric ($n_1 = 1.4$ and $n_2 = 3.5$), and hence the dielectric environment seen by large-wavelength electromagnetic fields is transparent. This explains the nearly perfect transmittance in the metamaterial regime depicted in Fig. 1.5.

1.4 Hyperbolic metamaterials

As briefly mentioned above, all-dielectric multilayer metamaterials exhibit a purely dielectric response in the deep subwavelength limit, where they are transmissive (Fig. 1.5). By striking contrast, new and exciting effects arise from stacking metallic and dielectric layers to compose planar metallodielectric metamaterials, termed hyperbolic metamaterials (HMMs). The field of HMMs has flourished within the last six years [31–33], however the concept behind their fundamental properties was discussed as early as in 2001 by I. V. Lindell *et al.* in [34], and in 2003 by D. R. Smith and D. Schurig in [35]. A wide range of their exciting properties and functionalities arise from their unnaturally anisotropic response. To our knowledge, HMMs are the most anisotropic composite materials reported. In what follows, we introduce HMMs and compare them to natural substances.

The frequency dispersion of electromagnetic waves propagating in a bulk isotropic material is expressed through the equation

$$|\vec{k}| = n\omega/c \quad (1.3)$$

where \vec{k} is the wavevector of the wave, n is the refractive index of the material and c is the speed of light in vacuum. By contrast, many dielectric materials, for example sapphire, hexagonal boron nitride (hBN), silicon carbide (SiC), and others, are uniaxially anisotropic. In the absence of any magnetic properties, the dielectric response of uniaxially anisotropic materials is described by the dielectric permittivity tensor $\vec{\epsilon}_{\text{eff}} = \text{diag}\{\epsilon_o, \epsilon_o, \epsilon_e\}$, where ϵ_o and ϵ_e are the ordinary and extraordinary components of the tensor. The ordinary directions (x and y axes) refer to the ones normal to the optical axis of the material, whereas the extraordinary direction coincides with the optical axis (z axis). Ignoring the y -direction, the dispersion equation of uniaxially anisotropic crystals is

$$\frac{k_x^2}{\epsilon_e} + \frac{k_z^2}{\epsilon_o} = \frac{\omega^2}{c^2} \quad (1.4)$$

By fixing the frequency ω in the dispersion equations (1.3) and (1.4), we obtain the angular dependence of the wavevector, or k -space of the material, which is also termed equifrequency contour (EFC). The EFC shape determines fundamental electromagnetic properties of material systems and is useful in describing light-matter interactions. As shown in Fig. 1.6a, the EFC of an isotropic material is a perfect circle with radius $n\omega/c$. By contrast, uniaxially anisotropic dielectrics have elliptical EFCs as depicted in Fig. 1.6b. Typically, dielectric materials occurring naturally do not exhibit extreme anisotropy; the most uniaxially anisotropic dielectric substances are nematic liquid crystals with birefringence values $\Delta n = \sqrt{\epsilon_e} - \sqrt{\epsilon_o} \sim 0.4$.

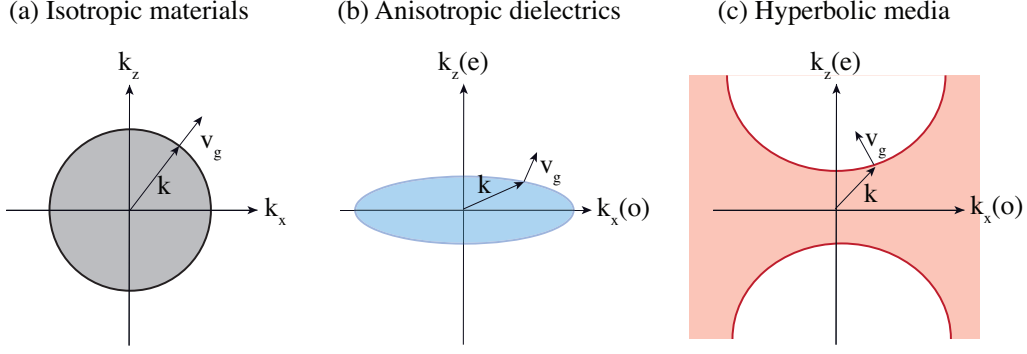


Figure 1.6: Equifrequency contours for (a) an isotropic dielectric medium (Eq. (1.3)), (b) an anisotropic uniaxial dielectric material (Eq. (1.4) with $\epsilon_o\epsilon_e > 0$) and (c) for a hyperbolic medium (Eq. (1.4) with $\epsilon_o\epsilon_e < 0$).

By contrast, a hyperbolic medium is one for which the dielectric (or magnetic) properties along different coordinate directions are opposite in sign, i.e., $\epsilon_o\epsilon_e < 0$ ($\mu_o\mu_e < 0$). A naturally occurring material that exhibits this response is hBN [36], however, for hBN this response is physically bound to the IR regime and to a rather narrowband frequency regime. In the case of a hyperbolic medium, the EFC is no longer a closed surface as in Fig. 1.6b. By contrast, from Eq. (1.4), the EFC opens up into a hyperbola, as shown in Fig. 1.6c.

The EFC diagram is useful, among others, in computing the group velocity and density of optical states for bulk propagating modes in material systems. Namely, given the dispersion equation $\omega(\vec{k})$, the group velocity is [2]

$$\vec{v}_g = \frac{\partial\omega}{\partial\vec{k}} \quad (1.5)$$

Hence, the group velocity vector is normal to the EFC and points in the direction of its displacement as a function of increasing frequency [2, 37]. From Fig. 1.6a and Eq.(1.3), we see that, for light propagation in isotropic materials, the direction of the group velocity \vec{v}_g coincides with the direction of propagation, i.e., the direction of \vec{k} . By contrast, due to the elliptical EFC shape of anisotropic dielectric media (Fig. 1.6b), the propagation direction may differ from the group velocity, however the two typically define an acute angle due to small birefringence values in naturally occurring materials. The case of HMMs is of special interest as, in this case, \vec{v}_g and \vec{k} can form an obtuse angle, a consequence of $\epsilon_o\epsilon_e < 0$, allowing for all-angle negative refraction. Negative refraction and its implications have been widely reported within the last decade using HMMs [36–40].

HMMs are also often utilized as metamaterial platforms for enhancing the luminescence properties of quantum emitters [41, 42]. The fundamental parameter re-

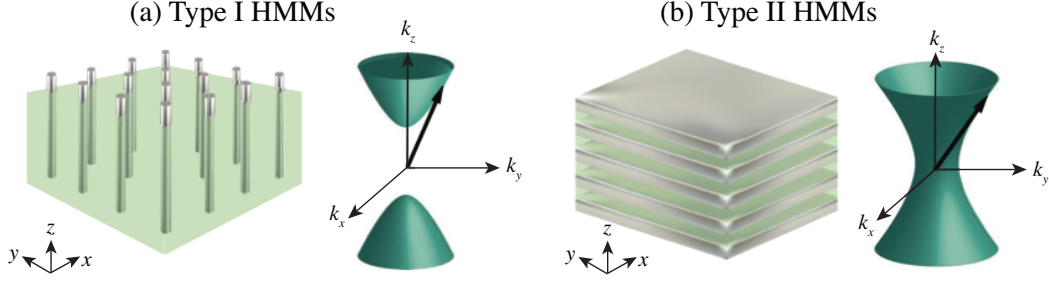


Figure 1.7: The physical implementation and corresponding equipfrequency contours for (a) type I HMMs, with metallic wires in a dielectric host, and for (b) type II HMMs, with metallodielectric multilayers. Figure adapted from [33].

sponsible for this functionality is the density of optical states (DOS), which is often enhanced using HMMs. Particularly, the DOS is given by [30, 41, 43]

$$D(\omega) = \left(\frac{L}{2\pi}\right)^2 \int_{\text{Shell}} d^3\vec{k} \quad (1.6)$$

where L^3 is the physical volume of the system and the quantity $\int_{\text{Shell}} d^3\vec{k}$ expresses the volume enclosed by two EFCs corresponding to frequencies ω and $\omega + d\omega$, respectively. Therefore, the open-shaped EFCs that HMMs exhibit (Fig. 1.6c) result in larger DOS compared to conventional isotropic or anisotropic dielectric media (Fig. 1.6a and b, respectively). Based on the large DOS of HMMs, many interesting phenomena have been recently discussed in the literature, including topological transitions in metamaterials [42], Purcell factor enhancement [41, 44] and directional light emission [45].

The physical realization of HMMs requires composite structures with drastically different dielectric properties along different coordinate directions, in order to induce the $\epsilon_o\epsilon_e < 0$ response that we discussed above. To date, there are two well known ways to realize HMMs; the first one is with metallic wires in a dielectric host, or, vice versa, with dielectric wires in a metallic host. In this case, depicted in Fig. 1.7a, the out-of-plane (z) or extraordinary permittivity is negative, $\epsilon_e < 0$, while in the ordinary directions (x and y), the response is dielectric with $\epsilon_o > 0$. This type of hyperbolic response is typically referred to as type I and its three-dimensional EFC is shown in Fig. 1.7a.

Type II HMMs are ones that support $\epsilon_o < 0$ while $\epsilon_e > 0$. This type of response is easily achievable with metallodielectric multilayer metamaterials (Fig. 1.7b). The hyperbolic response of metallodielectric multilayers can be interpreted as follows: along the ordinary directions (x and y in Fig. 1.7b), the metallic layers dominate

as charge carriers are free to transport without encountering dielectric barriers, and hence the system behaves as an effective metal with negative permittivity. By contrast, in the extraordinary (z) direction, the dielectric layers act as barriers of conduction and the system responds as an effective dielectric with positive permittivity. We note that there are certain frequency regimes at which type I hyperbolic response can be observed with metallodielectric layered metamaterials [32, 33].

1.5 Scope and structure of the thesis

The scope of this thesis is to provide theoretical and computational tools to model the response of planar heterostructures, mainly in the subwavelength limit and focusing on planar HMMs, together with providing approaches for characterizing them experimentally. Until now, the response of planar HMMs has been mainly modeled with effective medium approximations that date back to 1985 [46]. A large portion of the thesis is focused in addressing certain properties of planar heterostructures that previous EMAs or other approaches, discussed in detail in Chapter 2, tend to omit [47]. Hence, we unveil and address in detail in Chapter 3 the magnetic response of planar heterostructures, typically expressed through the effective magnetic permeability $\vec{\mu}_{\text{eff}}$. Until now, the consensus in metamaterials research was that planar metamaterials do not possess magnetic properties and $\vec{\mu}_{\text{eff}} = \mathbb{I}$. By contrast, in Chapter 3 we propose a concept for tailoring the effective magnetic response within planar, unpatterned, 1D multilayer structures [12]. We show theoretically and experimentally that the magnitude and sign of the permeability tensor may be engineered at will and we discuss its implications. In Chapter 4, inspired by our results in Chapter 3, we focus on the implications of artificial magnetism on the surface waves that propagate on planar heterostructures. Previously, HMMs has been considered to mainly support transverse-magnetic (TM) polarized surface plasmon polaritons due to the metallic layers that support plasmons below their plasma frequency. By inducing artificial magnetism in HMMs, we show that it is possible to guide transverse-electric (TE) polarized surface waves simultaneously with their TM counterpart. We particularly focus on transition-metal dichalcogenides and polar dielectric media and discuss regimes of simultaneously TM and TE, i.e. unpolarized, surface wave propagation with the purpose of generalizing previously polarization-dependent plasmonic properties of metals.

In Chapter 5, we switch gears and discuss possible means of inducing active tunability in planar arrangements, with the scope of actively controlling the dispersion characteristics of metamaterials. Practical implications of these results pertain to optical components, for example in optical switches, tunable polarizers, active displays and holography. We discuss the visible frequency range where transparent

conductive oxides (TCOs) can act as tunable materials for inducing active tunability in TCO-based planar HMMs [48]. At IR frequencies, we discuss graphene as the tunable component, that, through carrier injection, can also tune the response of graphene-based HMMs.

Finally, in Chapter 6 we transition to heterostructures composed purely of two-dimensional materials, and demonstrate that doped graphite, composed of doped graphene mono-layers, or graphene/hBN heterostructures can behave as “supermetals”, surpassing the perfect-electric-conductor response of noble metals at IR frequencies [18].

We hope that the results of this thesis demonstrate the potential of artificial matter as a field of study for designing novel optical materials.

METAMATERIALS' HOMOGENIZATION

“Essentially, all models are wrong, but some are useful.”

George Box, Science and Statistics, 1976

2.1 The concept of homogenization and S-parameter retrieval

The objective in metamaterials' research is to design composite media for expanding the properties of naturally available materials. Hence, it is often necessary to design meta-atoms with complex geometrical arrangements that are drastically different from the periodic arrangement of atoms in naturally occurring crystalline materials (Fig. 1.1a). As can be inferred from the complex metamaterial shapes shown in Fig.1.1b and in Fig. 2.1a, where we show typical SRRs, wire arrays, multilayers and plasmonic nanoparticles, it is often computationally inefficient, if not impossible, to attempt solving Maxwell's boundary condition at each boundary of the problem. An alternative approach is necessary for modeling complex structures and predicting macroscopic phenomena. As mentioned in Chapter 1, provided that the wavelength of the incident electromagnetic field is much larger than the unit of the metamaterial, it is possible to assign effective parameters that describe the collective response of a system [14].

This assignment of effective parameters, namely effective dielectric permittivity ϵ_{eff} and magnetic permeability μ_{eff} , is termed homogenization. There exists a variety of methods dedicated to metamaterials' homogenization, ranging from effective medium approximations (EMAs) initially developed in the early 1980's [46, 49–52], field-averaging approaches [53] and integral method [54–56], and S-parameter retrievals. Here, we will focus on S-parameter approaches, initially formulated in the 2000's by Smith *et al.* in [57, 58] and by Chen *et al.* [59].

Conceptually, it is convenient to replace an inhomogeneous composite medium, which typically consists of a collection of scattering objects, by a homogeneous medium that exhibits identical scattering response to electromagnetic fields, namely, the same complex transmission and reflection coefficients, t and r . This correspondence is demonstrated in Fig. 2.1a and b. The composite medium in Fig. 2.1a could be, for example, an array of SRRs, or plasmonic nanoparticles, nanowire arrays or a multilayer metamaterial, the meta-atoms of which could be arranged periodically or

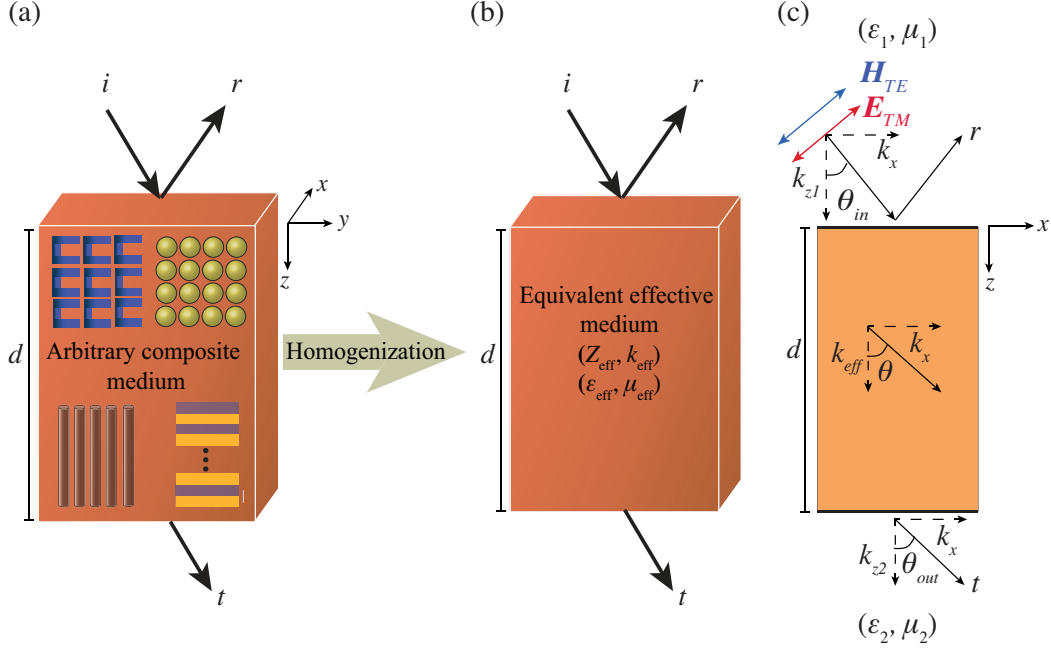


Figure 2.1: (a) An arbitrary composite medium could consist of any combination of meta-atoms in any arrangement, for example split ring resonators, plasmonic nanoparticles, nanowires or multilayers. (b) An equivalent homogeneous medium that exhibits the same scattering properties as (a) and is described with an effective permittivity ϵ_{eff} and an effective permeability μ_{eff} . (c) Schematic and definition of parameters with respect to Eqs. (2.3), (2.4).

aperiodically. This is the fundamental concept of the S-parameter retrieval approach [57–60], which we explain in detail in what follows.

Let us start by examining the case of a finite slab of thickness d of an isotropic and homogeneous material with dielectric permittivity ϵ and magnetic permeability μ . Two equivalent parameters that can be introduced to describe the response of the slab are the refractive index and the impedance, $n = \sqrt{\epsilon\mu}$ and $Z = \sqrt{\mu/\epsilon}$, respectively. By convention, we define the two linear polarizations as shown in Fig. 2.1c: transverse electric (TE) polarized waves, alternatively known as s-waves, have an electric field vector transverse to the plane of incidence ($E_y \neq 0$). Similarly, transverse magnetic (TM) polarized waves, or p-waves, have a magnetic field vector transverse to the plane of incidence ($H_y \neq 0$).

The basis of the S-parameter retrieval lies on the fact that the complex transmission and reflection coefficients of an incident electromagnetic field, namely t and r , can be expressed analytically as functions of n and Z . In order to do this, we introduce $k_{\text{eff}} \equiv k_z = n(\omega/c)\cos\theta$ and $\xi = Z^p\omega/c$, where $p = -1$ for TE polarization while $p = 1$ for TM polarization, and θ is the refraction angle inside the slab, as shown in

Fig. 2.1c, which can be calculated through Snell's law in the case of homogeneous substances. In terms of these quantities, the complex transmission and reflection coefficients, as expressed by Menzel *et al.* in [60], are:

$$t(k, \xi) = \frac{2k_1 \xi A}{\xi(k_1 + k_2)\cos(kd) - i(\xi^2 + k_1 k_2)\sin(kd)} \quad (2.1)$$

$$r(k, \xi) = \frac{\xi(k_1 - k_2)\cos(kd) + i(\xi^2 - k_1 k_2)\sin(kd)}{\xi(k_1 + k_2)\cos(kd) - i(\xi^2 + k_1 k_2)\sin(kd)} \quad (2.2)$$

where $k_{1,2} = \alpha^{1,2} k_{z1,2}$. We have $k_{z1,2} = n_{1,2}(\omega/c)\cos\theta_{\text{in,out}}$ where $n_{1,2} = \sqrt{\epsilon_{1,2}\mu_{1,2}}$, the refractive indices of the surrounding media, and $\epsilon_1, \mu_1, \epsilon_2, \mu_2$ are the dielectric and magnetic properties of the surrounding media, as shown in Fig. 2.1c. We define $\alpha^i = 1/\mu_i$ for TE polarization and $\alpha^i = 1/\epsilon_i$ for TM polarization. In Eq. (2.1), the factor A amounts to $A = 1$ for TE polarization, whereas $A = \sqrt{\epsilon_1\mu_2/\epsilon_2\mu_1}$. By inverting Eqs. (2.1, 2.2), we can obtain the expressions for k and ξ :

$$kd = \pm \arccos\left(\frac{k_1(1 - r^2) + k_2(t/A)^2}{(t/A)[k_1(1 - r) + k_2(1 + r)]}\right) \pm 2m\pi \quad (2.3)$$

$$\xi = \pm \sqrt{\frac{k_1^2(r - 1)^2 - k_2(t/A)^2}{(r + 1)^2 - (t/A)^2}} \quad (2.4)$$

Eqs. (2.3), (2.4) hold for any angle of incidence, embedded in $k_{1,2}$. Additional constraints must be imposed in order to select the correct sign and branch in Eq. (2.3) and the correct sign in Eq. (2.4). For this, we use the physical requirements for continuity and passivity. Namely, by starting the retrieval calculations from the quasistatic limit $\omega \rightarrow \infty$, the branch $m = 0$ is selected. Subsequently decreasing the frequency requires adjusting the branch number in order to ensure continuity of the wavenumber k . Furthermore, we must ensure exponential decay for waves propagating in the positive z direction. Assuming time-dependence of the form $\vec{E}(t, \vec{r}) = \vec{E}(\vec{r})e^{i(\vec{k}\vec{r} - \omega t)}$, the imaginary part of k must be selected to be positive, which fixes the sign in Eq. (2.3). Finally a passive medium requires $\text{Re}(Z) > 0$, fixing the sign in Eq. (2.4).

For complex geometries like the ones schematically presented in Fig. 2.1a, the scattering properties t, r (also termed S-parameters, hence the name S-parameter retrieval) are usually calculated with numerical methods, for example High Frequency Structure Simulator (HFSS) finite elements approaches, Lumerical Finite Difference Time Domain (FDTD) simulators, Comsol Multiphysics or the Fourier Modal method [60, 61]. In what follows, we will refer to the calculation of t and r

as the *forward problem*, in contrast to the *inverse problem*, being the calculation of k and ξ through Eqs. (2.3), (2.4), given t , r (see Fig. 2.4).

In the case of inhomogeneous substances, the parameter $k = k_{\text{eff}}$ is the effective wavenumber of the metamaterial, the determination of which is the scope of homogenization. k_{eff} together with ξ allow decoupling of the effective dielectric permittivity ϵ_{eff} from the magnetic permeability μ_{eff} . For the two linear polarizations we have:

$$\mu(k_x, \omega) = \frac{k}{\xi(k_x, \omega)} \text{ (TE)} \quad , \quad \epsilon(k_x, \omega) = \frac{k}{\xi(k_x, \omega)} \text{ (TM)} \quad (2.5)$$

For TE (TM) polarization, the dielectric permittivity ϵ_{eff} (magnetic permeability μ_{eff}) is obtained through the dispersion equation for isotropic materials:

$$\frac{k_x^2 + k^2}{\epsilon_{\text{eff}} \mu_{\text{eff}}} = \frac{\omega^2}{c^2} \quad (2.6)$$

where $k_x = n_{1,2}(\omega/c)\sin\theta_{1,2} = k_{//}$ is a conserved quantity that defines the angle of incidence and frequency. For isotropic metamaterials, an effective index may be introduced, defined as:

$$n_{\text{eff}} = \pm \frac{\sqrt{k_x^2 + k(k_x, \omega)^2}}{\omega/c} \quad (2.7)$$

Eqs. (2.3), (2.4) are fundamental in understanding the S-parameter retrieval approach, and have been very widely used in order to obtain and report extraordinary electromagnetic properties in 2D and 3D metamaterials. Examples include metallic strip metamaterials [62], SRRs [13, 17, 57–59], fishnet structures [60] and others [37]. The method describe here is general and can be applied to obtain the effective parameters (ϵ_{eff} and μ_{eff}) along different coordinate directions for any inhomogeneous slab, in the quasistatic limit. Despite its generality, the S-parameter approach must be used with caution and the derived parameters ϵ_{eff} and μ_{eff} have to be assessed critically.

We briefly highlight that for the retrieval to be valid, in other words for the dielectric and magnetic effective parameters to be a useful macroscopic description of the metamaterial, the system under consideration oughts to be in the subwavelength limit. Issues of non-locality and spatial dispersion, i.e. the dependence of effective parameters on the wavenumber, arise when the metamaterial unit cell is not deeply subwavelength [63]. In this regime, unphysical properties may occur, for example negative $\text{Im}(\epsilon_{\text{eff}}, \mu_{\text{eff}})$. The conditions under which it is appropriate and useful to introduce effective parameters for describing the macroscopic response of metamaterials remains an area of active debate and research, see, for example [54, 63–66].

We stress that the parameters introduced here ($\epsilon_{\text{eff}}, \mu_{\text{eff}}$) are, in general, angle of incidence dependent. By contrast, the material parameters of naturally occurring material systems are, in general, angle independent, a property referred to as locality. In order to obtain local material parameters from $\epsilon_{\text{eff}}, \mu_{\text{eff}}$, further corrections are necessary, depending on the symmetry of the metamaterial arrangement. We discuss this in more detail in Section 2.4.

Additionally, to accurately employ the S-parameter retrieval in subwavelength composite systems, they ought to be centrosymmetric with respect to their center in z . This is a requirement in order to ensure that the reflection, coming from incidence from either side (1 or 2 in Fig. 2.1c) is the same, so that the effective parameters do not depend on the incidence side, and avoid further non-locality complications (for a detailed discussion see [60, 65]). Furthermore, the applicability of the retrieval is limited to systems that maintain the polarization of incident light upon reflection and transmission (i.e. in the absence of depolarization effects).

2.2 Effective medium approximations and the Maxwell Garnett result for 1D metamaterials

Despite the extremely wide use and applicability of S-parameter retrieval approaches for 3D and 2D metamaterials [13, 17, 37, 57–60, 62], planar 1D multilayer metamaterials are typically treated with effective medium approximations (EMAs). Particularly, planar HMMs, introduced in Section 1.4, constructed of subwavelength metallic and dielectric layers are almost exclusively treated with EMAs [10, 31–33, 36, 38, 39, 41, 67–69]. The most commonly used approximation for modeling the dielectric permittivity of a planar 1D multilayer is the Maxwell Garnett approximation, developed in 1985. We present it below [46].

First we note that a planar heterostructure exhibits uniaxial anisotropy, hence the dielectric permittivity is a diagonal tensor, $\vec{\epsilon}_{\text{eff}} = \text{diag}\{\epsilon_x = \epsilon_o, \epsilon_y = \epsilon_o, \epsilon_z = \epsilon_e\}$, where ϵ_o and ϵ_e are the ordinary and extraordinary components of the tensor, corresponding to the directions in-plane and along the optical axis (z direction), respectively. Here we have assumed that the constituent materials of the planar heterostructure are isotropic and non-magnetic, for simplicity.

Now let us constrain ourselves to a purely periodic, infinite heterostructure composed of two materials with dielectric permittivities $\epsilon_{1,2}$ and thicknesses $l_{1,2}$, as shown schematically in Fig. 2.2. In order to compute ϵ_o , we must consider electric fields tangential to the heterostructure interfaces (x or y). The electric displacement field at each layer of the heterostructure is given by $D_{x1,2} = \epsilon_{1,2}E_{x1,2}$, and hence the average electric displacement over the heterostructure's period $\Lambda = l_1 + l_2$ is

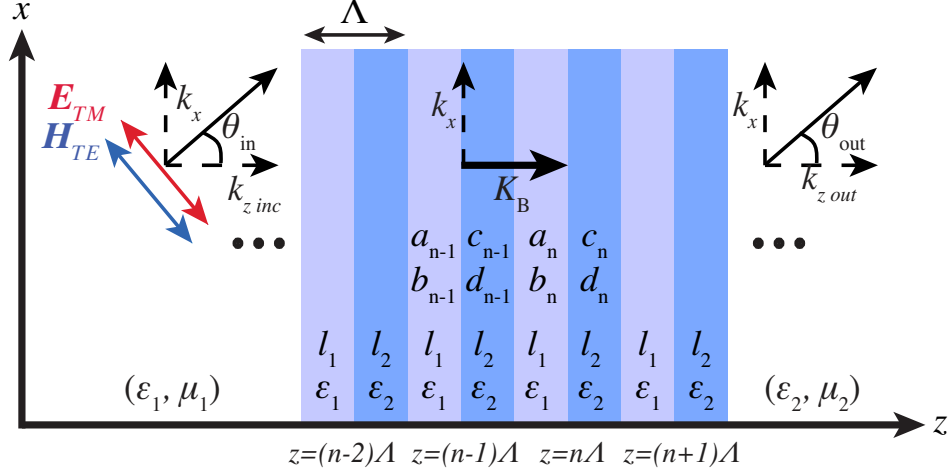


Figure 2.2: Schematic of an infinite periodic bilayer medium with parameters $(\epsilon_{1,2}, l_{1,2})$. K_B is the Bloch wavenumber discussed in Section 2.3. a_n, b_n, c_n, d_n are the forward and backward field amplitudes computed through the transfer matrix for layered media [1]. k_x is the in-plane wavenumber, which remains conserved, and $k_{z,inc/out}$ are the incident and outgoing out-of-plane wavenumbers.

$$\langle D_x \rangle = \frac{1}{l_1 + l_2} (l_1 \epsilon_1 E_{x1} + l_2 \epsilon_2 E_{x2}) \quad (2.8)$$

The basic assumption behind the Maxwell Garnett result lies in the following: by assuming $l_{1,2} \ll \lambda$, where λ is the free space wavelength of the incident field, we can make the approximation that the variation of the electric field E_x inside the heterostructure is extremely slow and can be neglected. By further employing Maxwell's boundary condition for the continuity of the tangential electric field across a boundary, we arrive at $E_{x1} = E_{x2} = \langle E_x \rangle$. Thus, from Eq. (2.8) and Maxwell's constitutive equation $D = \epsilon E$, we obtain

$$\epsilon_o = \frac{1}{l_1 + l_2} (l_1 \epsilon_1 + l_2 \epsilon_2) \quad (2.9)$$

Analogously, the average value of E_z is

$$\langle E_z \rangle = \frac{1}{l_1 + l_2} \left(l_1 \frac{D_{z1}}{\epsilon_1} + l_2 \frac{D_{z2}}{\epsilon_2} \right) \quad (2.10)$$

By employing Maxwell's boundary condition for the continuity of the normal component of the electric displacement and, again, assuming no field variation within a period Λ of the heterostructure, we have $D_{z1} = D_{z2} = \langle D_z \rangle$. Using Maxwell's constitutive equation $D = \epsilon E$, we obtain

$$\frac{1}{\epsilon_e} = \frac{1}{l_1 + l_2} \left(\frac{l_1}{\epsilon_1} + \frac{l_2}{\epsilon_2} \right) \quad (2.11)$$

Eqs. (2.9), (2.11) summarize the Maxwell Garnett result [46]. It is important to emphasize that the validity of the Maxwell Garnett EMA is dependent upon the accuracy of the assumption that the fields exhibit negligible variation within the metamaterial unit cell. For this to be true, the index contrast between the two materials that compose the heterostructure ($\sqrt{\epsilon_1} - \sqrt{\epsilon_2}$) ought to be small. Furthermore, EMA approaches, including the Maxwell Garnett result, typically pertain to a bilayer arrangement that is infinite and purely periodic [46, 49–52]. Finally, as seen from the analysis above, there has been no reference to magnetic effective properties. Traditional EMAs for planar heterostructures typically assume $\mu_{\text{eff}} = 1$ along all coordinate directions. This is justified with the argument that the absence of any circular inclusions in a 1D arrangement of layers precludes the induction of currents distributions that could resemble a magnetic dipole response. For more details on the accuracy of this assumption, see Chapter 3.

In contrast to EMAs, the applicability of S-parameter approaches is not limited in terms of the number of unit cells and constituent materials; the interior of the slab of thickness d (see Fig. 2.1a) can be composed of any arrangement of meta-atoms, as long as they are subwavelength and centrosymmetric, as mentioned in Section 2.1. Furthermore, by using an S-parameter approach that accounts for the finite thickness of the slab, displayed with d in Fig. 2.1a, one can decouple the dielectric response from the magnetic one, through Eqs. (2.5) and (2.6). For more details see Chapter 3.

Despite the constraints under which the Maxwell Garnett EMA is valid, its simplicity (see Eqs. (2.9), (2.11)) makes it the most widely used method for approximating the response of a HMM [10, 31–33, 36, 38, 39, 41, 67–69].

2.3 The Bloch wavenumber

Another homogenization approach applicable to planar 1D heterostructures is the Bloch method [69–71], formulated, among others, in [1]. In its most widely used form discussed here, it is also constrained to purely periodic bilayer arrangements that are unbound, similar to EMAs. In contrast to EMAs, the Bloch result holds at any frequency range and is not limited to the quasistatic metamaterial limit. For example, the Bloch approach is also widely used for determining the band structure of 1D photonic crystals.

We start with a bilayer 1D arrangement that is periodic in the z -direction (see Fig. 2.2), with period Λ . This permittivity of this composite can be expressed through

$\epsilon(z + \Lambda) = \epsilon(z)$. This dielectric environment is seen by a propagating electric field equivalently to the way in which an electron wavefunction experiences a periodic potential in crystalline solids. Hence the formulation of this problem is identical to the Kronig-Penney model for the band theory of solids [1, 30]. Hence, solutions to the wave equation are given by

$$E_K(z, x) = E_K(z) e^{i(k_x x - \omega t)} e^{iK_B z} \quad (2.12)$$

where k_x is the in-plane wavenumber. K_B is the Bloch wavenumber that describes wave propagation in the z direction, together with $E_{K_B}(z)$. Using the Floquet theorem, we have for $E_K(z)$

$$E_K(z + \Lambda) = E_K(z) \quad (2.13)$$

Another formulation of wave propagation in the bilayer periodic layered medium depicted in Fig. 2.2 is with the traditional transfer matrix approach [1]. Based on it, the electric field is $E(z, x, t) = E(z) e^{i(k_x x - \omega t)}$, where $E(z)$ is expressed as a sum of forward and backward propagating plane waves:

$$E(z) = \begin{cases} a_n e^{ik_{z,1}(x-n\Lambda)} + b_n e^{-ik_{z,1}(x-n\Lambda)}, & n\Lambda - l_1 < z < n\Lambda \\ c_n e^{ik_{z,1}(x-n\Lambda)} + d_n e^{-ik_{z,2}(x-n\Lambda)}, & (n-1)\Lambda < z < n\Lambda - l_1 \end{cases} \quad (2.14)$$

The subscript n pertains to the layer order, as shown in Fig. 2.2. $k_{z,1}$ and $k_{z,2}$ are the out-of-plane wavenumbers at layers 1 and 2, respectively, given by $k_{z,1,2} = \sqrt{\epsilon_{1,2} \frac{\omega^2}{c^2} - k_x^2}$. The relative amplitudes a_n, b_n, c_n, d_n are determined through Maxwell's boundary conditions in a matrix form. The details of the matrix formalism can be found in [1]. Here, we briefly mention that wave propagation in consecutive unit cells is expressed through

$$\begin{pmatrix} a_{n-1} \\ b_{n-1} \end{pmatrix} = \begin{pmatrix} A & B \\ C & D \end{pmatrix} \begin{pmatrix} a_n \\ b_n \end{pmatrix} \quad (2.15)$$

where A, B, C, D are the transfer matrix elements for the unit cell, presented in Appendix A.1 for both TE and TM polarizations. In terms of this representation and from Eq. (2.13) together with S, we obtain

$$\begin{pmatrix} a_n \\ b_n \end{pmatrix} = e^{iK_B \Lambda} \begin{pmatrix} a_{n-1} \\ b_{n-1} \end{pmatrix} \quad (2.16)$$

Using Eq. (2.15), we obtain

$$\begin{pmatrix} A & B \\ C & D \end{pmatrix} \begin{pmatrix} a_n \\ b_n \end{pmatrix} = e^{-iK_B\Lambda} \begin{pmatrix} a_n \\ b_n \end{pmatrix} \quad (2.17)$$

By solving Eq. (2.17) for the Bloch wavenumber, we get

$$\cos(K_B\Lambda) = \frac{A + D}{2} \quad (2.18)$$

Eq. (2.18) expresses a homogenization. Similar to the effective wavenumber k_{eff} that we introduced in Section 2.1 (Eq. (2.3)), the Bloch wavenumber K_B is an effective parameter introduced to simplify wave propagation inside the multilayer heterostructure. The left hand of Eq. (2.18) refers to the homogenized system, whereas the parameters A and D on right hand side pertain to the layered medium and are functions of $\epsilon_{1,2}$ and $l_{1,2}$.

Typically, in the case of HMMs, the Bloch wavenumber K_B is translated into an effective dielectric permittivity through the dispersion equation for uniaxial media (see Eq. 1.4 in Chapter 1), by being treated as the out-of-plane (k_z) wavenumber [69, 71]. The wavenumbers presented in Eqs. (2.3) and (2.17), pertaining to the S-parameter retrieval and to the Bloch approach, respectively, are useful for numerous reasons apart from serving the purpose of homogenization, as we will discuss in more detail in Chapter 4. In the limit of a purely periodic infinite medium, Eq. (2.18) is identical to Eq. (2.3). For details see Chapter 4.

2.4 S-parameter retrieval for 1D metamaterials

The procedure presented in Section 2.1 describes a homogenization for obtaining effective parameters ϵ_{eff} and μ_{eff} for any composite system, at any angle of incidence for either of the two linear polarizations. These results, formulated initially in [60] are the generalization of previous approaches [57–59], which provided effective parameters for a particular set of incidence direction and field polarization, i.e. for a particular set of $(\vec{k}, \vec{E}, \vec{H})$. Despite the generality of the S-parameter retrieval for oblique incidence, the derived effective parameters do not hold the same meaning as the dielectric permittivity and magnetic permeability of naturally existing materials.

Particularly, the angle of incidence and polarization dependence of the effective parameters hints that they do not provide direct information about the medium itself. We will refer to the effective parameters derived from the S-parameter retrieval of Section 2.1 [60] as *wave* parameters, emphasizing on the fact that they depend on the wave polarization and angle of incidence, and we will use the symbols $\epsilon_{\text{TE/TM}}(\theta_{\text{in}})$,

$\mu_{\text{TE/TM}}(\theta_{\text{in}})$ to refer to them. Their angle of incidence dependence typically arises from intrinsic anisotropy that is not explicitly accounted for by the mere application of the retrieval discussed in Section 2.1. In contrast to wave parameters, which are scalars, we introduce the notion of *material* parameters, which are a global description of a system and are, thus, polarization independent and also independent of the angle of incidence in the absence of spatial dispersion [72]. Hence, in their most general form, material parameters are tensors with tensor elements that are independent of polarization, angle of incidence and total thickness of the medium [2]. This is, for example, the case for naturally occurring materials, the optical properties of which are global. By contrast, wave parameters of metamaterials do not necessarily satisfy these conditions [57, 65, 73]. We shall refer to material parameters with $\vec{\epsilon} = \text{diag}\{\epsilon_{xx}, \epsilon_{yy}, \epsilon_{zz}\}$ and $\vec{\mu} = \text{diag}\{\mu_{xx}, \mu_{yy}, \mu_{zz}\}$.

The representation of the intrinsic electromagnetic properties of any system in terms of tensorial dielectric permittivity and magnetic permeability, i.e. material parameters, is useful and general. From a theoretical point of view, it provides a concise description of a system that is independent of the excitation conditions (angle of incidence, polarization, etc). From an experimental point of view, material parameters are easily captured with conventional methods like spectroscopic ellipsometry; by rotating a sample to probe different crystal orientations, all the tensor elements may be obtained. By contrast, it is not straightforward nor meaningful to experimentally probe wave parameters, $\epsilon_{\text{TE/TM}}(\theta_{\text{in}})$, $\mu_{\text{TE/TM}}(\theta_{\text{in}})$ with conventional material characterization schemes.

The optimal way to obtain material parameters for metamaterials is to perform *ab initio* electronic structure calculations of the meta-atoms arrangements, similar to natural materials. However this requires very large scale computations and is currently computationally intractable in terms of CPU performance and memory. An alternative approach is to take into account the symmetry group of the metamaterial arrangement and to utilize the dispersion equations for its particular class of anisotropy; isotropic, uniaxial, or biaxial (in the absence of magnetoelectric coupling). The dispersion equation, for a general bianisotropic medium with tensorial dielectric permittivity $\vec{\epsilon}$ and tensorial magnetic permeability $\vec{\mu}$ is obtained through Helmholtz's equation

$$\vec{k} \times \vec{\mu}^{-1}(\vec{k} \times \vec{E}) + \omega^2 \vec{\epsilon} \vec{E} = 0 \quad (2.19)$$

In this chapter we present a method developed for determination of material parameters for metamaterials with uniaxial anisotropy [47]. We shall refer to this method as material parameter retrieval, as opposed to the S-parameter retrieval described

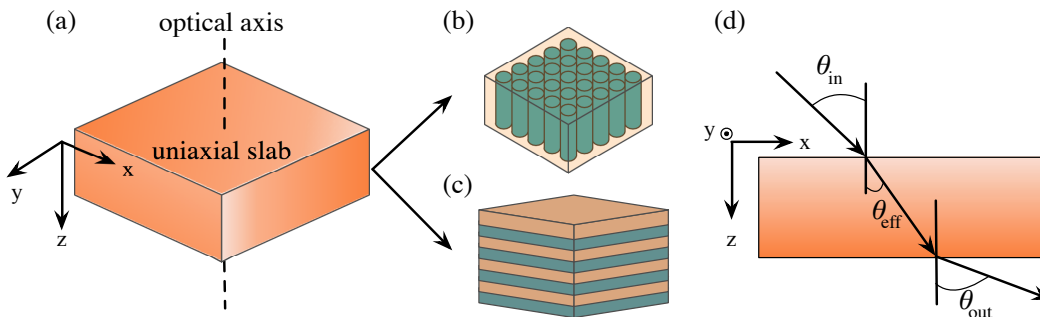


Figure 2.3: (a) Three-dimensional representation of the composite uniaxial slab that can be, among others, (b) a nanowire array or (c) a multilayer meta-material. (d) Projection of (a) onto the xz plane and our convention for the angle of incidence.

in Section 2.1 [60], which we will refer to as wave parameter retrieval. We are motivated to investigate uniaxial metamaterials due to their extraordinary properties in the limit of parameters of opposite sign along different coordinate directions, which we briefly discussed for the case of HMMs in Section 1.4. The two particular configurations that are of special interest are nanowire arrays (Fig. 2.3b) and multilayers (Fig. 2.3c).

For a uniaxial medium, the permittivity and permeability tensors are of the form $\vec{\epsilon} = \text{diag}\{\epsilon_{xx} = \epsilon_o, \epsilon_{yy} = \epsilon_o, \epsilon_{zz} = \epsilon_e\}$, and $\vec{\mu} = \text{diag}\{\mu_{xx} = \mu_o, \mu_{yy} = \mu_o, \mu_{zz} = \mu_e\}$, respectively. The subscript -o pertains to the directions normal to the optical axis (x and y here, see Fig. 2.3(a)), or ordinary direction, whereas -e pertains to the optical axis, or extraordinary direction. Carrying out the algebra of Eq. (2.19) for uniaxial permittivity and permeability tensors, for TE polarization (defined in Fig. 2.2) we obtain

$$\frac{k_x^2 + k_y^2}{\epsilon_o(\omega, \vec{k})\mu_e(\omega, \vec{k})} + \frac{k_z^2}{\epsilon_o(\omega, \vec{k})\mu_o(\omega, \vec{k})} = k_o^2 \quad (2.20)$$

For TM polarization, the dispersion is:

$$\frac{k_x^2 + k_y^2}{\epsilon_e(\omega, \vec{k})\mu_o(\omega, \vec{k})} + \frac{k_z^2}{\epsilon_o(\omega, \vec{k})\mu_o(\omega, \vec{k})} = k_o^2 \quad (2.21)$$

The dependence of the material parameters ϵ_o , ϵ_o , ϵ_o , ϵ_o on the wavenumber \vec{k} is referred to as spatial-dispersion or non-locality. Spatial dispersion may play some role in systems that are not in the extreme deep subwavelength limit [72, 74]. Without loss of generality, we consider propagation in the xz plane (i.e.

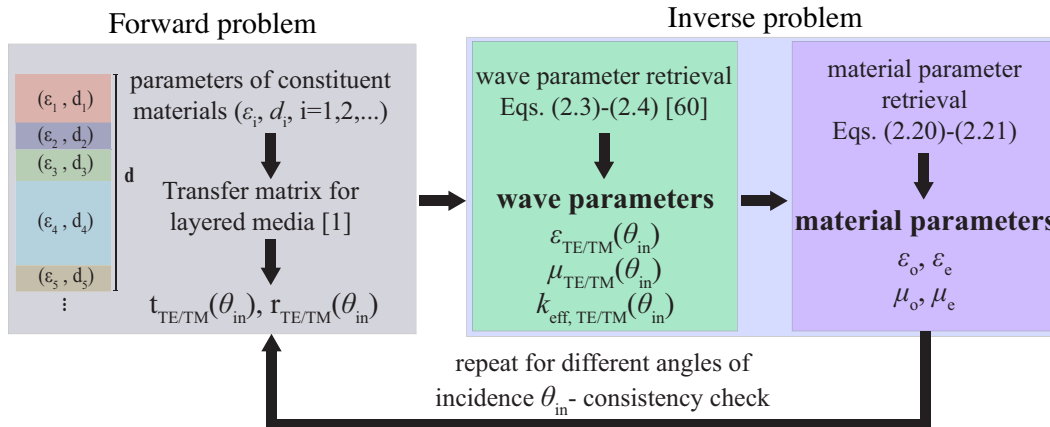


Figure 2.4: Flow chart of material parameter retrieval for uniaxial metamaterials.

$k_y = 0$). As shown in Fig. 2.2, k_x is the tangential wavenumber, which is conserved and equal to $k_x = n_1 k_o \sin(\theta_{in}) = n_2 k_o \sin(\theta_{out})$, where $k_o = \omega/c$. Considering the effective medium with effective parameters $\epsilon_{TE/TM}(\theta_{in})$, $\mu_{TE/TM}(\theta_{in})$, we have $n_{TE/TM}(\theta_{in}) = \sqrt{\epsilon_{TE/TM} \mu_{TE/TM}}$, hence $k_x = n_{TE/TM} k_o \sin(\theta_{eff_{TE/TM}})$, where θ_{eff} is the effective refracted angle in the effective medium, as shown in Figs. 2.1, 2.3. With knowledge of $n_{TE/TM}$ through the material parameter retrieval, we easily obtain $\theta_{eff_{TE/TM}}$. Similarly to k_x , the normal component of the wavevector is $k_z = n_{TE/TM} k_o \cos(\theta_{eff})$. However k_z is also the effective wavenumber, obtained through Eq. (2.3). From the above, Eqs. (2.20), (2.21) yield

$$\frac{\sin^2(\theta_{eff_{TE}})}{\epsilon_o \mu_e} + \frac{\cos^2(\theta_{eff_{TE}})}{\epsilon_o \mu_o} = \frac{1}{\epsilon_{TE}(\theta_{in}) \mu_{TE}(\theta_{in})} \quad (2.22)$$

and

$$\frac{\sin^2(\theta_{eff_{TM}})}{\epsilon_e \mu_o} + \frac{\cos^2(\theta_{eff_{TM}})}{\epsilon_o \mu_o} = \frac{1}{\epsilon_{TM}(\theta_{in}) \mu_{TM}(\theta_{in})} \quad (2.23)$$

for TE and TM polarization, respectively.

Eqs. (2.22), (2.23) connect the wave parameters $\epsilon_{TE/TM}$, $\mu_{TE/TM}$ with the material parameters $\epsilon_{o/e}$, $\mu_{o/e}$. At normal incidence $\theta_{in} = 0$ and $k_x = 0$, hence $\sin(\theta_{eff}) = 0$ and $\epsilon_o = \epsilon_{eff_{TE}}(\theta_{in} = 0) = \epsilon_{eff_{TM}}(\theta_{in} = 0)$ and $\mu_o = \mu_{eff_{TE}}(\theta_{in} = 0) = \mu_{eff_{TM}}(\theta_{in} = 0)$. This is expected since at normal incidence the two linear polarizations are degenerate.

By having already retrieved the ordinary parameters ϵ_o , μ_o , the wave parameter retrieval may be applied at oblique incidence for TE (TM) polarization, for obtaining μ_e (ϵ_e), through Eqs. (2.22), (2.23) for non-zero $\cos(\theta_{eff_{TE/TM}})$. Repeating this

process for different angles of incidence allows us to determine the degree of spatial dispersion of the system under consideration. This procedure is schematically outlined in Fig. 2.4.

2.5 A sanity check

To illustrate the validity of the described retrieval approach, let us first apply it to an example case. We select a 50 nm slab of silver (Ag), for which we have *a priori* knowledge of its parameters: $\epsilon_o = \epsilon_e = \epsilon_{\text{Ag}}$ and $\mu_o = \mu_e = 1$. We model ϵ_{Ag} with a five-poles Drude-Lorentz [75] and calculate its transmission and reflection coefficients for TE and TM polarization, using the transfer matrix approach [1]. By applying the wave parameter retrieval (see terminology in Fig. 2.4), we obtain the parameters $\epsilon_{\text{TE/TM}}(k_{//})$ and $\mu_{\text{TE/TM}}(k_{//})$, presented in Fig. 2.5 as a function of the incident angle since $k_{//} = k_o \sin \theta_{\text{in}}$, where $k_o = \frac{2\pi}{\lambda}$.

For TE polarization and for all incident angles, the effective parameters ϵ_{TE} and μ_{TE} are nearly angle independent; see Figs. 2.5a, b, e, f. Furthermore, we have $\epsilon_{\text{TE}} = \epsilon_{\text{Ag}}$ and $\mu_{\text{TE}} = 1 + i0$. Although this is the expected result for both linear polarizations, TM polarization yields a different response. As can be seen from Figs. 2.5c, d, g, h, ϵ_{TM} is strongly dependent on the angle of incidence, which demonstrates that it is not an intrinsic material parameter, as we know *a priori* that silver is isotropic, and hence it has an angle independent dielectric response. Furthermore, μ_{TM} drastically deviates from unity and is also strongly dependent on the angle of incidence, leading to the same conclusion. Therefore, it is obvious that the wave parameter retrieval does not yield the properties of silver. By contrast the parameters $\epsilon_{\text{TE/TM}}$ and $\mu_{\text{TE/TM}}$ depend on the illumination conditions (e.g., polarization, angle of incidence), hence they do not provide direct information regarding the intrinsic properties of the system under consideration.

This issue was addressed in our discussion in Section 2.4. By utilizing Eqs. (2.20), (2.21), we obtain the material parameters for the example system, namely $\epsilon_{o/e}$ and $\mu_{o/e}$, shown in Fig. 2.6. As expected, and contrary to the wave parameters, $\epsilon_{o/e}$ and $\mu_{o/e}$ are angle independent and exactly reproduce the optical response of silver: $\epsilon_o = \epsilon_e = \epsilon_{\text{Ag}}$ and $\mu_o = \mu_e = 1 + i0$.

This example serves as a sanity check for validating the accuracy of the material parameter retrieval for planar systems, described in Section 2.4. A similar sanity check can be applied to any homogeneous material slab with known parameters, as long as some loss is involved in the system in terms of a non-zero imaginary part in at least one of $\epsilon_{o/e}$, $\mu_{o/e}$. This is necessary in order for the sign ambiguity in Eq. (2.3) to be resolved (see discussion in Section 2.1).

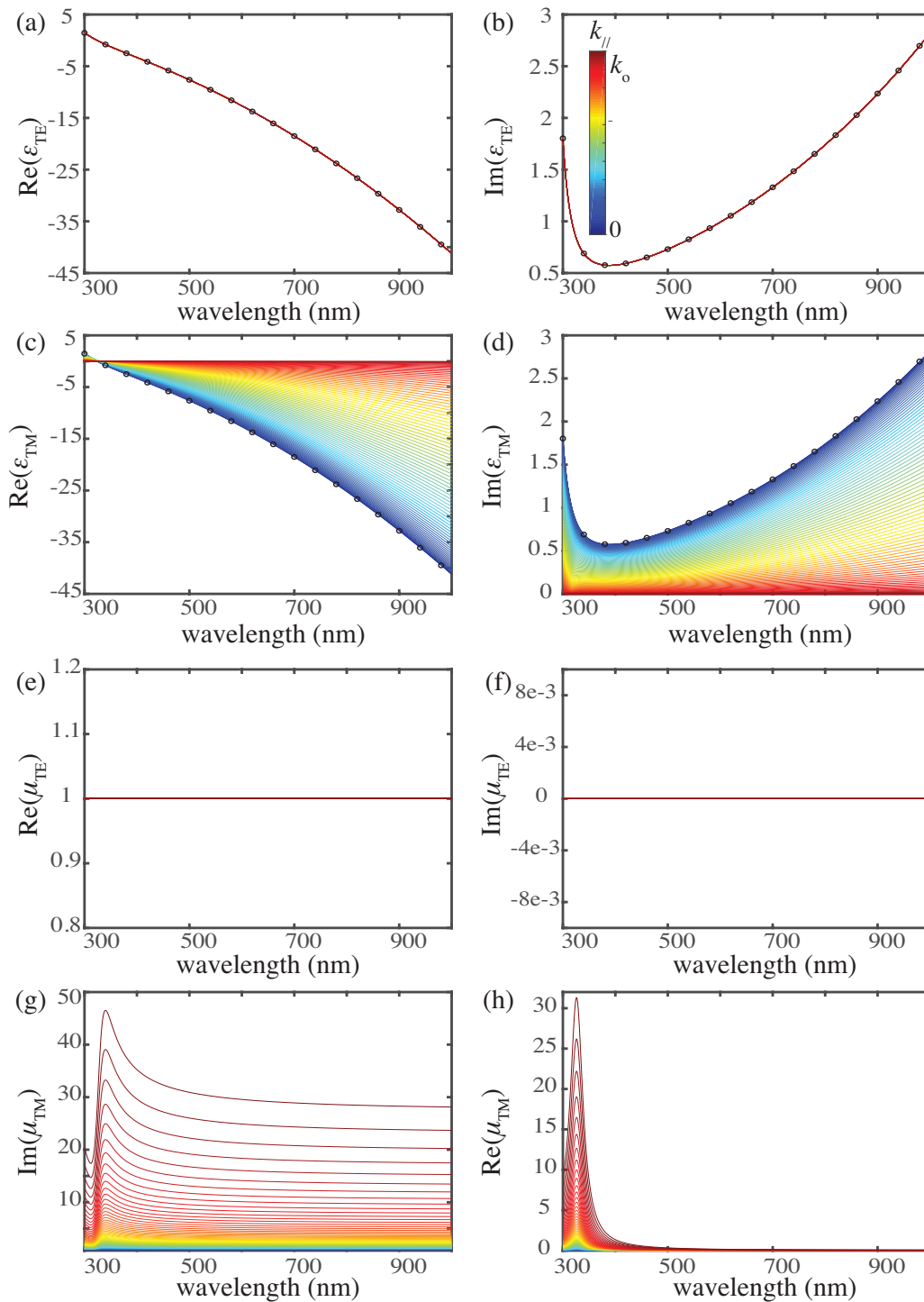


Figure 2.5: Effective wave parameters for a slab of silver of thickness 50 nm. (a) $\text{Re}(\epsilon_{\text{TE}}(k_{//}))$, (b) $\text{Im}(\epsilon_{\text{TE}}(k_{//}))$, (c) $\text{Re}(\epsilon_{\text{TM}}(k_{//}))$, (d) $\text{Im}(\epsilon_{\text{TM}}(k_{//}))$, (e) $\text{Re}(\mu_{\text{TE}}(k_{//}))$, (f) $\text{Im}(\mu_{\text{TE}}(k_{//}))$, (g) $\text{Re}(\mu_{\text{TM}}(k_{//}))$, (h) $\text{Im}(\mu_{\text{TM}}(k_{//}))$, where $k_{//} = k_0 \sin \theta_{\text{in}}$. Black dotted lines in (a)-(d) correspond to the dielectric permittivity of silver ϵ_{Ag} .

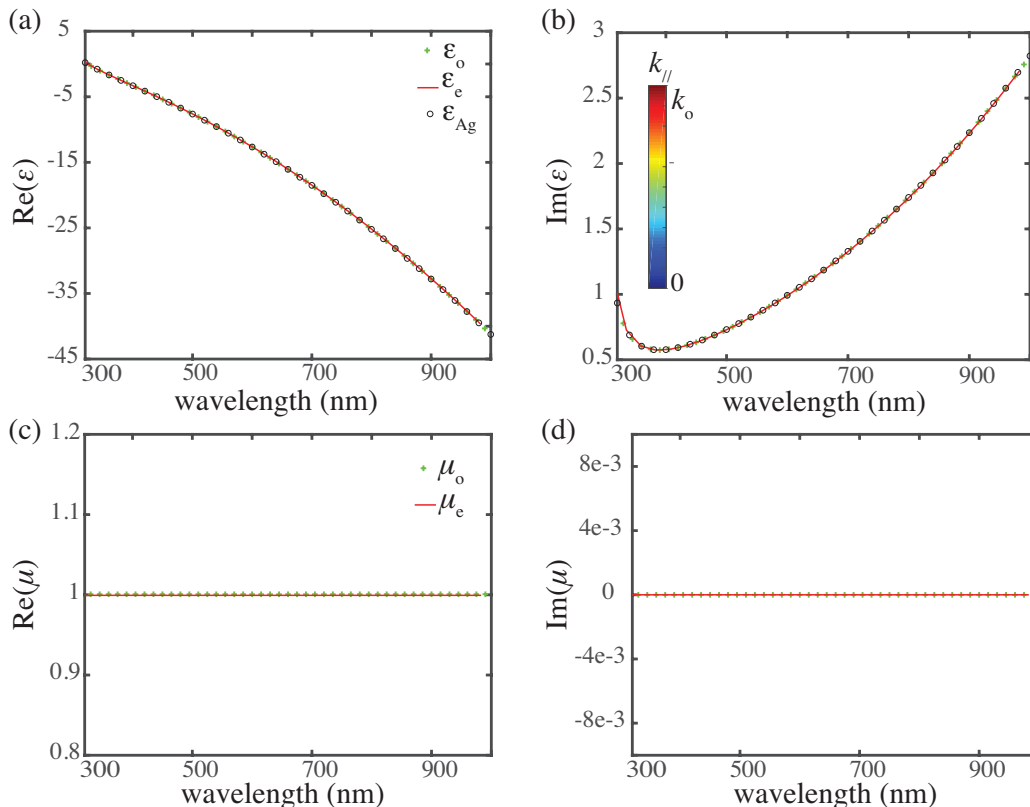


Figure 2.6: Restored material parameters for a slab of silver of thickness 50 nm. (a) $\text{Re}(\epsilon_{o/e}(k_{//}))$, (b) $\text{Im}(\epsilon_{o/e}(k_{//}))$, (c) $\text{Re}(\mu_{o/e}(k_{//}))$, (d) $\text{Im}(\mu_{o/e}(k_{//}))$.

2.6 Comparison between S-parameter retrieval and EMAs: $\mu \neq 1$!

By establishing (a) the difference between the nature of wave and material parameters in Section 2.4 and (b) the validity of the material parameter retrieval in Section 2.5, we proceed to examine multilayer configurations, which is the main topic of interest in the thesis. We study a layered system composed of Ag/SiO₂ subwavelength layers of thickness 20 nm each, terminated with SiO₂. As discussed in Section 1.4, metallodielectric multilayer metamaterials exhibit a hyperbolic dispersion, arising from their unusual property $\epsilon_o \epsilon_e < 0$. Here, we illustrate this and compare our results to traditional EMAs.

As illustrated in Fig. 2.4, we start by using the transfer matrix approach for computing the transmission and reflection coefficients of our multilayer system of varying number of layers for TE and TM polarization and angles of incidence from 0 to 90 degrees, hence $k_{//} \in [0, k_o]$, as in the previous example. By first obtaining the wave parameters $\epsilon_{\text{TE/TM}}$, $\mu_{\text{TE/TM}}$, which we omit presenting as they do not provide any physical insight (see discussion in previous section), we obtain the effective tensorial

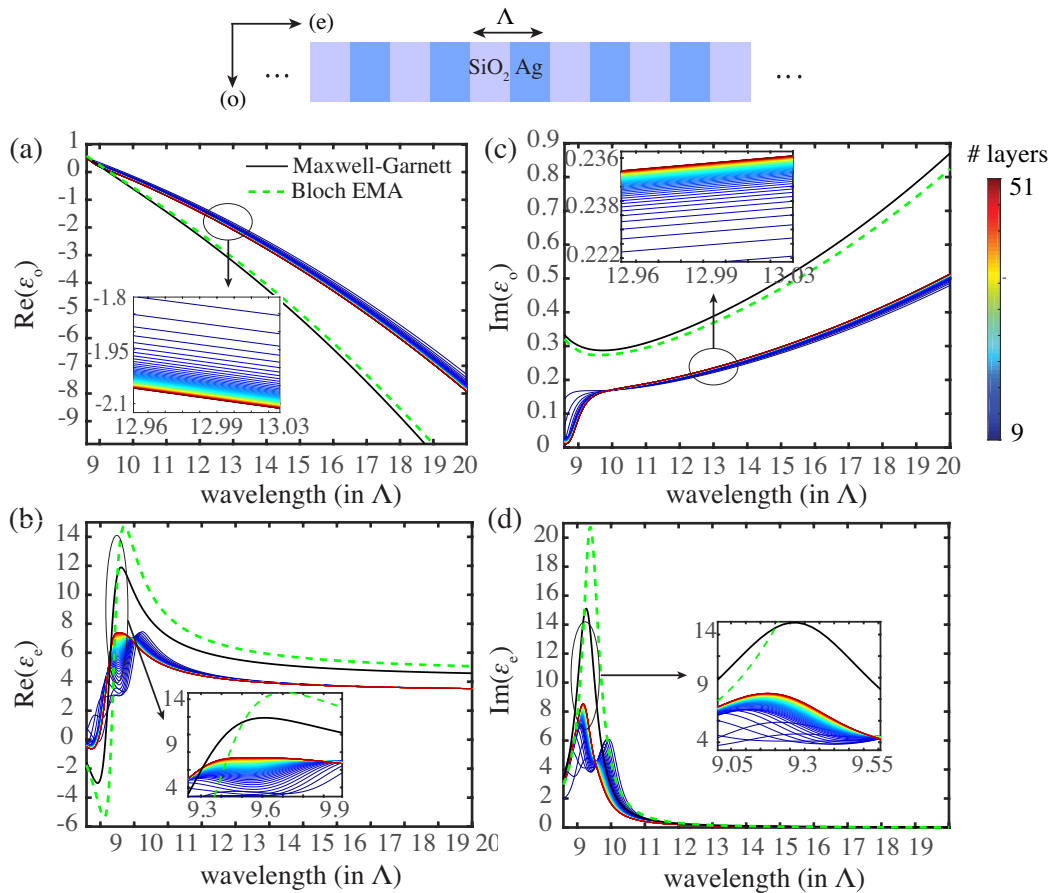


Figure 2.7: Effective dielectric permittivity for a multilayer HMM composed of Ag/SiO₂ layers [47]. (a) $\text{Re}(\epsilon_o)$, (b) $\text{Im}(\epsilon_o)$, (c) $\text{Re}(\epsilon_e)$, (d) $\text{Im}(\epsilon_e)$, and comparison with the Maxwell Garnett result [46] and a generalized non-local Bloch approach [69].

dielectric permittivity of the metamaterial, $\vec{\epsilon}_{\text{eff}} = \text{diag}\{\epsilon_o, \epsilon_o, \epsilon_e\}$, shown in Fig. 2.7.

As expected, the in-plane dielectric response is metallic, $\epsilon_o < 0$, due to the presence of Ag, which is a plasmonic metal with $\epsilon_{\text{Ag}} < 0$. By contrast, however, in the out-of-plane direction we have $\epsilon_e > 0$. This is justified as the dielectric (SiO₂) layers act as barriers of conduction, hence inducing a dielectric response [31, 47]. Therefore, in the long wavelength limit we indeed obtain $\epsilon_o \epsilon_e < 0$ and this configuration is hyperbolic. It is important to highlight the very weak dependence of the parameters ϵ_o , ϵ_e on the number of layers. This property is fundamental for material parameters to be valid, along with angle of incidence independence, which was justified in the previous section.

In Fig. 2.7 we also compare our results with the Maxwell Garnett EMA, which is the most widely used approach for approximating the response of HMMs, and with

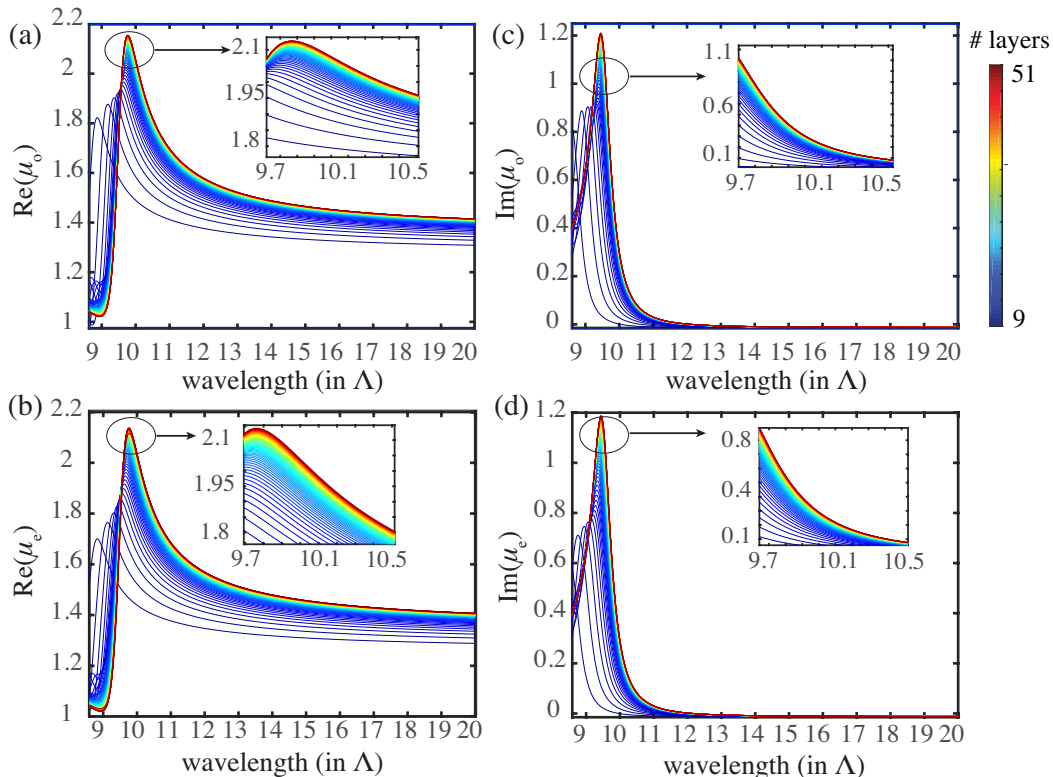


Figure 2.8: Effective magnetic permeability for a multilayer HMM composed of Ag/SiO₂ layers [47]. (a) $\text{Re}(\epsilon_o)$, (b) $\text{Im}(\epsilon_o)$, (c) $\text{Re}(\epsilon_e)$, (d) $\text{Im}(\epsilon_e)$.

a generalized non-local EMA based on the Bloch approach (see Section 2.3) [69]. The two EMAs slightly differ from each other as the Bloch-based EMA accounts for non-local effects, whereas the Maxwell Garnett result does not. Furthermore, the material parameter retrieval results differ from both EMAs. This is justified and expected because, as discussed in Sections 2.1, 2.2, 2.3, these EMAs pertain to an infinite periodic system, hence the finite thickness of the stack is not taken into account [1, 46, 47, 69]. By contrast, the basis of the S-parameter retrieval and its generalization to obtain material parameters lies on accounting for finite thickness effects. In fact, it is this additional information that allows decoupling the dielectric permittivity from the magnetic permeability, which we present in Fig. 2.8 [12].

We note that, as the number of layers is increased (see colorbar in Fig. 2.7), our results asymptotically approach the EMA results, along both the ordinary (in-plane) and extraordinary (out-of-plane) directions. This is consistent with the fact that the EMA results pertain to the infinite number of layers limit. We highlight, however, that even for fifty-one layers (twenty-five unit cells), the dielectric permittivity of a finite stack does not coincide with EMA results. Equivalent findings were reported in [47] for Ag/SiO₂ multilayers terminated by Ag, yielding the same conclusion: the

exact result produced by the material parameter retrieval discussed in this chapter deviates from traditionally used EMAs for at least up to thirty layers. We refer to our method as “*exact*” because it accounts for the finite thickness of the metamaterials and does not *a priori* assume that $\vec{\mu}_{\text{eff}} = \mathbb{I}$.

As far as the magnetic permeability $\vec{\mu}_{\text{eff}}$ is concerned, we present in Fig. 2.8 the parameters μ_o , μ_e . By raising the constraint of $\vec{\mu}_{\text{eff}} = \mathbb{I}$, imposed in previous EMA approaches that are widely used for approximating the response of HMMs [31, 32, 42, 76], we reveal that metallodielectric multilayer metamaterials exhibit a non-trivial magnetic response! Both μ_o and μ_e drastically deviate from unity, as they exhibit a resonance approximately at $\lambda = 10\Lambda$. To further emphasize on the physicality of these two parameters, we point out that, similar to ϵ_o , ϵ_e , μ_o , and μ_e also exhibit weak dependence on the number of layers.

2.7 Conclusion

In this chapter we presented a general method for retrieving the effective material parameters for metamaterials with uniaxial anisotropy (Fig. 2.3). The effective parameters we retrieve pertain to the diagonal elements of the permittivity and permeability tensors, $\vec{\epsilon}_{\text{eff}} = \text{diag}\{\epsilon_o, \epsilon_o, \epsilon_e\}$ and $\vec{\mu}_{\text{eff}} = \text{diag}\{\mu_o, \mu_o, \mu_e\}$, respectively. The retrieved parameters are angle of incidence independent, hence they are local material parameters. We apply our approach to planar metallodielectric metamaterials and arrive to the conclusion that their magnetic permeability deviates from unity. This is in contrast to the previous consensus [31, 32, 42, 76]. The details of our method can be supplementary found in [47].

The physical origin of the non-unity magnetic permeability shown in Fig. 2.8, along with its implications deserve special attention. Hence, we devote Chapter 3 to optical artificial magnetism with planar metamaterials and we present an analytical model for understanding this rather surprising result, together with experimental measurements on fabricated multilayer metamaterials. Additionally, we perform impedance matching sanity checks that confirm the validity of our results (please see Fig. 3.6 in Chapter 3).

ARTIFICIAL MAGNETISM IN PLANAR METAMATERIALS

“Science is made up of mistakes, but they are mistakes which it is useful to make, because they lead little by little to the truth.”

Jules Verne, A Journey to the Center of the Earth, 1864

3.1 Previous approaches: Artificial magnetism in 3D and 2D

In the optical spectral range, the magnetic response of most materials, given by the magnetic permeability μ , is generally weak. This is famously expressed by Landau and Lifshitz [2]: *“there is no meaning in using the magnetic susceptibility from the optical frequencies onward, and in discussing such phenomena, we must put $\mu = 1$ ”*. By contrast, in the optical regime, materials possess a diverse range of dielectric properties, expressed through the dielectric permittivity ϵ , which can be positive, negative or zero.

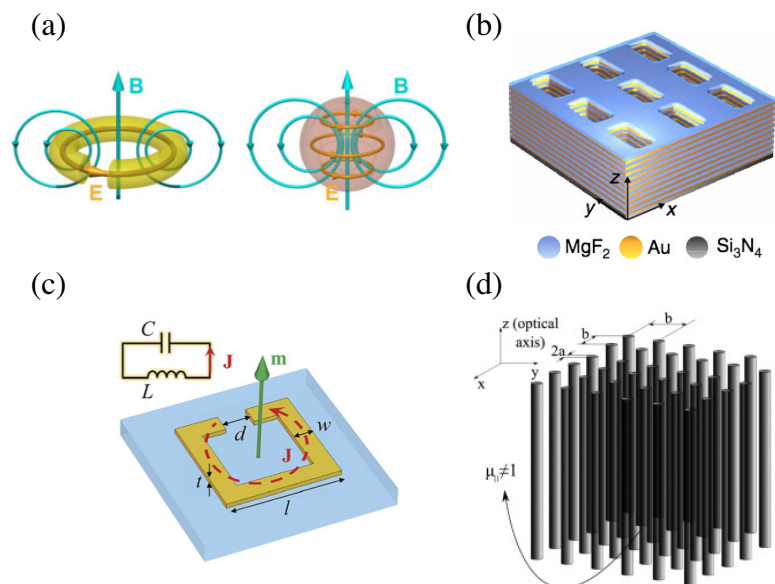


Figure 3.1: Previous results on artificial magnetism with 3D and 2D metamaterials. (a) dielectric rings and nanoparticles, adapted from [21], (b) fishnet metamaterials, adapted from [22], (c) SRRs, adapted from [11], (d) high- ϵ wire medium, adapted from [25].

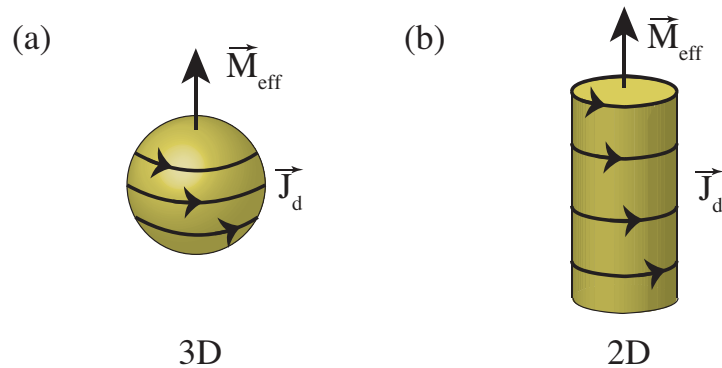


Figure 3.2: Main design motifs for 3D and 2D magnetic metamaterials. Induced magnetization in (a) dielectric nanoparticles (3D metamaterials) (b) in dielectric nanorods (2D metamaterials).

The weak magnetic response in natural materials has motivated a search for structures and systems that may exhibit magnetic properties arising from metamaterial design. Specifically, engineered displacement currents and conduction currents can act as sources of artificial magnetism when metamaterials are illuminated with electromagnetic fields [11]. Nonetheless, until now, the realization of such magnetic metamaterials has required rather complex resonant geometries [11, 77, 78], including arrays of paired thin metallic strips [62, 79], split ring resonators [80–82], and fishnet metamaterials [22], shown in Fig. 3.1 - structures that require sophisticated fabrication techniques at optical frequencies. The principle of operation of such magnetic metamaterials is outlined below.

A circulating electric current can create a magnetic dipole and is the key to inducing magnetism in magnet-free systems. Based on this principle, induction coils generate and induce magnetic flux, allowing to manipulate magnetic fields at radio frequencies (RF). The same concept is widespread in metamaterials design [83, 84]; similarly to the RF regime, by properly shaping metamaterial elements to produce a circulating current flow, magnetic dipoles are induced. Dielectric nanoparticles [20, 21, 85–88] and nanorods [25, 89] have been the building blocks for 3D and two 2D magnetic metamaterial structures, respectively (Fig. 3.2).

3.2 Parameter space for μ and ϵ

Despite astonishing previous reports on magnetic metamaterials within the last twenty years, it is east to see that harnessing artificial optical magnetism, namely at frequencies above the terahertz range, remains a challenging task. The experimental realization of 3D and 2D motifs requires multiple and complicated nanolithography steps, with precision in the nm-scale. By contrast, planar heterostructures and in

particular metallodielectric multilayer HMMs, discussed in the previous chapter, are straightforward to realize experimentally with well-established thin-film deposition techniques (see discussion in Section 1.3). However, such heterostructures, along with their all-dielectric counterparts, are generally considered non-magnetic [31, 32, 42, 46, 69, 76].

The rather simple geometrical structure of HMMs could drastically simplify the means by which we harness artificial magnetism. Furthermore, their hyperbolic dispersion constitutes them attractive candidates as a platform for investigating magnetic effects. Particularly, in contrast to their assumed-to-be-trivial magnetic response, their dielectric properties may be engineered at will along all coordinate directions, yielding interesting hyperbolic and plasmonic effects. Exciting phenomena attributed to dielectric hyperbolic response, $\epsilon_o\epsilon_e < 0$, include but are not limited to negative refraction [31, 36, 38–40, 90] without the need of a negative refractive index, hyper-lensing [9], extreme enhancement in the density of optical states [42] and interface-bound plasmonic modes [8, 71, 91–94]. Nevertheless, all these intriguing physical effects and related applications are limited to TM polarization, while phenomena related to TE polarized waves have remained largely unexplored. Utilizing the effective magnetic response (i.e. $\mu_{\text{eff}} = \text{diag}\{\mu_o, \mu_o, \mu_e\} \neq \mathbb{I}$) is necessary to harness and control arbitrary light polarization (TE as well as TM).

Namely, a uniaxial material with $\epsilon_o < 0$ while $\epsilon_e > 0$ supports negative refraction of phase for TM polarization. On the other hand, for $\epsilon_o > 0$ while $\epsilon_e < 0$, the material supports negative refraction of phase for the same polarization [2]. Furthermore, a plasmonic metal or a metamaterial with negative permittivity, $\epsilon < 0$, supports surface plasmonic waves. These properties are shown in the first quadrant of Fig. 3.3 and have been demonstrated with HMMs [31, 36, 38–40, 71, 90, 91].

By duality, a uniaxial material system with a hyperbolic *magnetic* response of the form $\mu_o < 0$ while $\mu_e > 0$ can allow for negative refraction of phase for TE polarization, demonstrated in the second quadrant of Fig. 3.3. Equivalently, if $\mu_o > 0$ while $\mu_e < 0$, negative refraction of energy would be supported for TE polarization (fourth quadrant in Fig. 3.3). Similarly, a negative μ will yield magnetic plasmons for TE polarization, the magnetic counterpart of surface plasmon polaritons (SPP), as demonstrated in the third quadrant of Fig. 3.3. Finally, gaining control over the magnetic permeability in planar systems can yield impedance-matched epsilon-and-mu-near-zero (EMNZ) optical responses (Fig. 3.3-middle) [96]. While it is straightforward to tailor the permittivity to cross zero in planar metamaterials [97], a simultaneously EMNZ metamaterial at optical frequencies has not yet been demonstrated. To date, none of the aforementioned exciting physical effects have

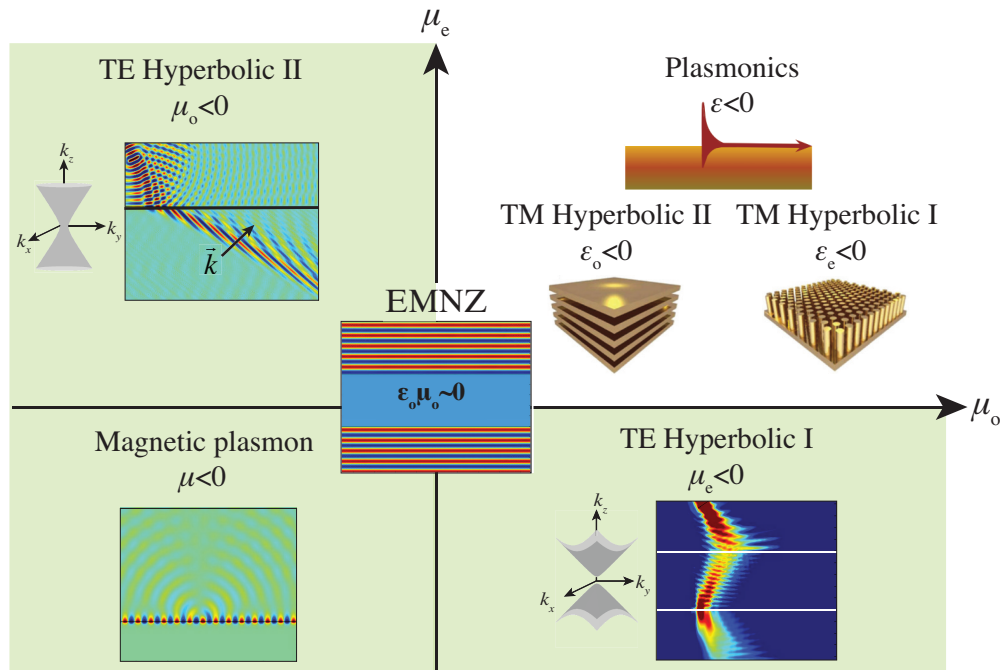


Figure 3.3: Parameter space for μ and ϵ in uniaxial structures. First quadrant: engineered dielectric response yields TM-polarization plasmonic surface waves ($\epsilon < 0$) and hyperbolic metamaterials of type I ($\epsilon_e < 0$) or II ($\epsilon_o < 0$), typically employed with metallic nanowires and metallodielectric multilayers, respectively (HMM schematics adapted from [95]). Second and fourth quadrants: Engineering μ_{eff} can yield TE-polarization hyperbolic response of type II ($\mu_o < 0$) or I ($\mu_e < 0$), supporting negative refraction of phase and energy, respectively. Middle: ϵ and μ near zero (EMNZ) regime: phase diagram demonstrating vanishing phase of incident light.

been demonstrated at high frequencies for TE polarization.

3.3 Artificial magnetism in 1D

Motivated to search for ways to induce artificial magnetism in planar systems, we start by considering a single subwavelength dielectric slab of refractive index n_{diel} and thickness d . When illuminated at normal incidence (z direction in Fig. 3.4a), the displacement current $\vec{J}_d = i\omega\epsilon_o(n_{\text{diel}}^2 - 1)\vec{E}$ induces a macroscopic effective magnetization $\vec{M}_{\text{eff}} = 1/2\mu_o \int (\vec{r} \times \vec{J}_d) dS$ [2, 25, 53]. By averaging the magnetic field, $\langle H \rangle = \int_{-d/2}^{d/2} H(z) dz$, we use $\mu_{\text{eff}} \simeq 1 + M_{\text{eff}}/(\mu_o \langle H \rangle)$ to obtain an empirical closed-form expression for the magnetic permeability:

$$\mu_{\text{eff}} \simeq 1 - \frac{n_{\text{diel}}^2 - 1}{2n_{\text{diel}}^2} \left\{ -1 + \frac{n_{\text{diel}}\pi d/\lambda}{\tan(n_{\text{diel}}\pi d/\lambda)} \right\} \quad (3.1)$$

By setting $n_{\text{diel}} = 1$, we recover the unity magnetic permeability of free space. From Eq. (3.1), we see that μ_{eff} diverges when $\tan(n_{\text{diel}}\pi d/\lambda) = 0$. This yields a magnetic resonant behavior at free space wavelengths $\lambda = n_{\text{diel}}d/\rho$, with $\rho = 1, 2, \dots$. At these wavelengths, the displacement current distribution is anti-symmetric, as shown in Fig. 3.4b for $\rho = 1, 2$. This anti-symmetric current flow closes a loop in $y = \pm\infty$ and induces a magnetization \vec{M}_{eff} that is opposite to the magnetic field of the incident wave (Fig. 3.4a), leading to a magnetic resonance. Eq. (3.1) enables estimating the design parameters for enhanced magnetic response; in the long-wavelength limit, only the fundamental and second order resonances, $\lambda = n_{\text{diel}}d, n_{\text{diel}}d/2$, play significant roles. In the visible and near IR, with layer thicknesses on the order of 10 – 100 nm, dielectric indices higher than $n_{\text{diel}} \sim 2$ are required for strong magnetic effects [98]. The same principle applies for grazing incidence, with the displacement current inducing a magnetic response in the extraordinary or, out-of-plane (z) direction. So far, we have shown that the circular shape designed to support a closed current loop is not a requirement for magnetic metamaterials. A planar structure suffices, for which the current loop closes in \pm infinity.

In order to make this magnetic response significant, we extend this principle to multilayer configurations. We first examine the case of two infinite parallel wires in air, carrying opposite currents (Fig. 3.5a). Their net current distribution induces a magnetic moment which scales with their distance, as dictated by $\vec{M}_{\text{eff}} \propto \vec{r} \times \vec{J}$. This is directly equivalent to a layered configuration composed of two high-index dielectrics separated by air. Their displacement current distribution can be anti-symmetric on resonance, as shown in Fig. 3.5b. By calculating their magnetic

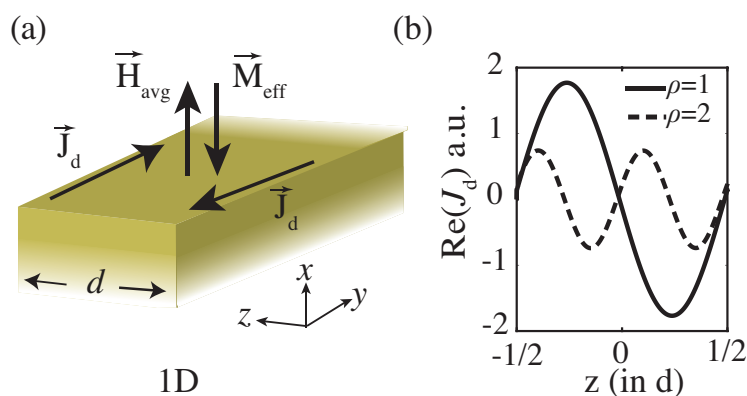


Figure 3.4: A 1D dielectric slab suffices for inducing artificial magnetism. (a) \vec{H}_{avg} is the average magnetic field which faces in the direction opposite to \vec{M}_{eff} . (b) Displacement current distribution at resonance for $\rho = 1, \rho = 2$, for a 90 nm slab of refractive index $n_{\text{diel}} = 4.5$.

permeability μ_{eff} [47], we confirm the magnetic character of this arrangement. As shown with the black curve in Fig.3.5c, μ_{eff} strongly deviates from unity.

The planar geometry does not require that the two high-index layers be separated by air; any sequence of alternating high-low-high refractive index materials will induce the same effect. For example, replacing the air region with a layer of metal, with $n_{\text{metal}} < 1$ at visible wavelengths, does not drastically change the magnetic response. This is shown in Fig. 3.5c with the red curve for a separation layer of silver. Therefore, at optical frequencies, metals do not contribute significantly to the magnetic response in this planar configuration. This is in contrast to the gigahertz regime, where the conduction current in the metallic components of resonant structures has been necessary for strong magnetic effects [79–82]. From the magnetic field distri-

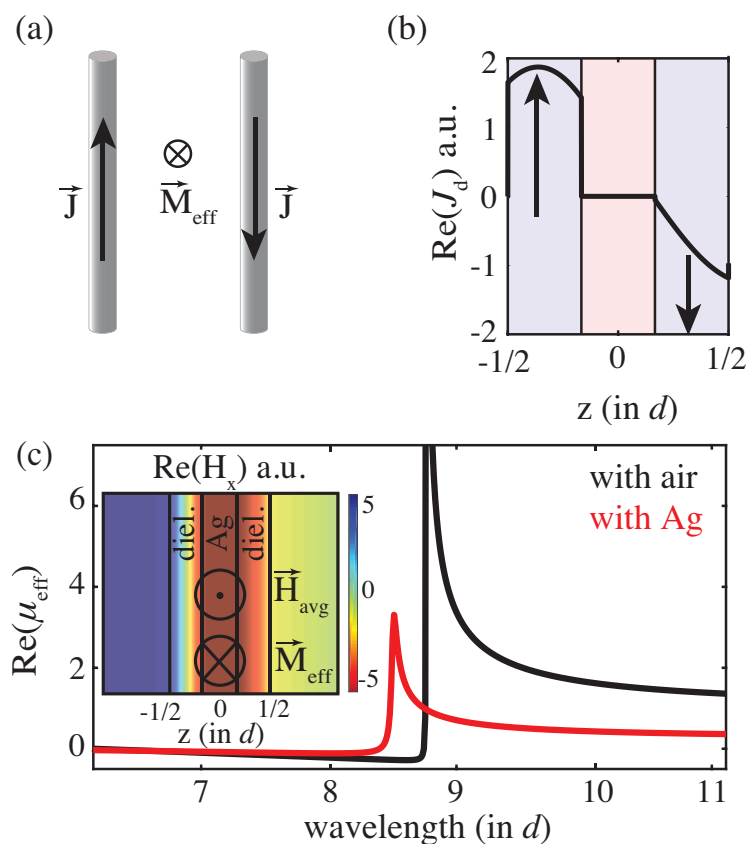


Figure 3.5: Enhancing 1D artificial magnetism with multilayer configurations. (a) Two infinite wires carrying opposite currents are equivalent to (b) two dielectric layers (blue shaded regions) separated by air (pink shaded region) in terms of their current distribution. Arrows in (b) indicate the direction of \vec{J}_d , which is anti-symmetric at resonance. (c) Effective permeability for two dielectric layers separated by air and silver. Inset: tangential magnetic field distribution at resonance: average magnetic field is opposite to \vec{M}_{eff} .

bution shown in the inset of Fig. 3.5c, one can see that the average magnetic field faces in the direction opposite to the magnetization, expressing a negative magnetic response for the dielectric/silver unit cell.

3.4 Another sanity check: Impedance matching

Here we showed that planar configurations, consisting of either metallodielectric multilayer HMMs or alternating high- and low-refractive index layers, possess magnetic properties. We are able to compute their magnetic permeability by utilizing an S-parameter retrieval-based approach (discussed in Chapter 2 and in [47]). Contrary to previously used EMA-based approaches that assume an infinite periodic arrangement [31, 32, 42, 46, 69, 76], our approach accounts for the finite thickness of the metamaterial. By lifting the assumption of an infinite medium, both transmission T and reflection R coefficients can be computed and utilized. This allows obtaining an effective wavenumber k_{eff} together with an effective impedance Z_{eff} [58, 99]. These parameters are then used to decouple the effective permittivity from the permeability through $k_{\text{eff}} = \sqrt{\epsilon_{\text{eff}}\mu_{\text{eff}}}\frac{\omega}{c}$ and $Z_{\text{eff}} = \sqrt{\frac{\mu_{\text{eff}}}{\epsilon_{\text{eff}}}}$. By contrast, Bloch-based approaches [1, 69] only consider a Bloch wavenumber K_{Bloch} , with no other information available for allowing decoupling μ_{eff} from ϵ_{eff} (for details see Section 2.3). Both the Maxwell Garnett EMA [46] and its Bloch-based generalizations (for example [69]) are based on the assumption that $\mu_{\text{eff}} = 1$. For a more detailed discussion see Chapter 2.

By letting the magnetic permeability μ_{eff} be a free parameter, instead of *a priori* setting $\mu_{\text{eff}} = 1$, we obtain magnetic resonances at wavelengths where magnetic dipole moments occur, as demonstrated in Figs. 3.4b, Fig. 3.5 b, c. This confirms the physicality of the non-unity μ ; magnetic resonances arise at wavelengths where the system supports loop-like current distributions.

Another way to establish the validity of the effective parameters is to perform an impedance-matching sanity check in the low loss limit. Based on electromagnetic theory, the impedance of a structure at normal incidence, $Z_{\text{eff}} = \sqrt{\frac{\mu_o}{\epsilon_o}}$, must be unity at transmittance $|T|^2$ maxima. As seen in Figs. 3.6a and b, the retrieved parameters ϵ_o and μ_o accurately describe the scattering properties of both metallodielectric and all-dielectric metamaterials of finite thickness, respectively. By contrast, not accounting for a magnetic permeability leads to inaccurate prediction of transmittance maxima. This is seen both by our S-retrieval-based approach while setting *a priori* the magnetic permeability to unity ($Z_{\mu=1}$), and with the traditional EMA; both approaches fail to predict the resonances.

In what follows, we focus on metallodielectric multilayer metamaterials due to their

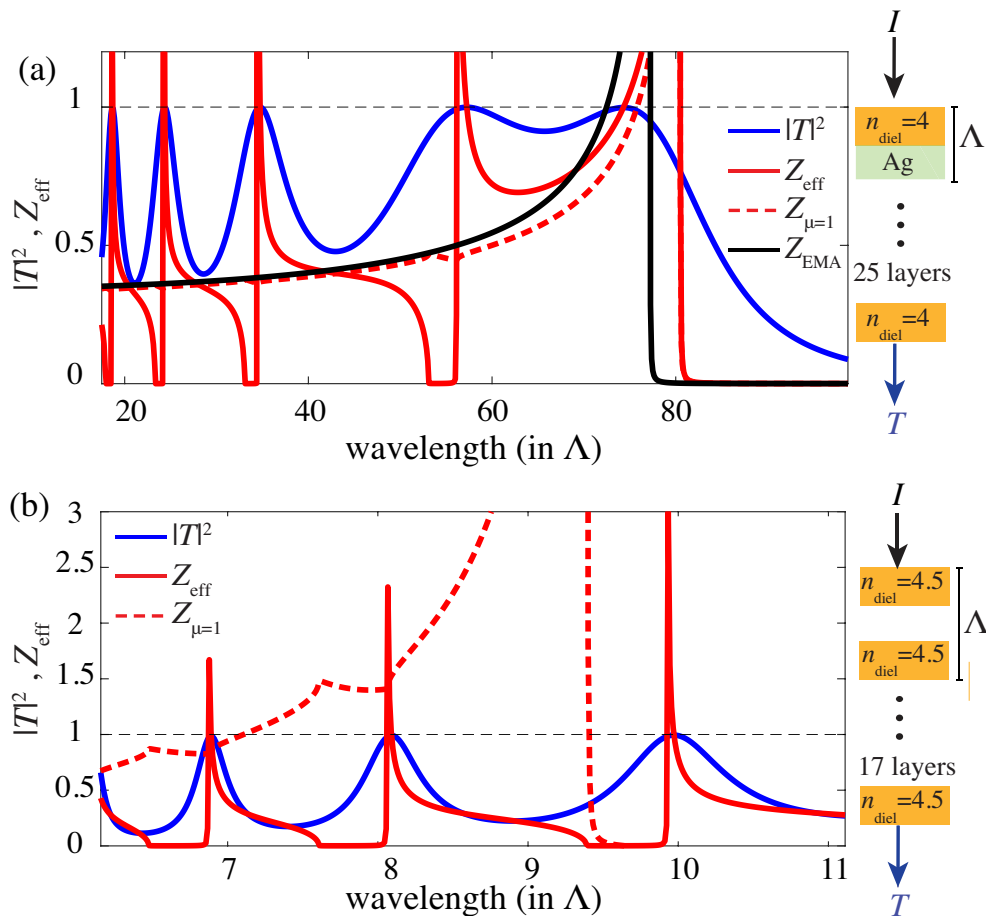


Figure 3.6: Impedance matching sanity check at normal incidence for (a) a twenty-five layers dielectric/Ag metamaterial, for $n_{\text{diel}} = 4$ and for (b) a seventeen layers all-dielectric $n_{\text{diel}} = 4.5$ /air metamaterial. The transmittance $|T|^2$ calculation (blue solid line) was performed with the transfer-matrix formalism for the physical multilayer system in the lossless limit. The dielectric and magnetic effective model ($Z_{\text{eff}} = \sqrt{\mu_{\text{eff}}\epsilon_{\text{eff}}}$) (red solid line) accurately captures the resonances unlike the non-magnetic approach ($Z_{\mu_{\text{eff}}=1}$) (red dashed line) and the Maxwell Garnett EMA (black solid line).

interesting hyperbolic response. We show experimentally that it is possible to induce a significant additional magnetic response if the dielectric layers are composed of high-index materials that are capable of supporting strong displacement currents at optical frequencies.

3.5 Experimental method: Spectroscopic ellipsometry for metamaterials

In order to experimentally validate the theoretical findings discussed in the previous sections, we fabricated metamaterials composed of SiO_2/Ag , TiO_2/Ag and Ge/Ag alternating layers. These dielectrics, with refractive indices at optical frequencies ranging from $n_{\text{SiO}_2} \simeq 1.5$ to $n_{\text{TiO}_2} \simeq 2$ and $n_{\text{Ge}} \simeq 4 - 4.5$, were selected in order to demonstrate experimentally that as the refractive index is increased, the magnetic effects are enhanced, as the empirical formula of Eq. (3.1) suggests. We prepared the layered SiO_2/Ag , TiO_2/Ag metamaterials by electron-beam evaporation onto Ge substrates. The Ge/Ag sample was deposited on a Si substrate to avoid interface effects with the first Ge layer. All samples discussed in this work contain layers of 30 nm of Ag. Each Ag layer was deposited by first seeding a 2 nm AgO layer that was reduced to Ag under vacuum, a process followed for obtaining smoother interfaces [100]. Atomic force microscopy measurements indicated Ag roughness of 2.13 nm. The thickness of the Ge, TiO_2 , and SiO_2 was aimed to be 40 nm. Deviations from the aimed thicknesses were measured with TEM, varying ± 20 nm. TEM images of the fabricated samples are displayed in Fig. 3.7.

First we measured the optical constants of the individual constituent layers in a variable angle spectroscopic ellipsometer (VASE) system from J. A. Woollam. We also determined their thicknesses with TEM imaging. We refer to this step as for forward problem, as indicated in the schematic of Fig. 3.8. Specifically, it pertains to fitting

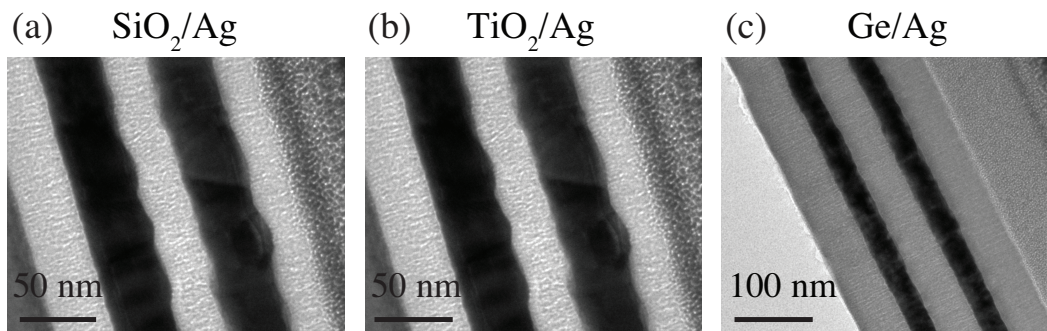


Figure 3.7: Transmission electron microscopy (TEM) images of fabricated samples. (a) SiO_2/Ag metamaterial, (b) TiO_2/Ag metamaterial, (c) Ge/Ag metamaterial.

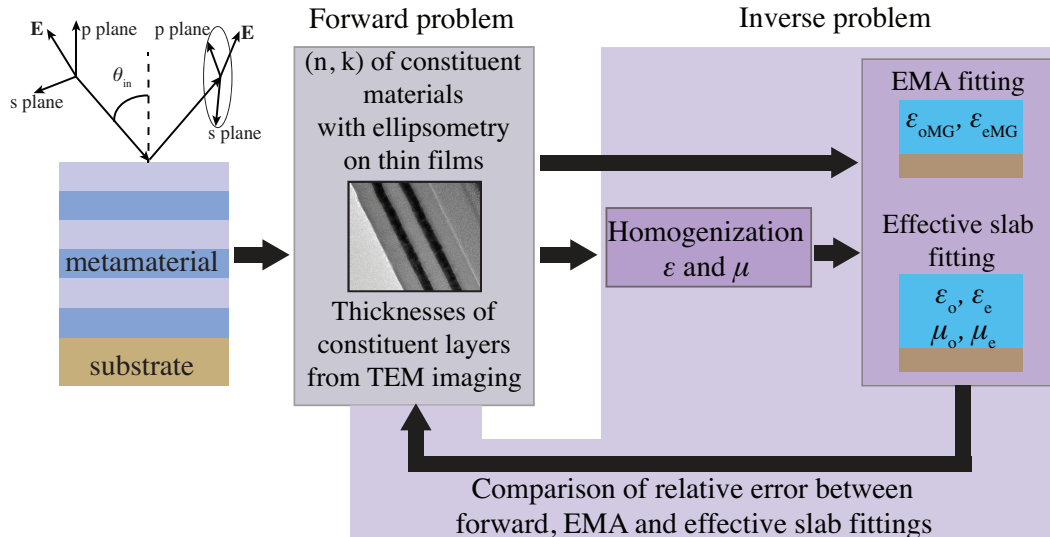


Figure 3.8: Experimental approach - Spectroscopic ellipsometry for uniaxial metamaterials. The forward problem involves fitting the experimental data using the physical multilayer geometry whereas the inverse problem pertains to the fitting of the effective parameters to the raw experimental data in a uniaxial and Kramers-Kronig consistent model (Meta6 from WVASE (Woollam Co.)).

the experimental data using the physical multilayer structure. By experimentally determining the thickness and optical properties of the metamaterials constituent layers, we were able to homogenize them by assigning them effective parameters (ϵ_o , ϵ_e , μ_o , μ_e) [47], while taking into account fabrication imperfections. We then performed ellipsometric measurements of the full metamaterial stacks and fitted the experimental data with the effective parameters we computed, in a uniaxial and Kramers-Kronig consistent model, while the total metamaterial thickness was held to the value determined through TEM. The fittings were over-determined as the number of incident angles exceeded the total number of fitted parameters. Additionally, we performed fittings using the EMA model for comparison. The VASE system utilizes a Levenberg-Marquardt regression algorithm for the fittings. We use the META6 model of WVASE to incorporate the uniaxial anisotropy.

3.6 Experimental verification of artificial magnetism in 1D

Here we display the fitted effective parameters ϵ_o , ϵ_e , μ_o , μ_e obtained through spectroscopic ellipsometry for the three samples discussed in Fig. 3.7. As expected from the previous sections, these metamaterials are hyperbolic in terms of their permittivity (in other words they are hyperbolic for TM polarization), i.e. $\epsilon_o\epsilon_e < 0$. Importantly, we confirm their magnetic character as their magnetic permeability deviates from unity along all coordinate directions.

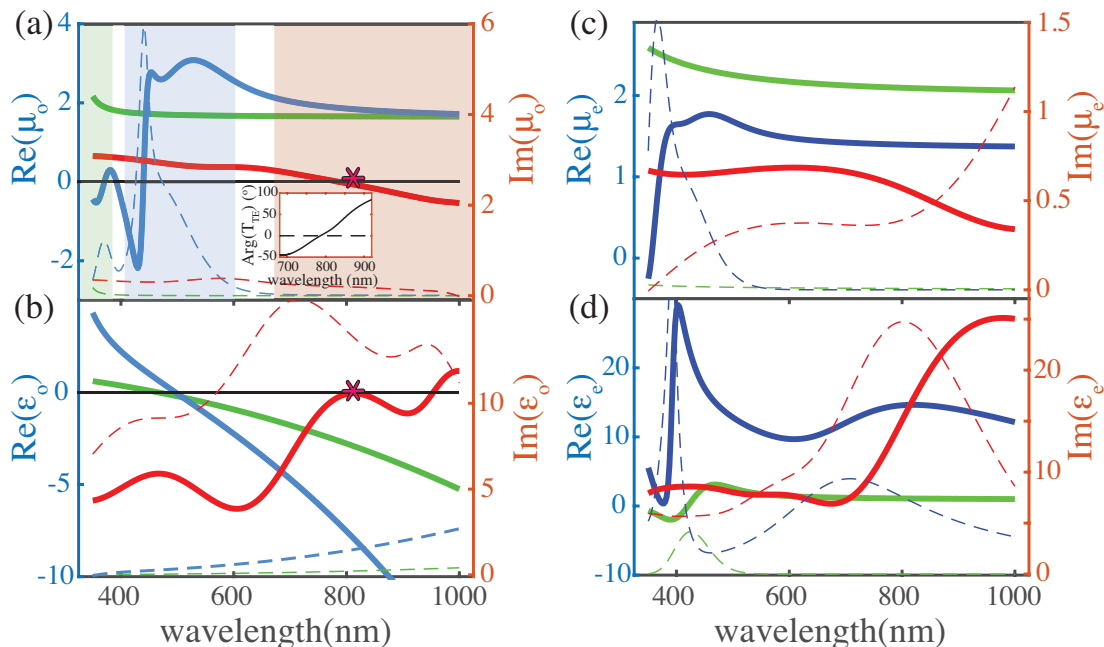


Figure 3.9: Experimentally determined (a) μ_o , (b) ϵ_o , (c) μ_e , (d) ϵ_e for SiO_2/Ag -green, TiO_2/Ag -blue, Ge/Ag -red metamaterials. Solid lines-real parts, dashed lines-imaginary parts. Shaded regions in (a) indicate the regime of magnetic resonances in μ_o for the studied metamaterials. Asterisks in (a) and (b) indicate the EMNZ wavelength for the Ge/Ag metamaterial. The EMNZ condition is confirmed by a vanishing phase of the transmission coefficient at the EMNZ wavelength, shown in the inset of (a).

Namely, Fig. 3.9a shows that increasing the dielectric index redshifts the magnetic resonance in the ordinary direction μ_o ; the SiO_2/Ag metamaterial supports a magnetic resonance in the long-wavelength ultraviolet (UV) regime (~ 300 nm), whereas the TiO_2/Ag and Ge/Ag metamaterials exhibit resonances in the blue (450 nm) and red (800 nm) part of the spectrum, respectively. The enhanced absorption in Ge at optical frequencies leads to considerable broadening of the Ge/Ag metamaterial magnetic resonance, yielding a broadband negative magnetic permeability for wavelengths above 800 nm. We note that previously reported metallodielectric HMMs have primarily featured dielectric layers with lower-refractive indices, such as LiF [101], Al_2O_3 [76, 102, 103] and TiO_2 [42]. Fig. 3.9 shows that, for layer thicknesses below ~ 50 nm, these lower-index dielectric/metal systems exhibit magnetic resonances in the UV-short wavelength visible regime.

Furthermore, the presence of Ag induces a negative ordinary permittivity ϵ_o (Fig. 3.9b), which, for the Ge/Ag metamaterial, becomes positive above 800 nm due to the high-index of Ge. Notably, ϵ_o crosses zero at 800 nm, similar to μ_o , as emphasized

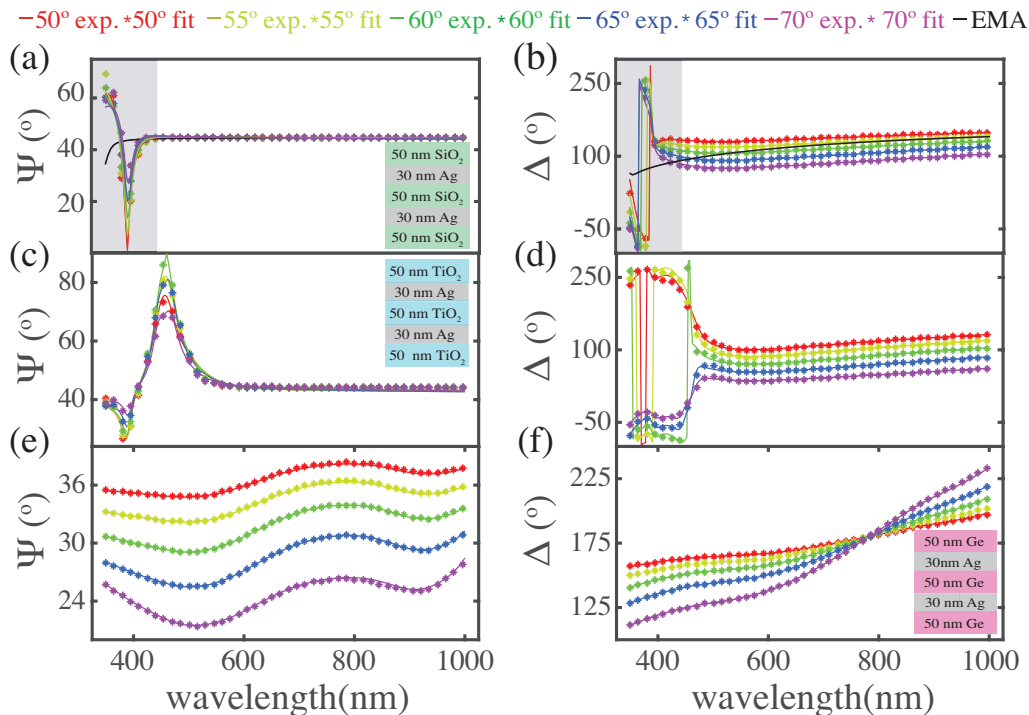


Figure 3.10: Panel pairs ((a), (b)), ((c), (d)) and ((e), (f)) show the agreement between raw experimental data, Ψ and Δ , and the ellipsometric fitting, for the SiO₂/Ag, TiO₂/Ag and Ge/Ag metamaterial, respectively. Shaded regions in (a), (b) emphasize the disagreement between experimental data and the effective medium approximation (EMA).

with the asterisks in Figs. 3.9a, b. Thus, the Ge/Ag metamaterial exhibits an EMNZ response at optical frequencies. The EMNZ condition is confirmed by transfer-matrix analytical calculations of the physical multilayer structure. As shown in the inset of Fig. 3.9a, the phase of the transmission coefficient vanishes at the EMNZ wavelength, demonstrating that electromagnetic fields propagate inside the metamaterial without phase advance [96].

By comparing μ_o and μ_e in Figs. 3.9a and c, respectively, one infers that increasing the dielectric index leads to enhanced magnetic anisotropy. The parameter μ_e only slightly deviates from μ_o for the SiO₂/Ag metamaterial, while the deviation is larger for the TiO₂/Ag one. For the Ge/Ag metamaterial, μ_e remains positive beyond 800 nm, while $\mu_o < 0$, indicating magnetic hyperbolic response for TE polarization. Furthermore, all three heterostructures exhibit hyperbolic response for TM polarization, with $\epsilon_o < 0$ and $\epsilon_e > 0$ (Figs. 3.9b, d). Consequently, the Ge/Ag metamaterial possesses double hyperbolic dispersion.

The ellipsometrically measured parameters Ψ and Δ correspond to the relative

change of polarization state in amplitude and phase, respectively, of a reflected beam off a sample. With respect to the complex reflection coefficients for TM and TE polarization, r_{TM} and r_{TE} , Ψ and Δ are defined as $r_{\text{TM}}/r_{\text{TE}} = \tan(\Psi)e^{i\Delta}$.

Figs. 3.10a-f demonstrate excellent agreement between fitting and raw experimental data. In Figs. 3.10a, b, we also provide a Maxwell Garnett EMA-based fit for the SiO_2/Ag metamaterial. The EMA fails to reproduce the experimentally measured features, in both Ψ and Δ (grey-shaded regions in Figs. 3.10a, b), which correspond to magnetic permeability resonances, as can be seen in Fig. 3.9a. These findings are consistent with the results discussed in Fig. 3.6. Similar EMA-based fits for the TiO_2/Ag and Ge/Ag metamaterials lead to large disagreement with the experimental data across the whole visible-near IR spectrum and are, thus, omitted. This disagreement is expected, as the EMA approach is based on the assumption that the electric field exhibits negligible or no variation within the lattice period [46], which does not apply to high-index dielectric layers (see Section 2.2 for details).

It should be noted that the dielectric hyperbolic response $\epsilon_o\epsilon_e < 0$ is broadband in planar systems, as seen in Figs. 3.9b, d. In contrast, the magnetic permeabilities deviate from unity in a resonant manner along both coordinate directions μ_o and μ_e , thereby making TE polarization-based phenomena more narrow-band in nature.

Here we established, theoretically and experimentally, that metallodielectric layered systems may be described with an effective magnetic permeability that deviates from unity across all coordinate directions. The purpose of introducing this parameter is to build a simple and intuitive description for understanding and predicting new phenomena, such as TE polarization response in planar systems. In what follows we discuss how the non-unity and, in particular, the negative and anisotropic magnetic response that we demonstrated (Fig. 3.9) manifests itself in the characteristics of TE polarized propagating modes (Fig. 3.11) and surface waves (Fig. 3.12).

3.7 Implications of $\mu \neq 1$ for bulk propagating modes

We utilize an example system of dielectric/silver alternating layers, similar to the one we investigate experimentally. To emphasize that enhanced magnetic response at optical frequencies requires high-index dielectrics, we let the refractive index of the dielectric material n_{diel} vary. The calculations and full-wave simulations presented here are performed in the actual, physical, multilayer geometry (Figs. 3.11a, d, e and Fig. 3.12) and compared with the homogeneous effective slab picture (ϵ_{eff} , μ_{eff} - Figs. 3.11b, c). This helps assess the validity of our model and emphasize the physicality of the magnetic resonances.

First, we perform transfer-matrix calculations for the example multilayer metama-

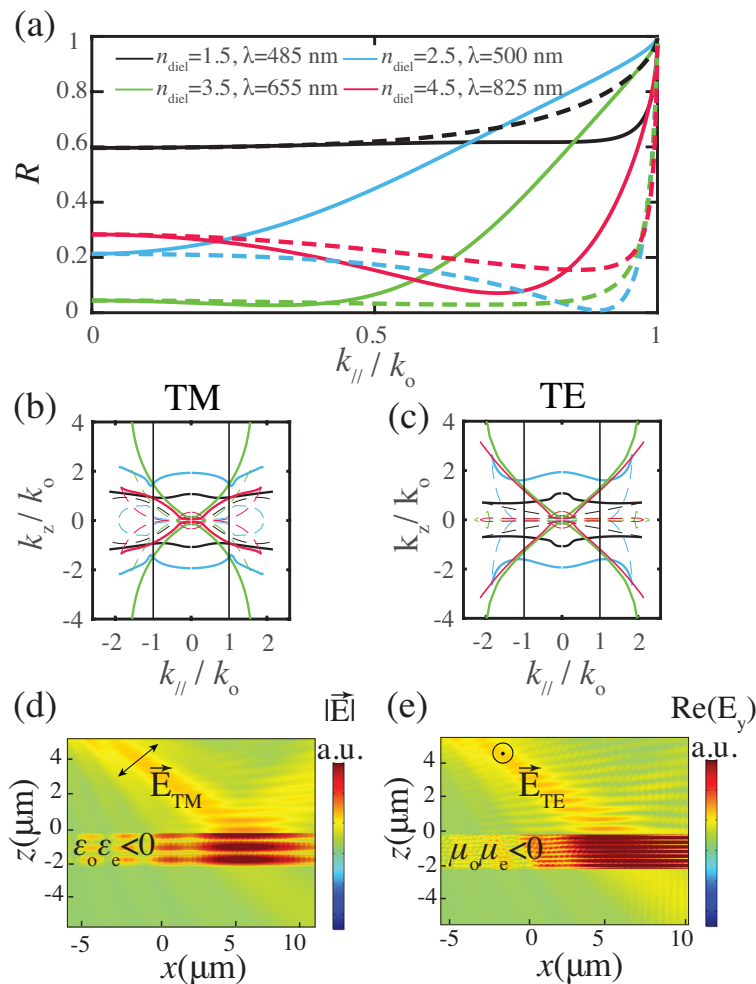


Figure 3.11: Analytical calculations of (a) reflectance and (b), (c) isofrequency diagrams for a metamaterial consisting of five alternating layers of dielectric n_{diel} : 55 nm/Ag: 25 nm. Solid lines in (a) correspond to TE polarization whereas dashed lines correspond to TM polarization. Solid lines in (b), (c) correspond to real parts whereas dashed lines correspond to imaginary parts. Vertical black lines in (b), (c) indicate the maximum free space in-plane wavenumber $k_{\parallel} = k_0$. Color code is the same for panels (a)-(c). (d), (e): Numerical simulation of a fifty-five layers dielectric ($n_{\text{diel}} = 4$)/Ag multilayer metamaterial. The surrounding medium has index $n_{\text{sur}} = 1.55$, allowing coupling of high- k modes. We increased the number of layers for clear visibility of field localization inside the structure. Strong field localization is the consequence of (d) dielectric hyperbolic dispersion for TM polarization ($\epsilon_0\epsilon_e < 0$) and (e) magnetic hyperbolic dispersion for TE polarization ($\mu_0\mu_e < 0$).

terial and we show in Fig. 3.11a the angle dependence for TE and TM reflectance. The strong angle dependence for TM polarization is well understood in the context of an equivalent homogeneous material with anisotropic effective dielectric response $\epsilon_o\epsilon_e < 0$. Bulk TM modes experience dispersion

$$\frac{k_x^2 + k_y^2}{\epsilon_e(\omega, \vec{k})\mu_o(\omega, \vec{k})} + \frac{k_z^2}{\epsilon_o(\omega, \vec{k})\mu_o(\omega, \vec{k})} = k_o^2 \quad (3.2)$$

where $k_o = \omega/c$. This dispersion is hyperbolic, as shown with isofrequency diagrams in Fig. 3.11b. Losses and spatial dispersion perturb the perfect hyperbolic shape [32]. In contrast to the TM modes, TE bulk modes interact with the magnetic anisotropy through the dispersion equation

$$\frac{k_x^2 + k_y^2}{\epsilon_o(\omega, \vec{k})\mu_e(\omega, \vec{k})} + \frac{k_z^2}{\epsilon_o(\omega, \vec{k})\mu_o(\omega, \vec{k})} = k_o^2 \quad (3.3)$$

which is plotted in Fig. 3.11c. For small wavenumbers ($k_{//}/k_o < 1$) and small dielectric indices n_{diel} , the isofrequency diagrams are circular, in other words, isotropic. This agrees well with our experimental results; as shown in Figs. 3.9a, c, for the SiO₂/Ag metamaterial, ordinary and extraordinary permeabilities do not drastically deviate from each other. Increasing the dielectric index opens the isofrequency contours, due to enhanced magnetic response in the ordinary direction (μ_o), which leads to magnetic anisotropy. We note that the displayed wavelengths are selected at resonances of μ_o . Open TE polarization isofrequency contours for $n_{\text{diel}} \geq 2$ are also consistent with experimental results; as shown in Fig. 3.9 for TiO₂ and Ge-based metamaterials, increasing n_{diel} enhances the anisotropy. This also agrees well with the picture of the physical multilayer structure, as shown in Fig. 3.11a; the TE reflectance indeed exhibits extreme angle dependence for increasing dielectric index. Strikingly, we observe a Brewster angle effect for TE polarization, which is unattainable in natural materials due to unity magnetic permeability at optical frequencies [104].

An open isofrequency surface can yield an enhancement in the density of optical states relative to free space. Physically, this may lead to strong interaction between incident light and a hyperbolic structure, and enhanced absorption when it is possible to couple to large wavenumbers from the surrounding medium [105, 106]. So far, only TM polarization has been considered to experience this exotic hyperbolic response in planar metallodielectric metamaterials, due to $\epsilon_o\epsilon_e < 0$ [32, 42, 76]. Based on the open isofrequency surfaces for both TE and TM polarizations in Figs. 3.11b, c, a high-index dielectric/metal multilayer metamaterial may exhibit distinct frequency regimes of *double*, that is, simultaneously TE and TM polarization,

hyperbolic-like response. To confirm this, we perform finite element simulations of a ($n_{\text{diel}} = 4$)/silver multilayer metamaterial for both linear polarizations and set the index of the surrounding medium to $n_{\text{sur}} = 1.55$ to allow coupling to larger wavenumbers. To facilitate visualizing the interaction between the fields and the metamaterial, we consider a thick structure consisting of fifty-five layers. Without loss of generality, we carry out the simulation in the low loss limit to unveil the physics while avoiding side effects due to losses. Fig. 3.11d demonstrates the well-known TM hyperbolic response since the electric field is strongly localized within the multilayer. Switching the polarization to TE (Fig. 3.11e), we observe similar hyperbolic behavior, which, however, cannot be attributed to dielectric anisotropic response as the electric field only experiences the in-plane dielectric permittivity ϵ_o (Eq.(3.3)). The TE enhanced absorption is associated with the $\mu_o\mu_e < 0$ condition [107]; the number of TE modes supported by this metamaterial in this frequency regime is drastically increased. For a more technical discussion regarding the counting of optical states, see Appendix A.2.

3.8 Implications of $\mu \neq 1$ for surface waves

Here we investigate surface wave propagation in our example system of a layered dielectric (n_{diel})/silver metamaterial. In order to identify the structure's eigenmodes, we utilize the mode condition $A(\omega, k_{//}) = 0$, where A is the 1-1 element of the transfer matrix for the layered system (see Eqs. (2.15)-(2.17) in the previous chapter) [1]. We implement this condition numerically using the reflection pole method [108]. In order to ensure surface-confined propagation with fields decaying in air and in the metamaterial, we impose an additional constraint for the waves to be located in the optical band gaps of both bounding media. We discuss our methodology in detail in Section 4.3.

Fig. 3.12a displays the dispersion for TM polarization. The identified surface waves bear similarity to typical SPPs on metallic interfaces [92, 109] and to plasmonic waves in metallodielectric waveguides and systems [93]. Their plasmonic nature is evident as their dispersion asymptotically approaches the surface plasma frequency, similar to SPPs. We show in Fig. 3.12c their field distribution (dashed lines), and compare to SPPs on an equivalent silver slab (black dotted lines). Such TM surface waves on metamaterial interfaces are often associated with an effective negative dielectric response [71, 91, 94]. This is consistent with our effective dielectric and magnetic model; as we showed experimentally in Fig. 3.9b, the ordinary permittivity is negative $\epsilon_o < 0$.

Performing the same analysis for TE polarized waves, we find that TE surface-bound modes also exist (Fig. 3.12b). Their dispersion is parabolic, resembling that

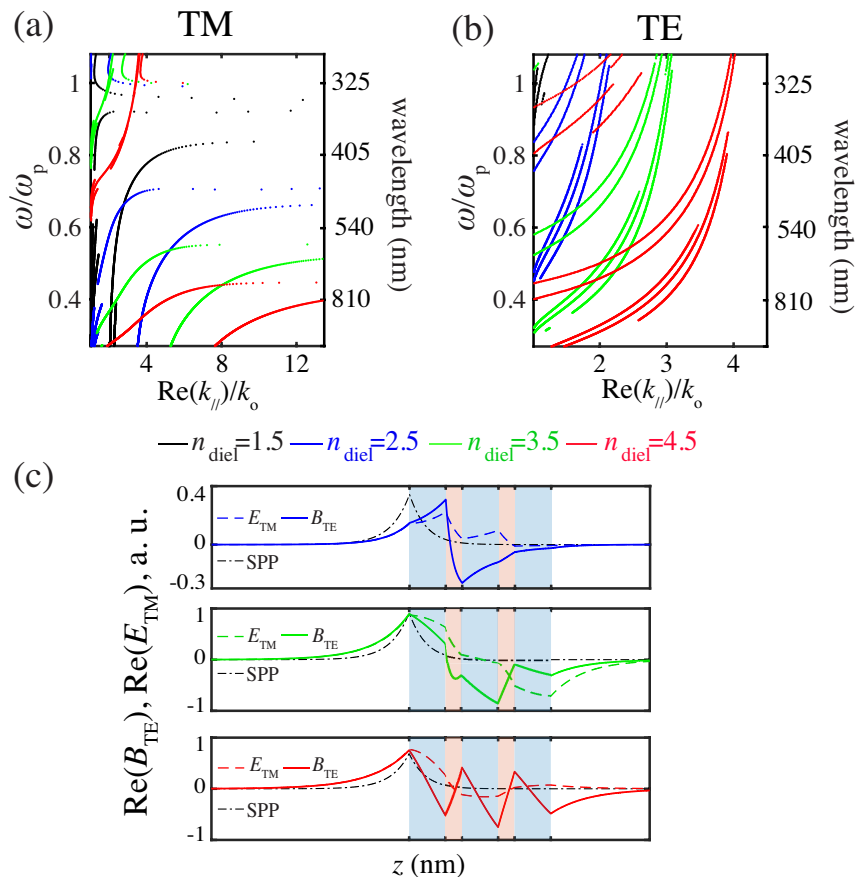


Figure 3.12: (a) TM and (b) TE surface wave dispersion for a metamaterial consisting of five alternating layers of dielectric n_{diel} : 55 nm/Ag: 25 nm. (c) Field profiles (incidence from the left) and comparison to a surface plasmon polariton (SPP) on an equivalent Ag slab (black dotted line). Calculations in (c) correspond to a wavelength of 620 nm for $n_{\text{diel}} = 2.5$, 880 nm for $n_{\text{diel}} = 3.5$ and 1100 nm for $n_{\text{diel}} = 4.5$. Blue shaded regions in (c) indicate dielectric layers whereas pink shaded regions indicate Ag.

of Tamm states in photonic crystals [94, 110]. However, here, we show that they also exist in the subwavelength metamaterial limit and can coexist with typical TM plasmonic surface waves. TE polarized Tamm states have been previously associated only qualitatively with some arbitrary negative net magnetic response [94]. Here, we confirm this hypothesis and explicitly connect the dispersion of Tamm states in planar metamaterials to values of magnetic permeabilities that were experimentally measured (Fig. 3.9). We further identify their physical origin, which is the strong displacement current supported in high-index dielectric layers with a loop-like distribution on resonance. These TE surface waves emerge in the visible regime for dielectric layers with refractive index $n_{\text{diel}} \geq 2$ (Fig. 3.12b), at frequencies where

the metamaterial exhibits a negative effective magnetic response. For this reason, these states may be seen as magnetic plasmons.

The frequency regimes in which double surface waves are supported demonstrate the possibility of exciting TM polarized plasmonic modes simultaneously with their TE counterparts in dielectric/metal pattern-free multilayers.

3.9 Conclusion

Here we have shown that non-unity effective magnetic permeability at optical frequencies can be obtained in 1D multilayer systems, arising from displacement currents in dielectric layers [12]. This makes it possible to tailor the magnetic response of planar hyperbolic metamaterials, which have been previously explored only for their dielectric permittivity features.

We experimentally demonstrated negative in-plane magnetic permeability in planar structures, which can lead to double hyperbolic metamaterials. This magnetic character was verified by performing simple impedance matching sanity checks that demonstrated the inadequacy of previously used EMA-based approaches for describing planar metamaterials of finite thickness, and the necessity to account for the magnetic permeability parameter.

By studying bulk and surface wave propagation, we have identified frequency regimes of a rather polarization-insensitive response. We reported the existence of TE polarized magnetic surface plasmons, attributed to negative magnetic permeability, which are complementary to typical TM polarized surface plasmonic modes in materials with negative dielectric permittivity. The results reported here can open new directions for tailoring wave propagation in artificial magnetic media in significantly simplified layered systems. The reported findings may enable the generalization of the unique properties of plasmonics and hyperbolic metamaterials, previously explored for TM polarized waves and negative permittivity media, for unpolarized light at optical frequencies.

The topic of unpolarized surface waves is of special interest; at optical frequencies, only the dielectric permittivity ϵ obtains negative values in natural material systems. Hence, typical SPPs are polarization dependent. Here we demonstrated that an artificial $\mu_{\text{eff}} < 0$ may be obtained with simple multilayer configurations, utilizing materials with relatively large refractive indices, for example Ge at optical frequencies. This realization motivates us to seek, in Chapter 4, for simplified material systems that can support omnipolarization surface-confined waves that can compete with SPPs in terms of propagation distance and confinement.

BEYOND PLASMONS: OMNIPOLARIZATION SURFACE WAVES

“God made the bulk; the surface was invented by the devil.”

Wolfgang Pauli

4.1 “*Large permittivity begets high-frequency magnetism*”

Electromagnetic surface waves and their interaction with matter provide a path for tailoring near-field optical phenomena. The rise of plasmonics holds promise for advancing a broad range of applications in medical technology [111], chemistry [112], lasers [113–115] and luminescence [116, 117], among others. Plasmons are coherent electron oscillations that propagate on a metallic surface [109]. Their intriguing properties originate from the special dispersion characteristics of Drude metals, and their uniqueness lies in their large mode confinement. Particularly, the frequency dispersion of a surface plasmon polariton (SPP) exhibits a characteristic asymptotically increasing in-plane wavenumber (Fig. 4.4), which is unbound in the lossless limit. Hence the modal wavelength of a surface plasmonic mode on a noble metal interface can be up to ten times reduced compared to free-space wavelengths [118]. For systems involving graphene, this confinement factor can even reach values of hundreds [119–121]. Despite their extraordinary properties, surface plasmonic waves are limited by polarization; they require an out-of plane electric field for their excitation, which makes them relevant only for TM polarized fields.

Most generally, the excitation of a TM polarized surface wave requires a material with negative dielectric permittivity ϵ . Apart from plasmonic metals with a broadband $\epsilon < 0$ below their plasma frequency, this response is also found at the Reststrahlen band of polar dielectric materials (red highlighted region in Fig. 4.1). Particularly, the permittivity of polar dielectric materials exhibits Lorentzian-shaped resonances, typically at mid-far IR frequencies, as a consequence of lattice vibrations, c.f. phonons, in their crystal structure. The Reststrahlen band’s $\epsilon < 0$ allows for excitation of surface phonon polaritons (SPhP), which are similar to SPPs but originate from bound charge oscillations in dielectrics, contrary to free charge carriers in metals [122–124].

A TE-equivalent to the SPP or SPhP requires a material with $\mu < 0$, however natural

magnetism typically vanishes at IR and visible frequencies [2, 11, 98] and magnetic plasmons do not occur naturally [12]. Motivated by this natural asymmetry, in Chapter 3 we demonstrated that layered 1D metamaterials can exhibit artificial magnetic properties. As a consequence, we showed that, as an alternative to a homogeneous material with $\mu < 0$, one can engineer layered systems with *effective* magnetic properties to support TE polarized surface waves simultaneously with their TM (plasmonic) counterparts [12]. From previous surface waves reports in layered media [94, 110, 125–128], it is unclear what material properties are required for achieving simultaneously TE and TM surface wave excitation. By contrast, in Chapter 3, we identified the origin of the artificial magnetic properties we report; it is the strong displacement current loops in dielectric layers that induces non-vanishing magnetic dipole moments.

The displacement current in a dielectric material is $\vec{J}_d = i\omega\epsilon_o(\epsilon - 1)\vec{E}$, therefore systems that contain high-permittivity materials will support a stronger displacement current. As natural magnetism vanishes at high frequencies, high-permittivity materials provide an alternative to inducing artificial magnetism and its implications [11, 12, 98], one of which is the appearance of TE surface waves. This realization is nicely captured in the title of the seminal work by R. Merlin in [98]; “*Large permittivity begets high-frequency magnetism*”.

In this chapter, we aim to alleviate the polarization dependence of SPPs and SPhPs, by searching for high-permittivity material systems that can accommodate TM polarized surface waves simultaneously with their TE counterparts, with degree of confinement similar to plasmons. In contrast to Chapter 3, where we focused on the geometrical structure of multilayer metamaterials, here we focus on simple configurations of single layers and, therefore, we search the material requirements for omnipolarization surface-confined wave propagation. In search for high-permittivity materials, we resort to dielectric and semiconducting systems that exhibit resonances at which the real part of their dielectric permittivity can reach very large values, on the order of hundreds (Fig. 4.1).

Such resonances can be found at IR frequencies near the phonon energies of polar dielectric materials, at the red side of their Reststrahlen band (see red curve in the green highlighted region in Fig. 4.1). Materials with strong phonon resonances are, among others, boron nitride (BN) [123, 130], silicon carbide (SiC) [124, 131, 132], silicon dioxide (SiO₂) [132], aluminum dioxide (Al₂O₃) and titanium dioxide (TiO₂) (see Fig. 4.2b). We emphasize that, in contrast to previous reports [123, 124, 131, 132] that focus on the Reststrahlen band and therefore on TM polarized SPhPs, here, we focus on the large *positive* dielectric permittivity regime of polar dielectrics

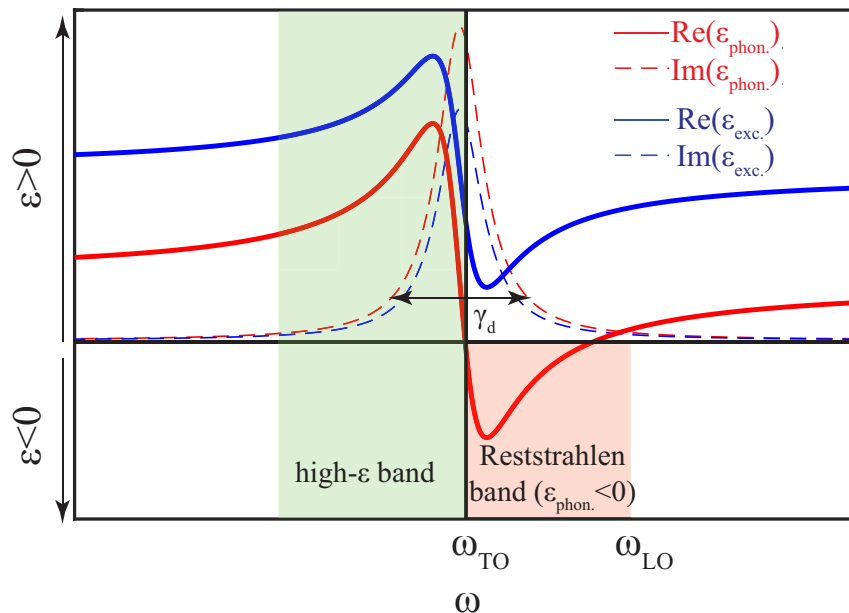


Figure 4.1: High permittivity resonances in polar dielectrics and excitonic materials. Red-Dielectric permittivity of a polar dielectric: ω_{TO} and ω_{LO} correspond to the transverse and longitudinal optical phonon energies, respectively [122]. Blue-Dielectric permittivity of an excitonic resonance, for example in TMDCs [129].

near their phonon energies. We demonstrate that, under certain conditions, polar dielectrics can support highly-confined surface waves for both linear polarizations.

Apart from phonons, other quasiparticles that support permittivity resonances at visible frequencies are excitons [134] in semiconducting materials. At their transition energies, they exhibit considerably large values of dielectric permittivity, without the negative permittivity regime of polar dielectrics, as shown with the blue curve in Fig. 4.1. Strong excitonic resonances can be found in typical semiconductors, for example Si, Ge, GaAs, or InP, as well as in a new emerging classes of two-dimensional materials, namely transition-metal dichalcogenides (TMDCs), for example molybdenum diselenide (MoS_2) and tungsten disulfide (WS_2) [128, 129] (see Fig. 4.2a).

The chapter is organized as follows. In Section 4.2, we outline a concept for surpassing the polarization dependence of plasmonics, and discuss material requirements that can yield omnipolarization surface waves with confinement factors that can compete with SPPs. In Section 4.3 we introduce a computational approach for surface wave calculations, inspired by the parameter retrieval that we introduced in Chapter 2. Although here we focus on single-layer configurations, our method is general and applies to any layered medium at any scale (c.f. metamaterial subwave-

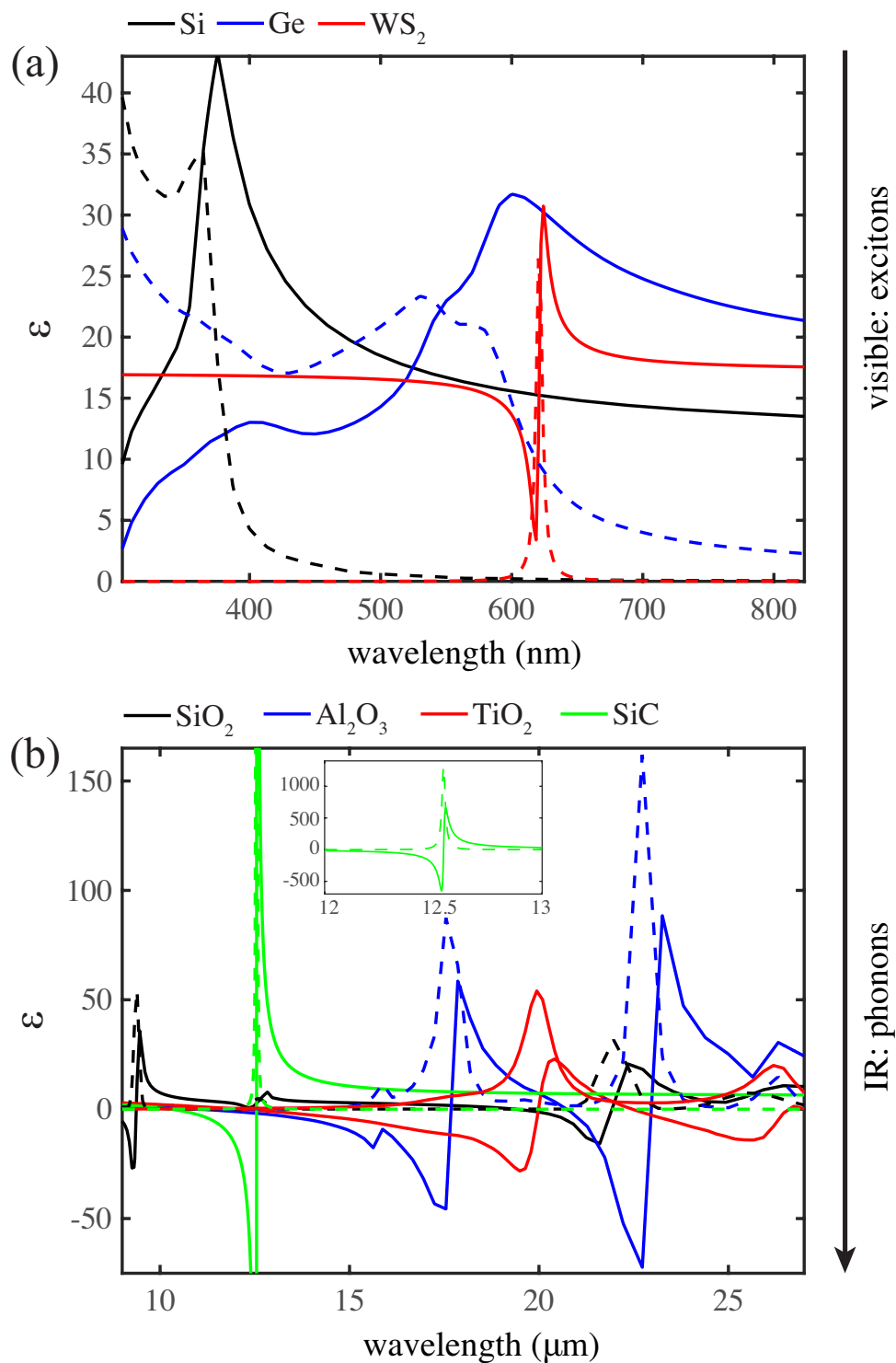


Figure 4.2: (a) Dielectric permittivity of Si, Ge [133], and WS_2 at visible frequencies. The permittivity of WS_2 was obtained by numerical fitting of the experimental data presented in [129] (see Section 4.8). (b) Dielectric permittivity of SiO_2 , Al_2O_3 , TiO_2 and SiC [124] at IR frequencies.

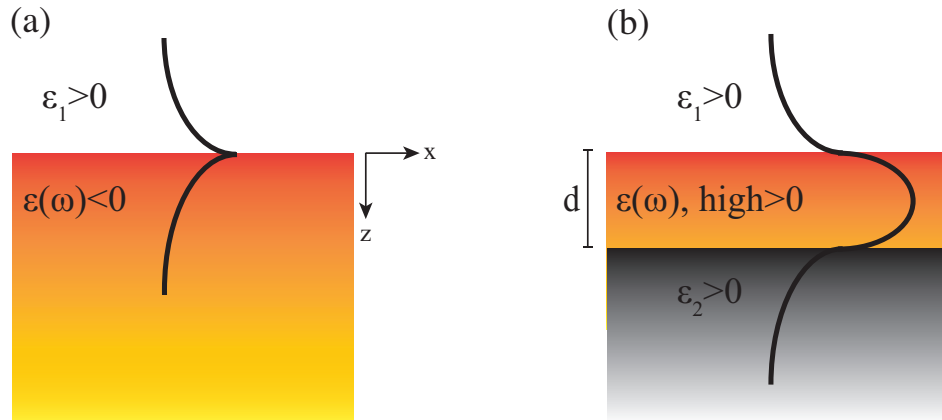


Figure 4.3: (a) A guided mode exists for TM polarization at the interface between media with opposite dielectric permittivities. This mode can be either a SPP or a SPhP on a plasmonic metal or a polar dielectric, respectively. (b) A mode can be guided inside a slab of a dielectric material with $\epsilon(\omega) > 0$, if it is bounded by media with lower dielectric permittivities, $\epsilon_{1,2} < \epsilon(\omega)$. The mode can be either TM or TE polarized.

length regime or thicker layers). It allows simultaneous determination of the band structure and all the eigenmodes supported in arbitrary layered systems of finite thickness. In Section 4.4 we introduce figures of merit for assessing the characteristics of surface waves. In Sections 4.5 and 4.6 we discuss the surface wave dispersion characteristics in plasmonic metals, polar dielectrics, and excitonic materials. These quasiparticles, namely plasmons, phonons, and excitons serve as a canvas of excitations for investigating omnipolarization surface wave propagation. In Sections 4.5, 4.7, 4.8 we consider realistic scenarios and show that certain materials, for example SiC and WS₂ at IR and visible frequencies, respectively, are promising candidates for supporting omnipolarization, phase-matched surface wave propagation that resembles the SPP dispersion. We compare our results with typical SPPs on Ag. Finally, in Sections 4.9, 4.10 we theoretically investigate the parameter space in which combinations of plasmons with phonons and excitons, respectively, can yield omnipolarization surface waves.

4.2 Material requirements for surface-confined propagation beyond plasmonics

We start our investigation by revisiting the boundary condition problem depicted in Fig. 4.3a, namely surface wave propagation at the interface between two unbound media with dielectric permittivities $\epsilon_1 > 0$ and $\epsilon(\omega)$. As is well known (see [109]), this problem has surface propagating solutions only for $\epsilon(\omega) < 0$ and for TM polarization. By considering a Drude metal, we model the dielectric permittivity $\epsilon(\omega)$ with

$$\epsilon_m(\omega) = \epsilon_{\infty,m} \left(1 - \frac{\omega_p^2}{\omega^2 + i\omega\gamma_m} \right) \quad (4.1)$$

where ω_p is the plasma frequency, γ_m the free carrier collision frequency, and $\epsilon_{\infty,m}$ is the high-frequency limit of the permittivity. Solution to the boundary condition problem of Fig. 4.3a yields the plasmonic dispersion

$$k_{//\text{SPP}}(\omega) = \sqrt{\frac{\epsilon(\omega)\epsilon_1}{\epsilon(\omega) + \epsilon_1}} k_o \quad (4.2)$$

where $k_{//\text{SPP}}$ is the in-plane wavenumber of the SPP surface wave, while $k_o = \omega/c$ is the free-space wavenumber. By considering the permittivity of Eq. (4.1) in the lossless limit, we display in Fig. 4.4 (black curve) the dispersion of a SPP mode, which asymptotically approaches to the value of $\sim \omega_p/\sqrt{2}$, as expected for $\epsilon_1 = 1$ [109]. We note that the x-axis ($k_{//}$) in Fig.4.4 is normalized to k_o in order to provide a direct estimate of the confinement. Namely, the effective wavelength of a surface wave is given by $\lambda_{\text{eff}} = 2\pi/\text{Re}(k_{//})$, hence the parameter $\text{Re}(k_{//})/k_o = \lambda_o/\lambda_{\text{eff}}$ represents the number of mode wavelengths that fit into the free-space wavelength of excitation, λ_o . Solutions for TE polarization do not exist for non-magnetic media; a TE polarized magnetic surface plasmon would require $\mu(\omega) < 0$, however at high frequencies, $\mu = 1$ in natural materials (see Chapter 3, [11, 12, 98]).

Now let us consider another waveguiding problem, that depicted in Fig. 4.3b, assuming positive values of dielectric permittivity, $\epsilon_{1,2}, \epsilon(\omega) > 0$. In the absence of frequency dispersion for the intermediate layer $\epsilon \neq f(\omega)$, this problem is the 1D version of a famous problem in silicon photonics; that of waveguiding optical power at a Si waveguide on an SiO₂ substrate. At the telecommunication frequency band near $\lambda_o \sim 1.5 \mu\text{m}$, we have $n_{\text{Si}} = 3.4$ and $n_{\text{SiO}_2} = 1.55$, and the dispersion of the waveguide is bounded between $n_{\text{SiO}_2} \leq k_{//}(\omega)/k_o \leq n_{\text{Si}}$. This regime of in-plane wavenumbers is highlighted in Fig. 4.4 with blue color. The guided modes can be either TE or TM polarized, or both, depending on the thickness of the intermediate layer, d .

Similar conclusions can be made for any high- ϵ material slab between regions of lower $\epsilon_{1,2}$ in Fig. 4.3b; assuming that the top region is air ($\epsilon_1 = 1$), the frequency dispersion of $k_{//}(\omega)$ will be bounded by the largest value of ϵ . Wave propagation inside the intermediate layer of thickness d in Fig. 4.3b is described via $k_{//}^2 + k_z^2 = \epsilon(\omega)k_o^2$, where k_z is the out-of-plane wavenumber. As explained above, the quantity $k_{//}$ defines the degree of confinement of an interface-localized wave. Hence, its maximum possible value

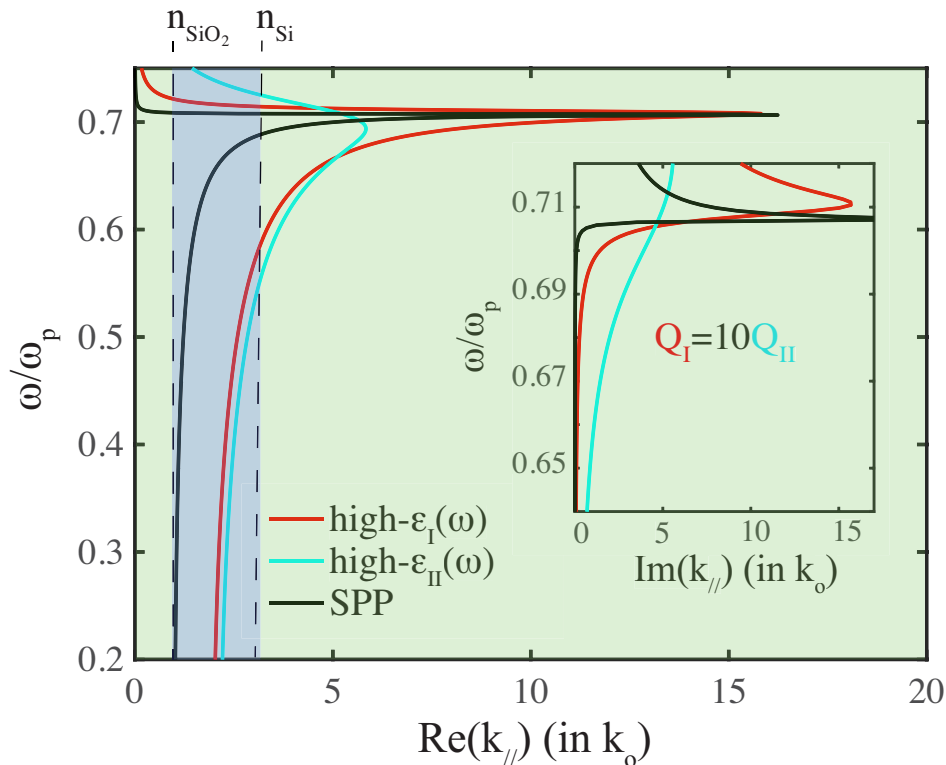


Figure 4.4: Black line corresponds to the SPP dispersion $k_{//\text{SPP}} = \sqrt{\frac{\epsilon(\omega)\epsilon_1}{\epsilon(\omega)+\epsilon_1}}k_o$, for a Drude material with $\epsilon(\omega) < 0$ (Eq. (4.1)), while $\epsilon_1 = 1$ (see Fig. 4.3a). Red and cyan curves correspond to $k_{//\text{max}} = \sqrt{\epsilon(\omega)}k_o$ for the boundary condition problem in Fig. 4.3b, where $\epsilon(\omega)$ is the high- ϵ permittivity of an excitonic material or a polar dielectric, at visible and IR frequencies, respectively, with $\gamma_{d,I} = 0.1\gamma_{d,II}$ (Eq. (4.4)), or $Q_I = 10Q_{II}$. Inset shows the imaginary part of $k_{//}$, which corresponds to the losses along the propagation direction. We note that here we considered $\omega_p \sim \omega_{\text{TO}}$, with respect to Eqs. (4.1), (4.4).

$$k_{//\text{max}} = \sqrt{\epsilon(\omega)}k_o \quad (4.3)$$

highlights that the requirement for highly-confined mode is the large value of $\epsilon(\omega)$. As mentioned in Section 4.1, high-permittivity resonances are found in polar dielectric and excitonic materials, at IR and visible frequencies, respectively. The permittivity dispersion of a polar dielectric material can be modeled with [124]

$$\epsilon_{\text{phon}}(\omega) = \epsilon_{\infty,d} \left(1 + \frac{\omega_{\text{LO}}^2 - \omega_{\text{TO}}^2}{\omega_{\text{TO}}^2 - \omega^2 - i\omega\gamma_d} \right) \quad (4.4)$$

In Eq. (4.4), ω_{LO} and ω_{TO} correspond to the longitudinal and transverse phonon energies, respectively, and γ_d is the inverse phonon lifetime (Fig. 4.1). We note that

solution to the boundary condition problem depicted in Fig. 4.3a for frequencies ω at the Reststrahlen band of a polar dielectric material ($\epsilon_{\text{phon}} < 0$) will yield the SPhP dispersion, similar to SPPs, as we discuss in what follows (see Section 4.6). The permittivity of an excitonic material can also be modeled with Eq. (4.4), using a very large offset $\epsilon_{\infty,exc}$ to exclude the $\epsilon < 0$ frequency regime (Reststrahlen band in Fig. 4.1). For example, with Eq. (4.4), typical TMDCs [129] and semiconducting systems are modeled well at visible frequencies.

By considering a Lorentzian-shaped permittivity resonance of the form in Eq. (4.4), we select ω_{TO} (Eq. (4.4)) close to ω_p (Eq. (4.1)), and we display in Fig. 4.4 the parameter $k_{//\text{max}}$ (Eq. (4.3)). As can be seen, due to the high- ϵ regime, $k_{//}$ can compete with $k_{//\text{SPP}}$, and the modes due to high- ϵ can, in principle, be as confined as typical SPPs on Drude metals. However, as can be seen from Fig. 4.1, at the high- ϵ regime of polar dielectrics or excitonic materials, losses ($\text{Im}(\epsilon)$) are also increased, therefore dramatically decreasing the propagation distance of supported modes. The losses in polar dielectric and excitonic materials are defined by the inverse of the phonon and exciton lifetime, respectively, shown in Fig. 4.1 with the generic parameter γ_d , which defines the width of the permittivity resonance. In Fig. 4.4 we consider two different values of $\gamma_{d,\text{I,II}}$, with $\gamma_{d,\text{I}} = 0.1\gamma_{d,\text{II}}$. As can be from the parameter $\text{Im}(k_{//\text{max}})$ displayed in the inset of Fig. 4.4, small values of γ_d yield longer-distance mode propagation. It is useful to introduce the material quality factor, defined as

$$Q = \frac{\omega_{\text{TO}}}{\gamma_d} \quad (4.5)$$

From the two different values of $\gamma_{d,\text{I,II}}$ in Fig. 4.4, we have $Q_{\text{I}} = 10Q_{\text{II}}$. It is clear that the parameter Q ought to be large for large propagation distances and high-confinement factors. Hence, here we focus on high- Q polar dielectric and excitonic materials at IR and visible frequencies, respectively, and seek for omnipolarization surface-localized wave propagation.

Prior to delving into the details of designing material systems that support highly-confined surface-localized wave propagation for both linear polarizations, we outline in the following section our computational approach.

4.3 Generalized retrieval approach for surface wave computations

The problem of a wave propagating at a single interface between two media may be analytically treated [109], however larger systems require semi-analytical or numerical approaches [93, 109, 135]. Although in the following sections we focus on either single interfaces or single slabs, we note that interesting physical effects also

arise in multilayer heterostructures [12, 94, 110, 125–127]. For example, typical photonic, leaky modes appear at the pass-bands of all-dielectric, infinite periodic photonic crystals [1], while hybrid plasmonic modes arise in metallodielectric multilayer waveguides [93] and subwavelength hyperbolic metamaterials [12, 32, 71]. For multilayer heterostructures that include more than two interfaces, numerical approaches are typically employed for computing the propagation constants of surface waves [108, 136–144]. The majority of previous approaches is limited in applicability in that they are either only able to handle a small number of interfaces [140] or an infinite arrangement [1], or in that they are not able to distinguish between photonic and surface-confined modes. By contrast, the method presented here applies to any layered configuration and allows distinction between photonic and surface-confined eigenmodes.

In Fig. 4.5 we distinguish between photonic modes and surface-confined ones. A photonic mode is defined as one that exhibits sinusoidal propagation in the direction normal to the interface, inside the medium of interest (which can be either a homogeneous material or a composite medium), as shown in Fig. 4.5a. Hence, a photonic or leaky mode is not strongly confined to the interface between two media. Mathematically, assuming propagation of the form $\sim e^{i(k_{//}x+k_{\text{eff}}z-\omega t)}$, where $k_{\text{eff}} = k_z$, this translates to an out-of-plane propagation constant k_{eff} that is purely real in all-dielectric media, or has $\text{Re}(k_{\text{eff}}) \gg \text{Im}(k_{\text{eff}})$ in lossy media. By contrast, a surface-confined mode is one that exponentially decays away from the waveguiding interface, as shown in Fig. 4.5b. In mathematical terms, this corresponds to a purely imaginary k_{eff} in all-dielectric media, or to $\text{Im}(k_{\text{eff}}) \gg \text{Re}(k_{\text{eff}})$ in lossy media.

A schematic of the structures we investigate is displayed in Fig. 4.6a. We consider a layered arrangement consisting of an arbitrary number of layers of non-magnetic materials in an arbitrary sequence, with layer thicknesses that may be in the metamaterial subwavelength limit ($d_i \ll \lambda_o$, where λ_o is the free-space wavelength) or thicker. Hence, we emphasize that our approach is generic and not limited to the metamaterial regime. In order to compute the fields, we use the transfer matrix formalism for layered media of finite thickness [1]. Similar to the transfer matrix for an infinite and purely periodic medium, discussed in Section 2.3 and in Appendix A.1, for a layered arrangement of finite number of layers, N , we have the transfer matrix \vec{M} connecting the incident and transmitted and reflected waves through

$$\begin{pmatrix} A_o \\ B_o \end{pmatrix} = \begin{pmatrix} m_{11} & m_{12} \\ m_{21} & m_{22} \end{pmatrix} \begin{pmatrix} A_N \\ B_N \end{pmatrix} \quad (4.6)$$

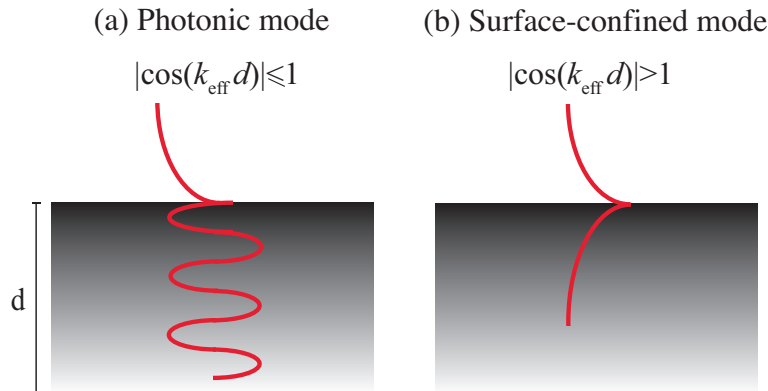


Figure 4.5: Definition of (a) a photonic and (b) a surface-confined mode.

where A_o and B_o are the amplitudes of the incident and reflected wave, respectively, as defined in Fig. 2.2. A_N is the transmitted amplitude, while $B_N = 0$ if waves are launched only from the left side, with respect to Fig. 2.2. For details, see [1]. By letting the frequency ω and the in-plane wavenumber $k_{//}$ vary, we obtain the elements $m_{11}(k_{//}, \omega)$ and $m_{21}(k_{//}, \omega)$, based on which the transmission and reflection coefficients are defined as $t = 1/m_{11}$ and $r = m_{21}/m_{11}$, respectively.

We seek for surface waves by first determining the full set of eigenmodes of the structure, for which $t \rightarrow \infty$, $r \rightarrow \infty$. Alternatively, the eigenmodes are zeros of the matrix element $m_{11}(k_{//}, \omega)$. We employ the reflection pole method (RPM) [108], which is based on the residue theorem of complex analysis, for detecting those zeros in the complex plane. Zeros of the complex function m_{11} yield phase shifts of π , which are detected by seeking for peaks of its derivative $\text{Arg}(m_{11})$ per frequency and wavenumber (Fig. 4.6b). As a result, we obtain pairs of $(\omega, k_{//})$, that excite eigenmodes. For more details regarding the RPM, see [108]. We note that that this approach can be generalized to account for anisotropic materials by replacing the traditional 2×2 transfer matrix [1] with a 4×4 formalism. See, for example [145–147].

However, not all eigenmodes of a heterostructure constitute surface waves. For a wave to be surface-localized, it is required to be located inside the optical band gap of both bounding media [148], which, in the case studied here, are air and an arbitrary layered heterostructure (Fig. 4.6a). A plane wave is located inside the band gap of free-space when simply $k_{//} > k_o$. As discussed above (see Fig. 4.5), for the wave to be inside the band gap of the arbitrary layered heterostructure, its out-of-plane wavenumber k_{eff} oughts to have a non-zero imaginary part, assuring decay away from the interface $z = 0$. Nevertheless, k_{eff} is not a always a well-defined quantity. For an A-B-A-.. purely periodic infinite photonic crystal, wave propagation in the

z -direction is accurately expressed in terms of the Bloch wavenumber K_B , discussed in Section 2.3 and given by Eq. (2.18). However, the Bloch wavenumber K_B is inappropriate for any other system, for example a random aperiodic arrangement, chirped or non-centrosymmetric multilayer.

In order to circumvent this limitation, we propose an alternative description of the composite medium, for describing a complete surface wave detection scheme that applies to *any* layered arrangement. Our approach originates from, but is not limited to, metamaterials' homogenization (see Chapter 2). Particularly, it is based on the S-parameter retrieval, discussed in Section 2.1. As explained in Section 2.1, an arbitrary composite system of finite thickness d and known scattering properties, namely complex transmission and reflection coefficients, t and r (Fig. 4.6a), can be represented by an effective impedance and an effective out-of-plane wavenumber, Z_{eff} and k_{eff} , respectively, given by Eqs. (2.3) and (2.4). Typically, based on the subwavelength size of the meta-atoms (thickness of layers in the 1D case examined here), these effective parameters are translated to effective dielectric permittivity and magnetic permeability through $k_{\text{eff}} = \sqrt{\epsilon_{\text{eff}}\mu_{\text{eff}}}\frac{\omega}{c}$ and $Z_{\text{eff}} = \sqrt{\frac{\mu_{\text{eff}}}{\epsilon_{\text{eff}}}}$. The conditions under which the assignment of effective parameters ϵ_{eff} and μ_{eff} is valid are complex [54, 74] and remain an area of literature debate [57, 63, 98].

We stress, however, that in contrast to the validity of ϵ_{eff} and μ_{eff} , it is always valid to describe *any* system in terms of the effective wavenumber k_{eff} and the effective impedance Z_{eff} (Eqs. (2.3) and (2.4), respectively). For the purpose of surface waves computations, and for the distinction between photonic and surface-confined modes, only the effective wavenumber k_{eff} is required. Particularly, k_{eff} is directly associated with the scattering coefficients t and r (Eq. 2.3) [58, 60, 99], and hence it can be used for describing an arbitrary heterostructure at any scale, not necessarily in the metamaterial subwavelength limit, as long as t and r may be computed. As a sanity check, we note that k_{eff} in Eq.(2.3) is identical to the Bloch wavenumber K_B in Eq. (2.18) in the special case of an unbound and purely periodic medium composed of two alternating materials, when the cladding and substrate have the same optical constants ($\epsilon_1 = \epsilon_2$, see Figs. 2.1, 2.2). In this case, Eq. (2.3) reduces to Eq.(2.18). This is easily seen by expressing t and r in Eq. (2.3) in terms of transfer matrix elements, using the identity $\det(\vec{M}) = 1$, and the fact that $m_{21} = m_{12}^*$, for purely dielectric materials (where m_{21} and m_{12} are purely imaginary), and $m_{21} = -m_{12}$, for dispersive materials [1].

To recap, for an excitation to be considered as a surface wave, three conditions must be satisfied; first, it has to be an eigenmode of the structure, which we evaluate with the RPM ($m_{11} = 0$); second, it has to be in the band gap of the surrounding medium

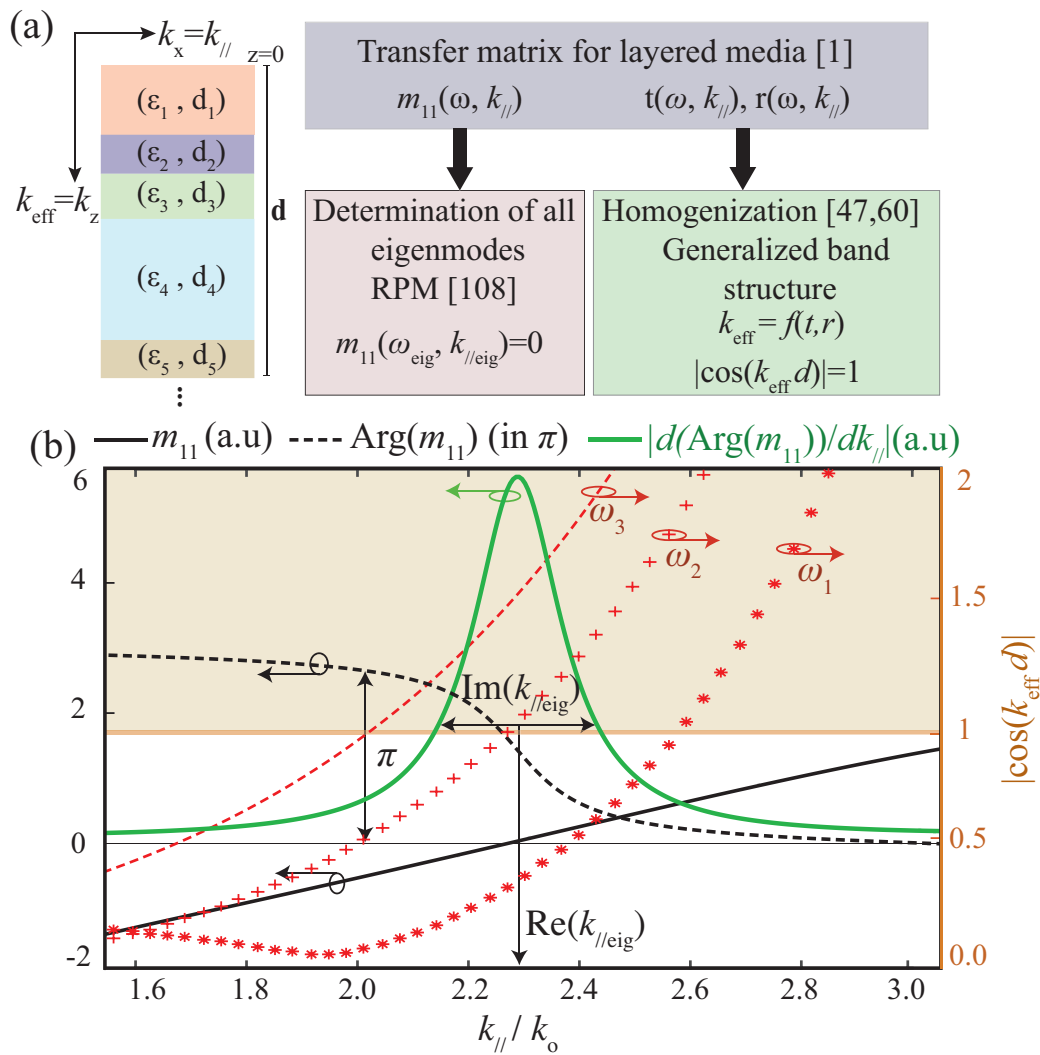


Figure 4.6: (a) Left-schematic of an arbitrary layered system, right-computational approach flow chart. (b) Combination of RPM [108] with our generalized band structure calculation (inspired by [60]) for the distinction between different types of eigenmodes. At the eigenmode in-plane wavenumber $k_{//\text{eig}}$, m_{11} vanishes (black solid curve), $\text{Arg}(m_{11})$ jumps by π (black dashed curve), and its derivative $\frac{d\text{Arg}(m_{11})}{dk_{//}}$ resonates (green curve). The highlighted region corresponds to a band gap, for which $|\cos(k_{\text{eff}}d)| > 1$. For frequency ω_1 , the mode is photonic, as it resides inside the band, whereas for ω_2 the mode is located at the band edge. For ω_3 , the mode is a surface-confined, propagating at the air/heterostructure interface.

($k_{//} > k_o$); and third, it has to be in the band gap of the planar heterostructure. This third condition is implemented by introducing the notion of a generalized band structure, applicable to *any* planar configuration. A band is a set of $(\omega, k_{//})$ for which

$$|\cos(k_{\text{eff}}(\omega, k_{//})d)| \leq 1 \quad (4.7)$$

In the case of lossless media, this condition yields a purely real k_{eff} , whereas for systems with loss we have $\text{Re}(k_{\text{eff}}) \gg \text{Im}(k_{\text{eff}})$. Surface waves exist in the exterior of a band or at its edge, for which $|\cos(k_{\text{eff}}d)| \geq 1$. To demonstrate this, we present in Fig. 4.6b an eigenmode of a planar structure. At the eigenmode's in-plane wavenumber $k_{//\text{eig}}$, the matrix element m_{11} vanishes, therefore its phase $\text{Arg}(m_{11})$ jumps by π . Taking the derivative of m_{11} with respect to $k_{//}$, we obtain a peak, as shown with the green curve. Its half-width-half-maximum (HWHM) corresponds to the in-plane decay length through $L = 1/2\text{Im}(k_{//\text{eig}})$ [108]. In order to determine the nature of the mode (c.f. photonic or surface-confined), we employ our generalized band edge condition, $|\cos(k_{\text{eff}}d)| = 1$. The quantity $|\cos(k_{\text{eff}}d)|$ is shown for three different frequencies ω_1, ω_2 and ω_3 . For ω_1 , $|\cos(k_{\text{eff}}d)| < 1$ at $k_{//\text{eig}}$, and this mode belongs to band, resulting in wave propagation inside the heterostructure, in other words it is a photonic mode. For ω_2 , the parameter $|\cos(k_{\text{eff}}d)|$ crosses unity at $k_{//\text{eig}}$ and this mode is located exactly at the band edge. Finally, for frequency ω_3 , the mode is inside the band gap, highlighted in Fig. 4.6b with the top orange shaded area, and the mode is forbidden from propagating inside the structure, hence it as a surface wave. By retrieving k_{eff} , we are also able to estimate the degree of confinement through the penetration depth $t = 1/2\text{Im}(k_{\text{eff}})$.

The discussion in this section applies to any layered configuration. However, we note that when the multilayer heterostructure is reduced to a single isotropic and homogeneous material slab with permittivity ϵ , the band condition (Eq. (4.7)) reduces to $k_{//} \leq k_{//\text{max}}$, where $k_{//\text{max}}$ is defined in Eq. (4.3). In what follows (Sections 4.6, 4.7, 4.8, 4.9, 4.10) we focus on modes located at the band edge of isotropic, positive ϵ media, where Eqs. (4.3) and (4.7) reduce to $k_{//} = k_{//\text{max}} = \sqrt{\epsilon(\omega)}k_o$ and $|\cos(k_{\text{eff}}(\omega, k_{//})d)| = 1$, respectively. Despite the fact that such band edge modes cannot be classified as strictly surface-confined, there exist classes of materials for which propagation is extremely confined, hence we refer to such modes as surface-confined as well. In the following section we introduce an additional metric of confinement that is independent of Eqs. (4.3) and (4.7).

4.4 Figures of merit for surface-confined propagation

In the following sections we evaluate realistic material systems and configurations for excitation and detection of omnipolarization surface waves. In order to assess the characteristics of these waves, we introduced figures of merit pertaining to their propagation distance and confinement.

In absolute terms, the propagation distance of a surface wave is given by $L = 1/2\text{Im}(k_{//})$. In order to obtain a normalized quantity that can be used as a figure of merit for comparison between different materials and different wavelength ranges (c.f. visible and IR regimes), we divide the propagation distance by the effective wavelength of the mode, $\lambda_{\text{eff}} = 2\pi/\text{Re}(k_{//})$. Hence, the effective propagation length L_{eff} is

$$L_{\text{eff}} \equiv \frac{\text{Re}(k_{//})}{\text{Im}(k_{//})} = 4\pi \frac{L}{\lambda_{\text{eff}}} \quad (4.8)$$

and expresses the number of mode wavelengths that a wave propagates before it decays.

Another quantity that deserves attention is the degree of confinement of a mode. In absolute terms, this can be expressed in terms of the cross-sectional area occupied by a mode. In the one-dimensional case studied here, this area is given by $A_{1\text{D}} = \frac{[\int I dz]^2}{\int I^2 dz}$, where I is the intensity profile of the mode ($E^2(z)$ or $B^2(z)$). By normalizing this quantity to the diffraction limited spot, which is $A_{\text{o,1D}} = \lambda_{\text{o}}/2$, we obtain the normalized cross-sectional area [149]

$$A_{\text{eff}} \equiv \frac{A_{1\text{D}}}{A_{\text{o,1D}}} = \frac{[\int I dz]^2 / \int I^2 dz}{\lambda_{\text{o}}/2} \quad (4.9)$$

where the limits of integration are taken to be on the order of tens to hundreds of free-space wavelengths away from region where the wave is localized.

Finally, another metric of confinement is the number effective wavelengths of the mode that fit in the free-space wavelength of excitation, λ_{o} . This quantity is simply given by $\lambda_{\text{o}}/\lambda_{\text{eff}} = \text{Re}(k_{//})/k_{\text{o}}$.

4.5 Theory of plasmons and results for silver

We start by investigating SPPs in a Drude metal, which serves as a sanity check for confirming the validity of the method we introduced in Section 4.3. We examine the case of a semi-infinite slab of metal and a thin slab in air, for which we expect the existence of one and two SPP modes, respectively, as a consequence of the number of interfaces in each case.

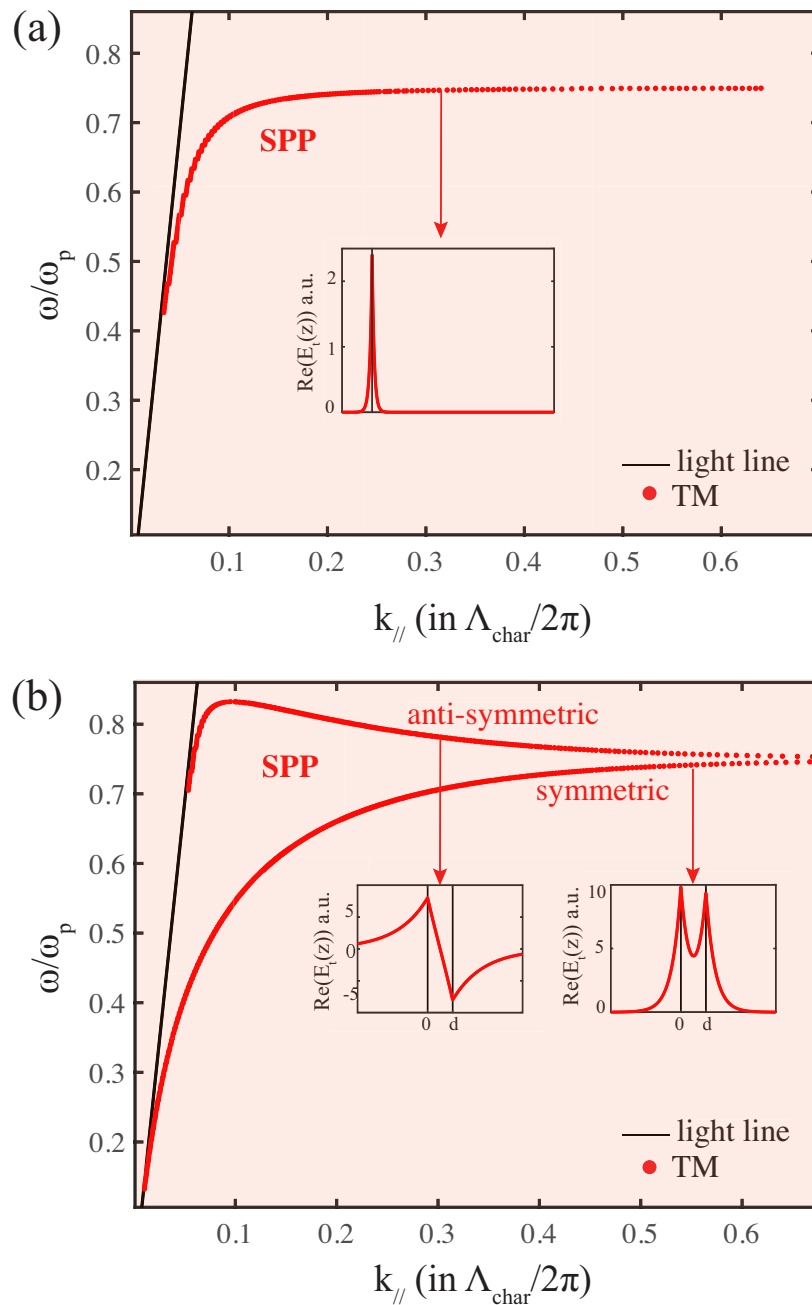


Figure 4.7: Dispersion of a TM polarized surface plasmon polariton on a Drude metal. (a) Semi-infinite case and (b) finite slab with thickness $d_m = \lambda_p/30$. For both (a) and (b) $\Lambda_{\text{char}} = \lambda_p/30$. The free-space light line is shown with black. Insets show field profiles. For case (b) the two modes are the anti-symmetric (left) and symmetric (right) plasmonic modes.

We model the metallic Drude permittivity with Eq. (4.1). By performing the transfer matrix, retrieval and RPM approaches described in Section 4.3, we show in Fig. 4.7 the dispersion of a TM polarized SPP on (a) a semi-infinite slab of a Drude metal and (b) on a finite slab with thickness $d_m = \lambda_p/30$, where $\lambda_p = 2\pi c/\omega_p$. The SPP dispersion asymptotically approaches the value of $\sim \omega_p/\sqrt{2}$, as expected [92, 109, 118]. In the case of a finite and thin slab, the dispersion is composed of two branches as expected, since there exist two interfaces to support SPP propagation. The two branches correspond to the symmetric and anti-symmetric modes. The field profiles in both semi-infinite and finite thickness cases demonstrate the good surface-confinement characteristics of SPPs. The symmetric mode is even as a function of z , whereas the anti-symmetric mode is odd in z . Across the whole frequency range displayed in Figs. 4.7 (a), (b), the permittivity of the metal is negative, $\epsilon_m < 0$. Hence, the out-of-plane wavenumber is imaginary ($k_z^2 = k_{\text{eff}}^2 = \epsilon_m k_o^2 - k_{//}^2 < 0$) and, based on our definition of a photonic band (Eq. 4.7), the SPP belongs in a band gap region. Therefore, it is a surface-confined mode, which confirms the validity of our photonic band criterion.

We proceed by studying SPP propagation on a semi-infinite slab of silver at UV-visible frequencies, near the plasma frequency of Ag, which is taken here to be $\omega_{p,\text{Ag}} = 9.6$ eV [150]. The results of SPPs on silver serve as a reference point in terms of confinement and propagation length, for the realistic cases we examine in the following sections.

A schematic of the geometry we study is shown in Fig. 4.8a, where we include a grating that allows excitation of SPPs, with $k_{//} > k_o$, from free space ($k_{//} \leq k_o$). Namely, the grating's period γ determines the in-plane wavenumber via

$$k_{//} = 2\pi/\gamma \quad (4.10)$$

In order to directly compare the degree of confinement, in terms of number of modal wavelengths λ_{eff} that fit in the free-space wavelength λ_o , between different cases, we normalize the x-axis in the dispersion curve of Fig. 4.8b to k_o . Hence, since $\lambda_o/\lambda_{\text{eff}} \equiv \text{Re}(k_{//})/k_o$, we see that the modal wavelength of SPPs on Ag can be up to six times reduced compared to the free-space wavelength in this frequency range.

Furthermore, as expected, the dispersion of TM polarized SPP modes on Ag asymptotically approaches to the value of $\sim \omega_{p,\text{Ag}}/\sqrt{2}$ (Fig. 4.8b). The field profile of the SPP mode is shown in the inset of Fig. 4.8b and is highly localized at the air/silver interface. As the frequency increases, the in-plane wavenumber $k_{//}$ increases, hence SPPs have access to higher confinement. We calculate the normalized cross-sectional

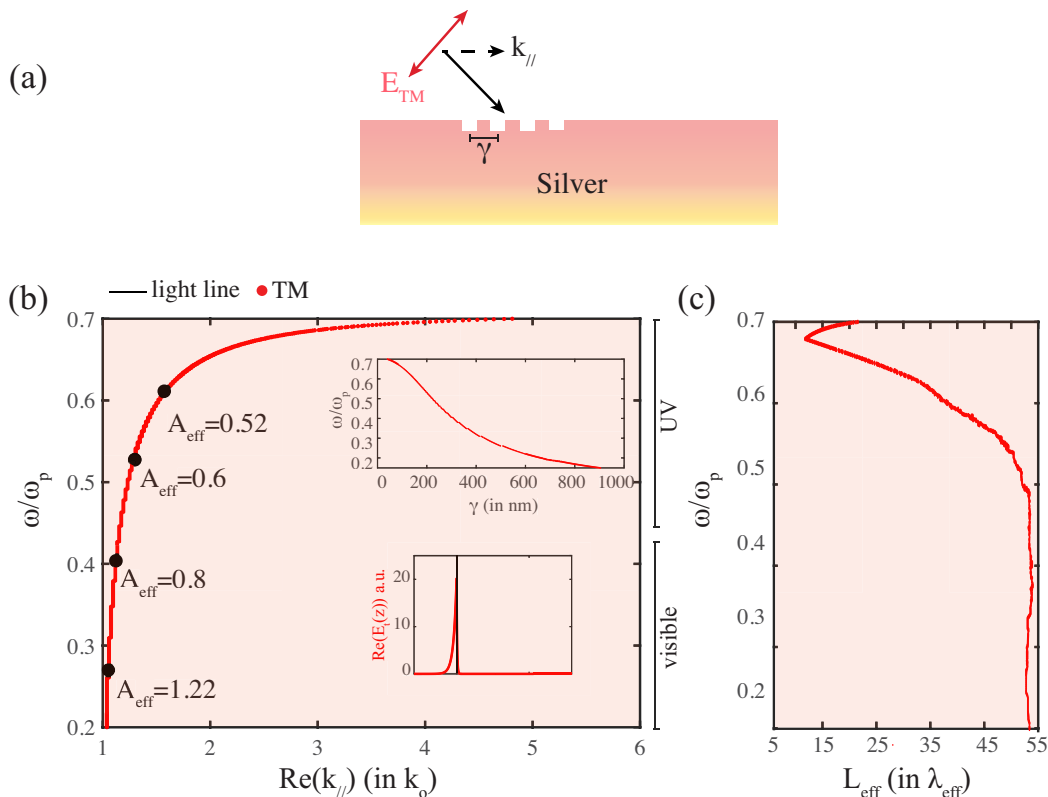


Figure 4.8: (a) Schematic of a semi-infinite slab of Ag and a grating with period γ for SPP excitation. (b) Dispersion of surface plasmon polaritons on a semi-infinite slab of Ag. The parameters for Ag were taken from [150]: $\omega_p = 9.6$ eV and $\gamma_m = 22.8$ meV/cm in Eq. (4.7). The free-space light line is the vertical line at $k_{//}/k_o = 1$. Top inset shows the grating period γ required for excitation of SPPs. Bottom inset corresponds to the SPP field profile. A_{eff} is the effective mode volume, as defined in Eq. (4.9). (c) Effective propagation length of SPPs on Ag, as defined in Eq. (4.8).

area of the SPP modes by first calculating the fields at different frequencies, and the results range from $A_{\text{eff}} \sim 1.2$ to $A_{\text{eff}} \sim 0.5$ for frequencies in the far UV and visible regimes, respectively (see black points in Fig. 4.8b).

Plasmonic modes in silver can propagate for up to ~ 50 times their effective wavelength λ_{eff} , as shown in Fig. 4.8c. The slight oscillations in the $L_{\text{eff}}(\omega)$ curve originate from our computational approach; as discussed in Section 4.3, the parameter $\text{Im}(k_{//})$ (which is inversely proportional to L_{eff} , see Eq. (4.8)) is defined as the HWHM of peaks in the derivative of m_{11} with respect to $k_{//}$ (see green curve in Fig. 4.6) and the accuracy of the peaks detection scheme depends on computational power.

Finally, we calculate the parameter γ , corresponding to the grating period required

for excitation of SPPs. This parameter is shown in the top inset of Fig. 4.8b and ranges from 300 nm to 900 nm for excitation with visible light [8, 135, 151].

4.6 Phonons and excitons

So far we have established the validity of the scheme introduced in Section 4.3 for detecting photonic and surface-confined modes in layered systems, by accurately obtaining the SPP dispersion in plasmonic metals (Section 4.5). Here, we return to the search for surface-confined waves that resemble the SPP dispersion but, contrary to SPPs, are simultaneously TE and TM polarized. For this we investigate polar dielectrics and excitonic materials, based on the concept discussed in Section 4.2. We revisit the problem of a slab of thickness d of a polar dielectric or excitonic material (Fig. 4.3b). Initially, we perform calculations in two extreme cases (a) an thick slab of polar dielectric and excitonic material and (b) a thin slab, compared to the free-space wavelength λ_o . In case (a), Fabry-Pérot resonances exist leading to multiple photonic bands for both linear polarizations. By contrast, in case (b), due to the small thickness of the slab, we obtain a single-mode for a single-polarization per frequency.

We model the permittivity of both the polar dielectric and the excitonic material with Eq. (4.4). We select a characteristic length defined as $\Lambda_{\text{char,phon/exc}} = \pi c / \omega_{\text{TO}} \sqrt{\epsilon_{\text{phon/exc}}(\omega_{\text{TO}})}$. For the thick slab, or case (a), we select $d_{\text{phon/exc}} = 10\Lambda_{\text{char,phon/exc}}$. By contrast, for the thin slab, or case (b), we set $d_{\text{phon/exc}} = \Lambda_{\text{char,phon/exc}}$, which is small compared to the free-space wavelength, as $\epsilon_{\text{phon/exc}}(\omega_{\text{TO}})$ is taken to be rather large (Fig. 4.1).

In Fig. 4.9 we present the results of our calculations for an arbitrary polar dielectric material. For frequencies between ω_{TO} and ω_{LO} , i.e. in the Reststrahlen band highlighted with red, we have $\epsilon_{\text{phon}} < 0$, hence an SPhP mode occurs for TM polarization. The SPhP has two branches that correspond to the symmetric and anti-symmetric modes. In the inset of Figs. 4.9a and b we display their field profiles. These modes exhibit field profiles very similar to the SPP ones (Fig. 4.7b). Due to the negative sign of ϵ_{phon} in the Reststrahlen band, based on Eq. (4.3) and Eq. (4.7), the SPhPs belong to a band gap region and are surface-confined, in direct analogy to SPPs [122].

At frequencies slightly lower than ω_{TO} , i.e. in the regime of high- ϵ_{phon} , we obtain a number of modes, as can be seen in the grey highlighted region of Fig. 4.9a. Importantly, we obtain a mode that occurs for both linear polarizations right at the band edge of the material, for which $k_{//} = k_{//\text{max}} = \sqrt{\epsilon_{\text{phon}}}k_o$. For these high- $k_{//}$ modes, we present in the inset of Fig. 4.9a field profiles for both linear polariza-

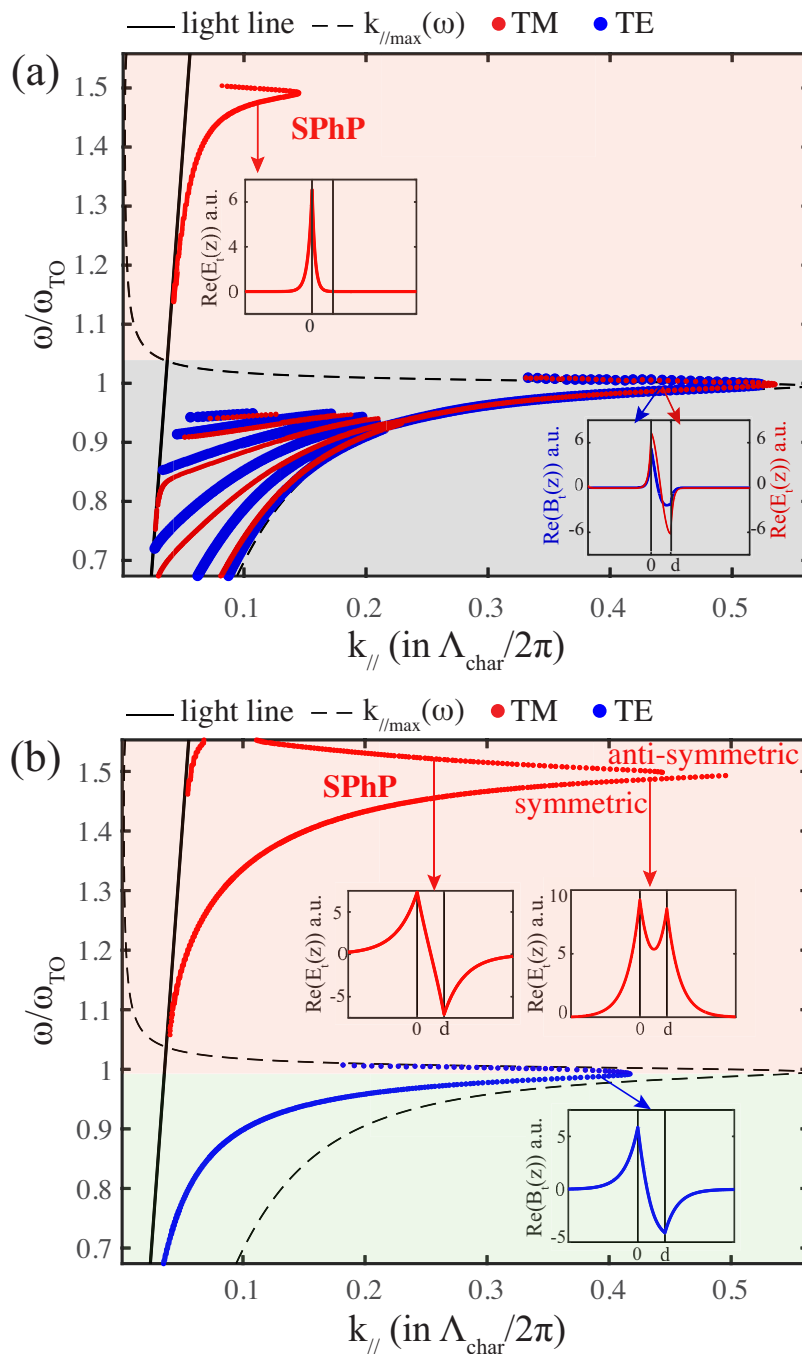


Figure 4.9: Dispersion of surface-confined and photonic modes in a polar dielectric material. The characteristic length is defined as $\Lambda_{\text{char}} = \pi c/\omega_{\text{TO}} \sqrt{\epsilon_{\text{phon}}(\omega_{\text{TO}})}$. Mode dispersions for (a) a thick slab with thickness $d_{\text{ph}} = 10\Lambda_{\text{char}}$ and (b) for a thin slab with thickness $d_{\text{ph}} = \Lambda_{\text{char}}$. The free-space light line is shown with black. Dashed line corresponds to $k_{//\text{max}} = \sqrt{\epsilon_{\text{phon}}(\omega)}k_0$. Insets show field profiles for (a) an omnipolarization mode located at the band edge (bottom) and a SPhP mode (top), and for (b) an anti-symmetric (top left) and a symmetric (top right) SPhP mode, and a highly-confined TE mode (bottom). The high- ϵ regime is highlighted with (a) grey and (b) green, indicating omnipolarization and TE polarized wave propagation, respectively. The Reststrahlen band is highlighted with red.

tions at a single frequency ω and wavenumber $k_{//}$. As these modes coexist in ω and $k_{//}$ for TE and TM polarizations, this allows single-frequency excitation and phase-matched propagation of omnipolarization surface waves. By decreasing the thickness of the slab, in Fig. 4.9b, we decouple to two polarizations and we only obtain a TE polarized mode near the band edge. Based on Eqs. (4.3), (4.7), the TE mode displayed in Fig.4.9b is classified as a photonic one, since $k_{//} < \sqrt{\epsilon_{\text{exc}}(\omega)}k_o$. However, it continues to exhibit good confinement characteristics, which is evident by the large values that $k_{//}$ obtains near the mode's resonance, at ω_{TO} . The confinement of these modes strongly depends on the quality factor of the polar dielectric, as we show in the following sections. This TE polarized mode disappears for $\omega > \omega_{\text{TO}}$ because $\epsilon_{\text{phon}} < 0$ in this frequency regime. Hence, the material becomes opaque for TE polarization and no modes are supported.

In Fig. 4.10 we perform analogous calculations for an arbitrary excitonic material. For a thick slab (Fig. 4.10a), we obtain a large number of photonic modes that, in contrast to the polar dielectric material, continue to exist at frequencies above ω_{TO} . This happens because an excitonic resonance does not involve a region of $\epsilon_{\text{exc}} < 0$ in contrast to the Reststrahlen band of polar dielectrics (see Fig. 4.1). Importantly, near ω_{TO} , we obtain modes at the band edge, with $k_{//} = k_{//\text{max}} = \sqrt{\epsilon_{\text{exc}}}k_o$, for both TE and TM polarizations, the field profiles of which are shown in the inset of Fig. 4.10a at a single frequency and wavenumber. Their degeneracy allows single-frequency excitation and phase-matched propagation of omnipolarization surface waves. The degree of surface-confinement of these band edge modes depends on the quality factor, Q , of the excitonic material, as we discuss in what follows. By decreasing the thickness of the excitonic material slab, we decouple the two polarizations, the modes of which occur at different frequencies, as shown in Fig. 4.10b. Namely, at frequencies below ω_{TO} , the high- ϵ_{exc} regime continues to yield a high- $k_{//}$ TE polarized mode. In contrast to the polar dielectric material, for which the TE polarized mode disappears for $\omega > \omega_{\text{TO}}$, due to $\epsilon_{\text{phon}} < 0$ at the Reststrahlen band, for the excitonic material we have $\epsilon_{\text{exc}} > 0$ even above ω_{TO} (Fig. 4.1). Hence, the TE mode continues to exist in the finite slab case (Fig. 4.10b), however it is no longer degenerate with the TM polarized one.

To conclude this section, we investigated two extreme cases of slabs of excitonic and polar dielectric materials; (a) a thick slab for which multiple photonic bands are supported and (b) a thin slab compared to the free-space wavelength. In case (a), for both polar dielectrics and excitonic materials, we obtain a mode for each linear polarization that occurs at the band edge, for which $k_{//} = k_{//\text{max}} = \sqrt{\epsilon_{\text{phon/exc}}}k_o$ (Figs. 4.9a, 4.10a). The magnitude of $k_{//}$ for this mode depends on the maximum value of the dielectric permittivity of the material, $\epsilon(\omega_{\text{TO}})$. Large values of ϵ near

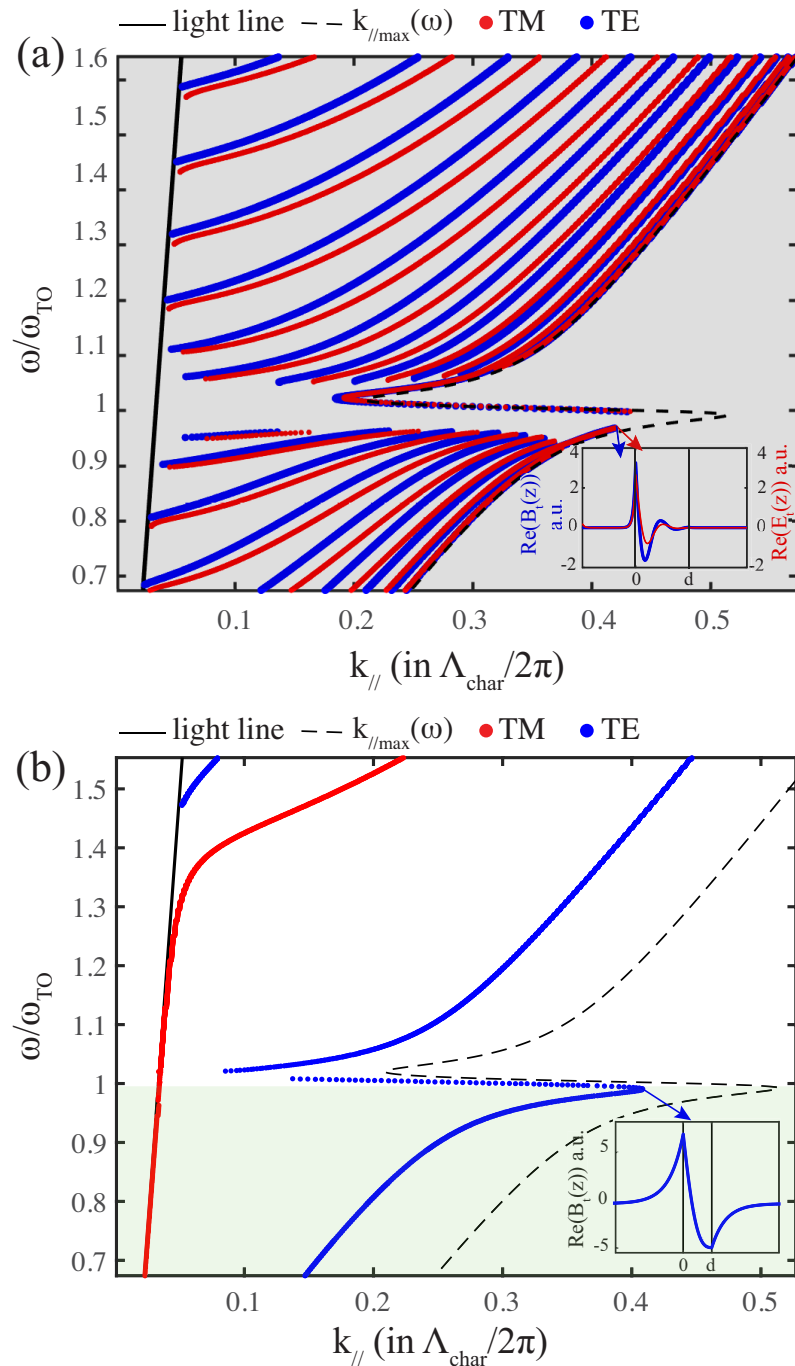


Figure 4.10: Dispersion of surface-confined and photonic modes in an excitonic material. The characteristic length is defined as $\Lambda_{\text{char}} = \pi c/\omega_{\text{TO}} \sqrt{\epsilon_{\text{exc}}(\omega_{\text{TO}})}$. Mode dispersions for (a) a thick slab with thickness $d_{\text{exc}} = 10\Lambda_{\text{char}}$ and (b) for a thin slab with thickness $d_{\text{exc}} = \Lambda_{\text{char}}$. The free-space light line is shown with black. Dashed line corresponds to $k_{//\text{max}} = \sqrt{\epsilon_{\text{exc}}(\omega)}k_0$. Insets show field profiles for (a) an omnipolarization mode located at the band edge, and for (b) a highly-confined TE mode. The high- ϵ regime is highlighted with (a) grey and (b) green, indicating omnipolarization and TE polarized wave propagation, respectively.

ω_{TO} can yield extremely confined surface modes with characteristics that can compete, or even surpass, the confinement factors of SPPs in noble metals. For thin slabs, in case (b), the two modes no longer overlap in frequency and wavenumber (Figs. 4.9b, 4.10b). The cutoff thickness at which the TE polarized and TM polarized band edge modes separate from each other depends on material properties (ω_{TO} , Q , etc). In Sections 4.7 and 4.8 we investigate high- Q polar dielectrics and excitonic materials, respectively, and seek for this cutoff slab thickness that will allow omnipolarization surface-localized wave propagation over large distances with large degree of confinement in thin slabs.

4.7 Surface-confined waves on SiC on Si

We proceed by investigating surface-confined modes in polar dielectrics. In selecting a material for our investigation, we seek record-high values of ϵ_{phon} near the phonon energy (see Fig. 4.1), simultaneously with low loss, to ensure high- Q (Eq. 4.5). One of the polar dielectric materials with record-high quality factors is SiC, with $\omega_{\text{TO,SiC}} = 797 \text{ cm}^{-1}$ and $\gamma_{\text{d,SiC}} = 2.2474 \times 10^{11} \text{ s}^{-1}$, hence $Q_{\text{SiC}} = 668$ [122]. Its dielectric permittivity is presented in Fig. 4.2b.

In Section 4.6 we showed that the TE and TM polarized band edge modes of a thick slab of polar dielectric material overlap in frequency and wavenumber (Fig. 4.9a). By confining the two modes in an ultra-thin slab, the two polarizations no longer exhibit overlapping dispersions curves (Fig. 4.9b). Here, we seek the cutoff thickness for a slab of SiC, that ensures omnipolarization surface-confined wave propagation near the band edge ($k_{//\text{max,SiC}} = \sqrt{\epsilon_{\text{SiC}}}k_0$). In order to investigate an experimentally realistic scenario, we consider that the SiC slab lies on top of an intrinsic Si substrate, with index $n_{\text{Si}} = 3.4$ [152] (see schematic in Fig. 4.11a). We find that for SiC on Si, this cutoff thickness is $d_{\text{SiC}} = 8\pi c/(\omega_{\text{TO,SiC}} \sqrt{\epsilon_{\text{SiC}}(\omega_{\text{TO,SiC}})}) = 3.22 \text{ }\mu\text{m}$.

As can be seen from Fig. 4.11b, at this thickness of SiC, higher order Fabry-Pérot-type propagation bands arise. These bands can be seen in Fig. 4.11b with the grey shaded regimes for TE polarization and they were obtained with the method discussed in Section 4.3. The dispersion curves that lie inside the propagation bands correspond to photonic modes that exhibit weak confinement characteristics (See Fig. 4.5a). In contrast, dispersion curves that lie in the exterior of the bands constitute surface-confined waves (Fig. 4.5b).

Here we focus on the high- $k_{//}$ modes that are in close proximity to the band edge of SiC, $k_{//\text{max,SiC}}$ (black dashed line in Fig. 4.11b). These modes lie in-between propagation bands, hence they are surface-confined. From the field profiles in the lower inset of Fig. 4.11b, we see that these modes are strongly localized inside the

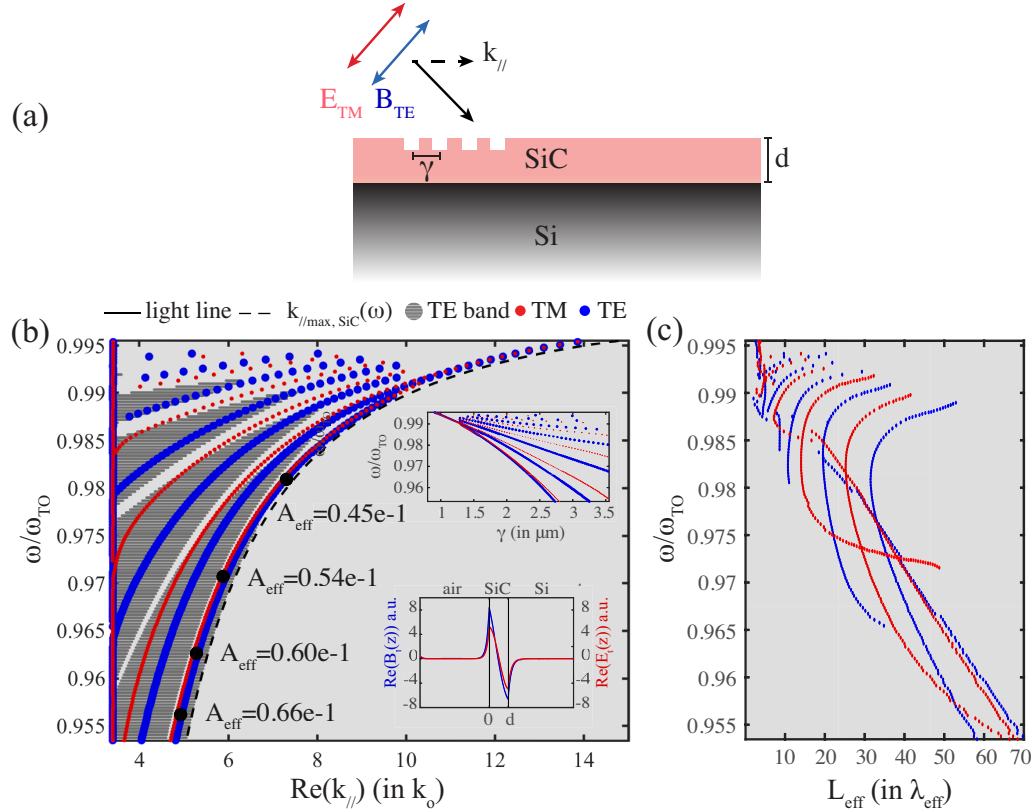


Figure 4.11: (a) Schematic of a slab of SiC on Si, and a grating with period γ for surface-confined waves excitation. (b) Dispersion of surface-confined waves on a slab of SiC with thickness $d_{\text{SiC}} = 8\pi c / (\omega_{\text{TO,SiC}} \sqrt{\epsilon_{\text{SiC}}(\omega_{\text{TO,SiC}})}) = 3.22 \mu\text{m}$ on Si. The parameters for SiC were taken from [122]: $\omega_{\text{TO,SiC}} = 797 \text{ cm}^{-1}$, $\omega_{\text{LO,SiC}} = 973 \text{ cm}^{-1}$ and $\gamma_{\text{d,SiC}} = 2.2474 \times 10^{11} \text{ s}^{-1}$ in Eq. (4.4). The refractive index of Si is taken $n_{\text{Si}} = 3.4$. The free-space light line is located at $k_{//}/k_0 = 1$ (off-axis). The modes located at $k_{//}/k_0 = 3.4$ are the band edge modes in bulk Si. The dashed line corresponds to $k_{//\text{max,SiC}} = \sqrt{\epsilon_{\text{SiC}}(\omega)}$, the band edge of SiC. Top inset shows the grating period γ required for excitation of the surface-confined waves. Bottom inset shows the TE and TM field profiles at a single-frequency ω and wavenumber $k_{//}$. A_{eff} is the effective mode volume, as defined in Eq. (4.9). (c) Effective propagation length of surface-confined waves on SiC on Si, as defined in Eq. (4.8).

SiC slab, and exhibit negligible leakage into the Si substrate. Their confinement factors are calculated as explained in Section 4.4. We obtain normalized mode cross-sectional areas that range from $A_{\text{eff}} \sim 0.04$ to $A_{\text{eff}} \sim 0.06$ for both TE and TM polarizations, as shown with the values displayed in Fig. 4.11b at different frequencies. Importantly, this confinement is larger than in the SPP modes in Ag ($A_{\text{eff}} \sim [0.5 - 1.2]$ in Fig. 4.8b). We note that the modes located at $k_{//} = 3.4k_0$ (y-axis in Fig. 4.11b) correspond to the photonic band edge of Si ($k_{//\text{max,Si}} = \sqrt{\epsilon_{\text{Si}}(\omega)}k_0$).

In an experiment, the excitation of these strongly surface-confined omnipolarization modes requires grating periods in the range of $\gamma \sim 1 \mu\text{m}$ to $\gamma \sim 2.5 \mu\text{m}$ for both TE and TM polarizations, as shown in the top inset in Fig. 4.11b. Importantly, as a consequence of the high- Q of SiC, these modes have large propagation distances. As shown in Fig. 4.11b, they propagate approximately 10 – 70 effective mode wavelengths before decaying, similar to SPPs on Ag (Fig. 4.8c). This constitutes them detectable in surface waves experiments, where detection is achieved in the far-field through input and output gratings, see, for example, [151].

Previous reports have considered high- Q polar dielectric materials for SPhP propagation at the Reststrahlen band [122]. In contrast, here we showed that the frequency regime where the permittivity of polar dielectrics obtains positive and large values (Fig. 4.1) can yield omnipolarization surface-confined propagation with characteristics similar to SPhPs, however accommodating both linear polarizations, therefore alleviating the TM polarization limitation of SPhPs. We emphasize that the requirement of high- Q is crucial for ensuring both a high degree of confinement and a long propagation distance.

4.8 Surface-confined waves on WS₂ on Si

Here, we perform an analysis similar to the one in the previous section, but for a high- Q excitonic material at visible frequencies, instead of a polar dielectric at IR frequencies. One class of materials that one could consider investigating is that of traditional semiconductors, for example Ge or Si. However, the quality factors of traditional semiconducting materials are rather low, which can be seen in Fig. 4.2a. In contrast, two-dimensional TMDCs have been recently investigated for their optical properties [129], and they show considerably higher Q 's, compared to bulk semiconductors. We select to investigate WS₂, the permittivity of which is plotted in Fig. 4.2a. By performing a numerical fitting (with Eq. (4.4)) to the experimental data reported by Li *et al.* in [129], we infer that $Q_{\text{WS}_2} \sim 113.2$. Based on our fitting, with respect to Eq. (4.4), we find that $\omega_{\text{TO,WS}_2} = 1.996 \text{ eV}$, $\omega_{\text{LO,WS}_2} = 2.009 \text{ eV}$, $\gamma_{\text{d,WS}_2} = 37.363 \text{ fs}$ and $\epsilon_{\infty,\text{WS}_2} = 17$.

In order to simulate an experimentally realistic scenario, we assume that the WS₂ is on top of a Si substrate, for which we set $n_{\text{Si}} = 3.4$ [152] (see schematic in Fig. 4.12a). As discussed in Section 4.6, we seek for the minimum (cutoff) thickness of a WS₂ slab, for which the band edge modes for the two linear polarizations continue to overlap. For the material parameters of WS₂, this thickness is $d_{\text{WS}_2} = 6\pi c / (\omega_{\text{TO,WS}_2} \sqrt{\epsilon_{\text{WS}_2}(\omega_{\text{TO,WS}_2})}) = 336$ nm.

For this thickness, we obtain the desirable high- $k_{//}$ modes near the band edge of WS₂ ($k_{//\text{max,WS}_2} = \sqrt{\epsilon_{\text{WS}_2}} k_o$), as shown in Fig. 4.12b. Additionally, higher order Fabry-Pérot-type modes with smaller $k_{//}$ also arise. However these higher order modes are not particularly surface-confined and we do not analyze them further.

We focus on the large- $k_{//}$ modes near the band edge of WS₂ (dashed line in Fig. 4.12b), the field profiles of which are shown in the inset of Fig. 4.12b. The fields are strongly-localized in the WS₂ slab and exhibit negligible leakage into the Si substrate. We compute their normalized cross-sectional area that ranges from $A_{\text{eff}} \sim 0.068$ to $A_{\text{eff}} \sim 0.081$ for both polarizations, surpassing the mode confinement of SPPs on silver at visible frequencies by an order of magnitude (Fig. 4.8b). Their propagation distance L_{eff} is very large and reaches values as high as $L = 800\lambda_{\text{eff}}$ in the lower-frequency regime near $\sim 0.75\omega_{\text{TO,WS}_2}$ (Fig. 4.12c). Finally, we show in the left inset of Fig. 4.12b the grating period, γ , required for single-frequency simultaneous excitation of TE and TM surface-confined waves on WS₂ on Si.

To conclude, in the present section and in the previous one, we discussed materials with permittivity resonances and high- Q , as platforms for omnipolarization, phase-matched surface-confined wave propagation. Our approach aimed to identify the minimum thickness of a slab of a positive-permittivity material, for which there exist modes near the band edge $k_{//\text{max}} = \sqrt{\epsilon} k_o$. Utilizing high- ϵ materials yields large degree of confinement, and focusing on high- Q material resonances can lead to large propagation distances. Based on these requirements, we focused on slabs of SiC and WS₂, as representatives of high- Q polar dielectrics and excitonic materials at IR and visible frequencies, respectively.

4.9 The case of a plasmon and a phonon

In this section and in the following one, we investigate theoretically the scenarios of combining a plasmon in a Drude metal (Fig. 4.7) with a phonon in a polar dielectric (Fig. 4.9) and with an exciton in an excitonic material (Fig. 4.10), respectively. Similar to the previous sections, we aim to identify regimes of omnipolarization surface wave propagation. However, in contrast to the discussion in Section 4.2, here, the origin of the overlap in the dispersions for TE and the TM modes is not

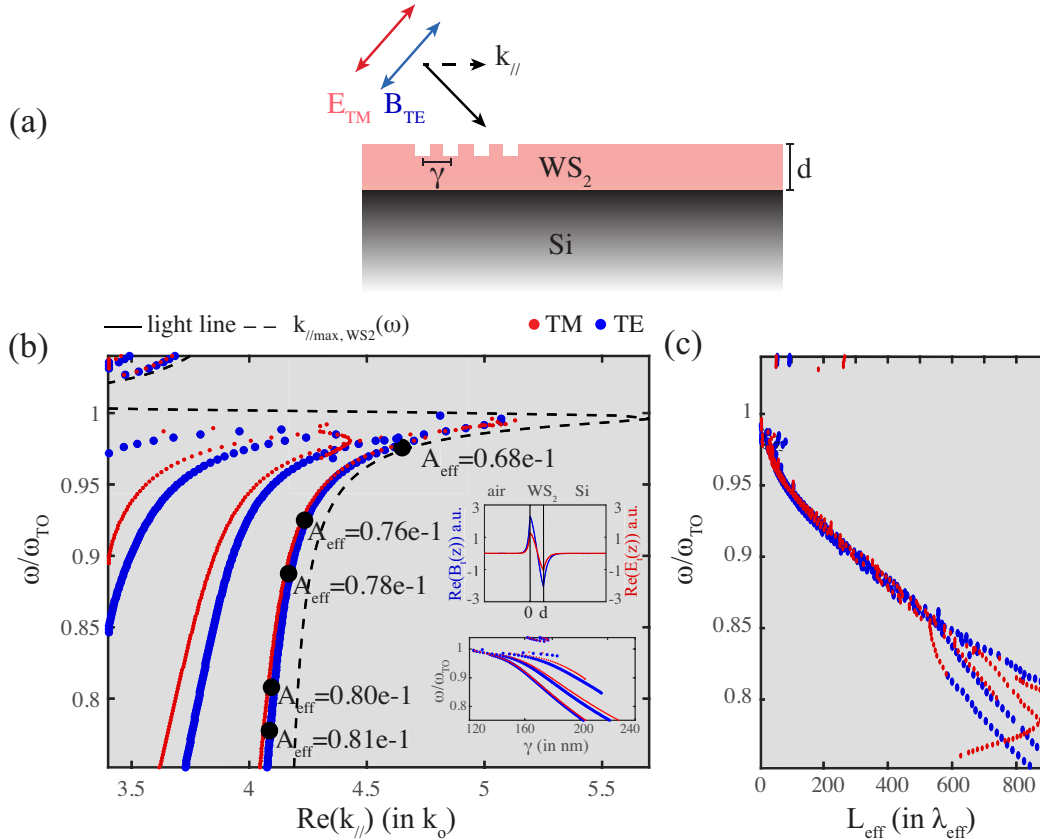


Figure 4.12: (a) Schematic of a slab of WS₂ on Si, and a grating with period γ for surface-confined waves excitation. (b) Dispersion of surface-confined waves on a slab of WS₂ with thickness $d_{\text{WS}_2} = 6\pi c / (\omega_{\text{TO,WS}_2} \sqrt{\epsilon_{\text{WS}_2}(\omega_{\text{TO,WS}_2})}) = 336$ nm on Si. The parameters for WS₂ were fitted from data reported in [129]: $\omega_{\text{TO,WS}_2} = 1.996$ eV, $\omega_{\text{LO,WS}_2} = 2.009$ eV, and $\gamma_{\text{d,WS}_2} = 37.363$ fs, in Eq. (4.4). The refractive index of Si is taken $n_{\text{Si}} = 3.4$. The free-space light line is located at $k_{//}/k_0 = 1$ (off-axis). The dashed line corresponds to $k_{//\text{max,WS}_2} = \sqrt{\epsilon_{\text{WS}_2}(\omega)}$, the band edge of WS₂. Left inset shows the grating period γ required for excitation of the surface-confined waves. Right inset shows the TE and TM field profiles at a single-frequency ω and wavenumber $k_{//}$. A_{eff} is the effective mode volume, as defined in Eq. (4.9). (c) Effective propagation length of surface-confined waves on WS₂ on Si, as defined in Eq. (4.8).

the band edge condition. In contrast, by assuming that the plasma frequency of the Drude metal, which serves here as a substrate, is considerably larger than ω_{TO} , the transverse optical phonon/exciton energy, the TM polarized SPP modes of the Drude metal are hybridized and obtain a frequency dispersion similar to the TE polarized band edge modes of the positive permittivity medium (polar dielectric or excitonic material).

We start by considering a system composed of a thin slab of polar dielectric material, with thickness $d_{\text{phon}} = \pi c / \omega_{\text{TO}} \sqrt{\epsilon_{\text{phon}}(\omega_{\text{TO}})}$ on a Drude metal substrate. We select the plasma frequency of the metal to be $\omega_{\text{p}} = \alpha \omega_{\text{TO}} \sqrt{1 + \epsilon_{\text{phon}}(\omega_{\text{TO}})}$, such that the surface plasma frequency of the plasmon is $\omega_{\text{sp}} \simeq \alpha \omega_{\text{TO}}$, and we set $\alpha = 2.5$. This selection of ω_{sp} locates the SPP on the linear, lower side of the dispersion (Fig. 4.7a). The relevant dispersion curves that we are combining in this configuration are: (i) the unbound SPP mode, shown in Fig. 4.7a, with (ii) the highly-confined TE polarized mode due to the phonon resonance, shown in Fig. 4.9b. The frequency regime in which this scenario becomes relevant is the IR range at which polar dielectric materials exhibit permittivity resonances (Fig. 4.2b).

A schematic of the geometry we study is shown in Fig. 4.13a, where we also include a grating that allows excitation of surface waves. As shown in Fig. 4.13b, by interfacing the TM polarized SPP mode of the Drude metal with the highly-confined band edge TE polarized mode of the polar dielectric, we position them in the same frequency range, and obtain almost overlapping dispersions for TE and TM polarization. However, here, the origin of the TM polarized mode is the plasmonic substrate, contrary to the previous sections. For completeness, we continue to include in Fig. 4.13b the curve corresponding to the band edge of the polar dielectric material, given by the equation $k_{//\text{max,phon}} = \sqrt{\epsilon_{\text{phon}}(\omega)} k_{\text{o}}$; as expected, the omnipolarization surface waves occur in the high- ϵ_{phon} frequency regime.

In the inset of Fig. 4.13b, we show the field profiles of the TE and the TM modes for the same frequency and wavenumber. Although the TE and TM dispersions do not exactly overlap, by selecting $\omega_{\text{TE}} = \omega_{\text{TM}}$ and $k_{//\text{TE}} = k_{//\text{TM}}$ we excite modes for both polarizations, with field profiles that show similar degree of confinement. The simultaneous excitation of modes for both polarizations is a consequence of the losses introduced in the system. Namely, the high- ϵ_{phon} regime is accompanied by large values of $\text{Im}(\epsilon_{\text{phon}})$ (see Fig. 4.1). Hence, the dispersions displayed in Fig. 4.13b extend to a small range of frequencies, $\pm \Delta\omega$, and wavenumbers, $\pm \Delta k_{//}$, around their central curves, which allows the TE and TM dispersions to overlap, as we emphasize with the purple highlighted regime.

In order to assess the feasibility of simultaneously exciting TE and TM polarized

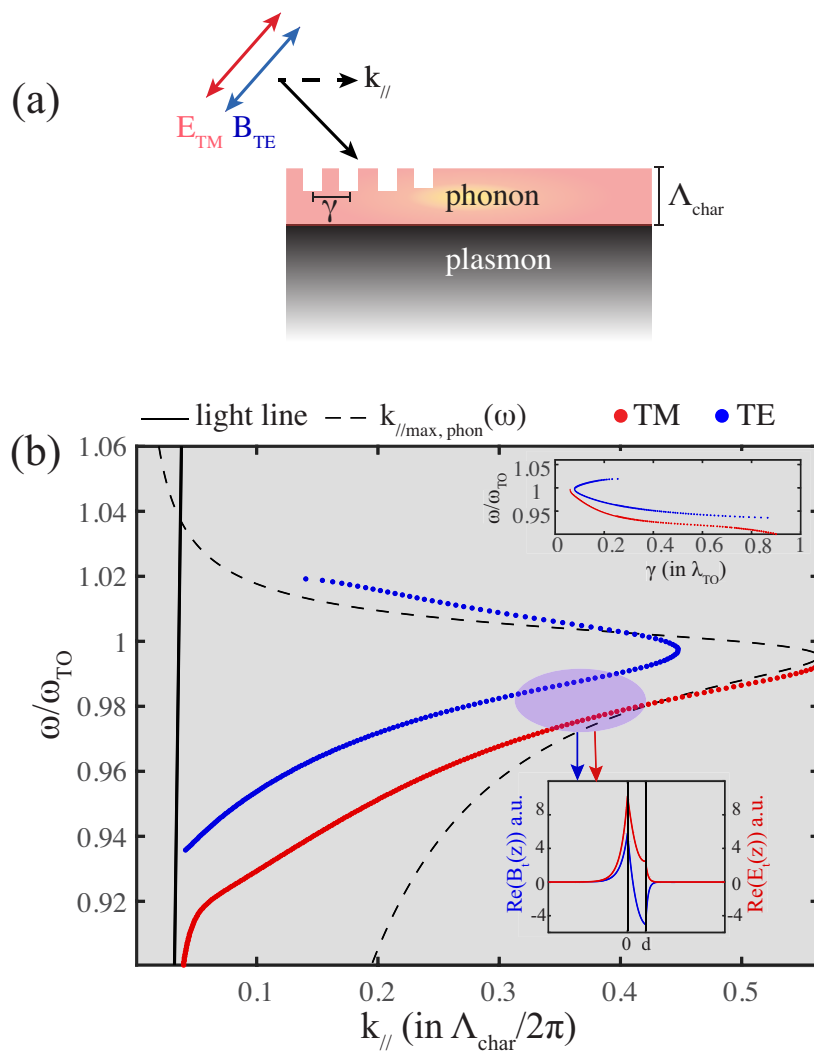


Figure 4.13: Omnipolarization surface waves from plasmons and phonons. (a) Schematic of a thin slab of polar dielectric material with thickness $d_{\text{ph}} = \pi c / \omega_{\text{TO}} \sqrt{\epsilon_{\text{phon}}(\omega_{\text{TO}})}$ on a Drude metal substrate, with $\omega_p = \alpha \omega_{\text{TO}} \sqrt{1 + \epsilon_{\text{phon}}(\omega_{\text{TO}})}$ ($\alpha = 2.5$). (b) Dispersion of surface-confined modes for TE and TM polarization, $\Lambda_{\text{char}} = d_{\text{ph}}$. The free-space light line is shown with black. Dashed line corresponds to $k_{//\text{max,phon}} = \sqrt{\epsilon_{\text{phon}}(\omega)} k_0$, the band edge of the polar dielectric. Lower inset shows field profiles for TE and TM polarization at the same frequency and wavenumber, $\omega_{\text{TE}} = \omega_{\text{TM}}$ and $k_{//\text{TE}} = k_{//\text{TM}}$. Top inset shows the grating period γ required for excitation of the modes.

surface-confined modes at a single-frequency and with a single grating, we calculate in the inset of Fig. 4.13b, the grating period γ required for TE and TM mode excitation. As can be seen, the grating periods for the two polarizations are almost identical, and their differences lie within the limits of fabrication imperfections ($\pm 0.1\lambda_{\text{TO}}$). The small differences in γ_{TE} and γ_{TM} , together with the aforementioned discussion regarding the losses in the system at frequencies near the high- ϵ_{phon} regime, ensure that omnipolarization surface waves can be excited in the configuration of Fig. 4.13a at a single-frequency. By selecting appropriately a high- Q polar dielectric material and a Drude metal, the plasma frequency of which can be tuned to approximately $\omega_{\text{p}} = 2.5\omega_{\text{TO}} \sqrt{1 + \epsilon_{\text{phon}}(\omega_{\text{TO}})}$, the surface waves shown in Fig. 4.13 may arise at IR frequencies, where the phonon energies of polar dielectric materials lie.

Here we combined a polar dielectric with positive permittivity ϵ_{phon} together with metal with negative permittivity ϵ_{m} , to achieve omnipolarization surface wave propagation. In principle, another possibility is to combine two different polar dielectric materials with slightly different frequencies of transverse and longitudinal phonons, $\omega_{\text{TO},1} \neq \omega_{\text{TO},2}$ and $\omega_{\text{LO},1} \neq \omega_{\text{LO},2}$, such as the Reststrahlen band of the first ($\epsilon_{\text{phon},1} < 0$) overlaps with the high- ϵ regime of the second ($\epsilon_{\text{phon},2} \gg 1$). There is an abundance of phonon resonances in different materials in the IR spectral range, hence it is straightforward to find such a combination of positive and negative permittivities. However, the frequency regimes near $\omega_{\text{TO},1}$, $\omega_{\text{TO},2}$ entail high loss (see Fig. 4.1), hence combining two polar dielectric materials near resonance will lead to very large damping constants of surface confined modes. Therefore, we do not investigate further the case of two phonons.

4.10 The case of a plasmon and an exciton

In analogy to the case examined above, here we investigate a thin slab of an excitonic material on a Drude metal substrate, in order to combine the highly-confined TE band edge mode due to the high- ϵ_{exc} regime (Fig. 4.10b) with the TM polarized SPP due to the plasmon of the metallic substrate (Fig. 4.7a). The frequency regime in which this scenario becomes relevant is the visible range at which excitonic materials exhibit permittivity resonances (Fig. 4.2a). We select a thickness of $d_{\text{exc}} = \pi c/\omega_{\text{TO}} \sqrt{\epsilon_{\text{exc}}(\omega_{\text{TO}})}$ for the excitonic material and a plasma frequency of $\omega_{\text{p}} = \alpha\omega_{\text{TO}} \sqrt{1 + \epsilon_{\text{exc}}(\omega_{\text{TO}})}$ for the metal. By setting $\alpha = 2.5$, we ensure that $\omega_{\text{sp}} \simeq \alpha\omega_{\text{TO}}$ is well-above ω_{TO} , hence, the plasmonic mode lies in the linear-regime, on the lower-frequency side of the SPP dispersion (see Fig. 4.7a). A schematic of the geometry we study is shown in Fig. 4.14a. We include a schematic of an input grating that allows excitation of surface waves from free space, via $k_{\parallel} = 2\pi/\gamma$.

As can be seen in Fig. 4.14b, we obtain a TE mode due to the high- ϵ_{exc} regime of

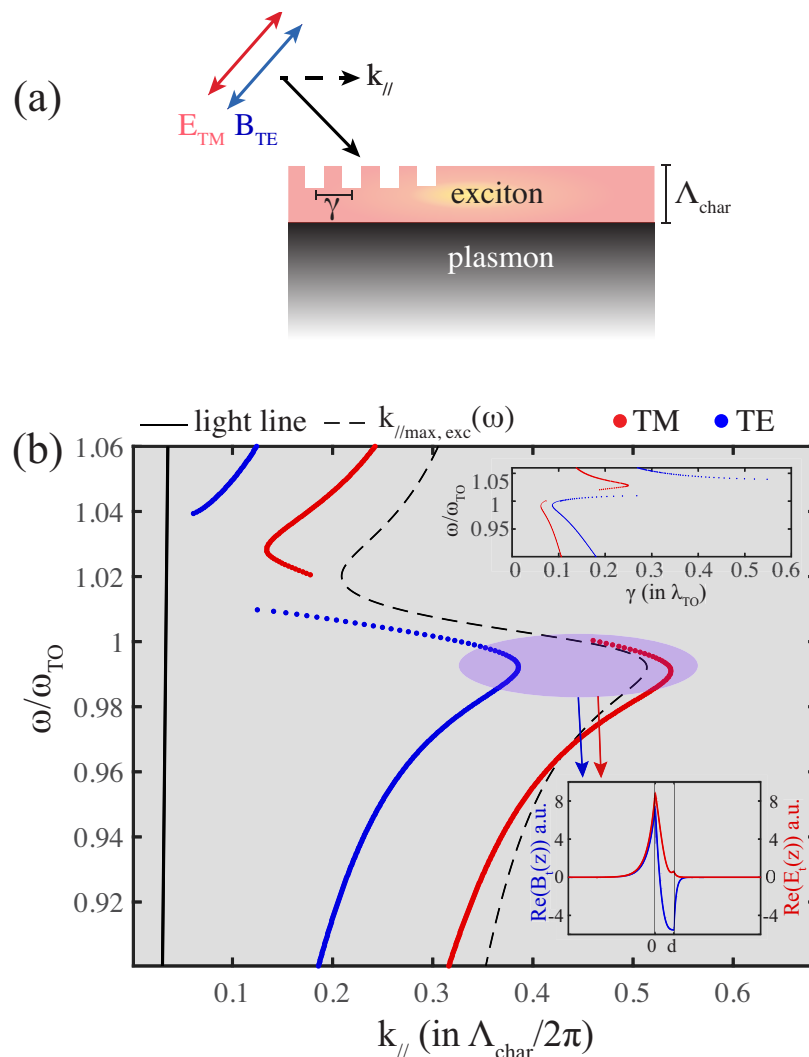


Figure 4.14: Omnipolarization surface waves from plasmons and excitons. (a) Schematic of a thin slab of an excitonic material with thickness $d_{\text{exc}} = \pi c / \omega_{\text{TO}} \sqrt{\epsilon_{\text{exc}}(\omega_{\text{TO}})}$ on a Drude metal substrate, with $\omega_p = \alpha \omega_{\text{TO}} \sqrt{1 + \epsilon_{\text{exc}}(\omega_{\text{TO}})}$ ($\alpha = 2.5$). (b) Dispersion of surface-confined modes for TE and TM polarization, $\Lambda_{\text{char}} = d_{\text{exc}}$. The free-space light line is shown with black. Dashed line corresponds to $k_{//\text{max,exc}} = \sqrt{\epsilon_{\text{exc}}(\omega)} k_0$, the band edge of the excitonic material. Lower inset shows field profiles for TE and TM polarization at the same frequency and wavenumber, $\omega_{\text{TE}} = \omega_{\text{TM}}$ and $k_{//\text{TE}} = k_{//\text{TM}}$. Top inset shows the grating period γ required for excitation of the modes.

the excitonic material, and a TM polarized hybrid-SPP mode due to the $\epsilon_m < 0$ of the metal. The typical SPP dispersion that is linear in the low- ω regime (Fig. 4.7a) is hybridized here due to the strong frequency dispersion of $\epsilon_{\text{exc}}(\omega)$ near ω_{TO} , and almost overlaps with the TE mode. For completeness, we continue to include the curve corresponding to the band edge of the excitonic material, given by the equation $k_{//\text{max,exc}} = \sqrt{\epsilon_{\text{exc}}(\omega)}k_0$; as expected, the omnipolarization surface waves arise in the high- ϵ_{exc} frequency regime.

Although the TE and TM dispersions do not exactly overlap, by selecting $\omega_{\text{TE}} = \omega_{\text{TM}}$ and $k_{//\text{TE}} = k_{//\text{TM}}$ we excite modes for both polarizations, the field profiles of which are displayed in the lower inset of Fig. 4.14b and exhibit similar degrees of surface-confinement. Similar to the comments made in the previous section, this simultaneous excitation occurs due to the losses introduced in the systems we study. Namely, near ω_{TO} , the excitonic material exhibits high damping (large $\text{Im}(\epsilon_{\text{exc}})$). Hence, the dispersions displayed in Fig. 4.14b extend to a small range of frequencies, $\pm\Delta\omega$, and wavenumbers, $\pm\Delta k_{//}$, around their central curves, which results in the overlap of the TE and TM modes dispersion curves, as emphasized with the purple highlighted regime.

In the top inset of Fig. 4.14b we calculate the grating period γ required for TE and TM mode excitation. The grating periods for the two polarizations are similar, and their differences lie within the limits of fabrication imperfections ($\pm 0.1\lambda_{\text{TO}}$, where λ_{TO} lies in the visible spectral range), ensuring simultaneously TE and TM polarized mode excitation with a single grating.

4.11 Conclusion

In this chapter we studied the high-permittivity frequency regime of polar dielectric materials and excitonic materials, at IR and visible frequencies, respectively. We showed that use of high- Q materials can lead to surface-confined waves that occur for both linear polarizations simultaneously, i.e. they can be excited at a single-frequency ($\omega_{\text{TE}} = \omega_{\text{TM}}$) and require a single grating for their excitation ($k_{//\text{TE}} = k_{//\text{TM}}$), hence they are also phase-matched.

We followed two different approaches; (i) the first one pertained to utilizing the polarization degeneracy of the band edge modes of a bulk polar dielectric or excitonic material. (ii) The latter approach entailed the combination of plasmonic metals with polar dielectrics and excitonic materials, at IR and visible frequencies, respectively, for omnipolarization surface waves. In this case, the TE and the TM modes have different origins; namely, the TM mode is a hybrid-SPP mode due to the plasmonic metal, whereas the TE mode originates from the dielectric's band edge.

With regards to (i), we demonstrated theoretically that use of SiC at IR frequencies and WS₂ at visible frequencies can yield omnipolarization surface-confined waves with higher degree of confinement and longer propagation distances, in comparison to SPPs in Ag. In Table 4.1, we summarize these results and provide a comparison between the cases we examined. We emphasize that SiC and WS₂ were selected due to their high- Q s (Eq. (4.5)), which is a crucial parameter for obtaining surface waves with good confinement characteristics and large propagation distances. We note, however, that, in contrast to the broadband nature of SPPs, the omnipolarization surface waves discussed here are narrowband in nature, and physically bound to the frequency range where phonons and excitons occur in naturally available materials.

Material	TE polarization	TM polarization
Semi-infinite Ag (visible)	A_{eff} N.A. L_{eff} N.A.	$A_{\text{eff}} \sim [0.5 - 1.2]$ $L_{\text{eff}} \sim [5 - 55]$
SiC on Si (IR)	$A_{\text{eff}} \sim [0.045 - 0.066]$ $L_{\text{eff}} \sim [10 - 70]$	$A_{\text{eff}} \sim [0.045 - 0.066]$ $L_{\text{eff}} \sim [10 - 70]$
WS ₂ on Si (visible)	$A_{\text{eff}} \sim [0.068 - 0.081]$ $L_{\text{eff}} \sim [10 - 800]$	$A_{\text{eff}} \sim [0.068 - 0.081]$ $L_{\text{eff}} \sim [10 - 800]$

Table 4.1: Comparison of figures of merit between SPPs in Ag (see Section 4.5) and omnipolarization surface-confined waves in SiC (see Section 4.7) and in WS₂ (see Section 4.8). A_{eff} is the cross-sectional area of the mode normalized to a diffraction limited spot $A_{\text{o,1D}} = \lambda_0/2$ (see (Eq. 4.9)). L_{eff} is the propagation length of the mode normalized to the effective wavelength of the mode (see Eq. (4.8)).

Regarding the latter approach (ii), we showed that combination of plasmons and excitons or plasmons and phonons, at visible and IR frequencies, respectively, can yield omnipolarization surface-confined propagation. In search for realistic configurations that may support such surface waves, it is highly desirable to be able to actively tune the plasma frequency of the plasmonic component to frequencies that match phonon energies (IR) or exciton resonances (visible). In the following chapter, we perform detailed investigations for inducing such active tunability in planar heterostructures in both visible and IR frequency regimes.

ACTIVE TUNABILITY IN PLANAR METAMATERIALS

“This field is not quite the same as other fields in physics in that it will not tell us more of fundamental physics but it is more like solid-state physics in the sense that it might tell us much of great interest about the strange phenomena that occur in complex situations.”

Richard P. Feynman, Plenty of Room at the Bottom, 1959

5.1 Tuning the optical response

The range of fundamental phenomena and applications achievable by metamaterials can be significantly expanded by actively tuning their effective electromagnetic parameters to enable dynamic control over their optical response. Such active control over metamaterials’ response can pave the way towards novel active optical components like holographic displays, improvement of liquid crystal display technology with solid-state materials, tunable polarizers, sensors and switches, slow-light media, and optical memories. Particularly, simultaneous control of phase and amplitude of fields scattered or transmitted through metamaterial-based optical components is challenging to achieve but highly desirable for holography and lidar technology [153, 154].

In this chapter, we investigate means for tuning the response of planar metamaterials along all coordinate directions, by focusing on their fundamental material parameters. By starting from intrinsic metamaterial properties (ϵ_{eff} and μ_{eff}), we can directly predict and control their dispersion characteristics. Control over the dispersion diagram or the EFC, introduced in Chapter 1 (see Section 1.4) is of interest from a more fundamental physics point of view as well (apart from tuning the scattering properties of metamaterials).

Namely, the past decade has revealed a plethora of new phenomena in electronic materials in condensed matter physics, and also in their photonic counterparts, arising from engineering their electronic band structure and photonic dispersion surface, respectively. Classical phenomena such as Lifshitz transitions [155] and Van Hove singularities that lead to extreme values of magnetoresistance arise from inducing transitions in the Fermi surface of electronic systems. Quantum mechanical effects such as those arising from Dirac-like dispersion surfaces, leading to topological Dirac

phases, are the result of band structure engineering, leading to three-dimensional semimetals [156] and topological insulators [157]. Photonic analogues of topological insulators, in other words photonic materials that support non-trivial topologically protected states against back-scattering, have been realized with helical waveguides in a honeycomb lattice [158], by engineering the dispersion characteristics of photonic crystals. The dispersion surface or EFC is also critical for engineering emission with hyperbolic media, as investigated and demonstrated experimentally in [42] (see discussion in Section 1.4). Particularly, in analogy to the Lifshitz transition in electronic systems, a transition from a closed EFC to an open, hyperbolic one, comes with a singularity in the density of optical states. By controlling the dielectric properties of HMMs along different coordinate directions, namely the near-zero bands of $\epsilon_{o,\text{eff}}$ and $\epsilon_{e,\text{eff}}$, the frequency regime of topological transitions becomes tunable [48].

This chapter is structured as follows: in Sections 5.2, 5.3, 5.4 we discuss means for inducing actively tunable response in planar metamaterials using transparent conductive oxides (TCOs). In Sections 5.5, 5.6 we investigate the use of graphene as an active medium. We show that field-effect-based gating, i.e. carrier accumulation and depletion, using TCOs, yields a largely tunable response along the optical axis of planar heterostructures, for frequencies below the UV range [48], while capacitor-based gating with graphene mono-layers leads to significant tuning along the in-plane direction.

We note that alternative tuning mechanisms include modifying the complex dielectric function of component materials via phase transitions [159] and electromechanical deformations [160]. In contrast to these, use of the field-effect and electronic gating via carrier injection are particularly attractive due to their robustness and very low power dissipation in steady state, having potential to yield power-efficient tunable metamaterials with ultrafast (fs) modulation speed. The field-effect has been recently investigated for optical modulators [153, 161–164] by using the spectral tunability of the electronic properties in TCOs or transition-metal nitrides [165] for modulating the modal effective index in waveguide configurations.

5.2 Transparent conductive oxides as active components

We start with the toy model shown in Fig. 5.1, demonstrating a metamaterial unit cell composed of two mirror-symmetric metal/oxide/semiconductor (MOS) sequence of layers. Instead of a traditional semiconductor, we investigate here TCO active layers. The charge carrier density of TCOs can be controlled by the number of oxygen vacancies when deposited, for example via RF sputtering deposition. More importantly, however, their charge carrier density can be tuned actively as well [153, 154, 159], when incorporated in MOS devices and gating between the metal and the

TCO is applied, injecting carriers in TCO accumulation and depletion regimes, as shown in Fig. 5.1 with light blue colors.

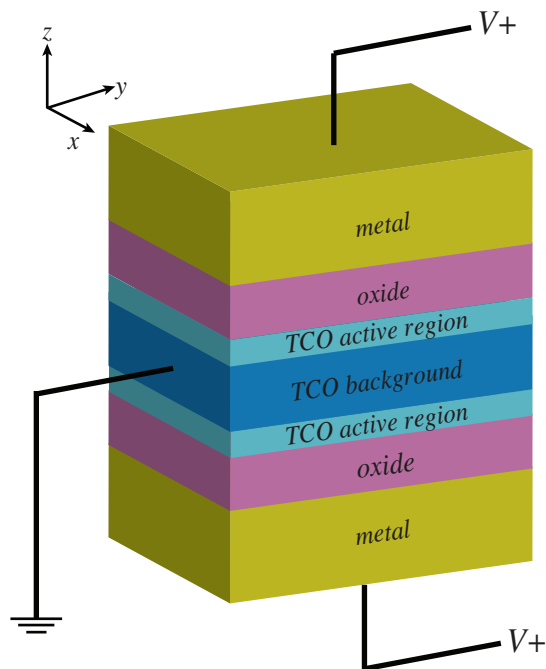


Figure 5.1: Schematic of TCO-based field-effect tunable hyperbolic metamaterial unit cell

Prior to delving into the details on the optical properties of the motif shown in Fig. 5.1, we discuss the field-effect mechanism using TCOs. We focus on indium tin oxide (ITO) as an example TCO, because it has been studied extensively in the literature [153, 161, 166–169] and its electronic properties are fairly well characterized experimentally [153, 161, 167, 170]. We emphasize, however, that the results discussed here can be extended to other TCOs, for example aluminum doped zinc oxide [166] and gallium doped zinc oxide [164, 166], or transition-metal nitrides and degenerately doped semiconductors [163].

The intrinsic parameter modulated via the field-effect, that is in turn used to induce optical tuning, is the charge carrier density, N_{acc} , in the active layers of accumulation and depletion (light blue colors in Fig. 5.1), relative to the background charge carrier density N_{b} . Ignoring detailed band bending effects, to first order, the charge carrier accumulation can be schematically modeled via a uniform layer with increased carrier concentration relative to the background TCO, with thickness given by the Debye length d . A simple electrostatic calculation on a metal/dielectric/TCO interface, as depicted in Fig. 5.1, dictates that:

$$\frac{V}{t} = \frac{eN_{\text{acc}}d}{k_{\text{diel}}\epsilon_0} \leq E_{\text{br}} \quad (5.1)$$

where V is the applied bias between the metal and the TCO, t is the thickness of the dielectric and k_{diel} is its DC dielectric constant, E_{br} is the corresponding breakdown field and ϵ_0 is the dielectric permittivity of free space. To achieve tunability within the visible regime, high-carrier density is required, on the order of $10^{19} - 10^{21}/\text{cm}^3$. Additionally, dielectric materials with very high breakdown fields are necessary. Previous reports have shown that ITO can be heavily doped using RF sputtering to yield a background carrier density, N_b , in the range $10^{19} - 10^{21}/\text{cm}^3$. Following previous experimental results [153, 161, 162, 167–170], we consider here a background carrier density of $N_b = 5 \times 10^{20}/\text{cm}^3$ and active tunability of the carrier density in the accumulation regimes of up to two orders of magnitude, assuming high-strength dielectric materials for the oxide layer (see Fig. 5.1). We note that here we only consider accumulation of carriers, however depletion can be achieved by simply inverting the bias polarization. We compute, in Table 5.1, using Eq. (5.1), the maximum achievable carrier concentration in the accumulation layer of ITO, for various high-strength dielectric materials whose breakdown fields have been reported. Different Debye lengths d for the ITO are also considered, consistent with the range of parameters observed in previous experimental results [153, 161, 162, 168].

High- k dielectric quality is important for sustaining high carrier concentrations in the accumulation layer. HfO_2 is particularly attractive due to its simultaneously large values of DC dielectric constant [171, 174, 176, 177] and its high breakdown field. We note that, apart from Sire *et al.* in [171] and Yota *et al.* in [174], Kim *et al.* in [178] have obtained breakdown fields as high as 36 MV/cm for large-area (up to $100\mu\text{m} \times 100\mu\text{m}$) planar field-effect electrode geometries, while values in the range 5 – 10 MV/cm have been broadly reported in the literature [179–181].

As far as the optical properties of TCOs at visible and IR frequencies are concerned, and particularly for the material of interest here, which is ITO, its dielectric permittivity is described with the Drude model [153, 161, 167, 170, 182].

$$\epsilon_{\text{ITO}} = \epsilon_{\infty} - \frac{\omega_p^2}{\omega^2 + i\omega\gamma} \quad (5.2)$$

where $\omega_p^2 = N_i e^2 / \epsilon_0 m_{\text{eff}}$, ϵ_{∞} is the high-frequency dielectric permittivity and m_{eff} is the effective mass. N_i is the carrier density, for $i = b, \text{acc}$ for the background and accumulation regions, respectively. Following previous experimental work [153, 161, 182], we take $\epsilon_{\infty} = 3.4$, $\gamma = 1.8 \times 10^{21}/\text{sec}$ and $m_{\text{eff}} = 0.35m_e$, where m_e

Dielectric	$N_{\text{acc}}, d = 0.5$	$N_{\text{acc}}, d = 1$	$N_{\text{acc}}, d = 2.5$	$N_{\text{acc}}, d = 5$
SiO ₂ $k_{\text{diel}} = 3.9$ [171, 172] $E_{\text{br}} = 30 - 40$ [171]	1.29 – 1.7	0.65 – 0.86	0.26 – 0.35	0.13 – 0.17
Al ₂ O ₃ $k_{\text{diel}} = 9$ [172] $E_{\text{br}} = 6 - 8$ [171, 173, 174]	0.6 – 0.8	0.3 – 0.4	0.12 – 0.16	0.06 – 0.08
Al ₂ O ₃ $k_{\text{diel}} = 10.3$ [174] $E_{\text{br}} = 6 - 8$ [171, 173, 174]	0.68 – 0.91	0.34 – 0.46	0.14 – 0.18	0.07 – 0.09
HfO ₂ $k_{\text{diel}} = 17$ [171] $E_{\text{br}} = 13$ [171]	2.4	1.2	0.48	0.24
HfO ₂ $k_{\text{diel}} = 18.7$ [174] $E_{\text{br}} = 5.6$ [174]	1.16	0.58	0.23	0.12
HfSiO ₄ $k_{\text{diel}} = 11$ [175] $E_{\text{br}} = 10$ [175]	1.22	0.61	0.24	0.12
HfSiO ₄ (with SiO ₂) $k_{\text{diel}} = 4.8 - 5.4$ [176] $E_{\text{br}} = 10$ [175]	0.53 – 0.6	0.27 – 0.3	0.11 – 0.12	0.05 – 0.06
HfSiO ₄ (with HfO ₂) $k_{\text{diel}} = 12.5 - 15.1$ [176] $E_{\text{br}} = 10$ [175]	1.38 – 1.67	0.69 – 0.83	0.28 – 0.33	0.14 – 0.17

Table 5.1: Maximum achievable carrier concentration in ITO accumulation layers for reported values of breakdown field and DC dielectric constants of high-strength dielectrics. The breakdown voltage E_{br} is given in MV/cm and the carrier density N_{acc} in $10^{21}/\text{cm}^3$. d is the accumulation layer thickness given in nm.

is the electronic rest mass. Starting from the background carrier density $N_{\text{b}} = 5 \times 10^{20}/\text{cm}^3$, we show in Fig. 5.2 the dielectric permittivity of ITO at visible-near IR frequencies for increasing carrier concentration. We highlight that carrier densities in the range $10^{20} - 10^{21}/\text{cm}^3$ yield an epsilon-near-zero (ENZ) response at visible frequencies, with ϵ_{ITO} transitioning from positive to negative values. In turn, this induces topological transitions in the dispersion surface of the metamaterial, as we discuss in what follows (see Figs. 5.6, 5.7, 5.8).

5.3 Tunable hyperbolic response at optical frequencies

Regarding the optical response of the metamaterial, we consider a toy model consisting of 20 nm of Ag (yellow layers in Fig. 5.1), separated by 15 nm of ITO (dark

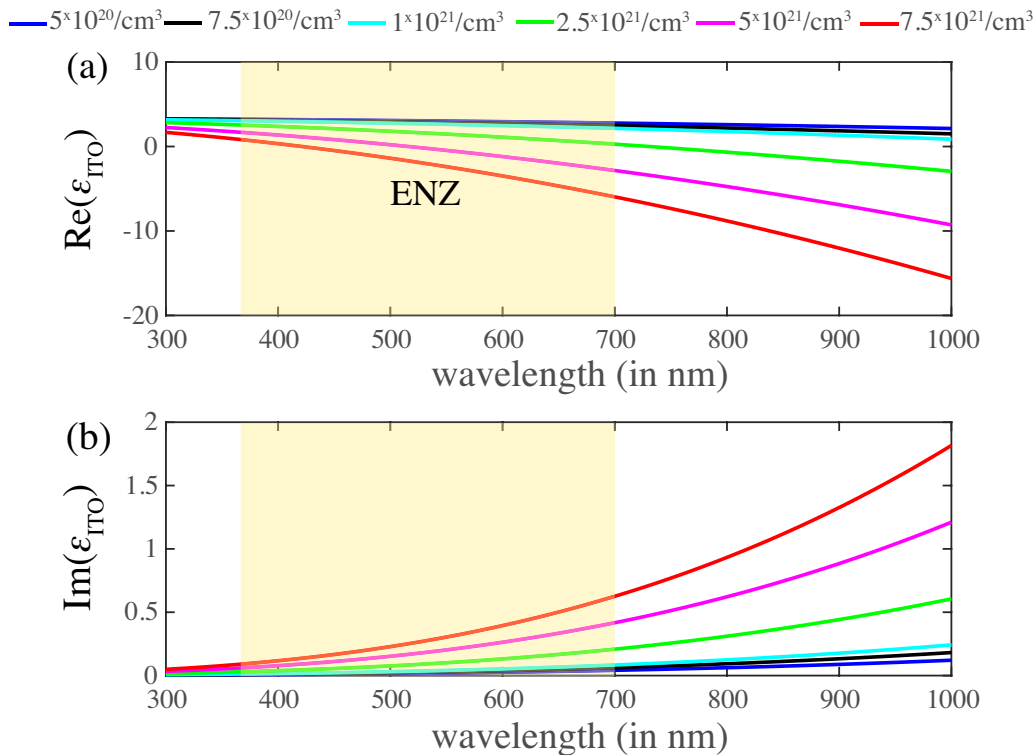


Figure 5.2: Complex dielectric permittivity of indium tin oxide at visible-near IR frequencies. (a) $\text{Re}(\epsilon_{\text{ITO}})$, (b) $\text{Im}(\epsilon_{\text{ITO}})$.

blue and light blue colors for background and accumulation layers, respectively, in Fig. 5.1). The two materials are electrically isolated from each other by 10 nm of HfO_2 dielectric layers (purple layers in Fig. 5.1). The thickness of HfO_2 was chosen to correspond to thicknesses routinely achievable in atomic layer deposition [173, 174]. The optical properties of Ag were taken from [75], while the Sellmeier equation with three poles was used for the refractive index of HfO_2 [183]. Under applied bias between the Ag and the ITO in the geometry of Fig. 5.1, we consider a 2.5 nm accumulation layer to be formed in the HfO_2 -ITO interface [153, 161, 162]. In Section 5.4 we perform a sensitivity analysis over the accumulation layer thickness and maximum carrier density modulation in order to comprehensively assess the tunability range for this design for various TCOs, transition-metal nitrides or degenerate semiconductors and high-k dielectrics. We model both the background ITO and the accumulation layer using the Drude model with higher carrier concentration compared to the background, as discussed above (see Eq. (5.2)).

The drastic change in the carrier concentration across the ITO background and accumulation layer interface yields tunable optical parameters. We use the parameter retrieval method discussed in Chapter 2 and in [47] to calculate the effective opti-

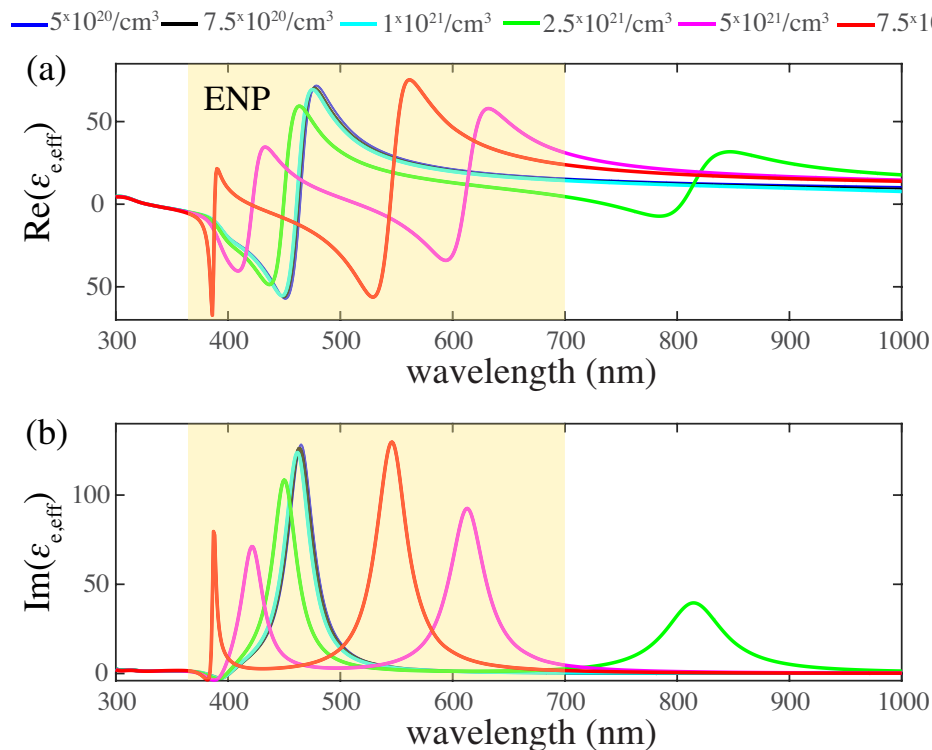


Figure 5.3: Extraordinary dielectric permittivity of the TCO-based tunable HMM depicted in Fig. 5.1. (a) $\text{Re}(\epsilon_{e,\text{eff}})$, (b) $\text{Im}(\epsilon_{e,\text{eff}})$. Legends correspond to varying carrier concentration in the ITO accumulation layer, N_{acc} .

cal parameters $\epsilon_{o,\text{eff}}$, $\epsilon_{e,\text{eff}}$ of this motif for increasing carrier concentration in the accumulation layer of ITO. We note that, no high-index layers are incorporated in the considered metamaterial, hence, following the results of Chapter 3, the magnetic permeability of this motif is approximately unity ($\mu_{o,\text{eff}} \approx \mu_{e,\text{eff}} \approx 1$), and the effective magnetic parameters are not discussed further.

As the carrier concentration in the accumulation layer of ITO increases under applied bias from the background value of $5 \times 10^{20}/\text{cm}^3$ up to $7.5 \times 10^{21}/\text{cm}^3$, corresponding to experimentally reported carrier concentration changes [161], the Lorentzian-shaped resonance in extraordinary permittivity $\epsilon_{e,\text{eff}}$ blue-shifts as seen in Fig. 5.3. This resonance arises from the coupling of the plasmonic modes supported on the metal/dielectric interfaces to the bulk high- k modes of the HMM [33]. The epsilon-near-pole (ENP) wavelength of this dominant resonance blue-shifts under applied bias by more than 60 nm, while remaining within the visible regime.

In contrast to $\epsilon_{e,\text{eff}}$ that is largely tunable, $\epsilon_{o,\text{eff}}$ does not exhibit significant tuning with increasing bias, as shown in Fig. 5.4. The weak dependence of $\epsilon_{o,\text{eff}}$ on N_{acc} is expected; the ITO accumulation layers are relatively thin (2.5 nm) compared to the

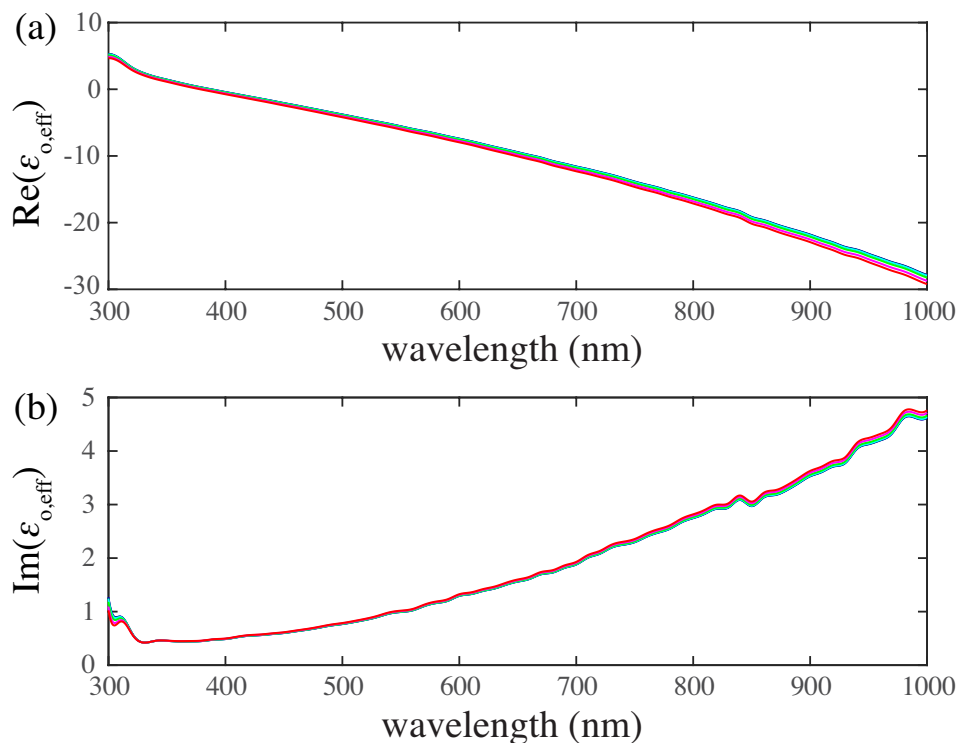


Figure 5.4: Ordinary dielectric permittivity of the TCO-based tunable HMM depicted in Fig. 5.1. (a) $\text{Re}(\epsilon_{o,\text{eff}})$, (b) $\text{Im}(\epsilon_{o,\text{eff}})$. Color map similar to Fig. 5.3.

Ag layers (20 nm), the response of which dominates along the in-plane direction, consistent with effective medium theories (see Section 2.2).

As discussed in Chapter 3, TM polarized bulk modes experience an extreme anisotropic response when propagating in planar HMMs, as dictated from Eq. (3.2). Similar to naturally occurring uniaxial materials [1], we introduce here an effective birefringence and dichroism for TM polarized modes, defined as $\text{Re}(\sqrt{\epsilon_{o,\text{eff}}\mu_{o,\text{eff}}}) - \text{Re}(\sqrt{\epsilon_{e,\text{eff}}\mu_{o,\text{eff}}})$ and $\text{Im}(\sqrt{\epsilon_{o,\text{eff}}\mu_{o,\text{eff}}}) - \text{Im}(\sqrt{\epsilon_{e,\text{eff}}\mu_{o,\text{eff}}})$, respectively. These parameters are shown in Fig. 5.5 for increasing carrier concentration in the accumulation layer of ITO. As expected, HMMs exhibit extreme anisotropies, which is manifest in large birefringence values. These by far exceed the birefringence of the most anisotropic natural materials like liquid crystals and other uniaxial inorganic crystals (c.f., Table 5.2). Notable is the broadband tunability of both birefringence and dichroism across the whole visible spectrum.

The tunability of the effective parameters presented in Figs. 5.3, 5.4 has an effect on the dispersion surface for TM polarized waves, as discussed in Chapter 3 (Eq.

(3.2)). This can be illustrated by defining a metamaterial figure of merit (FOM), $\text{FOM} = \text{Re}(k_{z,\text{eff}}) / \text{Im}(k_{z,\text{eff}})$. In Figs. 5.6 a, b, c we display this parameter for carrier concentration $N_{\text{acc}} = 5 \times 10^{20} / \text{cm}^3 = N_{\text{b}}$, $N_{\text{acc}} = 2.5 \times 10^{21} / \text{cm}^3$ and $N_{\text{acc}} = 7.5 \times 10^{21} / \text{cm}^3$, respectively. Active modulation of the ITO accumulation layer yields drastic changes in the metamaterial FOM. The “valleys” and “ridges” in Fig. 5.6 are a good criterion for identifying regions of enhanced and suppressed density of optical states, respectively [71]. Namely, the ridge in Fig. 5.6a, at wavelengths 400–500 nm, indicates a band gap where propagation is forbidden. The large FOM values away from the band gap regime emphasize the hyperbolic response of the heterostructure, supporting large- k values. As the bias is increased, in other words for increased carrier density, in Fig. 5.6b, an additional band gap is introduced at larger wavelengths 700–800 nm, due to the secondary Lorentzian-shaped resonance in $\epsilon_{e,\text{eff}}$, shown in Fig. 5.3 with green color. Further increase in the carrier density or applied bias (Fig. 5.6c) leads to further spectral shift of the valleys and ridges. We note that these figures of merit by far exceed previous generation metamaterials, due to the intrinsic property of HMMs to support spectral regions of $\epsilon_{o,\text{eff}}\epsilon_{e,\text{eff}} < 0$ and, therefore, large wavenumbers.

Material	Birefringence
Al_2O_3	0.08
LiNbO_3	0.085
Rutile	0.287
Nematic liquid crystals	0.4

Table 5.2: Birefringence $\text{Re}(\sqrt{\epsilon_o}) - \text{Re}(\sqrt{\epsilon_e})$ of anisotropic dielectric media

The tunable optical parameters for this metamaterial motif also yield changes in the isofrequency contours and topological transitions. In Fig. 5.7, we present the complex isofrequency contours for TM bulk modes. Both k_x and k_z are normalized to the free space wavenumber $k_o = \omega/c$. Application of DC bias across the HMM unit cell yields drastic changes in both the shape and type of the dispersion surface. Additionally, the surface area enclosed by the isofrequency contours, which is proportional to the total number of available optical states [41], changes significantly with changes in ITO accumulation layer carrier concentration, yielding a route to active control over the metamaterial optical density of states.

As can be seen from Fig. 5.7, for all the considered free-space wavelengths, the topology of the dispersion surface changes with the ITO carrier density. The EFC at wavelengths of 378 nm and 650 nm depict regions of type I and type II hyperbolic dispersion, respectively. Hyperbolic dispersion of type I is a consequence of the effective built-in dipole moment in the direction across the optical axis for oblique

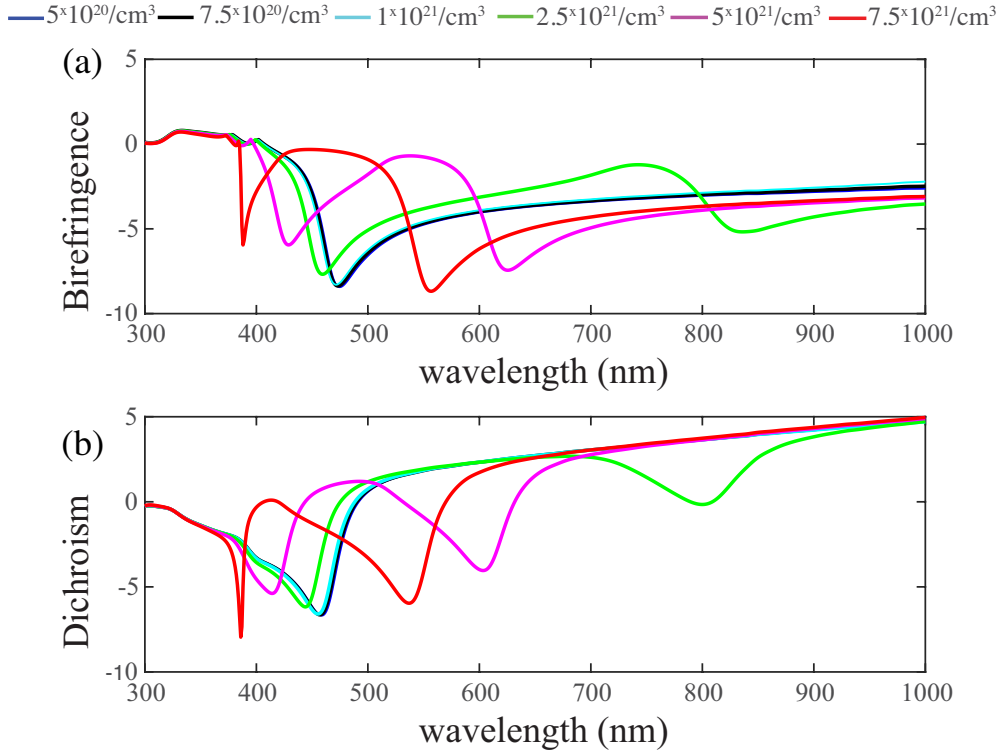


Figure 5.5: (a) Birefringence defined as $\text{Re}(\sqrt{\epsilon_{o,\text{eff}}\mu_{o,\text{eff}}}) - \text{Re}(\sqrt{\epsilon_{e,\text{eff}}\mu_{o,\text{eff}}})$, (b) Dichroism defined as $\text{Im}(\sqrt{\epsilon_{o,\text{eff}}\mu_{o,\text{eff}}}) - \text{Im}(\sqrt{\epsilon_{e,\text{eff}}\mu_{o,\text{eff}}})$. Legends correspond to varying carrier concentration in the ITO accumulation layer, N_{acc} .

incidence and TM polarization, yielding $\epsilon_{e,\text{eff}} < 0$. Type II hyperbolicity is the result of the metallic response of the metamaterial along the in-plane direction ($\epsilon_{o,\text{eff}} < 0$) and the dielectric response along the optical axis ($\epsilon_{e,\text{eff}} > 0$). Deviations of the EFCs from perfect hyperbolic shapes are attributed to loss and spatial dispersion (see Section 3.7).

For the wavelength of 520 nm, it is evident that the area enclosed by the real part of the isofrequency surface decreases for increasing ITO carrier density. Additionally, the losses increase with increasing ITO carrier density, as shown by the imaginary parts of the EFCs. This wavelength falls inside a photonic band gap region for the ITO carrier density $N_{\text{acc}} = 7.5 \times 10^{21}/\text{cm}^3$. At this carrier density, both parameters $\epsilon_{o,\text{eff}}$ and $\epsilon_{e,\text{eff}}$ are negative, leading to a forbidden band (see Eq. (3.2)). Hence, at this wavelength regime, the metamaterial experiences a topological transition from a hyperbolic state to a forbidden region with increasing carrier concentration. For 800 nm wavelength, a similar observation is made for the green curve corresponding to ITO carrier density of $N_{\text{acc}} = 2.5 \times 10^{21}/\text{cm}^3$. For this carrier concentration, the metamaterial exhibits a band gap, as also indicated in Fig. 5.6b.

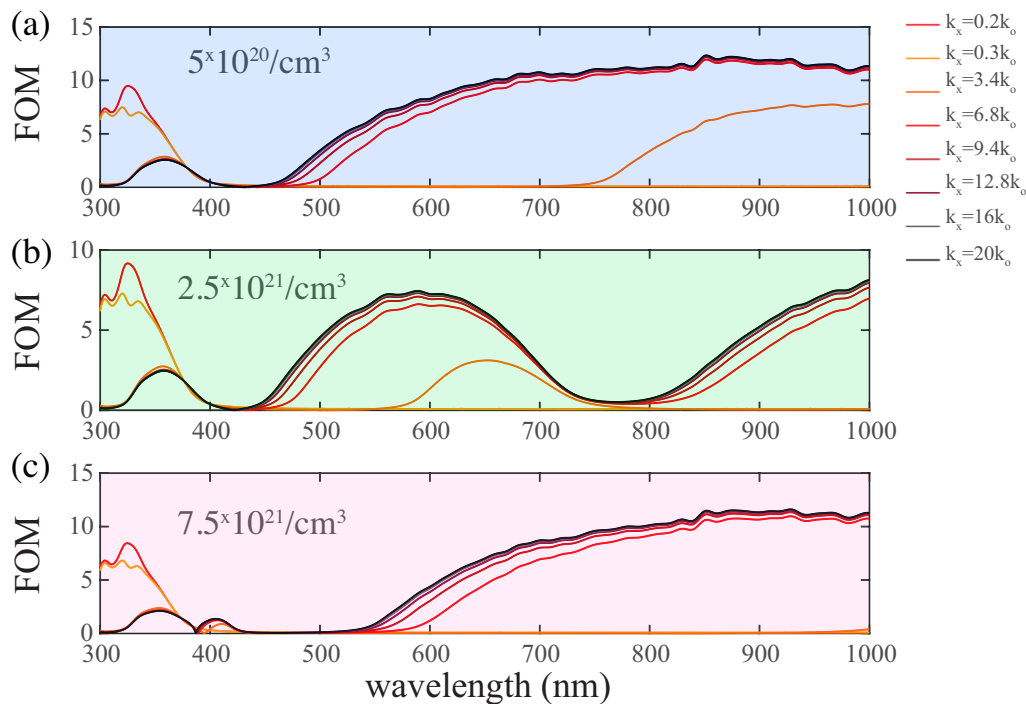


Figure 5.6: Tunable figure of merit defined as $\text{Re}(k_z)/\text{Im}(k_z)$ of the TCO-based tunable HMM depicted in Fig. 5.1. Panels (a), (b), (c) correspond, respectively, to $N_{\text{acc}} = 5 \times 10^{20}/\text{cm}^3 = N_{\text{b}}$, $N_{\text{acc}} = 2.5 \times 10^{21}/\text{cm}^3$ and $N_{\text{acc}} = 7.5 \times 10^{21}/\text{cm}^3$.

To illustrate the effects of tunable optical parameters on the effective band structure, we show in Fig. 5.8 the change in the topology of the frequency-dependent three-dimensional dispersion surface for the two extreme cases of charge carrier concentration in the ITO accumulation layer, in the lossless limit. Within the optical regime, we see an effective omnidirectional band gap (noticeable in the band diagram along both the k_x and k_z axes in Figs. 5.8a, b, respectively), whose band edges can be tuned by varying the applied bias. Additionally, we notice the appearance of a new effective band gap and a new hyperbolic region, for larger accumulation layer carrier concentration changes ($N_{\text{acc}} = 7.5 \times 10^{21}/\text{cm}^3$ in Figs. 5.8c, d). Hence, the field-effect provides sufficient change of the conductive oxide permittivity to allow for spectral shifting of the hyperbolic regions and band gaps of HMMs and even to allow for active opening and closing of band gaps.

5.4 Sensitivity analysis

As shown in Eq. (5.1), the parameter that principally defines the tunability range of the effective optical properties of our metamaterial is the product $N_{\text{acc}}d$, where

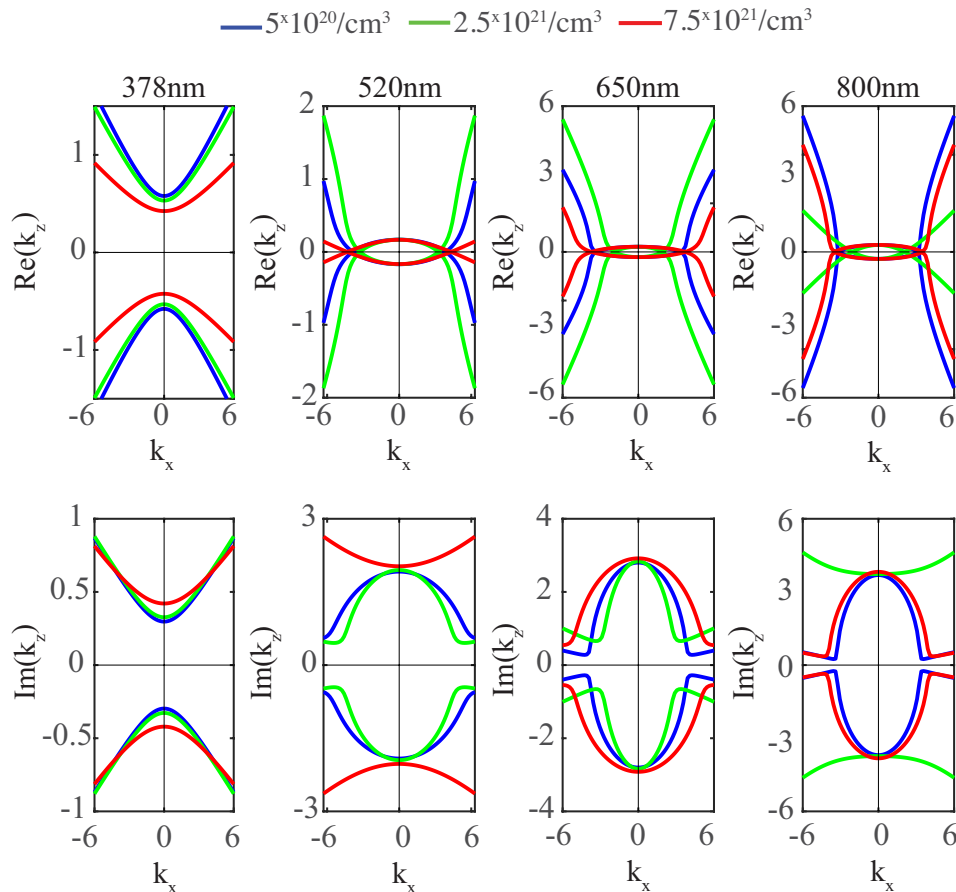


Figure 5.7: Complex isofrequency contours at different wavelengths for the TCO-based tunable HMM depicted in Fig. 5.1. Blue, green and red colors correspond, respectively, to $N_{\text{acc}} = 5 \times 10^{20}/\text{cm}^3 = N_{\text{b}}$, $N_{\text{acc}} = 2.5 \times 10^{21}/\text{cm}^3$ and $N_{\text{acc}} = 7.5 \times 10^{21}/\text{cm}^3$. k_x and k_z are normalized to the free space wavenumber $k_0 = \omega/c$

N_{acc} is the maximum achievable carrier concentration in the accumulation layer of the TCO before electrical breakdown occurs, and d is the Debye length or thickness of the accumulation layer. We perform a sensitivity analysis of the retrieved extraordinary permittivity $\epsilon_{\text{e,eff}}$, separately as a function of N_{acc} and d , since $\epsilon_{\text{e,eff}}$ is the optical parameter most drastically affected by the field-effect (Fig. 5.3). Both for N_{acc} and d , we consider values within the range of previous experimental reports [153, 161, 162, 167–169]. We suggest that this approach can provide useful insight here, and also for other semiconductors and TCOs or transition-metal nitrides, as active constituent materials in field-effect tunable metamaterial realizations. In Fig. 5.9 we illustrate the tunability of the ENP region of the primary Lorentzian resonance (Fig. 5.3).

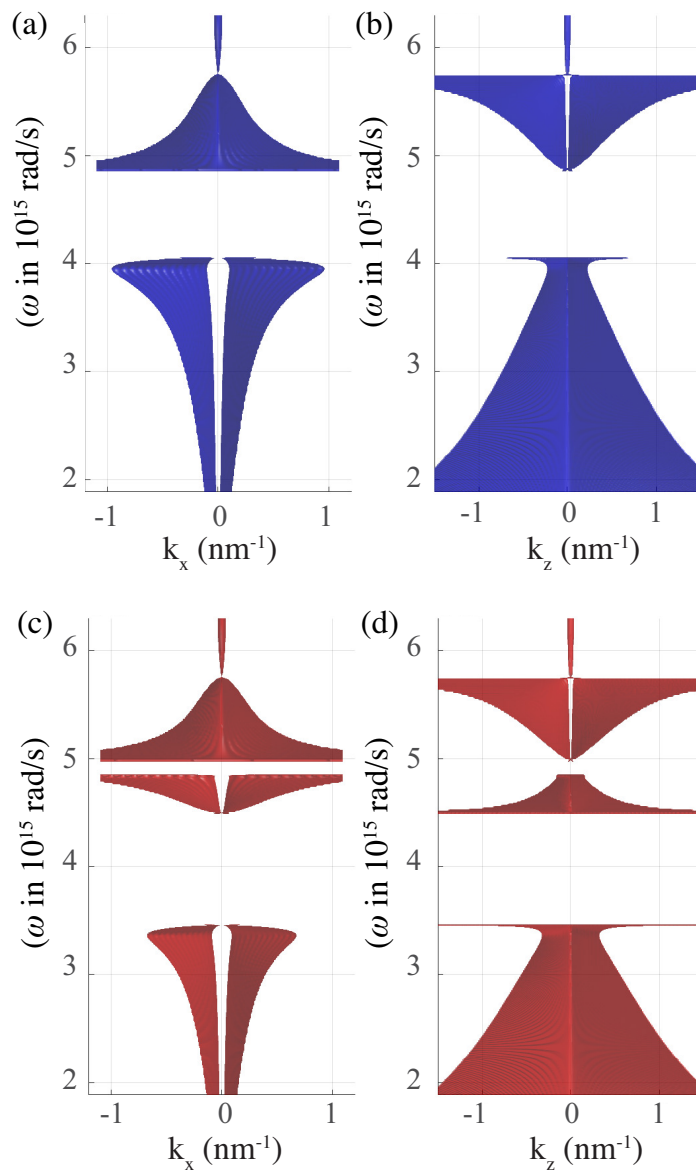


Figure 5.8: Three-dimensional tunable dispersion surface for the TCO-based tunable HMM depicted in Fig. 5.1. (a) along the k_x axis and (b) along the k_z axis for $N_{\text{acc}} = 5 \times 10^{20}/\text{cm}^3 = N_b$. (c) along the k_x axis and (d) along the k_z axis for $N_{\text{acc}} = 7.5 \times 10^{21}/\text{cm}^3$.

Both the carrier concentration N_{acc} and the Debye length d drastically impact the spectral shift of $\epsilon_{e,\text{eff}}$. As expected, thicker accumulation layers (i.e. larger d) is desirable as it introduces larger shifts of the ENP. Similarly, being able to gate TCO materials at very high carrier densities is also desirable for increased optical tuning. We emphasize here on the importance of the electrical quality of the oxide layer, which is critical for achieving experimentally observable spectral tuning.

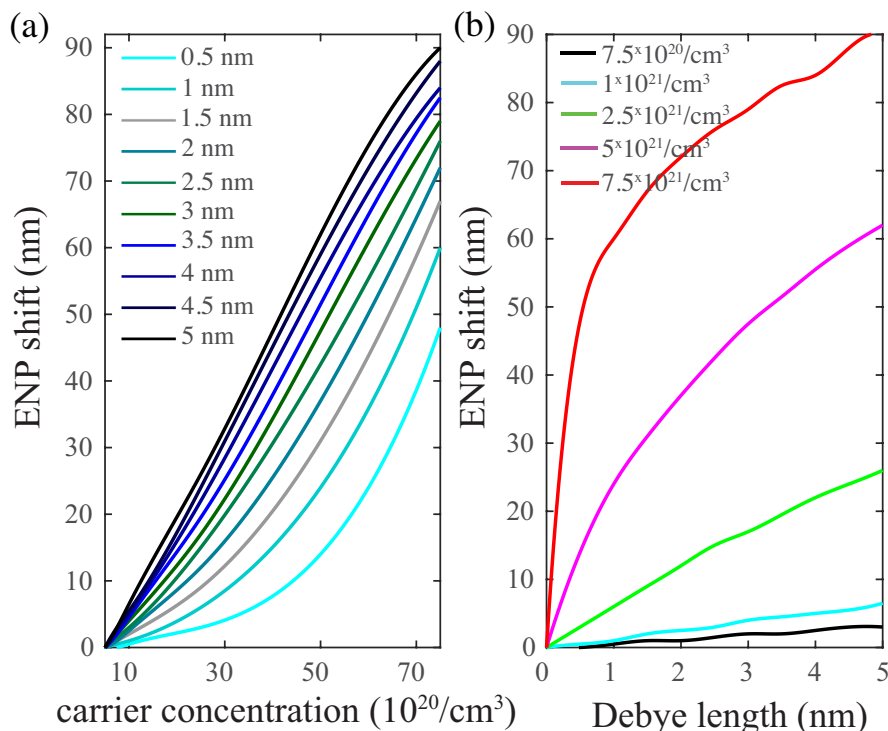


Figure 5.9: Effects of the electronic properties of ITO on the ENP wavelength of $\epsilon_{e,\text{eff}}$. (a) Dependence of the ENP shift on the carrier concentration N_{acc} , for varying Debye lengths indicated with the legends. (b) Dependence of the ENP shift on the Debye length, for varying maximum achievable carrier concentration in the accumulation layer before breakdown occurs.

5.5 Graphene as an active component

Graphene is a two-dimensional, single-atom thick semimetal, initially extracted from graphite in 2004, by A. Geim and K. Novoselov [184]. From its two-dimensional nature arises the intriguing property of exhibiting linear electronic dispersion of the form $E \propto |\vec{k}|$ near its charge neutrality point (CNP), as shown in Fig. 5.10a. This is in contrast to conventional metallic systems where the electronic dispersion is parabolic ($E \propto |\vec{k}|^2$). At the Dirac point or CNP, the density of electronic states vanishes, however it is possible to tune graphene Fermi's level E_F via carrier injection, chemically or by electrostatic changes to the carrier concentration [5, 120, 121, 184]. Hence the conductance of graphene σ , and therefore its optical properties can be actively modulated in motifs where graphene is gated against another conducting material.

Another interesting aspect of graphene is its ability to guide extremely confined surface plasmonic modes [120, 121], with confinement factors that exceed any three-

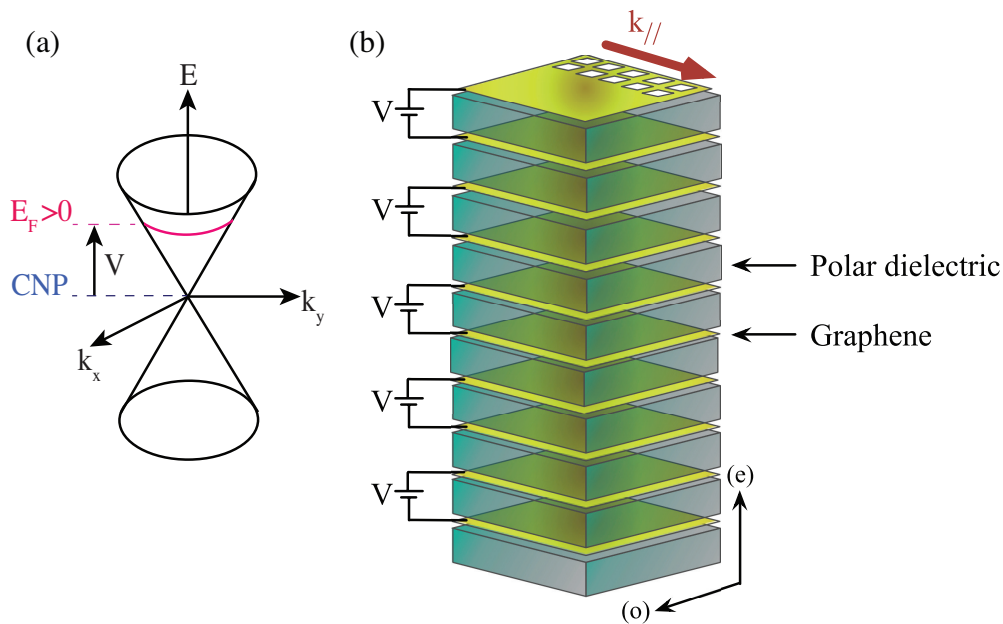


Figure 5.10: (a) Graphene's Dirac cone. Here E and k_x , k_z are the energy and wavenumbers of electrons, respectively, not to be confused with the wavenumber $k_{//}$ in (b), which pertains to the incident electromagnetic field's wavenumber. (b) Schematic of graphene-based tunable hyperbolic metamaterial unit cell. Directions (o) and (e) refer to the ordinary and extraordinary axes.

dimensional, bulk plasmonic metal. In contrast to plasmonic metals or to the TCO family discussed in the previous sections, graphene's lower carrier density yields plasmonic properties in the IR range. Hence, it is an intriguing material to investigate as a tunable metallic component in planar graphene/dielectric HMM configurations (Fig. 5.10b).

In modeling graphene, we take its conductance at different values of E_F from the semi-analytical model provided in [185]. In order to account for two-dimensional materials in the conventional transfer matrix approach discussed in Section 2.3 and in Appendix A.1, we modify Maxwell's boundary conditions for the magnetic field, to consider a non-zero surface current density $\vec{J} = \sigma \vec{E}$ induced by the incident electric field \vec{E} [186]. This results in the transfer matrix for graphene $\vec{M}_{\text{graphene}}$ (or any two-dimensional material described via a sheet conductance σ), given by

$$\vec{M}_{\text{graphene}} = \begin{pmatrix} 1 & 0 \\ -4\pi\sigma/c & 1 \end{pmatrix} \quad (5.3)$$

which is to be multiplied with the transfer matrix of Eq. (2.15), for multilayer

heterostructures involving both two-dimensional and conventional three-dimensional materials.

5.6 Tunable hyperbolic response at infrared frequencies

We envisage multilayer configurations of alternating graphene/high-strength dielectric layers as depicted in Fig. 5.10b. Similar configurations have been considered in [186] and in [187], however in previous reports, the dielectric layers were assumed to be non-dispersive. We highlight that, typically, in the IR regime, dielectric materials exhibit phonon resonances as discussed in Chapter 4. For this reason, and in order to examine a parameter space of experimentally reasonable configurations, we assume here a typical polar dielectric response with Lorentzian-shaped resonances, as discussed in Fig. 4.1. We particularly focus our studies in SiO₂ dielectric layers, due to the widespread use of SiO₂ as an insulating material in graphene experiments [5, 120]. As a result of accounting for phonon resonances, we observe interesting ENZ regimes for the composite metamaterial, at IR frequencies. Such a response is typically unfound in natural plasmonic metals, where the ENZ regime is physically bound to UV-visible frequencies.

We perform transfer matrix calculations for the example system of Fig. 5.10b, for SiO₂ layers of thickness 100 nm, achievable either with electron-beam or thermal evaporation, or growth on a Si substrate, for higher material quality. We consider changes in graphene's Fermi level E_F from CNP, up to 1 eV. These can be induced by gating the graphene mono-layers either against each other, as shown in Fig. 5.10b, or against a common ground, which could be, for example, a substrate (such as doped Si, which is commonly used for graphene experiments). The ordinary and extraordinary permittivities of the metamaterial, $\epsilon_{o,\text{eff}}$ and $\epsilon_{e,\text{eff}}$, at different E_F , are shown in Fig. 5.11. The effective parameters calculations were performed using the parameter retrieval approach discussed in Chapter 2 and in [47].

Similar to the TCO-based metamaterial investigated above, the graphene-based metamaterial studied here does not exhibit interesting magnetic properties ($\mu_{o,\text{eff}} \approx \mu_{e,\text{eff}} \approx 1$). This may seem counter-intuitive, as in Chapters 3 and 4 we emphasized that strong artificial magnetic effects require high- ϵ values to support strong displacement currents \vec{J}_{disp} [98] (see Section 3.3), and the polar dielectric medium (SiO₂) does exhibit high- ϵ near its phonon resonances ($\sim 10\mu\text{m}$ and $\sim 20\mu\text{m}$). However, as discussed in Section 3.3, for strong magnetic effects, the high- ϵ layers should be separated by some distance r so that a magnetic dipole moment $\vec{M}_{\text{eff}} \propto \vec{r} \times \vec{J}_{\text{disp}}$ is built. In the case examined here, the SiO₂ layers are separated by graphene mono-layer of negligible thickness, hence $r = 0$ and the magnetic effects are unimportant.

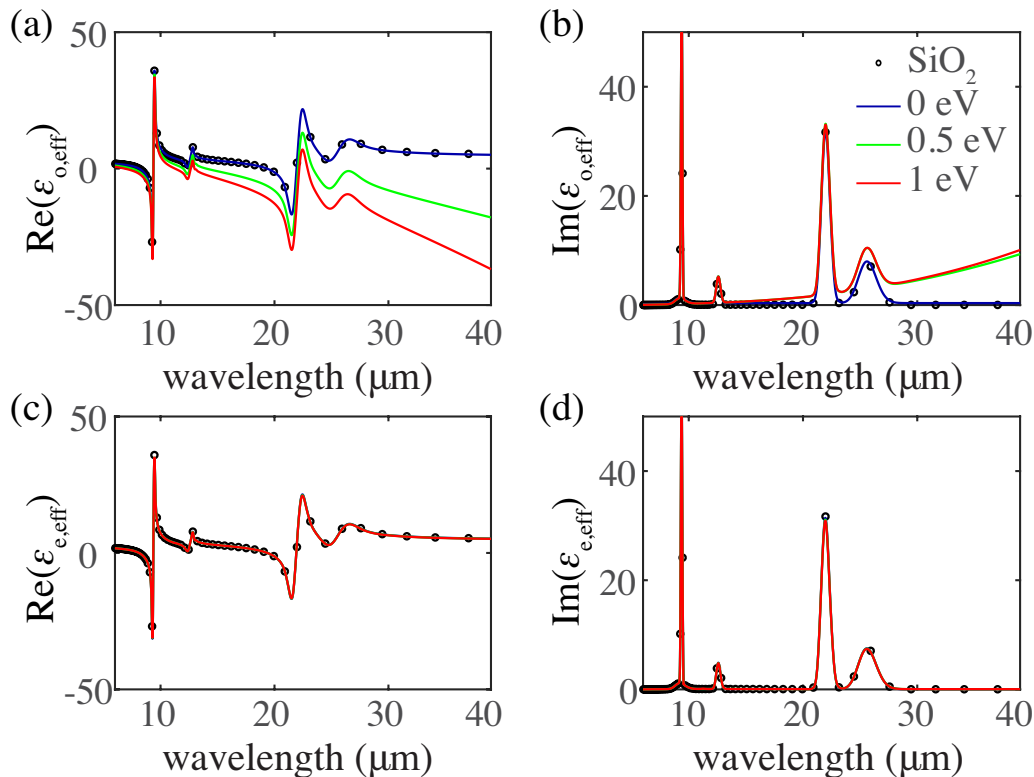


Figure 5.11: Complex effective dielectric permittivity of the graphene/SiO₂ HMM depicted in Fig. 5.10, for different E_F corresponding to different applied bias V . (a) $\text{Re}(\epsilon_{o,\text{eff}})$, (b) $\text{Im}(\epsilon_{o,\text{eff}})$, (c) $\text{Re}(\epsilon_{e,\text{eff}})$, (d) $\text{Im}(\epsilon_{e,\text{eff}})$.

It is noteworthy that the extraordinary permittivity $\epsilon_{e,\text{eff}}$ of the metamaterial coincides exactly with the permittivity of SiO₂, ϵ_{SiO_2} , as shown in Figs. 5.11c, d, for all considered gating levels or values of E_F . This occurs due to the two-dimensional nature of graphene; electric fields with out-of-plane (z) components do not experience the graphene's response and, instead, feel a purely dielectric environment.

By contrast, the ordinary permittivity $\epsilon_{o,\text{eff}}$ is largely tunable as depicted in Figs. 5.11a, b. At $E_F = 0$, we obtain $\epsilon_{o,\text{eff}} = \epsilon_{e,\text{eff}} = \epsilon_{\text{SiO}_2}$. This result is expected; as explained above, at $E_F = 0$ eV, graphene has a vanishing density of electronic states, hence it is not conductive and its effect on the optical properties of the metamaterial is negligible, along all coordinate directions. By increasing E_F , we observe an induced metallic response along the in-plane direction, i.e. for electric fields with a component parallel to the metamaterial's interfaces. Maximum tunability of $\epsilon_{o,\text{eff}}$ is observed at and below the phonon frequencies of the SiO₂. Particularly, we observe two induced and tunable ENZ regimes for $\epsilon_{o,\text{eff}}$, near the two phonons, i.e. at wavelengths $\sim 10\mu\text{m}$ and $\sim 20\mu\text{m}$. In Fig. 5.12 we provide an enlarged view of

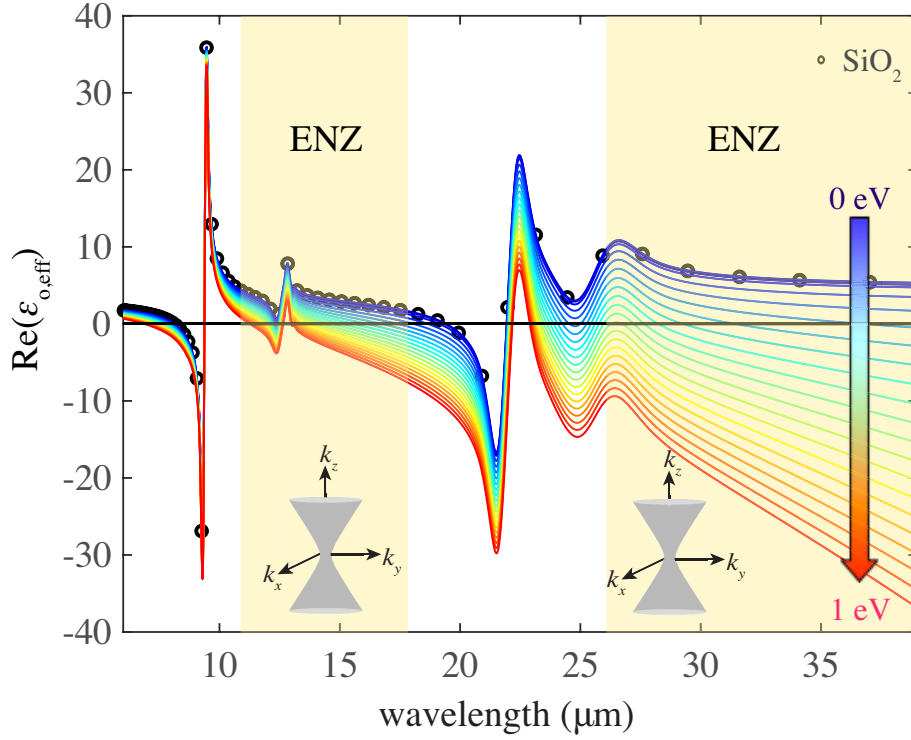


Figure 5.12: $\text{Re}(\epsilon_{o,\text{eff}})$ of the graphene/SiO₂ HMM depicted in Fig. 5.10, for different E_F corresponding to different applied bias V . The highlighted regions correspond to epsilon-near-zero regimes and topological transitions from elliptical to hyperbolic dispersion.

$\text{Re}(\epsilon_{o,\text{eff}})$.

With the reminder that $\epsilon_{e,\text{eff}} = \epsilon_{\text{SiO}_2}$ for all considered values of E_F , we infer from Fig. 5.12 that this metamaterial exhibits topological transitions of its dispersion surface from the elliptical state ($\epsilon_{o,\text{eff}}\epsilon_{e,\text{eff}} > 0$) to the hyperbolic state ($\epsilon_{o,\text{eff}} < 0$, $\epsilon_{e,\text{eff}} > 0$), as higher gate bias V is applied, i.e. for increasing values of E_F . These transitions occur at wavelengths between the two SiO₂ phonons and also for wavelengths above the 20 μm phonon. In order to quantify the degree of hyperbolicity and to estimate the range of observable changes in the metamaterial's dispersion, we consider the equipfrequency contours for bulk, TM polarized propagating modes (see Eq. (3.2)) at different wavelengths, as shown in Fig. 5.13.

From Fig. 5.13a, at small wavelengths where the tunability range is small as shown in Fig. 5.12, the EFC does not change considerably for different values of E_F . Particularly, since $\epsilon_{o,\text{eff}}$ is not largely tunable in this regime of wavelengths, we have $\epsilon_{o,\text{eff}} \approx \epsilon_{e,\text{eff}}$, hence the response is almost isotropic, as confirmed with the circular shape of the EFCs in Fig. 5.13a. Small changes in the shape of the EFC

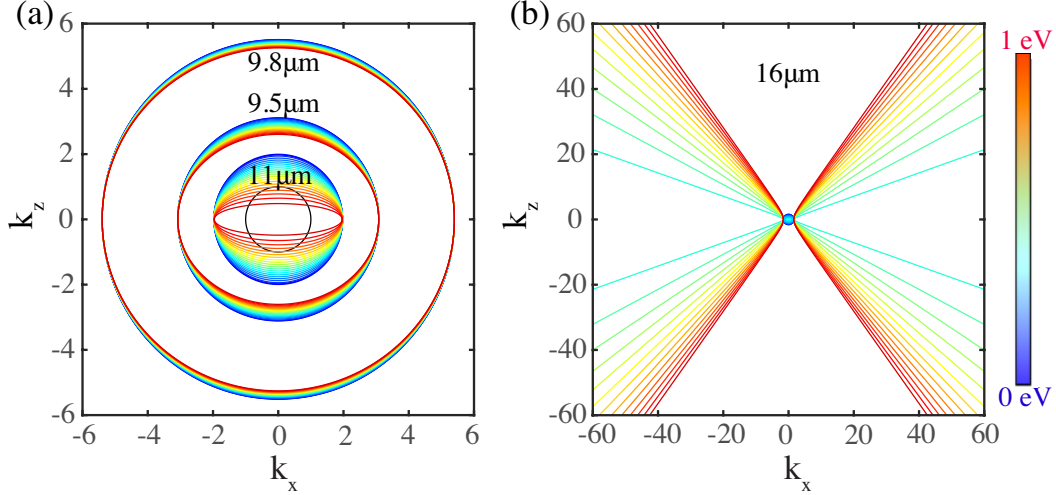


Figure 5.13: Isofrequency contours at different wavelengths for the graphene/SiO₂ HMM depicted in Fig. 5.10, for different E_F corresponding to different applied bias V . (a) Elliptical regime corresponding to wavelengths at which $\epsilon_{o,\text{eff}}\epsilon_{e,\text{eff}} > 0$, (b) hyperbolic regime for wavelength $16\mu\text{m}$, at which $\epsilon_{o,\text{eff}}\epsilon_{e,\text{eff}} < 0$. k_x and k_z are normalized to the free space wavenumber $k_o = \omega/c$.

from circular to elliptical arise from small changes in $\epsilon_{o,\text{eff}}$ with respect to $\epsilon_{e,\text{eff}}$. By contrast to the small wavelength regime, between the two phonons of SiO₂ ($\sim 10\mu\text{m}$ and $\sim 20\mu\text{m}$), the response of this metamaterial changes dramatically with applied bias or increased E_F . This is shown with the EFC in Fig. 5.13b, for a wavelength of $16\mu\text{m}$. At small values of E_F , $\epsilon_{o,\text{eff}} \approx \epsilon_{e,\text{eff}}$ and the response is isotropic. With increasing E_F , $\epsilon_{o,\text{eff}}$ becomes negative, hence the EFC opens up into a hyperboloid. Notably, the range of achievable wavenumbers k_z is dramatically increased in the hyperbolic regime, where we have $k_z \sim 60k_o$.

A considerable impediment in practically utilizing the large wavenumbers supported in traditional metallodielectric multilayer hyperbolic media -and, as a consequence, their large density of optical states- is to find means of coupling into these high- k states from free space ($k_{//} \leq k_o$) [71]. In the case of graphene-based HMMs, however, this issue is easily circumvented, as even unpatterned graphene provides access to wavenumbers as large as $k_{//} \sim 20k_o$ due to its plasmonic properties below its plasma frequency [120, 121]. Importantly, by patterning graphene, we can access wavenumbers as large as $k_{//} \sim 100k_o$ [120, 121], for which we display a patterned top-most graphene layer in Fig. 5.10b. Hence, with graphene/dielectric multilayer HMM configurations (Fig. 5.10b), it becomes possible to achieve confinement factors for bulk propagating modes (apart from guided surface plasmonic modes) below the diffraction limit.

5.7 Conclusion

In conclusion, we outlined methods for electronically tuning the response of planar hyperbolic metamaterials at visible and IR frequencies, using transparent conductive oxides and graphene as active components, respectively.

In the visible regime, we introduced a field-effect gating scheme for electrical modulation of the permittivity in transparent conductive oxide layers. By incorporating a TCO into a typical metallodielectric metamaterial and altering the carrier density in accumulation regions, we observe the opening and closing of optical omnidirectional band gaps controlled by applied bias, which corresponds to a tunable figure of merit with values as high as 15 in the hyperbolic regime while vanishing at the band gaps. The field-effect allows spectral tunability of the effective extraordinary permittivity ($\epsilon_{e,\text{eff}}$) along the optical axis (z direction). We predict blue shifts of $\epsilon_{e,\text{eff}}$ near its resonance by more than 60 nm in the visible regime. This also gives rise to broadband tunability of the effective birefringence and dichroism, with potential for novel photonic devices like tunable metallodielectric waveguides, optical sensors, filters and polarizers. Such active control over the complex parameters of metamaterials is also essential for slow light media and holographic displays. Our sensitivity analysis with respect to changes in the TCO carrier concentration and accumulation layer thickness indicates the robustness of the field-effect as a tuning mechanism. The straightforward fabrication of multilayer metamaterials by thin-film deposition techniques suggests that the experimental realization of tunable field-effect metamaterials with active materials such as TCOs, transition-metal nitrides or degenerately doped semiconductors is well within reach.

In the IR regime, we envisage graphene as a tunable element, integrated into planar heterostructures that allow carrier injection for optical tuning. Particularly, we investigate heterostructures composed of alternating layers of graphene and high-strength polar dielectric materials. Via electrostatic gating in graphene layers, one is able to actively alter the Fermi level E_F , which in turn yields an overall tunable response of the metamaterial. In contrast to the visible regime where the formation of accumulation and depletion regions along the optical axis (z) yields tunable extraordinary permittivity, the two-dimensional nature of graphene yields optical tuning in the direction parallel to the layers, i.e. for the ordinary permittivity $\epsilon_{o,\text{eff}}$. By raising previous assumptions regarding the non-dispersive nature of the dielectric layers, we observe largely tunable values of $\epsilon_{o,\text{eff}}$ near the phonon resonances of the dielectric material. The tunability of the effective parameters extends across a wide range of frequencies, from the IR to the microwave regime. The extraordinary plasmonic properties of graphene allow large confinement factors and coupling into very high- k modes ($k_{//} \sim 100k_o$), taking full advantage of the hyperbolic response

of planar metalodielectric heterostructures.

By combining the two concepts outlined above, i.e. (i) carrier injection in accumulation regions of TCOs, transition-metal nitrides or degenerately doped semiconductors via the field-effect and (ii) carrier injection in graphene via electrostatic gating, one may envision gaining active control and tunable response along all coordinate directions simultaneously, for frequencies ranging from the IR to the microwave regime.

ULTRA-LIGHT VAN DER WAALS HETEROSTRUCTURES AS SUPERMETALS

“What could we do with layered structures with just the right layers? What would the properties of materials be if we could really arrange the atoms the way we want them? They would be very interesting to investigate theoretically.”

Richard P. Feynman, Plenty of Room at the Bottom, 1959

6.1 What makes a perfect reflector? Beyond noble metals

In this final chapter, we search for artificial matter that exhibits ultra-reflective properties. Although the question of what makes a perfect reflector may seem rather fundamental, the search for perfect reflection is motivated by technological needs and applications. Particularly, nearly perfect reflection is a requirement in designing compact waveguides that operate based on total-internal-reflection. It is also a necessary functionality for state-of-the-art aerospace technology, where the quality factor of a mirror is a crucial parameter. Perfectly reflecting materials are also necessary for engineering emission, serving as back-reflectors in absorbing systems for solar energy technologies [5, 188], as well as for cloaking macroscopic objects, such as aircrafts.

So far, engineering reflection has been discussed in Chapter 1, in the context of photonic crystals and particularly Bragg mirrors. However, Bragg mirrors are limited by narrow bandwidth as can be seen from Fig. 1.5. Aside from Bragg reflectors, broadband perfect reflection requires high electrical conductance, in other words low electrical resistivity, typically found in noble metals with large charge carrier density. In Table 6.1, we list the twenty most conductive elemental metals, sorted with increasing bulk room-temperature resistivity $\rho_{o,rt}$ [189]. In the far-IR, certain metals act as perfect electrical conductors (PECs). A PEC is formally defined as a material with $\text{Re}(\epsilon) \rightarrow -\infty$, while $\text{Im}(\epsilon) \rightarrow 0$ that reflects perfectly. Critical parameters for a PEC are the carrier relaxation time τ , which ought to be small for highly conductive materials with few collisions and low loss ($\text{Im}(\epsilon) \rightarrow 0$), and the Fermi velocity v_f , which needs to be large for carriers (electrons) with high mobility. From Table 6.1 it is clear that gold (Au) and silver (Ag) outperform other metals and are the two most widely used materials for mirroring systems in the mid-long-wave IR.

Element	$\rho_{o,rt}$ ($\mu\Omega$ cm)	v_f (10^5 m/s)	τ (fs)
Silver	1.587	14.48	36.8
Cooper	1.678	11.09	36.0
Gold	2.214	13.82	27.3
Aluminum	2.650	15.99	11.8
Calcium	3.36	4.80	73.6
Beryllium	3.56	12.62	37.0/59.1
Magnesium	4.39	11.63	19.6/16.6
Rhodium	4.7	6.67	10.3
Sodium	4.77	10.21	30.2
Iridium	5.2	8.54	8.30
Tungsten	5.28	9.71	16.0
Molybdenum	5.34	9.18	12.2
Zinc	5.9	15.66	11.5/8.31
Cobalt	6.2	2.55	21.2/17.6
Nickel	6.93	2.34	14.5
Potassium	7.20	7.94	39.7
Cadmium	7.5	15.55	11.1/9.18
Ruthenium	7.8	7.24	8.82/7.07
Indium	8.8	16.32	5.27/5.05
Osmium	8.9	8.19	8.54/6.19

Table 6.1: List of the twenty most conductive elemental metals sorted with increasing bulk room-temperature resistivity $\rho_{o,rt}$ from [189]. For hexagonal and tetragonal crystal structures (hexagonal closely packed and body-centered tetragonal), the two listed values are for transport perpendicular and parallel to the hexagonal/tetragonal axis.

However, in all conventional noble metals, the high density of states near the Fermi level leads to a rather small relaxation time, which is on the order of tens of fs (see Table 6.1). Furthermore, increased ohmic losses, expressed through the imaginary part of the dielectric permittivity, $\text{Im}(\epsilon)$, further limit the performance of noble metals as PECs. The degree of mobility of charge carriers can be measured in terms of their effective mass, and noble metals typically exhibit a rather large effective mass, approximately equal to the free electron mass [189]. Finally, we note that conventional noble metals have high mass density. Decreasing mass density is highly desirable, for example in space exploration devices and systems.

6.2 Graphene-based van der Waals heterostructures

In contrast to the aforementioned limitations of noble metals, the two-dimensional nature of graphene and its unique linear electronic dispersion yield a much larger relaxation time, due to its lower electronic density of states, as well as an effective

mass approaching zero, both of which enhance the carrier mobility in comparison to metals [184]. Although graphene typically has lower carrier density than Ag and Au, its important features of high mobility and tunable Fermi level, for example through external bias or carrier injection, motivate us to seek for graphene-based heterostructures that may surpass the photonic and plasmonic properties of noble metals [18].

To circumvent the issue of low carrier density in graphene, we investigate a large number of graphene sheets stacked in combination with other two-dimensional materials in layered arrangements, termed van der Waals (vdW) heterostructures [15, 190]. While the electronic and phononic properties of graphene-based heterostructures have been widely investigated, photonic research on these materials has previously focused on graphene layers separated by hundreds of nanometers to micrometers [186, 191–194]. In contrast, here [18] we focus on Angstrom (Å)-scale photonics, where graphene and hexagonal boron nitride (hBN) mono-layers are at their equilibrium separation (3.3–3.4 Å), as shown in Fig. 6.1a; We also investigate doped graphite, where graphene sheets are at their equilibrium separation (3.3–3.4 Å); results for the free-standing graphene case with double the layer spacing are shown throughout for comparison to highlight the effect of interlayer interactions. These interlayer electronic interactions are accounted for using *ab initio* electronic calculations [195] and make this Å-scale regime distinct from conventional photonic crystals and metamaterials. We compare the performance of these heterostructures as reflectors with silver and gold.

6.3 Computational approach and effective mass

For a layered arrangement composed of two-dimensional materials, the dominant in-plane (ordinary) dielectric response is conveniently expressed through the effective medium theory [185] as

$$\epsilon_{\infty//}(\omega) = 1 + \frac{i\sigma(\omega)}{\omega d} \quad (6.1)$$

where d is the spacing between adjacent layers and $\sigma(\omega)$ is the sheet conductance of the mono-layer, $\sigma(\omega) = \sigma_{\text{intra}}(\omega) + \sigma_{\text{direct}}(\omega)$. The first term captures the intraband response of free carriers in the material, and the second term describes the effect of interband transitions and is evaluated using Fermi’s Golden rule. Both terms are computed using previously developed density functional theory (DFT)-based *ab initio* predictions that are outlined in detail in Appendix A.3 [195–197]. We note that, in computing the conductance of 2D materials stacked in vdW heterostructures, the

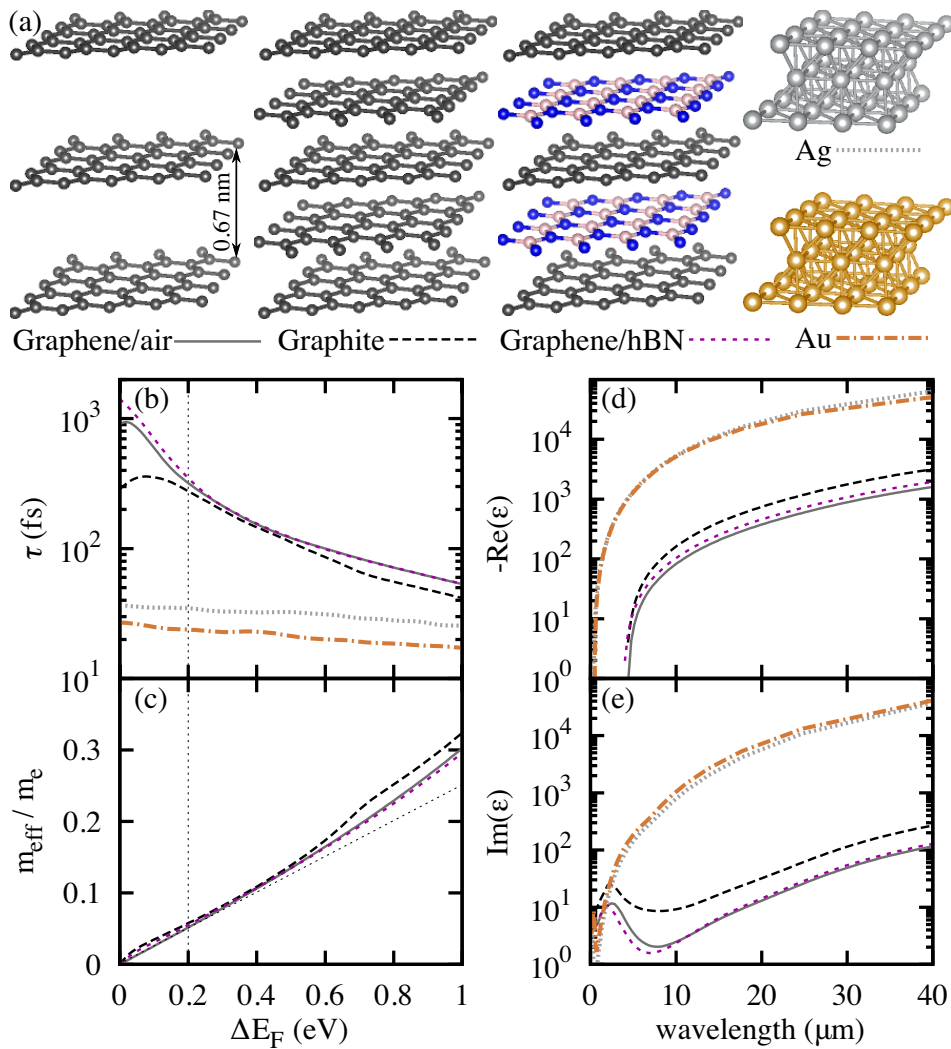


Figure 6.1: (a) Schematics of 2D materials, graphene-based vdW heterostructures and 3D noble metals. (b) Comparison of the average lifetime τ as a function of the Fermi level in 2D materials, heterostructures and the best-case 3D metals: Ag and Au. (c) The effective mass parameter for the stack, as a function of the E_F , connects our analytical understanding of Å-scale metamaterials with *ab initio* calculations. In panels (d) and (e) we show the $\text{Re}(\epsilon)$ and $\text{Im}(\epsilon)$ of graphene-based heterostructures in comparison with the permittivity of Au and Ag. Results for the heterostructures are shown at 0.2 eV Fermi level, as this is the doping regime where they reflect maximally for wavelengths above 10 μm .

effects of the environment and the electronic interactions between adjacent layers are fully accounted for.

The dielectric permittivities of the vdW heterostructures examined here are presented in Figs. 6.1d, e in the limit of infinite number of layers, and compared with the response of Ag and Au. We point out that results pertaining to Ag and Au are also derived *ab initio* [196, 197] assuming perfect crystalline metals. At low frequencies, intraband transitions dominate and the response of the heterostructures resembles a typical Drude material. In this limit of low frequencies we are, thus, able to approximate the dielectric response of the vdW heterostructures with the Drude model via

$$\epsilon_{\text{Drude}} = \epsilon = 1 - \frac{\omega_{\text{p}}^2}{\omega^2 + i\omega\gamma_{\text{D}}} \quad (6.2)$$

where $\omega_{\text{p}}^2 = n_{3\text{D}}e^2/\epsilon_0 m_{\text{eff,D}}$, where ϵ_0 is the dielectric permittivity of free space, $\gamma_{\text{D}}^{-1} = \tau_{\text{D}}$ is the Drude carrier relaxation time and $n_{3\text{D}}$ is the three-dimensional carrier density of the heterostructure. $m_{\text{eff,D}}$ is the Drude effective mass that we seek to estimate.

Let us assume an arrangement of N_{g} graphene mono-layers separated by distance d . The in-plane two-dimensional carrier density of graphene is given by $n_{2\text{D}} = E_{\text{F}}^2/(\pi\hbar^2 v_{\text{F}}^2)$ [193]. The three-dimensional carrier density of the heterostructure is then given by

$$n_{3\text{D}} = n_{2\text{D}} \frac{N_{\text{g}}}{(N_{\text{g}} - 1)d} = \frac{E_{\text{F}}^2}{\pi\hbar^2 v_{\text{F}}^2} \frac{N_{\text{g}}}{(N_{\text{g}} - 1)d} \quad (6.3)$$

In the mid-far IR, where intraband transitions dominate, the conductance of graphene can be approximated with the analytical expression [185, 193]

$$\sigma = \sigma_{\text{intra}} = \frac{ie^2 E_{\text{F}}}{\pi\hbar^2(\omega + i\gamma_{\text{g}})} \quad (6.4)$$

where $\gamma_{\text{g}}^{-1} = \tau_{\text{g}}$ is the *ab initio* computed carrier relaxation time in graphene [195], the computation of which is discussed in Appendix A.3. By equating Eqs. (6.1) and (6.2) using the analysis above, we obtain

$$m_{\text{eff,D}} = \frac{N_{\text{G}}}{N_{\text{G}} - 1} \frac{E_{\text{F}}}{v_{\text{F}}^2} \quad (6.5)$$

and

$$\tau_{\text{D}} = \tau_{\text{g}} \quad (6.6)$$

Eqs. (6.5), (6.6) are useful in allowing us to build intuition about the response of the vdW heterostructures as effective media with an effective mass that, in the large number of layers, reduces to $m_{\text{eff}} = \frac{E_F}{v_F^2}$. Furthermore, unsurprisingly, from Eq. (6.6) we derive that in the in-plane direction, in other words, for electromagnetic fields incident normal to the layers, the carrier relaxation time of the three-dimensional heterostructures is equal to the scattering time of the mono-layer itself.

In Figs. 6.1b, c we respectively show the parameters τ and m_{eff} of the graphene-based heterostructures as a function of the change in Fermi level ΔE_F from the neutral value (Dirac point). We highlight the extremely large $\tau \sim 1$ ps for undoped graphene in air, which drops to ~ 200 fs in graphite due to interlayer interactions. In contrast, encapsulating graphene with boron nitride layers increases the undoped τ even further to ~ 2 ps, despite having the same spacing between adjacent mono-layers as in graphite. With increasing E_F and carrier density, τ drops rapidly. This is a consequence of increasing the phase-space for electron-phonon scattering, which in turn is due to increased electronic density of states near the Fermi level, $g(E_F)$. For comparison, we also show the *emphab* initio computed relaxation times for noble metals, gold and silver, which are much smaller (~ 30 and 40 fs respectively) and mostly insensitive to E_F since $g(E_F)$ depends weakly on E_F . We further note that E_F cannot be changed easily for these metals in experiments.

Regarding the effective mass for the vdW heterostructures, m_{eff} increases linearly in the ideal case of perfect linear dispersion, with slight deviations due to band structure effects (Fig. 6.1c). We highlight that m_{eff} for the vdW heterostructures is consistently smaller than $m_{\text{eff}} \approx m_e$ of metals. Concluding, the graphene-based heterostructures have a much higher τ and a lower m_{eff} . These properties in graphene-based heterostructures compared to noble metals motivate us to investigate their optical properties.

Although, from Figs. 6.1b, c, the maximum electronic scattering time and minimum effective mass are seen at the charge neutrality point ($\Delta E_F \approx 0$ eV), graphene at 0 eV does not contain enough carriers to produce a strong metallic response. We find that $\Delta E_F \approx 0.2$ eV is the optimum doping level which provides the best tradeoff between increasing carrier density and correspondingly decreasing scattering time. Figs. 6.1d, e compare the real and imaginary parts of the in-plane permittivity of the graphene heterostructures with those of noble metals at this carrier density, in the infinite number of layers limit. The real parts of the permittivities of the heterostructures in the IR are smaller than that of the noble metals by typically two orders of magnitude. However, the ratio of imaginary to real parts is smaller by an extra factor of 2 – 3. This smaller imaginary-to-real ratio compensates for

the lower plasma frequency and makes the graphene-based heterostructures better reflectors in the IR due to reduced losses, as we discuss below. We point out here that results pertaining to Ag and Au are also derived *ab initio*, assuming perfect crystalline metals.

To realistically compare the utility of graphene vdW heterostructures as reflectors, we transition from the infinite stacks of considered above to stacks of finite thickness. To do this, we perform electromagnetic transfer matrix calculations for layered media [1]. Contrary to materials of finite thickness, we modify Maxwell's boundary conditions to account for a non-vanishing surface current density, arising from the two-dimensional sheet conductance of the mono-layers, as discussed in Section 5.5 [186].

6.4 Shinier than gold and silver!

In Fig. 6.2 we show the reflectance of the vdW materials for the bulk (semi-infinite) limit, as well as for finite stacks of 1000, 500, and 250 sheets and compare with the Ag/Au slabs of the same mass per area, which is the relevant metric for ultraviolet reflectors. The reflectance of the vdW heterostructures surpasses that of noble metals above a critical wavelength, $\lambda > 10 \mu\text{m}$ for the semi-infinite case, $\lambda > 15 \mu\text{m}$ for 1000 layers, $\lambda > 20 \mu\text{m}$ for 500 layers, and $\lambda > 20 \mu\text{m}$ for 250 layers.

We note that silver and gold slabs of mass densities $19 \mu\text{g}/\text{cm}^2$ (that of 250 sheets) correspond to thicknesses of 18.1 nm and 9.85 nm, respectively. Despite the high-fidelity of state-of-the-art thin-film deposition systems, deposition of such ultra-thin silver and gold films is still known to lead to island formation and grain-boundary inhomogeneities that would further lessen the reflectance in realistic experimental conditions. Fabrication of graphene-based structures entails challenges as well, for example, issues with adhesion, buckling, and uniaxial tension, particularly when integrated with traditional dielectric materials [198]. However, recent experimental advances in assembly of vdW graphene heterostructures provide a pathway to uniform, large-scale components with potential for ultralight, long-IR mirrors [190, 199]. Furthermore, recent work has proposed Li-intercalated graphene layers (doped graphite-Fig. 6.1) as a potential system to realize the structures discussed here [200, 201]. Finally we emphasize that the high reflectivity of graphene-based vdW heterostructures discussed here critically requires sufficient free carriers (for which we selected $\Delta E_F \approx 0.2 \text{ eV}$). In contrast, undoped graphite with few free carriers exhibits a much lower reflectance of $\sim 75\%$ [202].

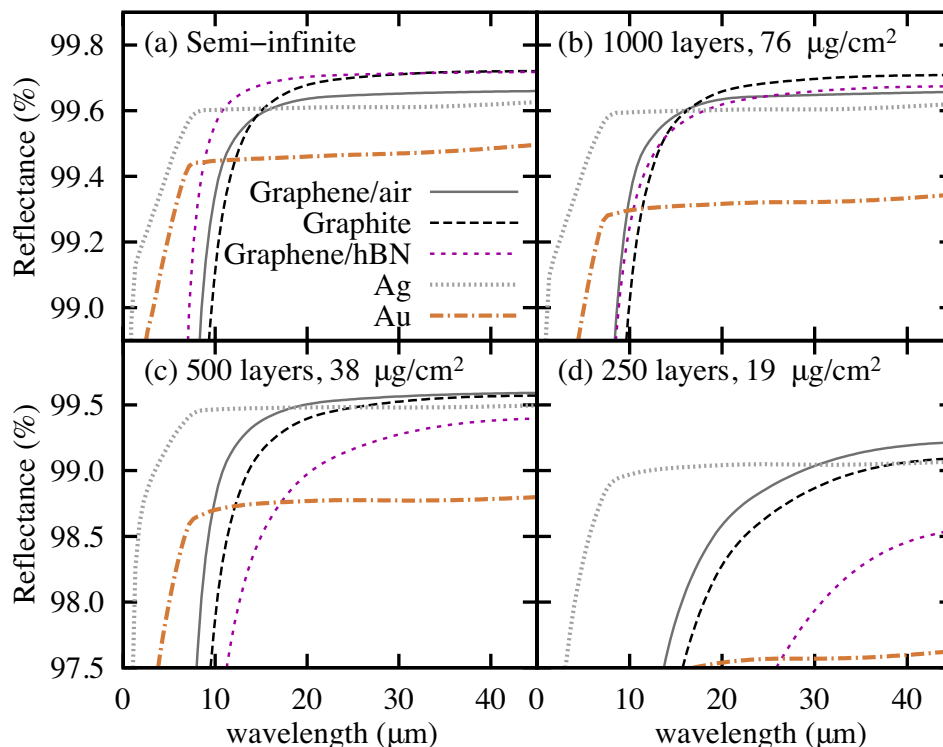


Figure 6.2: Normal incidence reflectance of graphene-air metamaterial, doped graphite, graphene-hBN heterostructure (all doped at 0.2 eV) and comparison to Ag and Au. The reflectance of graphene-based heterostructures surpasses conventional noble metals in the mid-IR, above 10 μm . Panels correspond to the same (per area) mass densities: (a): bulk, (b): 1000 layers, corresponding to 72.4 nm of Ag and 39.4 nm of Au. (c): 500 layers, corresponding to 36.2 nm of Ag and 19.7 nm of Au. (d): 250 layers, corresponding to 18.1 nm of Ag and 9.85 nm of Au. Note that the silver and gold values are based on *ab initio* results for perfect conditions and therefore are the theoretical limit for these metals. Experimentally realized metallic thin films will compromise the magnitude of reflectance.

6.5 Loss tangent and quality factors

In discussing the permittivities shown in Figs. 6.1d, e above, we noted that the ratio of imaginary to real permittivity (i.e. the loss tangent $\tan\delta$) was smaller in the vdW heterostructures than in noble metals, which resulted in lower losses. A metric that directly illustrates the superior performance of graphene heterostructures as plasmonic systems compared to noble metals is the material quality factor $Q = 1/\tan\delta = \text{Re}(\epsilon)/\text{Im}(\epsilon)$ and its inverse, the material loss tangent, shown in Fig. 6.3a. For the chosen doping level of 0.2 eV and for wavelengths $\lambda > 15 \mu\text{m}$, the vdW heterostructures are expected to show an order of magnitude higher performance as electromagnetic materials compared to noble metals, thereby making these materials

particularly suited for mid-long-wave IR applications. We note that the peaks in Fig. 6.3a correspond to the respective plasma frequency for each material system, for which $\text{Re}(\epsilon) \rightarrow 0$; vdW heterostructures have much lower carrier density compared to noble metals, hence their Q-factor peak is located approximately at $\lambda \approx 10 \mu\text{m}$. By contrast, noble metals that are highly doped have a plasma frequency in the UV-visible spectrum, with Q-factor peaks in this regime (below $\lambda \approx 1 \mu\text{m}$).

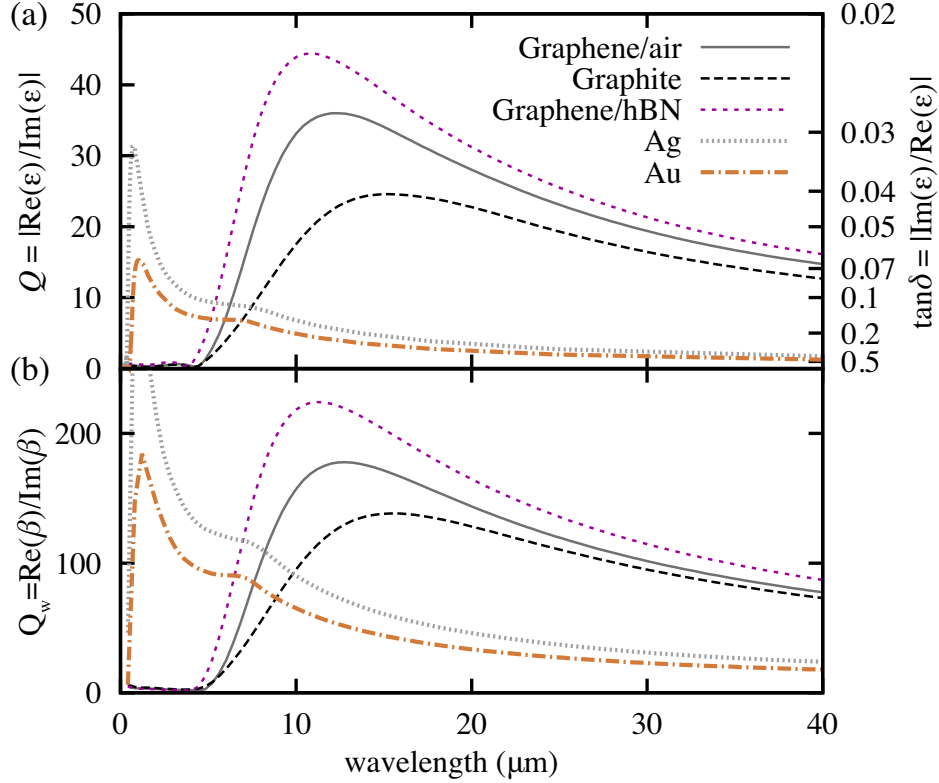


Figure 6.3: (a) Material quality factor $Q = \text{Re}(\epsilon)/\text{Im}(\epsilon)$ and loss tangent ($\tan \delta = Q^{-1}$) and (b) the plasmonic modal quality factor $Q_w = \text{Re}(\beta)/\text{Im}(\beta)$ for the symmetric mode in a metal/dielectric/metal waveguide, where the ‘metal’ is either a conventional noble metal or a vdW heterostructure and the dielectric is $0.1 \mu\text{m}$ of air.

6.6 Plasmonic propagation in vdW heterostructures

Finally, we investigate the performance of these materials in an alternating metal/dielectric/metal waveguide geometry. Such structures have been widely investigated in the visible part of the spectrum using plasmonic metals, such as Ag and Au [8, 92, 135]. On the basis of our results, we envision replacing the metal with a vdW heterostructure to improve performance for mid-IR applications. For simplicity, we take the dielectric to be $0.1 \mu\text{m}$ of air. We use our predicted dielectric functions in the formalism from

Alu *et al.* in [203] to evaluate the plasmonic in-plane wavenumber (β). Fig. 6.3b compares the plasmonic quality factor $Q_W = \text{Re}(\beta)/\text{Im}(\beta)$ for the symmetric mode between vdW heterostructures and noble metals, while in Fig. 6.4 we explicitly compare the corresponding dispersion relations. The plasmonic quality factor Q_W estimates the propagation length in number of mode-wavelengths, which shows a 3 – 5-fold improvement for the vdW heterostructures compared to noble metals for $\lambda > 15 \mu\text{m}$. In absolute terms, compared to propagation distances of 50 – 60 mode-wavelengths with use of Ag or Au in the mid-IR, a graphene/hBN- based waveguide supports propagation distances that may exceed 200 mode-wavelengths.

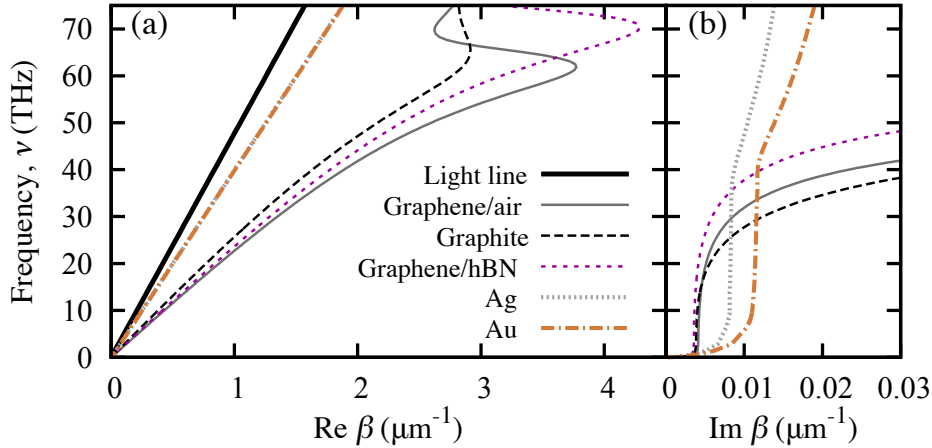


Figure 6.4: Comparison of dispersion relations for the symmetric mode in the metal/dielectric/metal waveguide considered in Fig. 6.3 (b). The larger $\text{Re}(\beta)$ with vdW heterostructures corresponds to smaller effective wavelength and improved mode confinement. The smaller $\text{Im}(\beta)$ for $\nu < 25$ THz yields a two-fold increase in the decay length of the mode.

Fig. 6.4 shows the dispersion relation of the symmetric waveguide mode, which asymptotically approaches the surface plasma frequency ω_{sp} [8, 92, 135], a typical trend for any plasmonic mode. The modal wavenumber ($\text{Re}(\beta)$) reaches a maximum at ω_{sp} and then returns towards the light line as losses increase and the mode becomes leaky. This feature is observable in the mid-IR frequency range for all the vdW heterostructures, with slightly different resonance frequencies ranging from 60 to 70 THz, while corresponding features for the noble metal waveguides will appear above 500 THz in the UV-visible regime as discussed above. The larger in-plane wavenumbers ($\text{Re}(\beta)$) of the modes in the vdW heterostructure-based waveguide lead to shorter in-plane effective wavelengths and correspondingly higher mode confinement in the directions perpendicular to the waveguide's interfaces. Furthermore, the smaller imaginary parts ($\text{Im}(\beta)$) illustrate larger propagation distances, as dis-

cussed in Fig. 6.3b.

6.7 Conclusion

Using a combination of *ab initio* DFT methods and optical transfer matrix calculations we showed that the long electron relaxation times in graphene-based vdW heterostructures lead to improved optical properties compared to noble metals, in the mid-long-IR regime. In particular, we predicted an order of magnitude improvement in terms of their material performance as plasmonic metals. Furthermore, we showed that graphene-based vdW heterostructures can surpass the reflectance limit of Ag and Au [18].

This suggests the possibility of replacing current noble metal components in optoelectronic devices with vdW heterostructures, which can also be tuned in real time, for example via external bias. Hence, our results hold promise for improved material performance in active waveguiding systems, Salisbury screens for perfect absorption, and engineering Purcell enhancements, among others. Furthermore, we highlight that vdW heterostructures exhibit substantially reduced mass density compared to noble metals, which constitutes them particularly relevant for aerospace applications, where mass density becomes an important figure of merit. The increased carrier density in graphene-based vdW heterostructures required for unlocking their low-loss plasmonic response in the mid-IR may be achieved by gating alternating graphene layers separated by hBN. The doping of graphite, for example with Li intercalation, is also an option for experimental realization of the concept proposed here [200, 201].

SUMMARY & OUTLOOK

“The science of today is the technology of tomorrow.”

Edward Teller

7.1 Summary

Research in artificial matter and light-matter interactions with metamaterials has experienced rapid advancement within the last twenty years, mainly due to technological progress in nanofabrication. Three-dimensional laser lithography and electron beams allow one to write structures with precision in the nanometer scale. Developed metamaterials have dramatically expanded the range of achievable electromagnetic properties and extraordinary values of dielectric permittivity and magnetic permeability have been reported, inaccessible with natural materials.

As miniaturization requirements increase, however, the structural complexity of metamaterials must reduce. For this reason, within the last decade, research in photonics has revisited an older problem; that of light propagation in planar, multi-layer and unpatterned systems. It is noteworthy that phenomena initially thought to be achievable only with complex three-dimensional arrangements are also supported, among other unprecedented effects, in planar metallodielectric multilayer (hyperbolic) metamaterials, which is the subject of this thesis.

We started our investigation by developing an inverse problem solver; a parameter retrieval approach that computes the macroscopic effective properties of any uniaxial metamaterial, and we studied planar metallodielectric multilayers; see Chapter 2 [47]. The purpose of introducing macroscopic effective parameters for metamaterials is to simplify the computation of wave propagation phenomena and to build intuition for their principle of operation. Contrary to the long-standing perception that in planar systems $\mu = 1$, we found and experimentally confirmed in Chapter 3 that such systems support magnetic dipole moments and exhibit artificial magnetic properties. We explicitly computed and verified experimentally extraordinary values of magnetic permeability ranging from positive, zero to negative values. These findings simplify the ways we can harness optical artificial magnetism, using simple thin-film deposition techniques without any lithography [12].

Until recently, most light-matter interactions were manipulated using the dielectric properties of matter, rather than its magnetic properties that vanish at frequencies above the THz range. An important example is the surface plasmon polariton, a surface wave that gave birth to the field of plasmonics, which occurs naturally only for $\epsilon < 0$ and for transverse magnetic polarization, due to lack of magnetic properties in natural substances. We showed in Chapter 3 that, using artificially magnetic multilayer metallodielectric metamaterials, *magnetic* plasmons can propagate simultaneously with typical SPPs, generalizing their properties for unpolarized light.

We further extended and simplified these results by identifying material systems where one obtains omnipolarization surface waves using high-permittivity materials, which are the best alternative to magnetic media that do not occur at high frequencies, see Chapter 4. We investigated polar dielectrics near their phonon energies at infrared frequencies and transition-metal dichalcogenides near their excitonic resonances at visible frequencies, in systems that support transverse electric polarized waves simultaneously with their TE counterparts (i.e. hybrid plasmonic waves).

Motivated by the possibility of creating actively tunable material systems, the response of which can be tuned dynamically, we transitioned in Chapter 5 to study active materials as components of planar metallodielectric metamaterials. We showed that use of transparent conductive oxides in traditional field-effect metal/oxide/semiconductor geometries can yield a tunable hyperbolic response at visible-near IR frequencies [48]. Similar findings were reported with the use of graphene, a two-dimensional semimetal that, when gated, alters its chemical potential and hence its optical response. As a component of a planar heterostructure, graphene can serve as a tunable element, via external bias, for obtaining tunable metamaterial functionalities for frequencies ranging from the near-IR up to the microwave regime.

In Chapter 6 we studied heterostructures composed of purely two-dimensional materials. Motivated by the Dirac dispersion of electronic states in graphene that gives practically zero effective mass, and by its very large electronic relaxation times compared to noble metals, we sought for graphene-based van der Waals heterostructures that act as supermetals [18]. By comparing these material systems with noble metals, namely silver and gold, we obtain a 3- to 5-fold improvement in material quality factors that may hold promise for future optical components with reflectivity that surpasses the Ag and Au limit. The additional advantage of an order of magnitude lower mass density of van der Waals heterostructures compared to noble metals, these arrangements can be particularly useful for space exploration applications

and systems.

7.2 Outlook

Therefore, having developed knowledge in the following areas: (i) artificial magnetism in one-dimension, using planar structures, (ii) omnipolarization surface waves, (iii) actively tunable response via external bias at visible and IR frequencies, and (iv) modeling van der Waals heterostructures and inducing perfect electrical conductor response, we proceed by envisioning areas in which these ideas can be applied and expanded. We further seek and comment on relevant applications where the discussed concepts may be employed.

All-van der Waals perfect absorbers

Nanophotonic devices that emit radiation efficiently and selectively across the IR range (700 nm-1 mm) hold promise for next generation energy technologies. Particularly, they allow electricity-free radiative cooling [204], the temperature reduction of hot objects passively, through emission of electromagnetic radiation. This functionality is key for reducing energy consumption, for example lowering the required cooling load in air-conditioned buildings, and consequently decreasing their sizable negative impact on energy use. Furthermore, energy-harvesting devices, e.g. solar cells, suffer from compromised performance when over-heated. Passive control of their cooling will lower their power consumption and allow robust operation.

Kirchhoff's law states that the far-field emission of a body equals its absorption. Achieving perfect absorption in nanophotonics typically employs an absorbing multilayer system composed of different materials, terminated with a back reflector able to redirect the otherwise-escaping radiation back into the structure [5]; see Fig. 7.1a. Current state-of-the-art radiative cooling approaches use conventional materials with individual layer thicknesses ranging between 13-80 nm [204]. For the back-side reflector, typically silver and gold are utilized due to their PEC-like response.

Based on our previous results on ultra-light perfect reflectors with van der Waals graphene-based heterostructures (Chapter 6 and [18]), we envisage here all-van der Waals-based perfect absorbers. Particularly, graphene-based heterostructures (including doped graphite and graphene/hexagonal boron nitride alternating monolayers) can comprise the back reflector with performance that surpasses Ag and Au (see Fig. 6.2). Furthermore, previous results on other two-dimensional materials, for example black phosphorus, transition-metal dichalcogenides (molybdenum

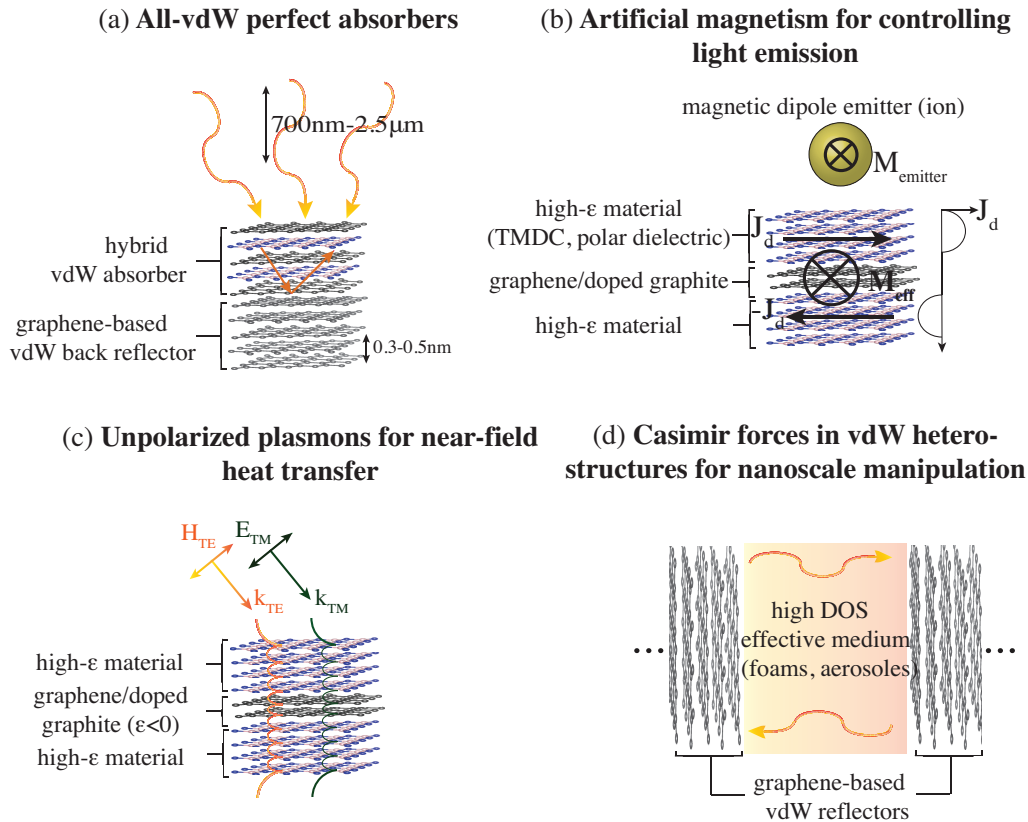


Figure 7.1: (a) All-van der Waals perfect absorbers, (b) Artificial magnetism for controlling light emission, (c) Unpolarized plasmonics for near-field heat transfer, (d) Casimir forces in van der Waals heterostructures.

and tungsten) [205] and others, suggest that the absorbing layer can also be completely replaced by two-dimensional materials, for realizing all-van der Waals-based perfect absorbers. Replacing conventional absorbing materials with van der Waals heterostructures for all of the structure's components will dramatically decrease the dimensions of perfect absorbing schemes down to the Angstrom scale, therefore allowing maximum light-matter interaction in minimum volume. Additionally, van der Waals heterostructures have significantly reduced mass density compared to conventional metals and dielectrics, therefore yielding ultra-light photonic devices. See Fig. 7.1a.

Artificial magnetism for controlling light emission

Light emission from solid-state quantum emitters impacts a variety of applications ranging from imaging fluorescence to performing simple quantum operations with light-emitting particles. Controlling the environment of a quantum emitter allows

engineering its emission properties, such as directionality, lifetime and polarization. Although light emission occurs due to both electric and magnetic dipoles, most applications pertaining to luminescence and emission control are limited to electric dipole transitions in ionic materials. This arises from the asymmetry in naturally occurring substances that exhibit a wide range of dielectric properties, expressed through the values of the permittivity values, ϵ , while at frequencies above the THz range the magnetic permeability of most materials is strictly unity, $\mu = 1$ (see Chapter 3). Therefore, strong interactions between matter and emitted electric fields can be achieved, whereas it is very challenging to observe strong optical interactions with magnetic dipole emitters using conventional materials.

As discussed in Chapter 3, the absence of high-frequency natural magnetism has motivated research in artificially magnetic metamaterials. Split-ring resonators and fishnet structures are currently the most widely reported magnetic elements at frequencies beyond THz. However, the structural complexity of such motifs constitutes them challenging to realize experimentally at IR and optical frequencies where light emission becomes relevant, requiring multiple lithographic steps with nanoscale precision. By contrast, our results discussed in Chapter 3 suggest that artificial magnetic response can be induced in planar multilayer arrangements, by utilizing dielectric layers that support strong loop-like displacement currents and, therefore, magnetic dipole moments [12].

We envision probing and enhancing light emission not only with electric dipoles but also by utilizing the magnetic nature of light in experimentally reasonable, planar geometries. Particularly, by engineering artificial magnetic dipoles to occur at frequencies where natural optical magnetic dipole transitions occur, for example in lanthanide ions such as trivalent erbium or europium [206], one can engineer the Purcell factor of magnetic dipole moments [207]. Furthermore, extending the concept of artificial magnetism to two-dimensional materials and van der Waals heterostructures, one can envisage ultra-thin van der Waals heterostructures for controlling light emission from electric and magnetic dipole emitters simultaneously, see Fig. 7.1b. Specifically, as discussed in Chapters 3 and 4, the key-requirement for inducing magnetic dipole moments in planar systems is very large permittivity ϵ . At visible and IR frequencies there exists a plethora of such two-dimensional materials, for example transition-metal dichalcogenides and polar dielectrics (c.f. hBN) near their excitonic and phonon resonances, respectively. Utilizing such ultra-thin planar heterostructures for emission control can also be advantageous as the emitter (ion)-heterostructure interaction occurs in a much smaller scale compared to bulky conventional photonic multilayers, yielding improved emission control.

Unpolarized plasmonics for near-field heat transfer

A broad range of applications in medical technology, chemistry, energy, lasers, and luminescence have advanced with the rise of plasmonics, which are surface-confined electromagnetic modes at the interface between a metallic and a dielectric medium (see Chapters 3, 4). Despite their well-known potential in achieving an extremely high degree of confinement [92], plasmonics are limited to negative dielectric permittivity ($\epsilon < 0$) materials and to electromagnetic fields polarized with an electric field normal to the direction of propagation, i.e. transverse magnetic fields. The counterpart of a plasmon for transverse electric polarization, i.e. a magnetic plasmon, has not been reported due to the absence of naturally occurring materials with negative magnetic permeability ($\mu < 0$). Combining transverse magnetic and transverse electric surface waves in ultra-thin heterostructures will increase the impact and relevance of plasmonics for technology. An important application is thermal control, and particularly near-field heat transfer, a process enabling exchanges rates beyond the Stefan-Boltzmann limit between objects separated by submicron distances, promising drastically improved throughput in thermophotovoltaics [208]. Heat transfer occurs via photon coupling between objects of different temperatures, through plasmonic surface waves. The polarization dependence of surface plasmons reduces their ability to tunnel photons to 50%, with the other half of the provided thermal energy being wasted.

Utilizing our results in Chapter 3, suggesting that μ can be negative in metallodielectric heterostructures, and from our results in Chapter 4 where we explicitly show transverse electric surface waves in materials with high- ϵ , we are motivated to imagine applications of omnidirectional surface waves in near-field heat transfer for energy applications. The relevant wavelength regime for solar applications is from the visible spectrum to approximately $3 \mu\text{m}$. In this regime, there exist a large canvas of naturally occurring materials with high- ϵ , for example polar dielectric materials near their phonon energies that lie at IR frequencies. In the world of two-dimensional materials, there are similar opportunities for magnetic surface waves, using transition-metal dichalcogenides, with excitonic resonances that lie at visible frequencies, and two-dimensional polar dielectric media, for example hexagonal boron nitride. Combining such materials with graphene [208], which supports transverse magnetic polarized plasmons, we envisage phase-matched omnipolarization propagation of surface waves in van der Waals heterostructures. Achieving excitation and detection of such waves can improve near-field heat transfer rates and high-temperature (600-1200K) solid-state energy conversion, see Fig. 7.1c.

Casimir forces in graphene-based heterostructures for nanoscale mechanical manipulation

Mechanical manipulation of nanoscale objects is key for nanomechanical devices in sensing and biomedicine. Mechanical control at the single-atom-level can also transform state-of-the-art fabrication techniques in two-dimensional materials to a new era; particularly, although two-dimensional materials exfoliation and transferring have dramatically advanced, a challenge that impedes their integration in real devices is graphene buckling, the phenomenon of a mono-layer of graphene experiencing uniaxial tension, leading to ripples in mono-layers that cannot remain truly flat [198].

Inspired by the results of Chapter 6, and particularly the fact that graphene-based van der Waals heterostructures perform as ultra-reflective metals in the mid-IR, we envision their use in enhancing Casimir interactions. Practical issues in materials processing and nanofabrication, c.f. buckling, adhesion and friction, may be resolved by actively controlling and mechanically manipulating one-atom-thick two-dimensional materials using Casimir forces. The Casimir force between two parallel uncharged conductors becomes dominant in the nanoscale, if the conductors exhibit a perfect electrical conductor response. Until now, noble metals have been the most extensively investigated materials for Casimir effects. By contrast, the Casimir energy between two graphene sheets is small and only measurable at cryogenic temperatures [209]. However, conductors are heavy, which constitutes them unsuitable for pursuing mechanical manipulation in the nanoscale, in contrast to graphene-based heterostructures (including graphite) that have an order of magnitude lower mass density. Additionally, contrary to a single graphene sheets, stacked arrangements of graphene mono-layers are ultra-reflective as we discussed in Chapter 6. This constitutes them suitable candidates for Casimir interactions in the nanoscale. We imagine configurations of parallel graphene-based heterostructures for controlling their mutual Casimir interaction.

Apart from the material quality of the conductors, the magnitude of the Casimir energy can be further controlled by engineering the electromagnetic environment between the two conductors. Namely, the Casimir energy scales with the density of optical states of the intermediate medium, which, in turn, scales with the refractive index. One may imagine using sparse arrays of high-refractive index foams or aerosol-based effective media inside the cavity, for enhancing the Casimir interaction as a result of (i) decreased weight load and (ii) increased number of available optical modes, respectively, see Fig. 7.1d.

The aforementioned concepts and ideas are merely a small subset of the opportunities arising from our ability to design materials on-demand. It is fascinating that today it is possible to selectively position two-dimensional mono-layers in configurations of stratified media with precision in the Angstrom-scale. This opens routes for controlling the interaction between light and matter at the single-atom level, where electronic and electromagnetic degrees of freedom compete. Complementary to the classical notion of a metamaterial, the properties of which are determined by its geometry, now it is possible to tailor light-matter interactions by simultaneously engineering geometry (layer sequencing) as well as fundamental material properties (electronic interactions between layers). The field of metamaterials is at a transition point where novel physical phenomena are rapidly adopted into practical devices for applications, and exciting times are ahead for a diverse array of technical disciplines including mathematicians, physicists, material scientists, chemists, engineers, and technologists.

BIBLIOGRAPHY

- [1] Pochi Yeh. *Optical Waves in Layered Media*. 2nd edition. Wiley Series in Pure and Applied Optics, (2005). ISBN: 9780471731924.
- [2] L.D. Landau, E.M. Lifshitz, and L. P. Pitaevskii. *Electrodynamics of Continuous Media*. 2nd edition. Vol. 8. Course of Theoretical Physics. Pergamon, (1984). ISBN: 9780080302751.
- [3] Claire M. Watts, Xianliang Liu, and Willie J. Padilla. “Metamaterial Electromagnetic Wave Absorbers”. *Advanced Materials* 24 (2012), OP98–OP120.
- [4] Mikhail Y. Shalaginov et al. “Enhancement of single-photon emission from nitrogen-vacancy centers with TiN/(Al,Sc)N hyperbolic metamaterial”. *Laser Photonics Reviews* 9 (2015), pp. 120–127.
- [5] Min Seok Jang et al. “Tunable large resonant absorption in a midinfrared graphene Salisbury screen”. *Phys. Rev. B* 90 (2014), p. 165409.
- [6] V. G. Veselago. “The Electrodynamics of Substances with Simultaneously Negative Values of ϵ and μ ”. *Sov. Phys. Usp.* 10 (1968), pp. 509–514.
- [7] J. B. Pendry. “Negative Refraction Makes a Perfect Lens”. *Phys. Rev. Lett.* 85 (2000), pp. 3966–3969.
- [8] Henri J. Lezec, Jennifer A. Dionne, and Harry A. Atwater. “Negative Refraction at Visible Frequencies”. *Science* 316 (2007), pp. 430–432.
- [9] Dylan Lu and Zhaowei Liu. “Hyperlenses and metalenses for far-field super-resolution imaging”. *Nature Communications* 3 (2012).
- [10] Hyesog Lee et al. “Development of optical hyperlens for imaging below the diffraction limit”. *Opt. Express* 15 (2007), pp. 15886–15891.
- [11] Francesco Monticone and Andrea Alu. “The quest for optical magnetism: from split-ring resonators to plasmonic nanoparticles and nano-clusters”. *J. Mater. Chem. C* 2 (2014), pp. 9059–9072.
- [12] Georgia T. Papadakis et al. “Optical magnetism in planar metamaterial heterostructures”. *Nature Communications* 9 (2018), p. 296.
- [13] D. R. Smith et al. “Composite Medium with Simultaneously Negative Permeability and Permittivity”. *Phys. Rev. Lett.* 84 (2000), pp. 4184–4187.
- [14] J. B. Pendry et al. “Magnetism from conductors and enhanced nonlinear phenomena”. *IEEE Transactions on Microwave Theory and Techniques* 47 (1999), pp. 2075–2084.

- [15] S. J. Haigh et al. “Cross-sectional imaging of individual layers and buried interfaces of graphene-based heterostructures and superlattices”. *Nature Materials* 11 (2012), p. 764.
- [16] Johannes Kaschke and Martin Wegener. “Gold triple-helix mid-infrared metamaterial by STED-inspired laser lithography”. *Opt. Lett.* 40 (2015), pp. 3986–3989.
- [17] D. R. Smith et al. “Composite Medium with Simultaneously Negative Permeability and Permittivity”. *Phys. Rev. Lett.* 84 (2000), pp. 4184–4187.
- [18] Georgia T. Papadakis et al. “Ultralight Angstrom-Scale Optimal Optical Reflectors”. *ACS Photonics* 5 (2018), pp. 384–389.
- [19] J. B. Pendry et al. “Extremely Low Frequency Plasmons in Metallic Mesostructures”. *Phys. Rev. Lett.* 76 (1996), pp. 4773–4776.
- [20] Andrey B. Evlyukhin et al. “Demonstration of Magnetic Dipole Resonances of Dielectric Nanospheres in the Visible Region”. *Nano Letters* 12 (2012), pp. 3749–3755.
- [21] Arseniy I. Kuznetsov et al. “Magnetic light”. *Scientific Reports* 2 (2012), p. 492.
- [22] Sergey S. Kruk et al. “Magnetic hyperbolic optical metamaterials”. *Nature Communications* 7 (2016), p. 11329.
- [23] M. Kafesaki et al. “Left-handed metamaterials: The fishnet structure and its variations”. *Phys. Rev. B* 75 (2007), p. 235114.
- [24] Gunnar Dolling et al. “Low-loss negative-index metamaterial at telecommunication wavelengths”. *Opt. Lett.* 31 (2006), pp. 1800–1802.
- [25] M. S. Mirmoosa, S. Yu. Kosulnikov, and C. R. Simovski. “Magnetic hyperbolic metamaterial of high-index nanowires”. *Phys. Rev. B* 94 (2016), p. 8.
- [26] Pochi Yeh, Amnon Yariv, and Chi-Shain Hong. “Electromagnetic propagation in periodic stratified media. I. General theory”. *J. Opt. Soc. Am.* 67 (1977), pp. 423–438.
- [27] P.St.J Russell, S Tredwell, and P.J Roberts. “Full photonic bandgaps and spontaneous emission control in 1D multilayer dielectric structures”. *Optics Communications* 160 (1999), pp. 66 –71.
- [28] Jorge A. Gaspar-Armenta and Francisco Villa. “Band-structure properties of one-dimensional photonic crystals under the formalism of equivalent systems”. *J. Opt. Soc. Am. B* 21 (2004), pp. 405–412.
- [29] Joshua N. Winn et al. “Omnidirectional reflection from a one-dimensional photonic crystal”. *Opt. Lett.* 23 (1998), pp. 1573–1575.

- [30] C. Kittel. *Introduction to Solid State Physics*. Wiley, (2004). ISBN: 9780471415268.
- [31] Alexander Poddubny et al. “Hyperbolic metamaterials”. *Nat Photon.* 7 (2013), pp. 948–957.
- [32] Vladimir P. Drachev, Viktor A. Podolskiy, and Alexander V. Kildishev. “Hyperbolic metamaterials: new physics behind a classical problem”. *Opt. Express* 21 (2013), pp. 15048–15064.
- [33] Yu Guo et al. “Applications of Hyperbolic Metamaterial Substrates”. *Advances in OptoElectronics* 2012 (2012), p. 452502.
- [34] I. V. Lindell et al. “BW media—media with negative parameters, capable of supporting backward waves”. *Microwave and Optical Technology Letters* 31 (2001), pp. 129–133.
- [35] D. R. Smith and D. Schurig. “Electromagnetic Wave Propagation in Media with Indefinite Permittivity and Permeability Tensors”. *Phys. Rev. Lett.* 90 (2003), p. 077405.
- [36] Xiao Lin et al. “All-angle negative refraction of highly squeezed plasmon and phonon polaritons in graphene–boron nitride heterostructures”. *Proceedings of the National Academy of Sciences* 114 (2017), pp. 6717–6721.
- [37] Ting Xu et al. “All-angle negative refraction and active flat lensing of ultraviolet light”. *Nature* 497 (2013), p. 470.
- [38] Zhaowei Liu et al. “Far-Field Optical Hyperlens Magnifying Sub-Diffraction-Limited Objects”. *Science* 315 (2007), pp. 1686–1686.
- [39] Anthony J. Hoffman et al. “Negative refraction in semiconductor metamaterials”. *Nature Materials* 6 (2007), p. 496.
- [40] Alexander A. High et al. “Visible-frequency hyperbolic metasurface”. *Nature* 522 (2015), pp. 192–196.
- [41] Z. Jacob et al. “Engineering photonic density of states using metamaterials”. *Applied Physics B* 100 (2010), pp. 215–218.
- [42] Harish N. S. Krishnamoorthy et al. “Topological Transitions in Metamaterials”. *Science* 336 (2012), pp. 205–209.
- [43] Max Born and Emil Wolf. *Principles of Optics*. 6th edition. Pergamon, (1980). ISBN: 9780080264820.
- [44] Dylan Lu et al. “Enhancing spontaneous emission rates of molecules using nanopatterned multilayer hyperbolic metamaterials”. *Nature Nanotechnology* 9 (2014), p. 48.
- [45] Lorenzo Ferrari et al. “Hyperbolic metamaterials for dispersion-assisted directional light emission”. *Nanoscale* 9 (2017), pp. 9034–9048.

- [46] V. M. Agranovich and V. E. Kravtsov. “Notes on crystal optics of superlattices”. *Solid State Communications* 55 (1985), pp. 85–90.
- [47] Georgia T. Papadakis et al. “Retrieval of material parameters for uniaxial metamaterials”. *Phys. Rev. B* 91 (2015), p. 155406.
- [48] Georgia T. Papadakis and Harry A. Atwater. “Field-effect induced tunability in hyperbolic metamaterials”. *Phys. Rev. B* 92 (2015), p. 184101.
- [49] D. E. Aspnes. “Local field effects and effective medium theory: A macroscopic perspective”. *American Journal of Physics* 50 (1982), p. 704.
- [50] J. I. Gittleman and B. Abeles. “Comparison of the effective medium and the Maxwell-Garnett predictions for the dielectric constants of granular metals”. *Phys. Rev. B* 15 (1977), pp. 3273–3275.
- [51] D. Stroud. “Generalized effective-medium approach to the conductivity of an inhomogeneous material”. *Phys. Rev. B* 12 (1975), pp. 3368–3373.
- [52] G. A. Niklasson, C. G. Granqvist, and O. Hunderi. “Effective medium models for the optical properties of inhomogeneous materials”. *Appl. Opt.* 20 (1981), pp. 26–30.
- [53] David R. Smith and John B. Pendry. “Homogenization of metamaterials by field averaging (invited paper)”. *J. Opt. Soc. Am. B* 23 (2006), pp. 391–403.
- [54] Andrea Alù. “Restoring the physical meaning of metamaterial constitutive parameters”. *Phys. Rev. B* 83 (2011), p. 081102.
- [55] Mário G. Silveirinha. “Metamaterial homogenization approach with application to the characterization of microstructured composites with negative parameters”. *Phys. Rev. B* 75 (2007), p. 115104.
- [56] Mário G. Silveirinha. “Generalized Lorentz-Lorenz formulas for microstructured materials”. *Phys. Rev. B* 76 (2007), p. 245117.
- [57] D. R. Smith et al. “Determination of effective permittivity and permeability of metamaterials from reflection and transmission coefficients”. *Phys. Rev. B* 65 (2002), p. 195104.
- [58] D. R. Smith et al. “Electromagnetic parameter retrieval from inhomogeneous metamaterials”. *Phys. Rev. E* 71 (2005), p. 036617.
- [59] Xudong Chen et al. “Robust method to retrieve the constitutive effective parameters of metamaterials”. *Phys. Rev. E* 70 (2004), p. 016608.
- [60] Christoph Menzel et al. “Retrieving effective parameters for metamaterials at oblique incidence”. *Phys. Rev. B* 77 (2008), p. 195328.
- [61] Lifeng Li. “New formulation of the Fourier modal method for crossed surface-relief gratings”. *J. Opt. Soc. Am. A* 14 (1997), pp. 2758–2767.

- [62] Uday K. Chettiar et al. “Negative index metamaterial combining magnetic resonators with metal films”. *Opt. Express* 14 (2006), pp. 7872–7877.
- [63] T. Koschny et al. “Resonant and antiresonant frequency dependence of the effective parameters of metamaterials”. *Phys. Rev. E* 68 (2003), p. 065602.
- [64] C.R. Simovski and S.A. Tretyakov. “On effective electromagnetic parameters of artificial nanostructured magnetic materials”. *Photonics and Nanostructures - Fundamentals and Applications* 8 (2010), pp. 254–263.
- [65] Christoph Menzel et al. “Validity of effective material parameters for optical fishnet metamaterials”. *Phys. Rev. B* 81 (2010), p. 035320.
- [66] Vadim A. Markel. “Can the imaginary part of permeability be negative?” *Phys. Rev. E* 78 (2008), p. 026608.
- [67] Anan Fang, Thomas Koschny, and Costas M. Soukoulis. “Optical anisotropic metamaterials: Negative refraction and focusing”. *Phys. Rev. B* 79 (2009), p. 245127.
- [68] Ayed Al Sayem et al. “Negative Refraction with Superior Transmission in Graphene-Hexagonal Boron Nitride (hBN) Multilayer Hyper Crystal”. *Scientific Reports* 6 (2016), p. 25442.
- [69] Xingjie Ni et al. “Loss-compensated and active hyperbolic metamaterials”. *Opt. Express* 19 (2011), pp. 25242–25254.
- [70] Salvatore Campione et al. “Realizing high-quality, ultralarge momentum states and ultrafast topological transitions using semiconductor hyperbolic metamaterials”. *J. Opt. Soc. Am. B* 32 (2015), pp. 1809–1815.
- [71] Evgenii E. Narimanov. “Photonic Hypercrystals”. *Phys. Rev. X* 4 (2014), p. 041014.
- [72] V. M. Agranovich et al. “Linear and nonlinear wave propagation in negative refraction metamaterials”. *Phys. Rev. B* 69 (2004), p. 165112.
- [73] Carsten Rockstuhl et al. “Resonances in complementary metamaterials and nanoapertures”. *Opt. Express* 16 (2008), pp. 2080–2090.
- [74] Andrea Alù and Nader Engheta. “Dynamical theory of artificial optical magnetism produced by rings of plasmonic nanoparticles”. *Phys. Rev. B* 78 (2008), p. 085112.
- [75] Aleksandar D. Rakić et al. “Optical properties of metallic films for vertical-cavity optoelectronic devices”. *Appl. Opt.* 37 (1998), pp. 5271–5283.

- [76] Z. Jacob et al. “Engineering photonic density of states using metamaterials”. *Applied Physics B* 100 (2010), pp. 215–218.
- [77] Vladimir M. Shalaev. “Optical negative-index metamaterials”. *Nat Photon.* 1 (2007), pp. 41–48.
- [78] James C. Ginn et al. “Realizing Optical Magnetism from Dielectric Metamaterials”. *Phys. Rev. Lett.* 108 (2012), p. 097402.
- [79] Gennady Shvets and Yaroslav A Urzhumov. “Negative index metamaterials based on two-dimensional metallic structures”. *Journal of Optics A: Pure and Applied Optics* 8 (2006), S122.
- [80] J. Zhou et al. “Saturation of the Magnetic Response of Split-Ring Resonators at Optical Frequencies”. *Phys. Rev. Lett.* 95 (2005), p. 223902.
- [81] Lutz Langguth and Harald Giessen. “Coupling strength of complex plasmonic structures in the multiple dipole approximation”. *Opt. Express* 19 (2011), pp. 22156–22166.
- [82] R. S. Penciu et al. “Multi-gap individual and coupled split-ring resonator structures”. *Opt. Express* 16 (2008), pp. 18131–18144.
- [83] Guy Lipworth et al. “Magnetic Metamaterial Superlens for Increased Range Wireless Power Transfer”. *Scientific Reports* 4 (2014), p. 3642.
- [84] F. Capolino. *Theory and Phenomena of Metamaterials*. Metamaterials Handbook Series. CRC Press, (2009). ISBN: 9781420054262.
- [85] Nader Engheta, Alessandro Salandrino, and Andrea Alù. “Circuit Elements at Optical Frequencies: Nanoinductors, Nanocapacitors, and Nanoresistors”. *Phys. Rev. Lett.* 95 (2005), p. 095504.
- [86] Hadiseh Alaeian and Jennifer A. Dionne. “Plasmon nanoparticle superlattices as optical-frequency magnetic metamaterials”. *Opt. Express* 20 (2012), pp. 15781–15796.
- [87] Saman Jahani and Zubin Jacob. “All-dielectric metamaterials”. *Nature Nano* 711 (2016), pp. 23–36.
- [88] Isabelle Staude and Jorg Schilling. “Metamaterial-inspired silicon nanophotonics”. *Nat Photon.* 11 (2017), pp. 247–284.
- [89] S O’Brien and J B Pendry. “Magnetic activity at infrared frequencies in structured metallic photonic crystals”. *Journal of Physics: Condensed Matter* 14 (2002), p. 6383.
- [90] Ting Xu et al. “All-angle negative refraction and active flat lensing of ultraviolet light”. *Nature* 497 (2013), p. 470.
- [91] Justin Elser and Viktor A. Podolskiy. “Scattering-Free Plasmonic Optics with Anisotropic Metamaterials”. *Phys. Rev. Lett.* 100 (2008), p. 066402.

- [92] Maier S. A and Atwater H. A. “Plasmonics: Localization and Guiding of Electromagnetic Energy in Metal/Dielectric Structures”. *Journal of Applied Physics* 98 (2005), p. 011101.
- [93] Jennifer A. Dionne et al. “Are negative index materials achievable with surface plasmon waveguides? A case study of three plasmonic geometries”. *Opt. Express* 16 (2008), pp. 19001–19017.
- [94] Y. t. Fang et al. “Tamm states of one-dimensional metal-dielectric photonic crystal”. *IET Optoelectronics* 7 (2013), pp. 9–13.
- [95] Polina V. Kapitanova et al. “Photonic spin Hall effect in hyperbolic metamaterials for polarization-controlled routing of subwavelength modes”. *Nature Communications* 5 (2014), p. 3226.
- [96] Ahmed M. Mahmoud and Nader Engheta. “Wave–matter interactions in epsilon-and-mu-near-zero structures”. *Nature Communications* 5 (2014).
- [97] Ruben Maas et al. “Experimental realization of an epsilon-near-zero metamaterial at visible wavelengths”. *Nat Photon* 7 (2013), pp. 907–912.
- [98] Roberto Merlin. “Metamaterials and the Landau–Lifshitz permeability argument: Large permittivity begets high-frequency magnetism”. *Proceedings of the National Academy of Sciences* 106 (2009), pp. 1693–1698.
- [99] Xudong Chen et al. “Robust method to retrieve the constitutive effective parameters of metamaterials”. *Phys. Rev. E* 70 (2004), p. 016608.
- [100] Krishnan Thyagarajan et al. “Highly Improved Fabrication of Ag and Al Nanostructures for UV and Nonlinear Plasmonics”. *Advanced Optical Materials* 4 (2016), pp. 871–876.
- [101] T. Tumkur et al. “Control of spontaneous emission in a volume of functionalized hyperbolic metamaterial”. *Appl. Phys. Lett.* 99 (2011), p. 15115.
- [102] J. Kim et al. “Improving the radiative decay rate for dye molecules with hyperbolic metamaterials”. *Opt. Express* 20 (2012), pp. 8100–8116.
- [103] X. Ni et al. “Effect of metallic and hyperbolic metamaterial surfaces on electric and magnetic dipole emission transitions”. *Applied Physics B* 103 (2011), pp. 553–558.
- [104] Ryosuke Watanabe, Masanobu Iwanaga, and Teruya Ishihara. “s-polarization Brewster’s angle of stratified metal–dielectric metamaterial in optical regime”. *Physica Status Solidi (b)* 245 (2008), pp. 2696–2701.
- [105] Conor T. Riley et al. “Near-perfect broadband absorption from hyperbolic metamaterial nanoparticles”. *Proceedings of the National Academy of Sciences* 114 (2017), pp. 1264–1268.

- [106] E. E. Narimanov et al. “Reduced reflection from roughened hyperbolic metamaterial”. *Opt. Express* 21 (2013), pp. 14956–14961.
- [107] G. V. Dedkov and A. A. Kyasov. “Equilibrium near and far electromagnetic field structures at a flat boundary of the half-space filled with a homogeneous dielectric (magnetic) medium”. *Technical Physics Letters* 32 (2006), pp. 223–225.
- [108] E. Anemogiannis, E. N. Glytsis, and T. K. Gaylord. “Determination of guided and leaky modes in lossless and lossy planar multilayer optical waveguides: reflection pole method and wavevector density method”. *Journal of Lightwave Technology* 17 (1999), pp. 929–941.
- [109] E. N. Economou. “Surface Plasmons in Thin Films”. *Phys. Rev.* 182 (1969), pp. 539–554.
- [110] A. P. Vinogradov et al. “Surface state peculiarities in one-dimensional photonic crystal interfaces”. *Phys. Rev. B* 74 (2006), p. 045128.
- [111] Jeffrey N. Anker et al. “Biosensing with plasmonic nanosensors”. *Nat Mater.* 7 (2008), pp. 442–453.
- [112] Manda Xiao et al. “Plasmon-enhanced chemical reactions”. *J. Mater. Chem. A* 1 (2013), pp. 5790–5805.
- [113] David J. Bergman and Mark I. Stockman. “Surface Plasmon Amplification by Stimulated Emission of Radiation: Quantum Generation of Coherent Surface Plasmons in Nanosystems”. *Phys. Rev. Lett.* 90 (2003), p. 027402.
- [114] Pierre Berini and Israel De Leon. “Surface plasmon-polariton amplifiers and lasers”. *Nat Photon* 6 (2012), pp. 16–24.
- [115] M. A. Noginov et al. “Stimulated Emission of Surface Plasmon Polaritons”. *Phys. Rev. Lett.* 101 (2008), p. 226806.
- [116] Toshihiro Nakamura. “Enhancement of Visible-Luminescence Saturation Intensity by Surface Plasmons in Ag/ZnO Films”. *Phys. Rev. Applied* 6 (2016), p. 044009.
- [117] Alexei Tcherniak et al. “One-Photon Plasmon Luminescence and Its Application to Correlation Spectroscopy as a Probe for Rotational and Translational Dynamics of Gold Nanorods”. *The Journal of Physical Chemistry C* 115 (2011), pp. 15938–15949.
- [118] Albert Polman and Harry A. Atwater. “Plasmonics: optics at the nanoscale”. *Materials Today* 8 (2005), p. 56.
- [119] Achim Woessner et al. “Highly confined low-loss plasmons in graphene–boron nitride heterostructures”. *Nature Materials* 14 (2015), pp. 421–425.

- [120] Victor W. Brar et al. “Highly Confined Tunable Mid-Infrared Plasmonics in Graphene Nanoresonators”. *Nano Letters* 13 (2013), pp. 2541–2547.
- [121] Ashkan Vakil and Nader Engheta. “Transformation Optics Using Graphene”. *Science* 332 (2011), pp. 1291–1294.
- [122] J.D. Caldwell et al. “Low-loss, infrared and terahertz nanophotonics using surface phonon polaritons”. *Nanophotonics* 4 (2015), pp. 44–68.
- [123] Peining Li et al. “Hyperbolic phonon-polaritons in boron nitride for near-field optical imaging and focusing”. *Nature Communications* 6 (2015), pp. 9059–9072.
- [124] Joshua D. Caldwell et al. “Low-Loss, Extreme Subdiffraction Photon Confinement via Silicon Carbide Localized Surface Phonon Polariton Resonators”. *Nano Letters* 13 (2013), pp. 3690–3697.
- [125] M. E. Sasin et al. “Tamm plasmon polaritons: Slow and spatially compact light”. *Applied Physics Letters* 92 (2008), p. 251112.
- [126] M. Kaliteevski et al. “Tamm plasmon-polaritons: Possible electromagnetic states at the interface of a metal and a dielectric Bragg mirror”. *Phys. Rev. B* 76 (2007), p. 165415.
- [127] G. Isic et al. “Tamm plasmon modes on semi-infinite metallodielectric superlattices”. *Scientific Reports* 7 (2018), p. 3746.
- [128] Jacob B. Khurgin. “Two-dimensional exciton-polariton-light guiding by transition metal dichalcogenide monolayers”. *Optica* 2 (2015), pp. 740–742.
- [129] Yilei Li et al. “Measurement of the optical dielectric function of monolayer transition-metal dichalcogenides: MoS₂, MoSe₂, WS₂, and WSe₂”. *Phys. Rev. B* 90 (2014), p. 205422.
- [130] S. Dai et al. “Tunable Phonon Polaritons in Atomically Thin van der Waals Crystals of Boron Nitride”. *Science* 343 (2014), pp. 1125–1129.
- [131] R. Hillenbrand, T. Taubner, and F. Keilmann. “Phonon-enhanced light-matter interaction at the nanometre scale”. *Nature* 418 (2002), pp. 159–162.
- [132] S. Amarie and F. Keilmann. “Broadband-infrared assessment of phonon resonance in scattering-type near-field microscopy”. *Phys. Rev. B* 83 (2011), p. 045404.
- [133] D. E. Aspnes and A. A. Studna. “Dielectric functions and optical parameters of Si, Ge, GaP, GaAs, GaSb, InP, InAs, and InSb from 1.5 to 6.0 eV”. *Phys. Rev. B* 27 (1983), pp. 985–1009. DOI: 10.1103/PhysRevB.27.985.

- [134] S. W. Koch et al. “Semiconductor excitons in new light”. *Nature Materials* 5 (2006), pp. 523–531.
- [135] J. A. Dionne et al. “Plasmon slot waveguides: Towards chip-scale propagation with subwavelength-scale localization”. *Phys. Rev. B* 73 (2006), p. 035407.
- [136] Chengkun Chen et al. “Efficient and accurate numerical analysis of multilayer planar optical waveguides in lossy anisotropic media”. *Opt. Express* 7 (2000), pp. 260–272.
- [137] R. Rodriguez-Berral, F. Mesa, and F. Medina. “Appropriate formulation of the Characteristic equation for open nonreciprocal Layered waveguides with different upper and lower half-spaces”. *IEEE Transactions on Microwave Theory and Techniques* 53 (2005), pp. 1613–1623.
- [138] J. Zhu, X. Zhang, and R. Song. “A Unified Mode Solver for Optical Waveguides Based on Mapped Barycentric Rational Chebyshev Differentiation Matrix”. *Journal of Lightwave Technology* 28 (2010), pp. 1802–1810.
- [139] Wen-Jeng Hsueh and Jhih-Chang Lin. “Stable and accurate method for modal analysis of multilayer waveguides using a graph approach”. *J. Opt. Soc. Am. A* 24 (2007), pp. 825–830.
- [140] Luke A. Sweatlock and Kenneth Diest. “Vanadium dioxide based plasmonic modulators”. *Opt. Express* 20 (2012), pp. 8700–8709.
- [141] A. Khalatpour et al. “Modified Smooth Transition Method for Determination of Complex Modes in Multilayer Waveguide Structures”. *Journal of Lightwave Technology* 28 (2010), pp. 2851–2855.
- [142] Y. Zhou et al. “Theoretical investigation of optimal propagation performance in multilayer long-range surface plasmon waveguide” (2010), pp. 1–5.
- [143] J. Petracek and K. Singh. “Determination of leaky modes in planar multilayer waveguides”. *IEEE Photonics Technology Letters* 14 (2002), pp. 810–812.
- [144] Amir Hosseini, Arthur Nieuwoudt, and Yehia Massoud. “Efficient simulation of subwavelength plasmonic waveguides using implicitly restarted Arnoldi”. *Opt. Express* 14 (2006), pp. 7291–7298.
- [145] Nikolai Christian Passler and Alexander Paarmann. “Generalized 4 × 4 matrix formalism for light propagation in anisotropic stratified media: study of surface phonon polaritons in polar dielectric heterostructures”. *J. Opt. Soc. Am. B* 34 (2017), pp. 2128–2139.
- [146] Pochi Yeh. “Electromagnetic propagation in birefringent layered media”. *J. Opt. Soc. Am.* 69 (1979), pp. 742–756.

- [147] Dwight W. Berreman. “Optics in Stratified and Anisotropic Media: 4×4 -Matrix Formulation”. *J. Opt. Soc. Am.* 62 (1972), pp. 502–510.
- [148] Meng Xiao, Z. Q. Zhang, and C. T. Chan. “Surface Impedance and Bulk Band Geometric Phases in One-Dimensional Systems”. *Phys. Rev. X* 4 (2014), p. 021017.
- [149] Artur R. Davoyan and Nader Engheta. “Salient Features of Deeply Subwavelength Guiding of Terahertz Radiation in Graphene-Coated Fibers”. *ACS Photonics* 3 (2016), pp. 737–742.
- [150] Martin G. Blaber, Matthew D. Arnold, and Michael J. Ford. “Search for the Ideal Plasmonic Nanoshell: The Effects of Surface Scattering and Alternatives to Gold and Silver”. *The Journal of Physical Chemistry C* 113 (2009), pp. 3041–3045.
- [151] Ewold Verhagen et al. “Near-field visualization of strongly confined surface plasmon polaritons in metal-insulator-metal waveguides”. *Nano Letters* 8 (2008), pp. 2925–2929.
- [152] H. H. Li. “Refractive index of silicon and germanium and its wavelength and temperature derivatives”. *Journal of Physical and Chemical Reference Data* 9 (1980), pp. 561–658.
- [153] Ho W. Lee et al. “Nanoscale Conducting Oxide PlasMOSTor”. *Nano Letters* 14 (2014), pp. 6463–6468.
- [154] Yao-Wei Huang et al. “Gate-Tunable Conducting Oxide Metasurfaces”. *Nano Letters* 16 (2016), pp. 5319–5325.
- [155] Suffian N. Khan and Duane D. Johnson. “Lifshitz Transition and Chemical Instabilities in $\text{Ba}_{1-x}\text{K}_x\text{Fe}_2\text{As}_2$ Superconductors”. *Phys. Rev. Lett.* 112 (2014), p. 156401.
- [156] Madhab Neupane et al. “Observation of a three-dimensional topological Dirac semimetal phase in high-mobility Cd_3As_2 ”. *Nature Communications* 5 (2014), p. 3786.
- [157] Y. L. Chen et al. “Experimental Realization of a Three-Dimensional Topological Insulator, Bi_2Te_3 ”. *Science* 325 (2009), pp. 178–181.
- [158] Mikael C. Rechtsman et al. “Photonic Floquet topological insulators”. *Nature* 496 (2013), p. 196.
- [159] Matthew J. Dicken et al. “Frequency tunable near-infrared metamaterials based on VO_2 phase transition”. *Opt. Express* 17 (2009), pp. 18330–18339.
- [160] Jun-Yu Ou et al. “An electromechanically reconfigurable plasmonic metamaterial operating in the near-infrared”. *Nature Nanotechnology* 8 (2013), p. 252.

- [161] Eyal Feigenbaum, Kenneth Diest, and Harry A. Atwater. “Unity-Order Index Change in Transparent Conducting Oxides at Visible Frequencies”. *Nano Letters* 10 (2010), pp. 2111–2116.
- [162] Z. Lu, W. Zhao, and K. Shi. “Ultracompact Electroabsorption Modulators Based on Tunable Epsilon-Near-Zero-Slot Waveguides”. *IEEE Photonics Journal* 4 (2012), pp. 735–740.
- [163] Shiyang Zhu, G. Q. Lo, and D. L. Kwong. “Phase modulation in horizontal metal-insulator-silicon-insulator-metal plasmonic waveguides”. *Opt. Express* 21 (2013), pp. 8320–8330.
- [164] Viktoriia E. Babicheva et al. “Towards CMOS-compatible nanophotonics: Ultra-compact modulators using alternative plasmonic materials”. *Opt. Express* 21 (2013), pp. 27326–27337.
- [165] Gururaj V. Naik, Jongbum Kim, and Alexandra Boltasseva. “Oxides and nitrides as alternative plasmonic materials in the optical range”. *Opt. Mater. Express* 1 (2011), pp. 1090–1099.
- [166] Alexandra Boltasseva and Harry A. Atwater. “Low-Loss Plasmonic Metamaterials”. *Science* 331 (2011), pp. 290–291.
- [167] Xiaoge Liu et al. “Quantification and impact of nonparabolicity of the conduction band of indium tin oxide on its plasmonic properties”. *Applied Physics Letters* 105 (2014), p. 181117.
- [168] Fei Yi et al. “Voltage tuning of plasmonic absorbers by indium tin oxide”. *Applied Physics Letters* 102 (2013), p. 221102.
- [169] Alok P. Vasudev et al. “Electro-optical modulation of a silicon waveguide with an “epsilon-near-zero” material”. *Opt. Express* 21 (2013), pp. 26387–26397.
- [170] F. Michelotti et al. “Thickness dependence of surface plasmon polariton dispersion in transparent conducting oxide films at 1.55 μm ”. *Opt. Lett.* 34 (2009), pp. 839–841.
- [171] Cédric Sire et al. “Statistics of electrical breakdown field in HfO₂ and SiO₂ films from millimeter to nanometer length scales”. *Applied Physics Letters* 91 (2007), p. 242905.
- [172] Carey M. Tanner et al. “Electrical performance of Al₂O₃ gate dielectric films deposited by atomic layer deposition on 4H-SiC”. *Applied Physics Letters* 91 (2007), p. 203510.
- [173] M.D. Groner et al. “Electrical characterization of thin Al₂O₃ films grown by atomic layer deposition on silicon and various metal substrates”. *Thin Solid Films* 413 (2002), pp. 186–197.

- [174] Jiro Yota, Hong Shen, and Ravi Ramanathan. “Characterization of atomic layer deposition HfO₂, Al₂O₃, and plasma-enhanced chemical vapor deposition Si₃N₄ as metal–insulator–metal capacitor dielectric for GaAs HBT technology”. *Journal of Vacuum Science & Technology A: Vacuum, Surfaces, and Films* 31 (2013), 01A134.
- [175] J. Robertson. “High dielectric constant oxides”. *Eur. Phys. J. Appl. Phys.* 28 (2004), pp. 265–291.
- [176] Z. M. Rittersma et al. “HfSiO₄ Dielectric Layers Deposited by ALD Using HfCl₄ and NH₂ (CH₂)₃Si (OC₂H₅)₃ Precursors”. *Journal of the Electrochemical Society* 151 (2004), pp. 716–722.
- [177] Flora M. Li et al. “High-k (k=30) amorphous hafnium oxide films from high rate room temperature deposition”. *Applied Physics Letters* 98 (2011), p. 252903.
- [178] Young Hee Kim et al. “Thickness dependence of Weibull slopes of HfO₂ gate dielectrics”. *IEEE Electron Device Letters* 24 (2003), pp. 40–42.
- [179] Woo-Jun Yoon and Paul R. Berger. “Atomic layer deposited HfO₂ gate dielectrics for low-voltage operating, high-performance poly-(3-hexythiophene) organic thin-film transistors”. *Organic Electronics* 11 (2010), pp. 1719–1722.
- [180] Mao Wei et al. “The effect of a HfO₂ insulator on the improvement of breakdown voltage in field-plated GaN-based HEMT”. *Chinese Physics B* 20 (2011), p. 097203.
- [181] Chin-Sheng Pang and Jenn-Gwo Hwu. “Improvement in the breakdown endurance of high- κ dielectric by utilizing stacking technology and adding sufficient interfacial layer”. *Nanoscale Research Letters* 9 (2014), p. 464.
- [182] Alok P. Vasudev et al. “Electro-optical modulation of a silicon waveguide with an epsilon-near-zero material”. *Opt. Express* 21 (2013), p. 26387.
- [183] D. L. Wood et al. “Optical properties of cubic hafnia stabilized with yttria”. *Appl. Opt.* 29 (1990), pp. 604–607.
- [184] K. S. Novoselov et al. “Two-dimensional gas of massless Dirac fermions in graphene”. *Nature* 438 (2005), p. 197.
- [185] L A Falkovsky. “Optical properties of graphene”. *Journal of Physics: Conference Series* 129 (2008), p. 012004.
- [186] Ivan V. Iorsh et al. “Hyperbolic metamaterials based on multilayer graphene structures”. *Phys. Rev. B* 87 (2013), p. 075416.
- [187] Mohamed A. K. Othman, Caner Guclu, and Filippo Capolino. “Graphene-based tunable hyperbolic metamaterials and enhanced near-field absorption”. *Opt. Express* 21 (2013), pp. 7614–7632.

- [188] Soo Jin Kim et al. “Creating semiconductor metafilms with designer absorption spectra”. *Nature Communications* 6 (2015), p. 7591.
- [189] Daniel Gall. “Electron mean free path in elemental metals”. *Journal of Applied Physics* 119 (2016), p. 085101.
- [190] Deep Jariwala, Tobin J. Marks, and Mark C.e Hersam. “Mixed-dimensional van der Waals heterostructures”. *Nature Materials* 16 (2017), p. 170.
- [191] Joshua D. Caldwell et al. “Atomic-scale photonic hybrids for mid-infrared and terahertz nanophotonics”. *Nature Nanotechnology* 11 (2016), p. 9.
- [192] S. Dai et al. “Graphene on hexagonal boron nitride as a tunable hyperbolic metamaterial”. *Nature Nanotechnology* 10 (2015), p. 682.
- [193] Antonio Politano and Gennaro Chiarello. “Plasmon modes in graphene: status and prospect”. *Nanoscale* 6 (2014), pp. 10927–10940.
- [194] Xiaomu Wang et al. “High-responsivity graphene/silicon-heterostructure waveguide photodetectors”. *Nature Photonics* 7 (2013), p. 888.
- [195] Prineha Narang et al. “Effects of Interlayer Coupling on Hot-Carrier Dynamics in Graphene-Derived van der Waals Heterostructures”. *Advanced Optical Materials* 5 (2017), p. 1600914.
- [196] Ana M. Brown et al. “Nonradiative Plasmon Decay and Hot Carrier Dynamics: Effects of Phonons, Surfaces, and Geometry”. *ACS Nano* 10 (2016), pp. 957–966.
- [197] Ana M. Brown et al. “Ab initio phonon coupling and optical response of hot electrons in plasmonic metals”. *Phys. Rev. B* 94 (2016), p. 075120.
- [198] Hui-Shen Shen, Yu-Mou Xu, and Chen-Li Zhang. “Graphene: Why buckling occurs?” *Applied Physics Letters* 102 (2013), p. 131905.
- [199] Yu-Ming Lin et al. “Wafer-Scale Graphene Integrated Circuit”. *Science* 332 (2011), pp. 1294–1297.
- [200] Sharmila N. Shirodkar and Efthimios Kaxiras. “Li intercalation at graphene / hexagonal boron nitride interfaces”. *Phys. Rev. B* 93 (2016), p. 245438.
- [201] S. N. Shirodkar et al. “Visible quantum plasmons in highly-doped few-layer graphene”. *arxiv.org* (2017).
- [202] E. A. Taft and H. R. Philipp. “Optical Properties of Graphite”. *Phys. Rev.* 138 (1965), A197–A202.
- [203] Andrea Alù and Nader Engheta. “Optical nanotransmission lines: synthesis of planar left-handed metamaterials in the infrared and visible regimes”. *J. Opt. Soc. Am. B* 23 (2006), pp. 571–583.
- [204] Aaswath P. Raman et al. “Magnetic hyperbolic optical metamaterials”. *Nature* 515 (2014), p. 540.

- [205] Deep Jariwala et al. “Near-Unity Absorption in van der Waals Semiconductors for Ultrathin Optoelectronics”. *Nano Letters* 16 (2016), pp. 5482–5487.
- [206] Tim H. Taminiau et al. “Quantifying the magnetic nature of light emission”. *Nature Communications* 3 (2012), p. 979.
- [207] Tianhua Feng et al. “Isotropic Magnetic Purcell Effect”. *ACS Photonics* 0 (2018), in press.
- [208] Ognjen Ilic et al. “Overcoming the black body limit in plasmonic and graphene near-field thermophotovoltaic systems”. *Opt. Express* 20 (2012), A366–A384.
- [209] Pablo Rodriguez-Lopez et al. “Casimir force phase transitions in the graphene family”. *Nature Communications* 8 (2017), p. 14699.
- [210] C. L. Cortes et al. “Quantum nanophotonics using hyperbolic metamaterials”. *Journal of Optics* 14 (2012), p. 063001.
- [211] Cristian L. Cortes and Zubin Jacob. “Photonic analog of a van Hove singularity in metamaterials”. *Phys. Rev. B* 88 (2013), p. 045407.
- [212] Torben Winzer and Ermin Malić. “Impact of Auger processes on carrier dynamics in graphene”. *Phys. Rev. B* 85 (2012), p. 241404.

A p p e n d i x A

APPENDIX

A.1 Transfer Matrix Equations for an infinite bilayer heterostructure

For a detailed presentation of the transfer matrix approach, the reader is encouraged to see [1]. In Section 2.3 we discussed the case of an unbound layered medium composed of two materials with indices $n_{1,2}$ (in the absence of magnetic properties we have $n_{1,2} = \sqrt{\epsilon_{1,2}}$) and thicknesses $l_{1,2}$ (see Fig. 2.2). We present below the transfer matrix elements A , B , C , D , referring to Eqs. (2.17)-(2.18). For TE polarization, we have:

$$A_{\text{TE}} = e^{-ik_{z,1}l_1} \left[\cos(k_{z,2}l_2) - \frac{1}{2}i \left(\frac{k_{z,2}}{k_{z,1}} + \frac{k_{z,1}}{k_{z,2}} \right) \sin(k_{z,2}l_2) \right] \quad (\text{A.1})$$

$$B_{\text{TE}} = e^{ik_{z,1}l_1} \left[-\frac{1}{2}i \left(\frac{k_{z,2}}{k_{z,1}} - \frac{k_{z,1}}{k_{z,2}} \right) \sin(k_{z,2}l_2) \right] \quad (\text{A.2})$$

$$C_{\text{TE}} = e^{-ik_{z,1}l_1} \left[\frac{1}{2}i \left(\frac{k_{z,2}}{k_{z,1}} - \frac{k_{z,1}}{k_{z,2}} \right) \sin(k_{z,2}l_2) \right] \quad (\text{A.3})$$

$$D_{\text{TE}} = e^{ik_{z,1}l_1} \left[\cos(k_{z,2}l_2) + \frac{1}{2}i \left(\frac{k_{z,2}}{k_{z,1}} + \frac{k_{z,1}}{k_{z,2}} \right) \sin(k_{z,2}l_2) \right] \quad (\text{A.4})$$

Similarly, for TM polarization, the matrix elements are:

$$A_{\text{TM}} = e^{-ik_{z,1}l_1} \left[\cos(k_{z,2}l_2) - \frac{1}{2}i \left(\frac{n_2^2 k_{z,1}}{n_1^2 k_{z,2}} + \frac{n_1^2 k_{z,2}}{n_2^2 k_{z,1}} \right) \sin(k_{z,2}l_2) \right] \quad (\text{A.5})$$

$$B_{\text{TM}} = e^{ik_{z,1}l_1} \left[-\frac{1}{2}i \left(\frac{n_2^2 k_{z,1}}{n_1^2 k_{z,2}} - \frac{n_1^2 k_{z,2}}{n_2^2 k_{z,1}} \right) \sin(k_{z,2}l_2) \right] \quad (\text{A.6})$$

$$C_{\text{TM}} = e^{-ik_{z,1}l_1} \left[\frac{1}{2}i \left(\frac{n_2^2 k_{z,1}}{n_1^2 k_{z,2}} - \frac{n_1^2 k_{z,2}}{n_2^2 k_{z,1}} \right) \sin(k_{z,2}l_2) \right] \quad (\text{A.7})$$

$$D_{\text{TM}} = e^{ik_{z,1}l_1} \left[\cos(k_{z,2}l_2) + \frac{1}{2}i \left(\frac{n_2^2 k_{z,1}}{n_1^2 k_{z,2}} - \frac{n_1^2 k_{z,2}}{n_2^2 k_{z,1}} \right) \sin(k_{z,2}l_2) \right] \quad (\text{A.8})$$

A.2 Counting optical states with the reflection pole method

In Section 3.8, and particularly in Fig. 3.11 we discussed the increase in the density of optical states (DOS) for multilayer configurations that, when homogenized, exhibit the response $\epsilon_o\epsilon_e < 0$ ($\mu_o\mu_e < 0$) for TM (TE) polarization. Here, we compute the number of optical states for the example system discussed in Fig. 3.11. We consider in-plane wavenumbers $k_{//}/k_o \in [0, n_{\text{diel}}]$ for radiation (bulk) modes, while $k_{//}/k_o > n_{\text{diel}}$ for surface waves, as discussed in detail in Section 4.3. Prior to reading this section, the reader is encouraged to study the reflection pole method (RPM) and its details (see Section 3.11 and [108]).

First, let's start with the physical picture of a multilayer system with complex reflection coefficients r_{TE} , r_{TM} , for the two linear polarizations. The analytical expression of the density of states is [210, 211]

$$\rho(\omega, d, \vec{k}) = \frac{3}{2|p|^2 k_1^3} \frac{k_{//}}{k_z} \left\{ \frac{1}{2} p_p^2 \left[(1+r_{\text{TE}} e^{2ik_z d}) k_1^2 + (1-r_{\text{TM}} e^{2ik_z d}) k_z^2 \right] + p_n^2 (1+r_{\text{TM}} e^{2ik_z d}) k_{//}^2 \right\} \quad (\text{A.9})$$

where p_p and p_n are the parallel and perpendicular components of a dipole moment located at distance d above the first planar interface, k_1 is the wavenumber in the incident medium and k_z is the normal component of the wavenumber inside the multilayer system. As explained in Section 3.8, the effective magnetic permeability has an effect mainly in the TE polarization characteristics of planar metamaterials, similar to the effective dielectric permittivity pertaining to TM properties. As can be seen from the first term in Eq. A.9, in order for the TE polarization to contribute to the density of optical states, the TE complex reflection coefficient must deviate from the value of -1 .

We perform analytical transfer matrix calculations and RPM calculations, together with finite element simulations investigating the TE properties of a fifty-five layers metamaterial consisting of silver and a dielectric material with refractive index n_{diel} , in the lossless limit, to simplify our analysis (similar to the one discussed in Figs. 3.11d, e). All finite element simulations were performed with the commercial package Comsol Multiphysics. We set the refractive index of the surrounding medium to be $n_{\text{sur}} = 1.55$, similar to Figs. 3.11d, e. Figs. A.1, A.2 show two cases: $n_{\text{diel}} = 1.55$ and $n_{\text{diel}} = 4$, respectively. The latter is the same as the case discussed in Fig. 3.11e.

In the case of $n_{\text{diel}} = 1.55$, no TE electromagnetic states couple to the multilayer metamaterial and its response is reflective as shown in Fig. A.1a. This is confirmed by analytical transfer matrix calculations of the TE reflectance (Fig. A.1d), which is almost unity, while absorption is negligible (Fig. A.1d). Furthermore, as can be

seen in Fig. A.1c, $\text{Re}(r_{\text{TE}})$ barely deviates from the value of -1 , indicating absence of TE polarization electromagnetic states, based on Eq. A.9. With use of the arguments explained in Section 4.3 regarding the RPM, we present the parameter $\frac{dm_{11\text{TE}}(\lambda)}{d\lambda}$ in Figs. A.1f and g for radiation (bulk) and bounded (surface) modes, respectively. No peaks are observed, confirming the absence of any TE states supported in the metamaterial in this frequency regime for the considered wavenumbers. The wavenumbers accounted for in Figs. A.1f, g are chosen based on the Gaussian beam in the finite element simulation shown in Fig. A.1a.

Furthermore, by homogenizing the layered metamaterial through [47], we obtain negative dielectric permittivity ϵ_o , while the magnetic permeabilities along both coordinate directions μ_o and μ_e remain positive (Fig. A.1b). For these values of ϵ_o , μ_o and μ_e , the dispersion equation for bulk propagating modes (Eq. 3.3) has no solutions, confirming further the absence of any optical states in this frequency regime.

By contrast, increasing the dielectric index to $n_{\text{diel}} = 4$ leads to a drastically different $\text{Re}(r_{\text{TE}})$ response, as shown in the simulation result of Supplementary Fig. A.2a. The metamaterial absorbs most of the incident field, as confirmed through analytical calculations showing enhanced TE absorption in Supplementary Fig. A.2e, while the TE reflectance vanishes at resonant wavelengths (Fig. A.2d). As seen in Fig. A.2c, now $\text{Re}(r_{\text{TE}})$ is drastically different from unity, indicating a TE contribution to the density of states, based on Eq. (A.9). The density of states enhancement is already obvious by the enhanced absorption, however we also show it explicitly in Fig. A.2f; the reflection pole peaks represent states and their number is equal to the number of bulk eigenmodes (or optical states) for the considered wavenumbers and wavelengths. The number of TE bound (surface) states is also enhanced, as peaks are also observed for wavenumbers $k_{\parallel}/k_o > n_{\text{sur}}$ (Fig. A.2g). This response is also interpreted in the effective homogeneous slab picture (with effective parameters ϵ_o , μ_o and μ_e); the TE response of the metamaterial is now hyperbolic as $\mu_o\mu_e < 0$ (Fig. A.2b). Similar to HMMs with $\epsilon_o\epsilon_e < 0$ supporting an enhanced density of TM states [41, 76, 210, 211], we show an equivalent response for TE polarization due to $\mu_o\mu_e < 0$.

A.3 Details on the electronic structure calculations in vdW heterostructures

Here we discuss the details for computing the electronic properties and sheet conductance of the graphene-based heterostructures discussed in Chapter 6. Both intraband and interband contributions to the sheet conductance discussed in Section 6.3 are extracted from the linearized Boltzmann equation using an *ab initio* collision

integral for the electron-phonon scattering processes [196]. The interband transitions term is evaluated using Fermi's Golden rule for the imaginary part, and then the Kramers-Kronig relation for the real part.

All these calculations use DFT predictions for the energies and matrix elements of both the electrons and the phonons, hence automatically accounting for electronic structure effects such as inter-layer interactions and response of electrons far from the Dirac point, as well as scattering against both acoustic and optical phonons including Umklapp and inter-valley processes. These calculations account for finite temperature occupations of electrons and phonons, as well as for the coupling of electrons with photons and phonons, thereby capturing all relevant radiative and non-radiative processes that contribute to the optical response. However, in this work, excitonic effects were neglected since the high free carrier density of the doped materials we consider would strongly screen electron-hole interactions [212]. See [196] for more details on the theoretical framework and references in [18].

For graphene and its heterostructures, changing the Fermi level E_F changes the equilibrium electron occupation factors in the Boltzmann equation as well as in Fermi's Golden rule. This affects both interband and intraband contributions to the sheet conductance, and we account for this by explicitly evaluating them for several different values of E_F , ranging from the neutral (undoped) value to ~ 1 eV above it. This computational treatment assumes ideal doping and neglects losses due to scattering by inactive dopants and defects introduced into the material; the effects of such nonidealities will be specific to the experimental strategy for doping and are not discussed here.

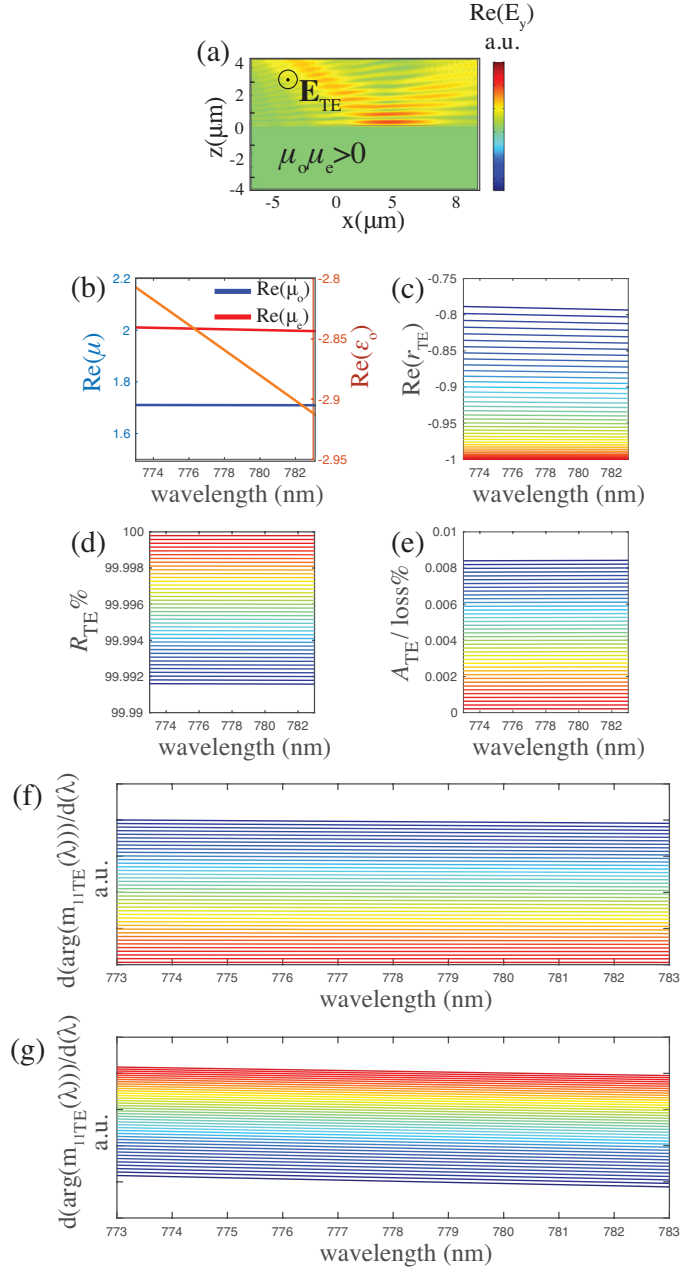


Figure A.1: (a) Simulation results for a fifty-five layers dielectric $n_{\text{diel}} = 1.5$: 50 nm/Ag: 20 nm multilayer metamaterial at 780 nm for TE polarization. The surrounding medium has index $n_{\text{sur}} = 1.55$. (b) Effective parameters for the metamaterial in (a). (c) $\text{Re}(r_{\text{TE}})$ barely deviates from the value of -1 . (d) TE polarization reflectance $R_{\text{TE}} = |r_{\text{TE}}|^2$. (e) TE polarization absorption. (f) reflection pole method for radiation (bulk) modes, (g) reflection pole method for bound (surface) modes. Note 1: (c), (d), (e), (f), (g) are transfer matrix analytical multilayer calculations for the multilayer described in (a). Note 2: For (c), (d), (e), (f): Colors: from blue to red: $k_{//}$ from $1.45k_o$ (blue) to $1.55k_o$ (red) - corresponding to the wavenumbers in the simulation of (a). Note 3: For (g): Colors: from blue to red: $k_{//}$ from $1.55k_o$ (blue) to $2k_o$ (red).

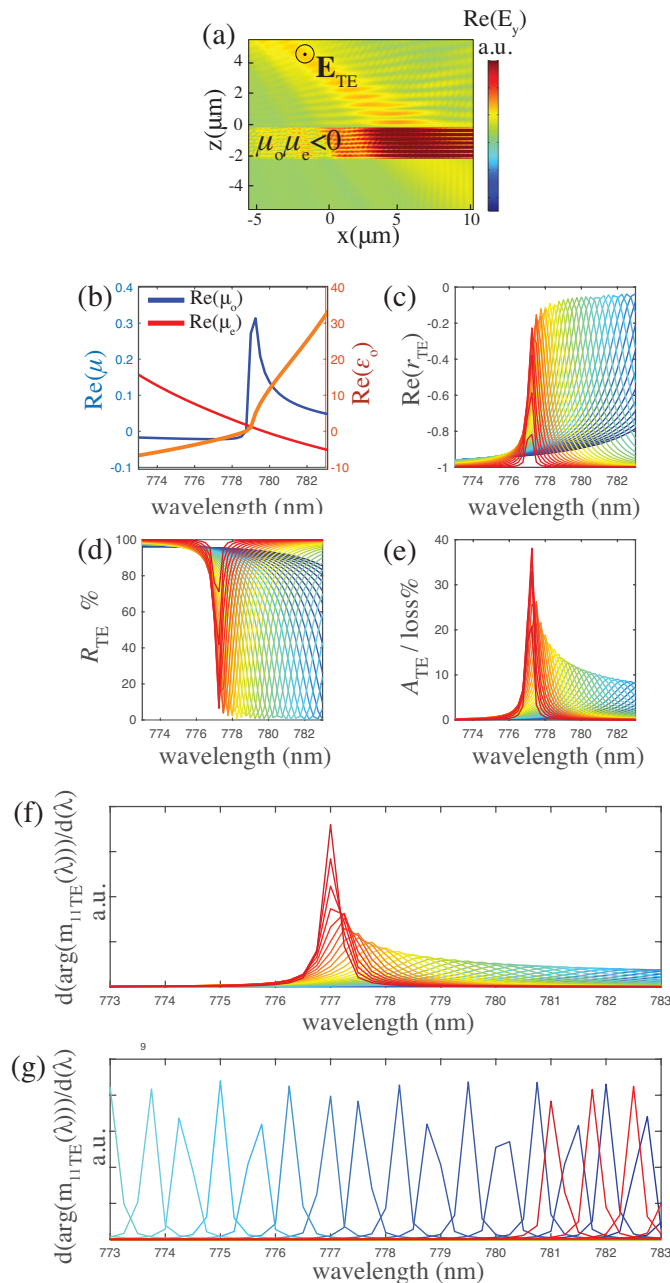


Figure A.2: (a) Simulation results for a fifty-five layers dielectric $n_{\text{diel}} = 4$: 50 nm/Ag: 20 nm multilayer metamaterial at 780 nm for TE polarization. The surrounding medium has index $n_{\text{sur}} = 1.55$. (b) Effective parameters for the metamaterial in (a). (c) $\text{Re}(r_{\text{TE}})$ deviates from the value of -1 indicating enhanced density of states. (d) TE polarization reflectance $R_{\text{TE}} = |r_{\text{TE}}|^2$. (e) TE polarization absorption. (f) reflection pole method for radiation (bulk) modes, (g) reflection pole method for bound (surface) modes. Note 1: (c), (d), (e), (f), (g) are transfer matrix analytical multilayer calculations for the multilayer described in (a). Note 2: For (c), (d), (e), (f): Colors: from blue to red: $k_{//}$ from $1.45k_o$ (blue) to $1.55k_o$ (red) - corresponding to the wavenumbers in the simulation of (a). Note 3: For (g): Colors: from blue to red: $k_{//}$ from $1.55k_o$ (blue) to $2k_o$ (red).